Hybrid High-Order methods for nonlinear solid mechanics

Nicolas Pignet

▶ **To cite this version:**

Nicolas Pignet. Hybrid High-Order methods for nonlinear solid mechanics. Numerical Analysis [math.NA]. Université Paris-Est Marne la Vallée, 2019. English. NNT : . tel-02318157

HAL Id: tel-02318157
https://theses.hal.science/tel-02318157

Submitted on 16 Oct 2019

HAL is a multi-disciplinary open access archive for the deposit and dissemination of scientific research documents, whether they are published or not. The documents may come from teaching and research institutions in France or abroad, or from public or private research centers.

L'archive ouverte pluridisciplinaire **HAL**, est destinée au dépôt et à la diffusion de documents scientifiques de niveau recherche, publiés ou non, émanant des établissements d'enseignement et de recherche français ou étrangers, des laboratoires publics ou privés.

UNIVERSITÉ PARIS-EST

THÈSE

PRÉSENTÉE POUR OBTENIR LE GRADE DE

DOCTEUR DE L'UNIVERSITÉ PARIS-EST

École doctorale MSTIC: mention Mathématiques Appliquées

par **Nicolas PIGNET**

Hybrid High-Order methods for nonlinear solid mechanics

Méthodes hybrides d'ordre élevé pour la mécanique des solides non-linéaire

---

Soutenue publiquement le 22 Octobre 2019 devant le jury de thèse composé de:

Dr. Mickaël Abbas	EDF R&D	Encadrant industriel
Pr. Grégoire Allaire	CMAP - École Polytechnique	Examinateur
Pr. Alexandre Ern	ENPC - Université Paris Est	Directeur de thèse
Dr. Patrice Hauret	Manufacture des Pneumatiques Michelin	Rapporteur
Pr. Patrick Hild	Université Paul Sabatier	Examinateur
Dr. Vanessa Lleras	Université Montpellier II	Examinatrice
Pr. Yves Renard	INSA Lyon	Rapporteur
Pr. Christian Wieners	Karlsruher Institut für Technologie	Examinateur

Résumé

Dans cette thèse, nous nous intéressons aux développements des méthodes hybrides d'ordre élevé (Hybrid High-Order, HHO, en anglais) pour la mécanique des solides non-linéaire. Les méthodes HHO sont formulées en termes d'inconnues de face portées par le squelette du maillage et d'inconnues dans les cellules qui sont ajoutées pour des raisons d'approximation et de stabilité de la méthode. Ces méthodes présentent de nombreux avantages dans le cadre de la mécanique des solides : *(i)* formulation primale ; *(ii)* suppression du verrouillage numérique dû aux problèmes d'incompressibilité ; *(iii)* ordre d'approximation arbitraire $k \geq 1$; *(iv)* utilisation de maillages polyédriques avec des interfaces possiblement non-conformes ; et *(v)* coûts numériques attractifs grâce à la condensation statique qui permet d'éliminer les inconnues portées par les cellules tout en maintenant un stencil compact. Dans cette thèse, des méthodes HHO en version primale sont développées pour résoudre le problème des grandes déformations hyperélastiques et des petites déformations plastiques. Une extension aux grandes déformations plastiques est ensuite présentée en utilisant le cadre des déformations logarithmiques. Enfin, un couplage avec une approche de type Nitsche a permis de traiter le problème du contact unilatéral de Signorini avec frottement de Tresca. Des taux de convergence optimaux en h^{k+1} ont été prouvés en norme d'énergie. L'ensemble de ces méthodes ont été implémentées à la fois dans la librairie open-source `disk++` et dans le code de calcul industriel open-source `code_aster`. De nombreux cas-tests bi- et tridimensionnels ont été réalisés afin de valider ces méthodes et de les comparer par rapport aux méthodes éléments finis H^1-conformes et mixtes.

Mot-clés : Méthodes hybrides d'ordre élevé, Absence de verrouillage, Maillages polyédriques, Grandes déformations, Plasticité, Contact unilatéral, Frottement de Tresca, Méthode de Nitsche.

Abstract

In this thesis, we are interested in the devising of Hybrid High-Order (HHO) methods for nonlinear solid mechanics. HHO methods are formulated in terms of face unknowns on the mesh skeleton. Cell unknowns are also introduced for the stability and approximation properties of the method. HHO methods offer several advantages in solid mechanics: *(i)* primal formulation; *(ii)* free of volumetric locking due to incompressibility constraints; *(iii)* arbitrary approximation order $k \geq 1$; *(iv)* support of polyhedral meshes with possibly non-matching interfaces; and *(v)* attractive computational costs due to the static condensation to eliminate locally cell unknowns while keeping a compact stencil. In this thesis, primal HHO methods are devised to solve the problem of finite hyperelastic deformations and small plastic deformations. An extension to finite elastoplastic deformations is also presented within a logarithmic strain framework. Finally, a combination with Nitsche's approach allows us to impose weakly the unilateral contact and Tresca friction conditions. Optimal convergence rates of order h^{k+1} are proved in the energy-norm. All these methods have been implemented in both the open-source library `disk++` and the open-source industrial software `code_aster`. Various two- and three-dimensional benchmarks are considered to validate these methods and compare them with H^1-conforming and mixed finite element methods.

Keywords: Hybrid High-Order methods, Locking-free, Polyhedral meshes, Large deformations, Plasticity, Unilateral contact, Tresca friction, Nitsche's method.

Remerciements

Cette thèse arrive à son terme après trois ans riches en émotions. On m'avait dit "tu verras une thèse c'est un marathon de trois ans couru à la vitesse d'un sprint". Je ne peux que confirmer.

Mes premiers remerciements vont naturellement à Alexandre mon directeur de thèse. Je ne peux que louer ses qualités scientifiques, pédagogiques et humaines. Je ne pensais pas faire et surtout apprendre autant de choses dans des domaines si variés et pour cela je lui dois beaucoup. Cette thèse, sans les nombreuses discussions, le recul et les bonnes idées qu'il m'a apporté, aurait été sans doute très différente.

En second lieu, je tiens également à remercier Mickaël pour son encadrement industriel. J'ai appris énormément sur la mécanique numérique en général. Je n'oublie pas les nombreuses séances de programmation sur `code_aster` que l'on a eu ensemble, les maux de tête provoqués, les astuces et contournements trouvés et cette phrase si souvent prononcée "Que c'est compliqué aster".

Je souhaite également remercier Patrice Hauret et Yves Renard de m'avoir fait l'honneur d'être rapporteur de ma thèse. Je tiens également à remercier Grégoire Allaire, Patrick Hild, Vanessa Lleras et Christian Wieners d'avoir accepté de faire partie de mon jury de thèse. Enfin, je suis très reconnaissant à Franz Chouly pour la collaboration qu'il a accepté de mener avec moi pendant cette thèse.

Je tiens à remercier Natacha, Guilhem et Jérôme d'avoir participé à chacun de mes comités de suivi de thèse pendant ces trois ans. Les discussions ont été très enrichissantes et certaines parties de ma thèse auraient été moins abouties sans cela.

Je pense que je n'aurais pas fait cette thèse sans Guillaume qui m'a pris en stage puis Patrick à Toulouse. Je vous en suis plus que reconnaissant.

En tant que doctorant CIFRE, j'ai passé beaucoup de temps à EDF R&D et surtout à T61 puis maintenant à T6A. Je dois saluer mes deux cobureaux et compagnons de thèse David et Mohammadou avec qui la thèse a paru un peu moins difficile. Il y a eu, avec mes collègues, toutes ces nombreuses discussions et moments de vie autour des cafés, des repas, des voyages et du sport que je n'oublierais pas. Un grand merci à ceux que je n'avais pas encore mentionné: Mathieu, Thomas, Ionel, les Nicolas, Dzifa, Jean-Pierre, Dominique, Frédéric, Astrid, Yubin, Léonard, Ting.

L'autre endroit où j'ai passé aussi beaucoup de temps avec plaisir c'est dans l'équipe SERENA. Merci à tous les doctorants et post-doc pour les discussions sans fin sur la cuisine, la politique, les sorties, les restaurants : Patrick, Matteo, Karol, Ani, Jad, Fred, Amina, Riccardo, Guillaume. J'ai également une pensée pour les autres membres de l'équipe avec qui j'ai pu manger, travailler, discuter : Géraldine, François, Michel, Martin, Florent, Simon. Je remercie aussi les autres doctorants du cermics.

Une thèse, c'est très long par moment et il faut donc d'excellents amis pour aller boire des coups, manger, se raconter nos vies, rigoler, se changer les idées, voyager et faire plein d'autres choses. Je tiens donc absolument à remercier mes amis d'enfance Fabien et Clément, la grande famille de Matmeca: Gabi, Flo, Matmau, Valou, Anne, Seb, François, Kelly, Broq, Chachou, Chris, Laura, Jojo, et Emma (c'est effectivement un château qu'il va falloir finir par réserver), Marc et Rémi à Toulouse, mes amis parisiens qui ont dû me supporter en thèse plus que quiconque: Léonard, Sylvain, Rosalie, Guillaume, Hélène et Delphine. Merci beaucoup à vous.

J'ai passé énormément de temps sur les stades durant toutes ces années, j'y ai vécu certains de mes meilleurs souvenirs, il est donc naturel que je remercie tout le monde, partenaires d'entrainement, entraineurs et surtout amis à Caen, à Talence et à Toulouse. Je dois en

particulier remercier David, Mohammed et Rémi qui m'ont apporté beaucoup plus que des conseils techniques, je leurs dois énormément sur le chemin accompli.

Enfin, je me dois de remercier ma famille, mes parents et ma soeur qui m'ont accompagné et soutenu dans tous mes choix.

CONTENTS

CHAPTER 1

INTRODUCTION

Dans ce chapitre, nous présentons le contexte, les enjeux et les objectifs de cette thèse. Nous introduisons ensuite les méthodes hybrides d'ordre élevé (Hybrid High-Order en anglais). Puis, nous décrivons les principaux problèmes issus de la mécanique des solides non-linéaire qui sont étudiés dans ce manuscrit : les grandes déformations plastiques et le problème de contact unilatéral de Signorini avec frottement de Tresca. Enfin, nous présentons le plan du manuscrit avec les principales contributions.

Sommaire

(a) Centrale nucléaire (b) Éoliennes offshore

Figure 1.1: Exemple d'installations de production électrique.

1.1 Contexte et enjeux industriels

Le groupe EDF (Électricité de France) a pour mission, en tant qu'exploitant de son parc de production électrique (nucléaire, hydraulique, éolien...), de contribuer à l'approvisionnement en électricité du territoire français. Pour cela, il doit maintenir en état ses installations de production, effectuer des éventuelles réparations et justifier auprès des autorités de leurs tenue aussi bien en fonctionnement qu'en cas d'incidents. En particulier, l'accident de Fukushima en 2011 a amené l'autorité de sûreté nucléaire (ASN) à rehausser ses exigences en termes de sécurité et de sûreté des installations de production. En outre, EDF souhaite prolonger la durée de vie de son parc nucléaire au-delà de 40 ans (voire 50 ans). Afin de répondre à ces nouvelles exigences de sûreté, tout en maîtrisant les coûts des réparations et de mise en conformité, EDF s'appuie de plus en plus sur la simulation numérique. Celle-ci s'avère être souvent le seul outil dont EDF dispose car la justification par des moyens expérimentaux en plus d'être coûteuse, est longue et complexe.

Dans ce contexte, EDF R&D développe en interne de nombreux codes de simulation numérique en fonction des problèmes physiques à traiter. En ce qui concerne la mécanique des structures, le département ERMES est en charge du développement du code de calcul éléments finis `code_aster` [111]. `code_aster` est un logiciel open-source développé depuis 1989 pour répondre et anticiper les besoins des départements d'ingénierie d'EDF ainsi que pour les besoins de la recherche menée en interne au sein de la R&D pour tout ce qui concerne la thermomécanique des structures non-linéaires. De plus, ce code est développé avec le système d'assurance-qualité qu'exige l'industrie nucléaire. Depuis plusieurs années, `code_aster` a été intégré au sein de la plateforme de simulation numérique `salome_meca` afin de disposer en open-source de tous les outils nécessaires à des études mécaniques complètes incluant notamment les pré- et post-traitements, et une interface graphique de mise en données.

Cette hausse des exigences en termes de sûreté de fonctionnement des unités de production implique de réaliser des simulations de plus en plus réalistes afin de justifier de la tenue des équipements au vieillissement ou à des aléas externes. Par exemple, en mécanique des structures non-linéaire, les études numériques dédiées à la durée de vie des structures métalliques entraînent l'utilisation de modèles numériques complexes afin d'obtenir des résultats très précis pouvant justifier la tenue des ouvrages sur le long terme. En particulier, ces problématiques englobent la tenue de la cuve d'un réacteur nucléaire, des générateurs de vapeur (GV), mais aussi des équipements de secours (cf Fig. 1.3). De même, des simulations sont souvent nécessaires pour justifier de la pertinence et de la qualité des opérations de maintenance

Figure 1.2: Plateforme de simulation `salome_meca` intégrant le logiciel `code_aster`.

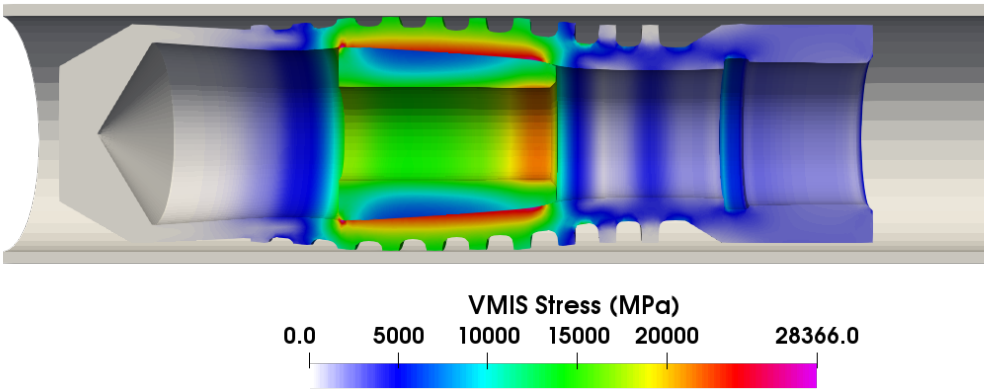

Figure 1.3: Simulation de la pose d'un bouchon dans un tube GV en grandes déformations plastiques avec contact frottant.

réalisées sur les équipements essentiels des installations nucléaires et conventionnelles.

Les principales difficultés numériques rencontrées lors de la simulation viennent de la présence de grandes déformations et du comportement des matériaux qui peuvent plastifier. Ces phénomènes engendrent des fortes non-linéarités dans le modèle qui peuvent en plus s'ajouter à d'autres comme celle du contact frottant. Différentes formulations éléments finis ont déjà été développées dans `code_aster` pour résoudre ces problèmes comme les éléments sous-intégrés ou des formulations mixtes. En particulier, cette thèse fait suite à une thèse sur le développement de formulations mixtes pour les grandes déformations plastiques [8]. Malheureusement, ces formulations présentent toujours certains inconvénients comme le manque de généricité, un problème de type point-selle à résoudre ou la présence d'oscillations numériques. C'est pour essayer de surmonter ces inconvénients que cette thèse sur l'extension des méthodes Hybrid High-Order à la mécanique des solides non-linéaire a été lancée.

1.2 Objectifs

Les principaux objectifs de cette thèse et le cahier des charges sont les suivants :

- Développement d'une méthode de discrétisation en formulation primale qui supprime le verrouillage numérique dû à l'incompressibilité.

- Développement d'une méthode générique qui supporte tous les types de mailles présentes dans `code_aster` (triangle, quadrangle, tétraèdre, hexaèdre, prisme, pyramide) et qui soit applicable en linéaire et quadratique.

- Applicabilité à toutes lois de comportement plastiques présentes dans `code_aster` sans modifications de celles-ci aussi bien en petites qu'en grandes déformations.
- Extension possible à d'autres problèmes physiques : thermique, dynamique, analyse spectrale.
- Implémentation et validation dans `code_aster`, avec le souhait de réutiliser au maximum l'architecture actuelle du code (assemblage, calculs locaux, structures de données).
- Intégration dans la version officielle de `code_aster` sous assurance qualité (documentations et cas tests)

1.3 Introduction aux méthodes Hybrid High-Order

Nous allons présenter dans cette section les méthodes Hybrid High-Order (HHO) par l'intermédiaire du problème de l'élasticité linéaire. Le but est de décrire les grands principes de construction des méthodes HHO. Par simplicité, nous supposons que le domaine $\Omega_0 \subset \mathbb{R}^d$, $1 \leq d \leq 3$, est un domaine polyédrique borné, connexe et avec un bord Lipschitzien $\Gamma := \partial\Omega_0$. Le domaine Ω_0 se déforme sous l'action d'un chargement volumique $\underline{f} \in L^2(\Omega_0;\mathbb{R}^d)$ et des conditions de type Dirichlet homogène sont imposées sur le bord Γ (pour simplifier). La formulation faible du problème est :

$$\begin{cases} \text{Trouver } \underline{u} \in H^1_0(\Omega_0;\mathbb{R}^d) \text{ tel que} \\ 2\mu(\boldsymbol{\nabla}^s\underline{u},\boldsymbol{\nabla}^s\underline{v})_{\boldsymbol{L}^2(\Omega_0)} + \lambda(\nabla\cdot\underline{u},\nabla\cdot\underline{v})_{L^2(\Omega_0)} = (\underline{f},\underline{v})_{\underline{L}^2(\Omega_0)}, \qquad \forall \underline{v} \in H^1_0(\Omega_0;\mathbb{R}^d), \end{cases} \tag{1.1}$$

où $H^1_0(\Omega_0;\mathbb{R}^d) = \left\{\underline{v} \in H^1(\Omega_0;\mathbb{R}^d) \,:\, \underline{v} = \underline{0} \text{ sur } \Gamma\right\}$, et $\mu > 0$ et $\lambda \geq 0$ sont les paramètres de Lamé du matériau. De plus, $\boldsymbol{\nabla}^s$ désigne la partie symétrique de l'opérateur gradient et $\nabla\cdot$ l'opérateur divergence.

1.3.1 Historiques et motivations

Ces méthodes HHO sont développées depuis quelques années par Di Pietro, Ern et leurs collaborateurs. Les premiers travaux portent sur les problèmes de la diffusion linéaire [91] et de l'élasticité linéaire [89]. Depuis, les méthodes HHO ont été étendues à des physiques différentes pour traiter des problèmes aussi bien linéaires que non-linéaires. Pour les problèmes linéaires, nous pouvons citer les travaux sur le problème de Stokes [93], sur la diffusion linéaire à coefficients variables [7, 90], sur l'advection-diffusion-réaction [86], sur le problème de Cahn–Hilliard [56], et sur les écoulements en milieux poreux fracturés [54, 55]. L'utilisation de maillages courbes est considérée dans [38] pour le problème de la diffusion linéaire. Pour les problèmes non-linéaires, nous pouvons citer les travaux sur le problème de Leray–Lions [84, 85], sur les équations de Navier–Stokes stationnaires [39, 94], sur les problèmes spectraux [46], et sur les fluides de Bingham [49]. En ce qui concerne plus particulièrement la mécanique des solides, il y a eu l'extension au problème de l'élasticité non-linéaire en petites déformations [40], au problème de Biot [32], aux équations des plaques de Kirchhoff–Love [33], et les travaux réalisés dans cette thèse sur l'hyperélasticité en grandes déformations [2], la plasticité en petites [3] et grandes [4] déformations et le contact unilatéral avec frottement de Tresca [62]. Les méthodes HHO ont également été étendues aux méthodes de domaines fictifs [45] et aux méthodes multi-échelles [72]. D'un point de vue numérique, un intérêt particulier a été porté à l'implémentation de ces méthodes de manière générique de façon à inclure les maillages polyédriques en dimension quelconque. Ces développements sont capitalisés au sein du

code open-source `disk++` au CERMICS. Les détails concernant l'implémentation sont donnés dans [71]. Pour finir, des revues des méthodes HHO sont disponibles dans [92] et [95].

Les méthodes HHO sont des méthodes non-conformes comme les méthodes de type Galerkin discontinu (dG), mais contrairement à ces dernières, elles sont formulées en termes d'inconnues de faces (portées par le squelette du maillage). Des inconnues dans les cellules sont aussi ajoutées pour des propriétés de stabilité et d'approximation (d'où le terme Hybrid). Ces inconnues de cellules peuvent être éliminées localement par condensation statique (ou complément de Schur). Le terme High-Order vient du fait que les méthodes HHO permettent de faire de l'ordre bas comme de l'ordre élevé sans modification de la méthode. La construction des méthodes HHO repose sur deux idées : *(i)* la reconstruction locale d'un gradient ou d'un potentiel à partir des inconnues de la cellule et des inconnues des faces en "mimant" une intégration par parties ; et *(ii)* un opérateur de stabilisation locale afin d'imposer faiblement sur chaque face de la cellule la consistance entre les inconnues de la face et la trace des inconnues de la cellule. Les méthodes HHO présentent de nombreux avantages : *(i)* ordre d'approximation arbitraire ($k \geq 0$ pour la diffusion linéaire et $k \geq 1$ pour l'élasticité linéaire) ; *(ii)* utilisation de maillages polyédriques avec des interfaces possiblement non-conformes (voir Fig. 1.4 pour des exemples de maillages); *(iii)* robustesse vis à vis des paramètres physiques (incompressibilité élastique, advection dominante...) ; *(iv)* coûts numériques attractifs grâce à la condensation statique qui permet d'éliminer les inconnues portées par les cellules tout en maintenant un stencil compact ; et *(v)* conservation locale des flux sur chaque cellule du maillage.

Le point *(iii)* est particulièrement pertinent dans le contexte de ce manuscrit, où nous nous intéressons aux problèmes de la mécanique des solides car les méthodes HHO vont nous permettre d'utiliser une formulation purement primale (sans ajout de multiplicateurs de Lagrange contrairement aux formulations mixtes) afin d'éliminer le verrouillage numérique issu de l'incompressibilité qui est habituellement présent pour les méthodes H^1-conformes. Quand au point *(ii)*, une motivation est de pouvoir réaliser un raffinement local du maillage sans devoir se préoccuper de l'éventuelle présence de nœuds orphelins comme dans les méthodes H^1-conformes. En effet, comme illustré à la Fig. 1.5, la présence des nœuds orphelins est gérée simplement en traitant la maille correspondante comme un polygone (ou un polyèdre).

1.3.2 Cadre discret

Nous considérons une famille de maillages $(\mathcal{T}_h)_{h>0}$, où pour chaque $h > 0$, le maillage $\mathcal{T}_h$ est composé de polyèdres ouverts, disjoints non-vides, qui ont des faces planes, et tels que $\overline{\Omega_0} = \bigcup_{T\in\mathcal{T}_h} \overline{T}$. La taille globale du maillage est décrite par le paramètre $h = \max_{T\in\mathcal{T}_h} h_T$, où h_T est le diamètre de la cellule T. Un sous-ensemble fermé F de $\overline{\Omega_0}$ est appelé une face si c'est un sous-ensemble ayant un intérieur relatif non-vide contenu dans un hyperplan affine H_F et si (i) soit il existe deux cellules distinctes $T_-, T_+ \in \mathcal{T}_h$ telles que $F = \partial T_- \cap \partial T_+ \cap H_F$ (et F est alors appelée une interface) ou (ii) il existe une cellule $T \in \mathcal{T}_h$ telle que $F = \partial T \cap \Gamma \cap H_F$ (et F est alors appelée une face de bord). Les faces du maillage sont réunies dans l'ensemble $\mathcal{F}_h$ qui est ainsi partitionné en deux sous-ensembles, $\mathcal{F}_h^{\mathrm{i}}$ l'ensemble des interfaces et $\mathcal{F}_h^{\mathrm{b}}$ l'ensemble des faces de bord. Pour tout $T \in \mathcal{T}_h$, $\mathcal{F}_{\partial T}$ désigne l'ensemble des faces du maillage qui sont incluses dans ∂T et $\underline{n}_T$ la normale sortante unitaire à la cellule T. Nous supposons dans la suite que la famille de maillages $(\mathcal{T}_h)_{h>0}$ est régulière au sens spécifié dans [89], c.à.d. pour tout $h > 0$, il existe un sous-maillage conforme de $\mathcal{T}_h$ composé de simplexes qui appartient à une famille régulière de maillages simpliciaux dans le sens habituel de Ciarlet [69] et tel que chaque cellule $T \in \mathcal{T}_h$ du maillage (respectivement, chaque face $F \in \mathcal{F}_h$) peut être décomposée en un nombre uniformément borné de sous-cellules (respectivement, sous-faces)

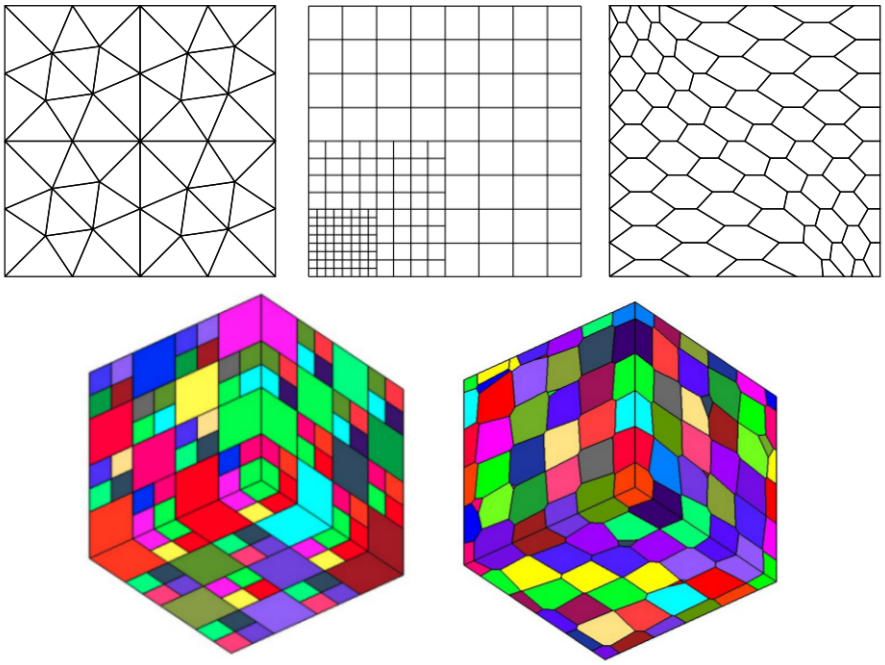

Figure 1.4: Exemples de maillages polyédriques supportés par les méthodes HHO.

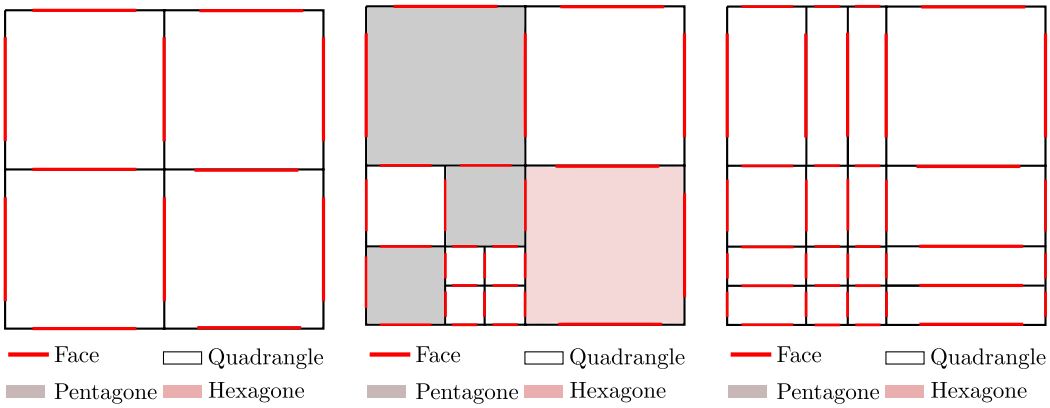

(a) Maillage initial (4 mailles) (b) Raffinement pour les méthodes HHO (10 mailles) (c) Raffinement pour les méthodes H^1-conformes (16 mailles)

Figure 1.5: Exemple de raffinement local traité par les méthodes HHO et par les méthodes H^1-conformes en partant d'un même maillage initial.

qui appartiennent à seulement une cellule du maillage (respectivement, à seulement une face ou à l'intérieur d'une cellule) avec un diamètre uniformément comparable.

Soit $k \geq 1$ un degré polynomial fixé. Dans chaque cellule $T \in \mathcal{T}_h$ du maillage, les inconnues HHO locales sont la paire $(\underline{v}_T, \underline{v}_{\partial T})$, où l'inconnue de cellule $\underline{v}_T \in \mathbb{P}_d^k(T;\mathbb{R}^d)$ est un polynôme à valeurs vectorielles à d-variables de degré au plus k dans la cellule T, et $\underline{v}_{\partial T} \in \mathbb{P}_{d-1}^k(\mathcal{F}_{\partial T};\mathbb{R}^d) := \times_{F\in\mathcal{F}_{\partial T}} \mathbb{P}_{d-1}^k(F;\mathbb{R}^d)$ est un polynôme à valeurs vectorielles défini par morceaux à $(d-1)$-variables de degré au plus k sur chaque face $F \in \mathcal{F}_{\partial T}$ de la cellule T. Nous écrivons de manière plus concise dans la suite que

$$\hat{\underline{v}}_T := (\underline{v}_T, \underline{v}_{\partial T}) \in \hat{\underline{U}}_T^k := \mathbb{P}_d^k(T;\mathbb{R}^d) \times \mathbb{P}_{d-1}^k(\mathcal{F}_{\partial T};\mathbb{R}^d). \tag{1.2}$$

Les degrés de liberté sont illustrés en Fig. 1.6, où un point représente un degré de liberté (mais par forcément un point physique d'évaluation) et la forme géométrique de la cellule est uniquement illustrative. Les degrés de liberté n'ont pas de sens physique a priori et d'un point de vue algébrique, ils correspondent simplement aux coefficients dans une base polynomiale. L'espace $\hat{\underline{U}}_T^k$ est muni de la semi-norme discrète locale suivante :

$$|\hat{\underline{v}}_T|_{1,T}^2 := \|\boldsymbol{\nabla}^s \underline{v}_T\|_{\boldsymbol{L}^2(T)}^2 + \|\eta_{\partial T}^{\frac{1}{2}}(\underline{v}_{T|\partial T} - \underline{v}_{\partial T})\|_{\underline{L}^2(\partial T)}^2, \tag{1.3}$$

avec la fonction constante par morceaux $\eta_{\partial T}$ telle que

$$\eta_{\partial T|F} = h_F^{-1}, \quad \forall F \in \mathcal{F}_{\partial T}, \tag{1.4}$$

où h_F est le diamètre de F. Nous introduisons également l'espace des mouvements de corps rigide sur T tel que

$$\underline{RM}(T) := \left\{ \underline{v} : T \to \mathbb{R}^d \mid \underline{v}(\underline{x}) = \underline{c} + \boldsymbol{\omega}\underline{x}, \text{ où } \underline{c} \in \mathbb{R}^d \text{ et } \boldsymbol{\omega} \in \boldsymbol{SO}^d \right\}. \tag{1.5}$$

où $\boldsymbol{SO}^d$ est l'ensemble des matrices de rotation dans l'espace euclidien réel. Notons que $\boldsymbol{\nabla}^s \underline{v} = \mathbf{0}$ est équivalent à $\underline{v} \in \underline{RM}(T)$ et que $\mathbb{P}_d^0(T;\mathbb{R}^d) \subsetneq \underline{RM}(T) \subsetneq \mathbb{P}_d^1(T;\mathbb{R}^d)$.

Lemme 1.1 *Pour tout $\hat{\underline{v}}_T \in \hat{\underline{U}}_T^k$, $|\hat{\underline{v}}_T|_{1,T} = 0$ si et seulement si $\underline{v}_T$ est un mouvement de corps rigide et que $\underline{v}_{\partial T}$ est la trace de $\underline{v}_T$ sur ∂T.*

Preuve. Remarquons que $|\hat{\underline{v}}_T|_{1,T} = 0$ équivaut à

$$\boldsymbol{\nabla}^s \underline{v}_T = \mathbf{0}, \quad \text{et} \quad \underline{v}_{T|\partial T} - \underline{v}_{\partial T} = \underline{0}. \tag{1.6}$$

Nous en déduisons que $\underline{v}_T$ est un mouvement de corps rigide car $\boldsymbol{\nabla}^s \underline{v}_T = \mathbf{0}$ et que $\underline{v}_{\partial T}$ est la trace de $\underline{v}_T$ sur ∂T car $\underline{v}_{T|\partial T} - \underline{v}_{\partial T} = \underline{0}$.

□

1.3.3 Opérateurs locaux de reconstruction et de stabilisation

Les méthodes HHO se basent sur la reconstruction de différentes quantités discrètes qui vont venir jouer le rôle de leur contre-partie continue dans la formulation du problème discret. Dans le cas de la discrétisation du problème de l'élasticité linéaire (1.1), le premier ingrédient clé est l'opérateur de reconstruction du gradient symétrique $\boldsymbol{E}_T^k : \hat{\underline{U}}_T^k \to \mathbb{P}_d^k(T;\mathbb{R}_{\text{sym}}^{d\times d})$ à partir de l'inconnue de cellule $\underline{v}_T \in \mathbb{P}_d^k(T;\mathbb{R}^d)$ et des inconnues de face $\underline{v}_{\partial T} \in \mathbb{P}_{d-1}^k(\mathcal{F}_{\partial T};\mathbb{R}^d)$ composant la paire $\hat{\underline{v}}_T = (\underline{v}_T, \underline{v}_{\partial T})$. Pour tout $\hat{\underline{v}}_T \in \hat{\underline{U}}_T^k$, le gradient symétrique reconstruit

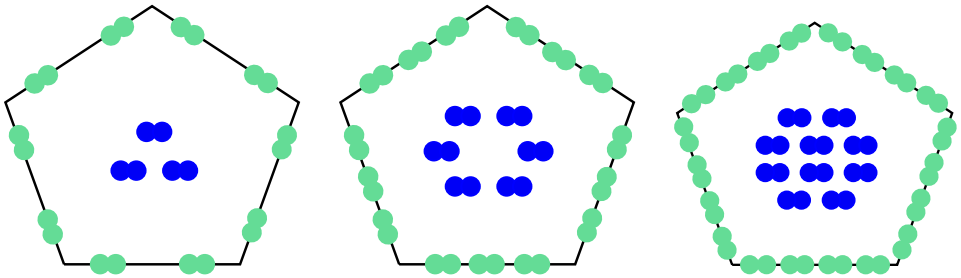

(a) $k = 1$ (b) $k = 2$ (c) $k = 3$

Figure 1.6: Cellule pentagonale T : degrés de liberté de la cellule (bleu) et des faces (vert) dans $\underline{\hat{U}}_T^k$ pour différentes valeurs de l'ordre d'approximation k dans le cas bidimensionnel. Chaque point représente un degré de liberté (c.à.d. un coefficient polynomial) mais pas forcément un point physique d'évaluation.

$\boldsymbol{E}_T^k(\underline{\hat{v}}_T) \in \mathbb{P}_d^k(T;\mathbb{R}^{d\times d}_{\rm sym})$ est obtenu en résolvant le problème local suivant: pour tout $\boldsymbol{\tau} \in \mathbb{P}_d^k(T;\mathbb{R}^{d\times d}_{\rm sym})$,

$$(\boldsymbol{E}_T^k(\underline{\hat{v}}_T), \boldsymbol{\tau})_{\boldsymbol{L}^2(T)} = (\boldsymbol{\nabla}^s \underline{v}_T, \boldsymbol{\tau})_{\boldsymbol{L}^2(T)} + (\underline{v}_{\partial T} - \underline{v}_{T|\partial T}, \boldsymbol{\tau}\, \underline{n}_T)_{\underline{L}^2(\partial T)}. \tag{1.7}$$

Résoudre ce problème implique de choisir une base polynomiale de $\mathbb{P}_d^k(T;\mathbb{R})$ seulement et d'inverser la matrice de masse associée pour chaque composante du tenseur $\boldsymbol{E}_T^k(\underline{\hat{v}}_T)$.

Le second ingrédient clé pour construire les méthodes HHO est l'opérateur de stabilisation locale qui permet d'imposer faiblement l'égalité entre les inconnues de face $\underline{v}_{\partial T}$ et la trace de l'inconnue de cellule $\underline{v}_{T|\partial T}$ par le biais d'une pénalisation au sens des moindres carrés de la différence $\underline{v}_{\partial T} - \underline{v}_{T|\partial T} \in \mathbb{P}_{d-1}^k(\mathcal{F}_{\partial T};\mathbb{R}^d)$. L'opérateur de stabilisation $\underline{S}_{\partial T}^k : \underline{\hat{U}}_T^k \to \mathbb{P}_{d-1}^k(\mathcal{F}_{\partial T};\mathbb{R}^d)$ est défini tel que, pour tout $\underline{\hat{v}}_T = (\underline{v}_T, \underline{v}_{\partial T}) \in \underline{\hat{U}}_T^k$:

$$\underline{S}_{\partial T}^k(\underline{\hat{v}}_T) = \underline{\Pi}_{\partial T}^k\big(\underline{v}_{\partial T} - \underline{D}_T^{k+1}(\underline{\hat{v}}_T)_{|\partial T}\big) - \underline{\Pi}_T^k\big(\underline{v}_T - \underline{D}_T^{k+1}(\underline{\hat{v}}_T)\big)_{|\partial T}, \tag{1.8}$$

où $\underline{\Pi}_T^k$ et $\underline{\Pi}_{\partial T}^k$ sont les projecteurs L^2-orthogonaux sur $\mathbb{P}_d^k(T;\mathbb{R}^d)$ et $\mathbb{P}_{d-1}^k(\mathcal{F}_{\partial T};\mathbb{R}^d)$ respectivement. De plus, l'opérateur local de reconstruction d'un champ de déplacement d'ordre supérieur $\underline{D}_T^{k+1} : \underline{\hat{U}}_T^k \to \mathbb{P}_d^{k+1}(T;\mathbb{R}^d)$ est défini tel que, pour tout $\underline{\hat{v}}_T \in \underline{\hat{U}}_T^k$, $\underline{D}_T^{k+1}(\underline{\hat{v}}_T) \in \mathbb{P}_d^{k+1}(T;\mathbb{R}^d)$ est obtenu en résolvant le problème de Neumann suivant: pour tout $\underline{w} \in \mathbb{P}_d^{k+1}(T;\mathbb{R}^d)$,

$$(\boldsymbol{\nabla}^s \underline{D}_T^{k+1}(\underline{\hat{v}}_T), \boldsymbol{\nabla}^s \underline{w})_{\boldsymbol{L}^2(T)} = (\boldsymbol{\nabla}^s \underline{v}_T, \boldsymbol{\nabla}^s \underline{w})_{\boldsymbol{L}^2(T)} + (\underline{v}_{\partial T} - \underline{v}_{T|\partial T}, \boldsymbol{\nabla}^s \underline{w}\, \underline{n}_T)_{\underline{L}^2(\partial T)}. \tag{1.9}$$

Cette reconstruction est définie de manière unique en imposant également les deux conditions

$$\int_T \underline{D}_T^{k+1}(\underline{\hat{v}}_T)\, dT = \int_T \underline{v}_T\, dT, \text{ et } \int_T \boldsymbol{\nabla}^{ss} \underline{D}_T^{k+1}(\underline{\hat{v}}_T)\, dT = \int_{\partial T} \frac{1}{2}(\underline{v}_{\partial T} \otimes \underline{n}_T - \underline{n}_T \otimes \underline{v}_{\partial T})\, d\partial T. \tag{1.10}$$

où $\boldsymbol{\nabla}^{ss}$ est la partie antisymétrique de l'opérateur gradient.

Comme $\boldsymbol{E}_T^k(\underline{\hat{v}}_T)$ n'est pas stable au sens où $\boldsymbol{E}_T^k(\underline{\hat{v}}_T) = \boldsymbol{0}$ n'implique pas nécessairement que $\underline{v}_{\partial T} = \underline{v}_{T|\partial T} = \underline{cst}$, il est nécessaire de coupler l'opérateur $\boldsymbol{E}_T^k$ à l'opérateur de stabilisation $\underline{S}_{\partial T}^k$. Ainsi, l'ajout de ce terme de stabilisation permet de retrouver une propriété de stabilité locale qui est nécessaire pour démontrer la coercivité du problème discret.

Lemme 1.2 (Stabilité et caractère borné) *Soit l'opérateur de reconstruction du gradient symétrique défini par* (1.7) *et l'opérateur de stabilisation défini par* (1.8)*. Soit* $\eta_{\partial T}$ *défini*

par (1.4). *Alors, il existe* $0 < \alpha_\flat < \alpha_\sharp < +\infty$, *indépendants de* h, *tels que, pour tout* $T \in \mathcal{T}_h$ *et tout* $\underline{\hat{v}}_T \in \underline{\hat{U}}_T^k$,

$$\alpha_\flat |\underline{\hat{v}}_T|_{1,T} \le \left(\|\boldsymbol{E}_T^k(\underline{\hat{v}}_T)\|_{\underline{L}^2(T)}^2 + \|\eta_{\partial T}^{\frac{1}{2}} \underline{S}_{\partial T}^k(\underline{\hat{v}}_T)\|_{L^2(\partial T)}^2 \right)^{\frac{1}{2}} \le \alpha_\sharp |\underline{\hat{v}}_T|_{1,T}. \tag{1.11}$$

Preuve. voir [89, Lemme 4].

□

Une autre propriété importante du gradient symétrique reconstruit est une propriété de commutativité qui est essentielle pour prouver la robustesse de la méthode dans la limite incompressible.

Lemme 1.3 (Commutativité) *Pour tout* $T \in \mathcal{T}_h$ *et tout* $\underline{v} \in H^1(T;\mathbb{R}^d)$, *l'égalité suivante est vraie :*

$$\boldsymbol{E}_T^k(\underline{\hat{I}}_T^k(\underline{v})) = \boldsymbol{\Pi}_T^k(\boldsymbol{\nabla}^s \underline{v}), \tag{1.12}$$

où $\underline{\hat{I}}_T^k : H^1(T;\mathbb{R}^d) \to \underline{\hat{U}}_T^k$ *est l'opérateur local de réduction tel que*

$$\underline{\hat{I}}_T^k(\underline{v}) = (\underline{\Pi}_T^k(\underline{v}), \underline{\Pi}_{\partial T}^k(\underline{v}_{|\partial T})). \tag{1.13}$$

Preuve. voir [89, Proposition 3].

□

Pour la suite, nous définissons également l'opérateur de divergence discret $D_T^k : \underline{\hat{U}}_T^k \to \mathbb{P}_d^k(T;\mathbb{R})$ tel que

$$D_T^k(\underline{\hat{v}}_T) := \mathrm{trace}(\boldsymbol{E}_T^k(\underline{\hat{v}}_T)), \quad \forall \underline{\hat{v}}_T \in \underline{\hat{U}}_T^k. \tag{1.14}$$

Remarque 1.4 (Variantes des méthodes HHO) *Il existe plusieurs variantes de la méthode HHO présentée ici. Une fois le degré polynomial* k *fixé pour les inconnues de face, l'inconnue de cellule peut être de degré polynomial* $l \in \{k-1, k, k+1\}$, $l \ge 1$, *sans changement des propriétés d'approximation et de stabilité (cf. [74]). Une autre variante est possible sur les maillages simpliciaux dans le cas où le degré* k *de l'inconnue de la cellule et des faces est le même. Il est alors possible de reconstruire un gradient stable dans le sens où il n'est alors plus nécessaire d'ajouter un terme de stabilisation (*$\underline{S}_{\partial T}^k \equiv \underline{0}$*). Pour cela, il suffit de le reconstruire dans un espace plus grand que* $\mathbb{P}_d^k(T;\mathbb{R}_{sym}^{d\times d})$ *qui contient au moins l'espace de Raviart–Thomas-Nédélec* $\mathbb{RTN}_d^k(T;\mathbb{R}^{d\times d}) := \mathbb{P}_d^k(T;\mathbb{R}^{d\times d}) \oplus (\mathbb{P}_d^{k,H}(T;\mathbb{R}^d) \otimes \underline{X})$, *où* $\mathbb{P}_d^{k,H}(T;\mathbb{R}^d)$ *est l'espace composé des polynômes homogènes de degré* k *et* $\underline{X} \in \mathbb{R}^d$ *est le point courant de la cellule (cf. [2, 87]).*

Remarque 1.5 (Connexion avec d'autres méthodes) *Les méthodes HHO présentent des connections plus ou moins étroites avec d'autres méthodes numériques développées ces dernières années. Pour les méthodes d'ordre bas, il existe des liens avec les méthodes volumes finis Hybrid Finite Volumes [119, 120] et Mixed Finite Volumes [101, 102], avec les méthodes Mimetic Finite Differences [42, 43, 154] (voir [103] pour un cadre unfié des trois méthodes précédentes), ainsi qu'avec les méthodes Compatible Discrete Operator [34, 35] et les Gradient Schemes [104, 105]. Pour les méthodes d'ordre supérieur, une connexion a été établie dans [74] entre les méthodes HHO, Hybridizable Discontinuous Galerkin (HDG) [76, 197] et nonconforming Virtual Element Methods (ncVEM) [18]. Les principales similitudes et différences entre les méthodes HHO, HDG, et ncVEM sont : (i) la reconstruction*

des opérateurs discrets pour HHO remplace les équations de flux pour HDG et ces opérateurs jouent le même rôle que les opérateurs de projection utilisés par ncVEM, et (ii) les opérateurs de stabilisation pour HHO et HDG sont définis d'un point de vue fonctionnel (et sont différents dans le cas où les inconnues de cellule ont le même degré que les inconnues de face) alors que pour ncVEM, ces opérateurs sont définis d'un point de vue algébrique tout en conduisant à des formes quadratiques équivalentes à HHO.

1.3.4 Problème global discret HHO

Définissons maintenant le problème global discret. Posons

$$\mathbb{P}_d^k(\mathcal{T}_h;\mathbb{R}^d) := \bigtimes_{T\in\mathcal{T}_h} \mathbb{P}_d^k(T;\mathbb{R}^d) \text{ et } \mathbb{P}_{d-1}^k(\mathcal{F}_h;\mathbb{R}^d) := \bigtimes_{F\in\mathcal{F}_h} \mathbb{P}_{d-1}^k(F;\mathbb{R}^d). \tag{1.15}$$

L'espace global des inconnues HHO est défini tel que

$$\underline{\hat{U}}_h^k := \mathbb{P}_d^k(\mathcal{T}_h;\mathbb{R}^d) \times \mathbb{P}_{d-1}^k(\mathcal{F}_h;\mathbb{R}^d). \tag{1.16}$$

Pour un élément générique $\underline{\hat{v}}_h \in \underline{\hat{U}}_h^k$, nous utilisons la notation $\underline{\hat{v}}_h = (\underline{v}_{\mathcal{T}_h}, \underline{v}_{\mathcal{F}_h})$. Pour toute cellule $T \in \mathcal{T}_h$ du maillage, nous notons $\underline{\hat{v}}_T \in \underline{\hat{U}}_T^k$ les composantes locales de $\underline{\hat{v}}_h$ liées à la cellule T et aux faces composant son bord ∂T, et pour toute face $F \in \mathcal{F}_h$, nous notons $\underline{v}_F$ la composante de $\underline{\hat{v}}_h$ liée à la face F. Des conditions aux limites de Dirichlet homogènes sont appliquées de manière forte sur les inconnues liées aux faces de bord $F \in \mathcal{F}_h^{\mathrm{b}}$. Nous introduisons pour cela le sous-espace

$$\underline{\hat{U}}_{h,0}^k := \left\{ \underline{\hat{v}}_h \in \underline{\hat{U}}_h^k \mid \underline{v}_F = \underline{0},\ \forall F \in \mathcal{F}_h^{\mathrm{b}} \right\}. \tag{1.17}$$

Nous définissons la fonction $\|\cdot\|_{\underline{\hat{U}}_{h,0}^k} : \underline{\hat{U}}_{h,0}^k \to \mathbb{R}$ telle que

$$\|\underline{\hat{v}}_h\|_{\underline{\hat{U}}_{h,0}^k}^2 := \sum_{T\in\mathcal{T}_h} |\underline{\hat{v}}_T|_{1,T}^2, \quad \forall \underline{\hat{v}}_h \in \underline{\hat{U}}_{h,0}^k. \tag{1.18}$$

Proposition 1.6 *La fonction $\|\cdot\|_{\underline{\hat{U}}_{h,0}^k}$ définit une norme sur $\underline{\hat{U}}_{h,0}^k$.*

Preuve. Il suffit de montrer que pour tout $\underline{\hat{v}}_h \in \underline{\hat{U}}_{h,0}^k$, $\|\underline{\hat{v}}_h\|_{\underline{\hat{U}}_{h,0}^k} = 0$ implique $\underline{v}_T = \underline{0}$ pour tout $T \in \mathcal{T}_h$ et $\underline{v}_F = \underline{0}$ pour tout $F \in \mathcal{F}_h$. Remarquons que $\|\underline{\hat{v}}_h\|_{\underline{\hat{U}}_{h,0}^k} = 0$ implique que pour tout $T \in \mathcal{T}_h$

$$\boldsymbol{\nabla}^s \underline{v}_T = \mathbf{0}, \quad \text{et} \quad \underline{v}_{T|F} - \underline{v}_F = \underline{0},\ \forall F \in \mathcal{F}_{\partial T}. \tag{1.19}$$

Prenons une cellule $T \in \mathcal{T}_h$ ayant au moins une face de bord $F \in \mathcal{F}_{\partial T} \cap \mathcal{F}_h^{\mathrm{b}}$, si bien que $\underline{v}_F = \underline{0}$. Alors $\underline{v}_{T|F} = \underline{0}$ car $\underline{v}_{T|F} - \underline{v}_F = \underline{0}$. En combinant cela à $\boldsymbol{\nabla}^s \underline{v}_T = \mathbf{0}$ et avec une inégalité de Korn, nous obtenons $\underline{v}_T = \underline{0}$. De plus, comme $\underline{v}_{T|F'} - \underline{v}_{F'} = \underline{0}$, $\forall F' \in \mathcal{F}_{\partial T} \setminus \{F\}$, nous en déduisons $\underline{v}_{F'} = \underline{0}$ pour tout $F' \in \mathcal{F}_{\partial T}$. Il suffit de prolonger ce raisonnement couche par couche de cellules jusqu'à avoir parcouru toutes les cellules $T \in \mathcal{T}_h$ et toutes les faces $F \in \mathcal{F}_h$.

□

Le problème discret est le suivant :

$$\begin{cases} \text{Trouver } \hat{\underline{u}}_h \in \hat{\underline{U}}_{h,0}^k \text{ tel que} \\ \displaystyle\sum_{T\in\mathcal{T}_h} a_T(\hat{\underline{u}}_T, \hat{\underline{v}}_T) = \sum_{T\in\mathcal{T}_h} (\underline{f}, \underline{v}_T)_{\underline{L}^2(T)}, \quad \forall \hat{\underline{v}}_h \in \hat{\underline{U}}_{h,0}^k, \end{cases} \tag{1.20}$$

avec

$$\begin{aligned} a_T(\hat{\underline{u}}_T, \hat{\underline{v}}_T) :=& 2\mu \left\{ (\boldsymbol{E}_T^k(\hat{\underline{u}}_T), \boldsymbol{E}_T^k(\hat{\underline{v}}_T))_{\boldsymbol{L}^2(T)} + (\eta_{\partial T} \underline{S}_{\partial T}^k(\hat{\underline{u}}_T), \underline{S}_{\partial T}^k(\hat{\underline{v}}_T))_{\underline{L}^2(\partial T)} \right\} \\ &+ \lambda (D_T^k(\hat{\underline{u}}_T), D_T^k(\hat{\underline{v}}_T))_{L^2(T)}. \end{aligned} \tag{1.21}$$

Le membre de droite dans (1.21) est obtenu en remplaçant les opérateurs continus par leurs versions discrètes et en ajoutant le terme de stabilisation. Nous pouvons montrer qu'il existe une unique solution $\hat{\underline{u}}_h \in \hat{\underline{U}}_{h,0}^k$ au problème (1.20) (cela découle de la propriété de stabilité locale du Lemme 1.2). De plus, comme les contributions dans (1.21) sont calculées de manière locale aux cellules, il est très facile de paralléliser ces calculs. Les méthodes HHO ont des taux de convergence optimaux sur des maillages généraux aussi bien en norme de l'énergie qu'en norme L^2 (sans hypothèse de régularité elliptique).

Théorème 1.1 (Erreur en norme de l'énergie) *Soit $k \geq 1$. Soit $\underline{u} \in H_0^1(\Omega_0;\mathbb{R}^d)$ l'unique solution du problème (1.1) et $\hat{\underline{u}}_h \in \hat{\underline{U}}_{h,0}^k$ l'unique solution du problème (1.20). En supposant également la régularité additionnelle $\underline{u} \in H^{k+2}(\Omega_0;\mathbb{R}^d)$, il existe une constante $C > 0$, indépendante de h, μ, et λ, telle que*

$$\left(\sum_{T\in\mathcal{T}_h} |\hat{\underline{I}}_T^k(\underline{u}) - \hat{\underline{u}}_T|_{1,T}^2 \right)^{\frac{1}{2}} \leq C h^{k+1} \left(2\mu |\underline{u}|_{\underline{H}^{k+2}(\Omega_0)} + \lambda |\nabla\cdot\underline{u}|_{H^{k+1}(\Omega_0)} \right). \tag{1.22}$$

Preuve. voir [89, Théorème 8].

□

Théorème 1.2 (Erreur en norme L^2) *Sous les hypothèses du Théorème 1.1 et en supposant la régularité elliptique pour le problème du modèle (1.1), il existe une constante $C > 0$, indépendante de h, μ, et λ, telle que*

$$\left(\sum_{T\in\mathcal{T}_h} \|\underline{\Pi}_T^k(\underline{u}) - \underline{u}_T\|_{\underline{L}^2(T)}^2 \right)^{\frac{1}{2}} \leq C h^{k+2} \left(2\mu |\underline{u}|_{\underline{H}^{k+2}(\Omega_0)} + \lambda |\nabla\cdot\underline{u}|_{H^{k+1}(\Omega_0)} \right). \tag{1.23}$$

Preuve. voir [89, Théorème 11].

□

Les estimations du Théorème 1.1 et du Théorème 1.2 sont robustes à limite incompressible puisqu'elles ne font intervenir que la régularité de $\nabla\cdot\underline{u}$ en fonction de λ. Ces taux de convergence sont confirmés numériquement ainsi que la robustesse. Enfin, il est important de rappeler que ces taux de convergence sont supérieurs d'un ordre à ceux obtenus pour des éléments finis H^1-conformes en utilisant des polynômes de degré k dans les cellules.

Remarque 1.7 (Structures minces et verrouillage en pincement) *Dans le cadre des structures minces où au moins une dimension est très inférieure aux autres (comme l'épaisseur pour les éléments de plaque) d'autres problèmes de verrouillage peuvent apparaitre. Un des principaux qui peut être rencontré pour les éléments finis linéaires H^1-conformes est le verrouillage en pincement (pinching locking en anglais). Ce verrouillage apparait car la déformation est constante dans l'épaisseur pour les éléments finis linéaires alors qu'une approximation linéaire est nécessaire dans l'épaisseur. Ce problème est résolu dans les méthodes HHO car le gradient symétrique reconstruit est au moins linéaire dans l'épaisseur, et ceci même pour $k = 1$. Des tests numériques avec les méthodes HHO viennent confirmer cette absence de verrouillage en pincement. Une étude numérique pour les méthodes HDG dans le cadre des structures minces en grandes déformations hyperélastiques est présentée dans Terrana & al. [203].*

1.3.5 Condensation statique et assemblage

Lors de l'implémentation des méthodes HHO dans un code de calcul, deux étapes sont particulièrement importantes. Il y a l'étape de condensation statique locale (ou complément de Schur) qui permet d'éliminer les inconnues de cellule $\underline{u}_{\mathcal{T}_h}$ et d'obtenir un problème global à résoudre plus petit car composé uniquement des inconnues de face $\underline{u}_{\mathcal{F}_h}$. La deuxième étape importante est l'étape d'assemblage du problème global à partir des contributions locales. Afin d'être plus pédagogique, nous présentons d'abord l'assemblage puis la condensation statique. Pour cela, nous illustrons ces différentes étapes sur un maillage composé de 7 cellules (cinq carrés et deux pentagones) et de 20 faces pour le cas $k = 1$. Ce maillage est illustré à la Fig. 1.7.

Pour les méthodes HHO comme pour les méthodes d'éléments finis classiques, le calcul des contributions élémentaires est local à chaque cellule $T \in \mathcal{T}_h$. Il faut ensuite assembler les contributions élémentaires dans la matrice globale (et le vecteur de chargement global) pour permettre le calcul de la solution globale discrète $\underline{\hat{u}}_h$. Cet assemblage est réalisé en remarquant que les inconnues portées par une face F sont partagées par les deux cellules partagent cette face. De plus, comme les inconnues portées par une cellule ne communiquant pas directement avec les autres cellules du maillage, il n'y a pas d'assemblage spécifique à faire (une simple copie des valeurs à réaliser). Le processus d'assemblage global est illustré à la Fig. 1.7 où à partir des contributions élémentaires de plusieurs cellules, le problème global est assemblé.

Comme les inconnues portées par une cellule $T \in \mathcal{T}_h$ ne communiquent pas directement avec les autres cellules du maillage, il y a une partie de la matrice assemblée du problème global qui a une structure diagonale par bloc où chaque bloc représente la contribution locale venant de l'inconnue $\underline{u}_T$ de chaque cellule. Chaque bloc étant symétrique défini positif, il est possible d'éliminer les inconnues $\underline{u}_{\mathcal{T}_h}$ cellule par cellule afin de se ramener à une matrice plus petite (composée uniquement des inconnues de face $\underline{u}_{\mathcal{F}_h}$). Ainsi, le nombre d'inconnues global de la discrétisation HHO est proportionnel à $k^{d-1}\,\mathrm{card}(\mathcal{F}_h)$ alors que pour les méthodes de type Galerkin discontinu, nous avons $k^d\,\mathrm{card}(\mathcal{T}_h)$, ce qui fait que les méthodes HHO sont attractives d'un point de vue coût numérique. Si nous avons besoin, après la résolution du problème discret, des valeurs de $\underline{u}_{\mathcal{T}_h}$, il suffit de rajouter une étape de décondensation statique localement à chaque cellule.

D'un point de vue implémentation, il est en général plus facile d'inverser l'ordre de ces opérations. Il faut mieux d'abord faire la condensation statique pour éliminer les inconnues de cellule, puis effectuer l'assemblage global sur les inconnues de face. L'enchaînement de ces différents étapes est présenté à la Fig. 1.8.

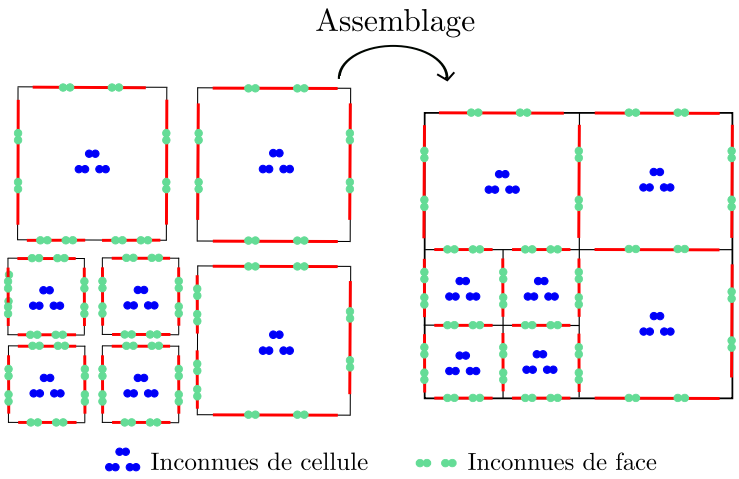

Figure 1.7: Processus d'assemblage des contributions locales en un problème global.

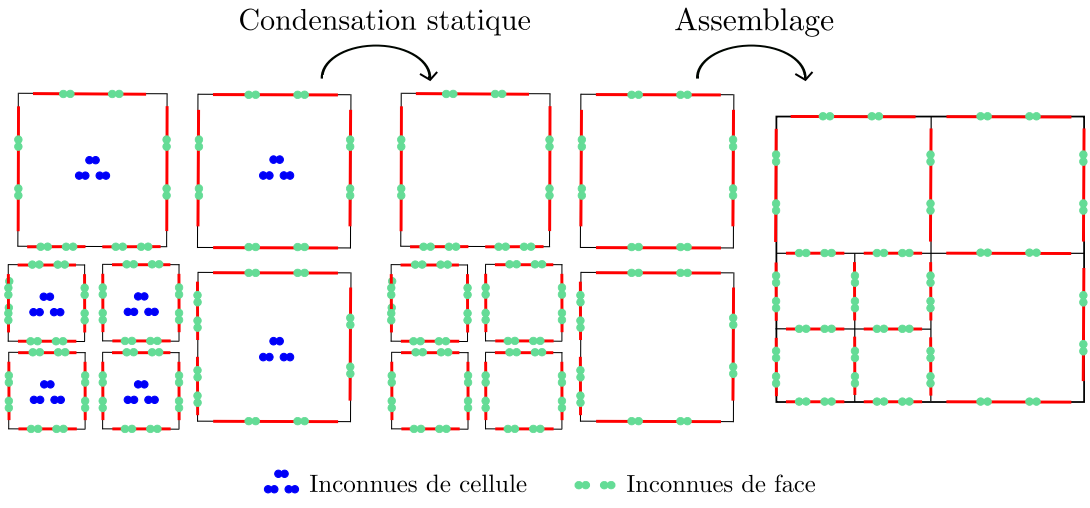

Figure 1.8: Processus complet: condensation statique puis assemblage du problème global en termes d'inconnues de face uniquement.

1.3.6 Résultats numériques

Nous allons présenter quelques résultats numériques sur les méthodes HHO. Pour cela, nous considérons le problème bidimensionnel sur le carré unitaire $\Omega_0 = [0;1]^2$ avec pour solution analytique $\underline{u} : \Omega_0 \to \mathbb{R}^2$ la fonction suivante :

$$u_x(x,y) = 0.2\sin(2\pi y)(\cos(2\pi x) - 1) + \frac{\sin(\pi x)\sin(\pi y)}{5+5\lambda},$$
$$u_y(x,y) = -0.2\sin(2\pi x)(\cos(2\pi y) - 1) + \frac{\sin(\pi x)\sin(\pi y)}{5+5\lambda}.$$

les coefficients de Lamé μ et λ étant pris égaux à $\mu = 1$ et $\lambda = 1000$. Dans un premier temps, nous regardons l'influence de l'ordre d'approximation k sur la solution discrète obtenue pour un maillage régulier composé de 256 quadrangles. Pour cela, la solution reconstruite à partir des inconnues cellules est tracée sur la Fig. 1.9 pour différents ordres $k \in [1;3]$. Comme attendu, la solution discrète obtenue est meilleure quand l'ordre d'approximation k augmente. De plus, la discontinuité de la solution $\underline{u}_{\mathcal{T}_h}$ est bien mise en évidence pour $k = 1$ et elle tend à se réduire notablement quand l'ordre d'approximation augmente (les discontinuités sont encore un peu présentes pour $k = 2$ et sont imperceptibles pour $k = 3$).

Dans un deuxième temps, nous regardons l'influence de la taille du maillage sur la solution discrète calculée pour $k = 1$. Pour cela, la solution reconstruite comme ci-dessus est tracée sur la Fig. 1.10 pour différents maillages triangulaires quasi-uniformes. La solution discrète obtenue est meilleure quand la taille du maillage diminue. De plus, les discontinuités de la solution discrète diminuent sensiblement avec la taille du maillage (les discontinuités sont quasiment invisibles sur le maillage composé de 1024 triangles).

En résumé, nous remarquons que les méthodes HHO donnent de très bons résultats et que les discontinuités de la solution discrète $\underline{u}_{\mathcal{T}_h}$ se réduisent sensiblement quand le maillage est de plus en plus fin ou quand l'ordre d'approximation augmente. La solution discrète obtenue est alors quasiment continue et est très proche de la solution que nous pouvons obtenir avec des éléments finis H^1-conformes (avec des taux de convergence meilleurs pour les méthodes HHO).

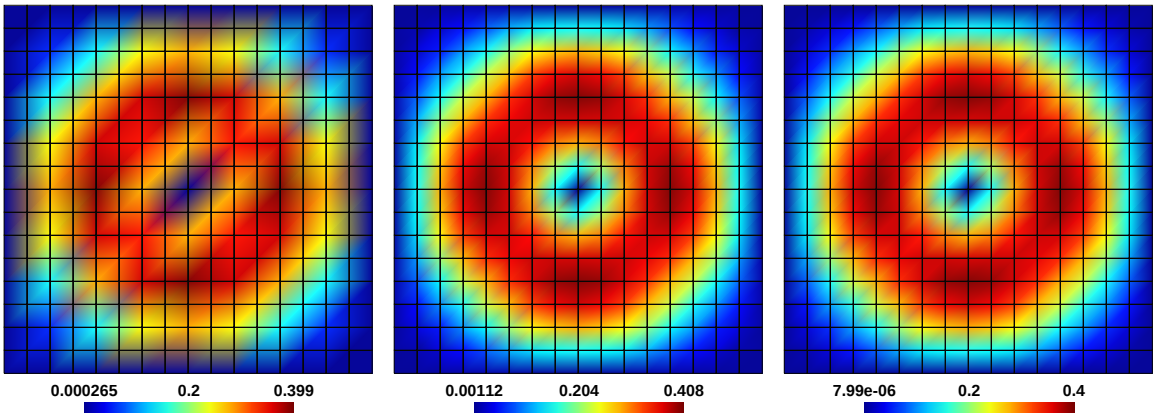

(a) $k = 1$ (b) $k = 2$ (c) $k = 3$

Figure 1.9: Norme euclidienne de la solution discrète reconstruite à partir des inconnues cellule sur un maillage régulier composé de 256 quadrangles et pour différents ordres d'approximation k.

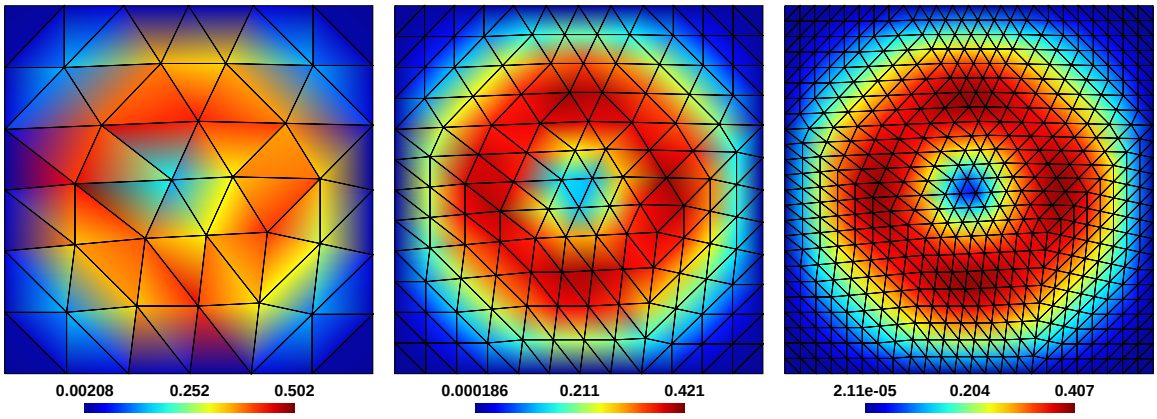

(a) 64 triangles (b) 256 triangles (c) 1024 triangles

Figure 1.10: Norme euclidienne de la solution discrète reconstruite à partir des inconnues cellule pour $k = 1$ et pour différents maillages triangulaires quasi-uniformes.

1.4 Grandes déformations et plasticité

Nous nous intéressons ici à deux types de non-linéarités que nous pouvons rencontrer en mécanique des solides. La première non-linéarité est la non-linéarité matérielle qui représente le fait que la relation entre le tenseur des déformations et le tenseur des contraintes n'est plus linéaire. Cette non-linéarité se rencontre dans la modélisation de la plasticité où les déformations irréversibles qui peuvent apparaître rendent nécessaire la prise en compte de l'histoire du matériau afin de pouvoir déterminer son état actuel. La deuxième non-linéarité est la non-linéarité géométrique qui apparaît lorsque la mesure des déformations n'est plus linéaire par-rapport au champ de déplacement. Cette deuxième non-linéarité se rencontre dans la modélisation des grandes déformations.

Pour décrire plus précisément ces deux non-linéarités et les problèmes numériques associés, nous nous intéressons au problème suivant. Nous considérons un corps déformable $\mathcal{B}_0$ représenté dans sa configuration de référence par le domaine polygonal/polyédrique $\Omega_0 \subset \mathbb{R}^d$, $d \in \{2, 3\}$. Le bord $\Gamma := \partial\Omega_0$ est partitionné en deux parties d'intersection vide Γ_{D} et Γ_{N}, où $\mathrm{mes}(\Gamma_{\mathrm{D}}) > 0$ pour bloquer les mouvements de corps rigides. Γ_{D} représente le bord de Dirichlet et Γ_{N} le bord de Neumann. Nous nous intéressons à une évolution quasi-statique sur l'intervalle de pseudo-temps $[0, t_F]$, $t_F > 0$, du corps $\mathcal{B}_0$ sous l'action du chargement volumique $\underline{f} : \Omega_0 \times [0, t_F] \to \mathbb{R}^d$, du chargement surfacique $\underline{t}_{\mathrm{N}} : \Gamma_{\mathrm{N}} \times [0, t_F] \to \mathbb{R}^d$ sur Γ_{N} et du déplacement imposé $\underline{u}_{\mathrm{D}} : \Gamma_{\mathrm{D}} \times [0, t_F] \to \mathbb{R}^d$ sur Γ_{D}. L'intervalle de pseudo-temps $[0, t_F]$ est discrétisé en N sous-intervalles tels que $t^0 = 0 < t^1 < \cdots < t^N = t_F$.

Nous introduisons l'espace de Hilbert des déplacements cinématiquement admissibles $\underline{V}_{\mathrm{D}}^n$, $0 \le n \le N$, et $\underline{V}_0$ des déplacements nuls sur le bord Γ_{D} :

$$\underline{V}_{\mathrm{D}}^n := \left\{ \underline{v} \in H^1(\Omega_0; \mathbb{R}^d) \ : \underline{v} = \underline{u}_{\mathrm{D}}(t^n) \text{ sur } \Gamma_{\mathrm{D}} \right\}, \quad \underline{V}_0 := \left\{ \underline{v} \in H^1(\Omega_0; \mathbb{R}^d) \ : \underline{v} = \underline{0} \text{ sur } \Gamma_{\mathrm{D}} \right\}.$$

1.4.1 Élasticité linéaire en petites déformations

Le modèle de l'élasticité linéaire est le modèle le plus simple que nous puissions utiliser en mécanique des solides. Il a été utilisé à la section précédente pour présenter les méthodes HHO. Dans ce cas, aucune non-linéarité n'est présente. Les déformations sont mesurées par

l'intermédiaire du tenseur des déformations linéarisées $\boldsymbol{\varepsilon} \in \mathbb{R}^{d\times d}_{\text{sym}}$ tel que

$$\boldsymbol{\varepsilon}(\underline{v}) = \frac{1}{2}(\boldsymbol{\nabla}\underline{v} + \boldsymbol{\nabla}\underline{v}^{T}), \tag{1.24}$$

pour tout $\underline{v} \in H^1(\Omega_0;\mathbb{R}^d)$. Le tenseur des déformations linéarisées dépend linéairement du champ de déplacement $\underline{v}$. Le tenseur des contraintes de Cauchy $\boldsymbol{\sigma} \in \mathbb{R}^{d\times d}_{\text{sym}}$ dépend lui aussi linéairement du tenseur des déformations linéarisées $\boldsymbol{\varepsilon}$:

$$\boldsymbol{\sigma}(\underline{v}) = 2\mu\boldsymbol{\varepsilon}(\underline{v}) + \lambda\,\text{trace}(\boldsymbol{\varepsilon}(\underline{v}))\boldsymbol{I}_d, \tag{1.25}$$

où $\mu > 0$ et $\lambda \geq 0$ sont les paramètres de Lamé du matériau et $\boldsymbol{I}_d$ le tenseur identité d'ordre d. En omettant la dépendance par rapport au temps, les équations d'équilibre à vérifier par le champ de déplacement $\underline{u} : \Omega_0 \to \mathbb{R}^d$ sont :

$$\begin{cases} -\underline{\nabla}\cdot\boldsymbol{\sigma}(\underline{u}) = \underline{f} & \text{dans } \Omega_0, \\ \underline{u} = \underline{u}_{\text{D}} & \text{sur } \Gamma_{\text{D}}, \\ \boldsymbol{\sigma}(\underline{u})\underline{N} = \underline{t}_{\text{N}} & \text{sur } \Gamma_{\text{N}}, \end{cases} \tag{1.26}$$

où $\underline{\nabla}\cdot$ est l'opérateur de divergence à valeurs vectorielles et $\underline{N}$ la normale sortante unitaire. Ainsi, la formulation faible du problème de l'élasticité linéaire en petites déformations est :

$$\begin{cases} \text{Trouver } \underline{u} \in \underline{V}_{\text{D}} \text{ tel que} \\ \displaystyle\int_{\Omega_0} \boldsymbol{\sigma}(\underline{u}) : \boldsymbol{\varepsilon}(\underline{v})\, d\Omega_0 = \int_{\Omega_0} \underline{f}\cdot\underline{v}\, d\Omega_0 + \int_{\Gamma_{\text{N}}} \underline{t}_{\text{N}}\cdot\underline{v}\, d\Gamma, \qquad \forall \underline{v} \in \underline{V}_0. \end{cases} \tag{1.27}$$

Le problème (1.27) admet une unique solution.

Une difficulté numérique apparaît à la limite incompressible quand $\lambda \to +\infty$. Cette limite incompressible se traduit par des déformations à trace nulle, $\text{trace}(\boldsymbol{\varepsilon}(\underline{v})) = 0$, ce qui revient à chercher un champ de déplacement à divergence nulle non trivial car $\text{trace}(\boldsymbol{\varepsilon}(\underline{v})) = \nabla\cdot\underline{v}$, où $\nabla\cdot$ est l'opérateur de divergence à valeur réelle. Si nous utilisons une discrétisation par éléments finis H^1-conformes, des problèmes de verrouillage numérique peuvent apparaître, ce qui se traduit par une sous-estimation des déplacements ou par des oscillations importantes de la trace du tenseur des contraintes de Cauchy.

1.4.2 Petites déformations plastiques

Les déformations plastiques se traduisent par la présence de déformations irréversibles. Il faut alors prendre en compte cette irréversibilité des déformations lors du calcul du tenseur des contraintes de Cauchy. Une hypothèse importante pour modéliser les déformations plastiques est que le tenseur des déformations linéarisées est décomposé en partie élastique $\boldsymbol{\varepsilon}^e$ et plastique $\boldsymbol{\varepsilon}^p$ sous la forme

$$\boldsymbol{\varepsilon}^e = \boldsymbol{\varepsilon} - \boldsymbol{\varepsilon}^p. \tag{1.28}$$

Les deux tenseurs $\boldsymbol{\varepsilon}^e$ et $\boldsymbol{\varepsilon}^p$ sont symétriques, et nous supposons également que les déformations plastiques sont incompressibles (ce qui est confirmé expérimentalement), c.à.d.,

$$\text{trace}(\boldsymbol{\varepsilon}^p) = 0. \tag{1.29}$$

Dans la suite, nous nous plaçons dans le cadre des matériaux standard généralisés développé initialement par Halphen & Son Nguyen [127] puis par Lemaitre & Chaboche [159]. Ce cadre permet de définir des modèles de plasticité thermodynamiquement admissibles. L'état local du matériau est décrit par le tenseur des déformations linéarisées $\boldsymbol{\varepsilon} \in \mathbb{R}^{d\times d}_{\text{sym}}$, le tenseur des

déformations plastiques $\boldsymbol{\varepsilon}^p \in \mathbb{R}^{d\times d}_{\text{sym}}$, et un ensemble de variables internes $\underline{\alpha} := (\alpha_1, \cdots, \alpha_m) \in \mathbb{R}^m$, qui contient typiquement au moins la déformation plastique équivalente $p \geq 0$. Par simplicité, nous notons $\underline{\chi} := (\boldsymbol{\varepsilon}^p, \underline{\alpha}) \in \underline{\mathcal{X}}$ les variables internes généralisées, où l'espace des variables internes généralisées est

$$\underline{\mathcal{X}} := \left\{ \underline{\chi} = (\boldsymbol{\varepsilon}^p, \underline{\alpha}) \in \mathbb{R}^{d\times d}_{\text{sym}} \times \mathbb{R}^m \mid \text{trace}(\boldsymbol{\varepsilon}^p) = 0 \right\}. \tag{1.30}$$

Enfin, nous supposons que la modèle de plasticité ne dépend pas du temps ni de la vitesse de déformation. Ainsi, nous considérons uniquement un problème sous forme incrémentale à résoudre sur $[0, t_F]$. La formulation faible du problème de plasticité incrémentale est : Pour tout $1 \leq n \leq N$ avec $\underline{u}^{n-1} \in \underline{V}^{n-1}_{\text{D}}$ et $\underline{\chi}^{n-1} \in L^2(\Omega_0; \underline{\mathcal{X}})$ donnés à partir du pas de pseudo-temps précédent ou de la condition initiale :

$$\left\{ \begin{array}{l} \text{Trouver } \underline{u}^n \in \underline{V}^n_{\text{D}} \text{ et } \underline{\chi}^n \in L^2(\Omega_0; \underline{\mathcal{X}}) \text{ tels que} \\ \displaystyle\int_{\Omega_0} \boldsymbol{\sigma}^n : \boldsymbol{\varepsilon}(\underline{v})\, d\Omega_0 = \int_{\Omega_0} \underline{f}^n \cdot \underline{v}\, d\Omega_0 + \int_{\Gamma_{\text{N}}} \underline{t}^n_{\text{N}} \cdot \underline{v}\, d\Gamma, \qquad \forall \underline{v} \in \underline{V}_0. \\ (\underline{\chi}^n, \boldsymbol{\sigma}^n) = \text{SMALL\_PLASTICITY}(\underline{\chi}^{n-1}, \boldsymbol{\varepsilon}(\underline{u}^{n-1}), \boldsymbol{\varepsilon}(\underline{u}^n)). \end{array} \right. \tag{1.31}$$

La procédure SMALL_PLASTICITY permet de calculer les nouvelles valeurs des variables internes généralisées $\underline{\chi}$ et du tenseur des contraintes $\boldsymbol{\sigma}$ à partir des valeurs précédentes des variables internes généralisées $\underline{\chi}^{n-1}$ et du tenseur des déformations $\boldsymbol{\varepsilon}^{n-1}$, et de la valeur actuelle du tenseur des déformations $\boldsymbol{\varepsilon}^n$. Les détails concernant le contenu de cette procédure peuvent être trouvés dans Simo & Hughes [83] et de Souza Neto, Peric & Owen [83] par exemple. Cette procédure contient typiquement des équations d'évolution incrémentales des variables internes généralisées. Pour un modèle de plasticité avec écrouissage positif, le problème (1.31) est bien posé.

Comme pour l'élasticité linéaire en petites déformations à la limite incompressible, l'incompressibilité des déformations plastiques, $\text{trace}(\boldsymbol{\varepsilon}^p) = 0$, peut provoquer des problèmes de verrouillage numérique.

1.4.3 Grandes déformations hyperélastiques

Quand les déformations deviennent importantes, l'hypothèse des petites déformations n'est plus valable et l'utilisation du tenseur des déformations linéarisées $\boldsymbol{\varepsilon}$ n'est plus réaliste. Il est alors nécessaire de changer la mesure des déformations afin d'obtenir des résultats plus réalistes.

Dans le cas d'un modèle de comportement hyperélastique, c.à.d. sans déformations plastiques irréversibles, plusieurs mesures de déformation sont possibles comme le tenseur du gradient des déformations $\boldsymbol{F} \in \mathbb{R}^{d\times d}_{+}$ ($\mathbb{R}^{d\times d}_{+}$ est l'ensemble des matrices dans $\mathbb{R}^{d\times d}$ ayant un déterminant strictement positif), le tenseur des déformations de Cauchy–Green droit $\boldsymbol{C} \in \mathbb{R}^{d\times d}_{\text{sym}}$, ou le tenseur des déformations de Green–Lagrange $\boldsymbol{E}^{GL} \in \mathbb{R}^{d\times d}_{\text{sym}}$. Ces tenseurs sont liés par les relations suivantes :

$$\boldsymbol{F}(\underline{v}) = \boldsymbol{I}_d + \boldsymbol{\nabla}\underline{v}, \quad \boldsymbol{C}(\underline{v}) = \boldsymbol{F}(\underline{v})^T \boldsymbol{F}(\underline{v}), \quad \text{et } \boldsymbol{E}^{GL}(\underline{v}) = \frac{1}{2}(\boldsymbol{C}(\underline{v}) - \boldsymbol{I}_d). \tag{1.32}$$

Un modèle couramment utilisé est le modèle hyperélastique néohookéen qui utilise comme mesure de déformation $\boldsymbol{F}$ et comme tenseur des contraintes $\boldsymbol{P}$ (Piola–Kirchhoff de première espèce) :

$$\boldsymbol{P}(\boldsymbol{F}) = \tilde{\mu}(\boldsymbol{F} - \boldsymbol{F}^{-T}) + \tilde{\lambda} J(J-1)\boldsymbol{F}^{-T}. \tag{1.33}$$

où $J = \det \boldsymbol{F}$, et $\tilde{\mu}$ et $\tilde{\lambda}$ sont les paramètres hyperélastiques du matériau. En omettant à nouveau la dépendance au temps et en supposant par simplicité que les chargements extérieurs sont morts (c'est à dire indépendants du champ de déplacement), les équations d'équilibre à vérifier en configuration lagrangienne [36, 70] par le champ de déplacement $\underline{u} : \Omega_0 \to \mathbb{R}^d$ sont :

$$\begin{cases} -\underline{\nabla}_X \cdot \boldsymbol{P}(\underline{u}) = \underline{f} & \text{dans } \Omega_0, \\ \underline{u} = \underline{u}_{\mathrm{D}} & \text{sur } \Gamma_{\mathrm{D}}, \\ \boldsymbol{P}(\underline{u})\underline{N} = \underline{t}_{\mathrm{N}} & \text{sur } \Gamma_{\mathrm{N}}, \end{cases} \tag{1.34}$$

où $\underline{\nabla}_X \cdot$ est l'opérateur de divergence à valeurs vectorielles par rapport aux coordonnées de référence et $\underline{N}$ la normale sortante unitaire dans la configuration de référence. Ainsi, la formulation faible du problème de l'hyperélasticité en configuration lagrangienne est :

$$\begin{cases} \text{Trouver } \underline{u} \in \underline{V}_{\mathrm{D}} \text{ tel que} \\ \displaystyle\int_{\Omega_0} \boldsymbol{P}(\boldsymbol{F}(\underline{u})) : \boldsymbol{\nabla} \underline{v} \, d\Omega_0 = \int_{\Omega_0} \underline{f} \cdot \underline{v} \, d\Omega_0 + \int_{\Gamma_{\mathrm{N}}} \underline{t}_{\mathrm{N}} \cdot \underline{v} \, d\Gamma, \qquad \forall \underline{v} \in \underline{V}_0. \end{cases} \tag{1.35}$$

Le problème (1.35) admet au moins une solution (Ball, [21]) car l'énergie hyperélastique associée à un matériau néohookéen est polyconvexe. Un traitement mathématique détaillé des problèmes hyperélastiques est présenté dans Ciarlet [70]. Il faut noter que nous sommes ici en présence d'une non-linéarité matérielle et d'une non-linéarité géométrique simultanément.

Le problème du verrouillage numérique intervient également à la limite incompressible, c.à.d. quand $\tilde{\lambda} \to +\infty$. De plus, une particularité des matériaux hyperélastiques en général est que la rigidité du matériau augmente quand les déformations augmentent, contrairement à la plasticité.

1.4.4 Grandes déformations plastiques

Un problème encore plus compliqué est celui des grandes déformations plastiques car les non-linéarités matérielle et géométrique sont présentes comme pour les grandes déformations hyperélastiques mais il faut en plus prendre en compte les déformations plastiques irréversibles. Deux modèles sont couramment utilisés : le modèle des déformations multiplicatives où une décomposition multiplicative (Simo, [189]) de $\boldsymbol{F}$ en partie élastique $\boldsymbol{F}^e$ et plastique $\boldsymbol{F}^p$ est supposée telles que $\boldsymbol{F} = \boldsymbol{F}^e \boldsymbol{F}^p$ et le modèle des déformations logarithmiques (Miehe, Apel & Lambrecht, [167]). Nous nous concentrons ici sur ce deuxième modèle car il a l'avantage de permettre une extension simple des lois plastiques en petites déformations aux grandes déformations moyennant un pré- et un post-traitement géométriques et une ré-identification des paramètres du matériau. Le tenseur des déformations logarithmiques $\boldsymbol{E} \in \mathbb{R}^{d\times d}_{\mathrm{sym}}$ est défini tel que

$$\boldsymbol{E} = \frac{1}{2} \ln(\boldsymbol{F}^T \boldsymbol{F}). \tag{1.36}$$

Comme pour le tenseur des déformations linéarisées $\boldsymbol{\varepsilon}$ dans le cas des petites déformations plastiques, nous supposons une décomposition additive du tenseur des déformations logarithmiques $\boldsymbol{E}$ en partie élastique $\boldsymbol{E}^e \in \mathbb{R}^{d\times d}_{\mathrm{sym}}$ et plastique $\boldsymbol{E}^p \in \mathbb{R}^{d\times d}_{\mathrm{sym}}$ telles que

$$\boldsymbol{E}^e = \boldsymbol{E} - \boldsymbol{E}^p. \tag{1.37}$$

Nous supposons également que les déformations logarithmiques plastiques sont incompressibles, c.à.d.,

$$\mathrm{trace}(\boldsymbol{E}^p) = 0. \tag{1.38}$$

Le fait de considérer cette même décomposition additive et cette même hypothèse d'incompressibilité plastique permet d'étendre facilement les lois plastiques écrites en petites déformations aux grandes déformations (moyennant un pré- et un post-traitement géométriques). Comme ci-dessus, nous nous plaçons dans le cadre des matériaux standard généralisés [127, 159]. L'état local du matériau est décrit par le tenseur des déformations logarithmiques $\boldsymbol{E} \in \mathbb{R}^{d\times d}_{\text{sym}}$, le tenseur des déformations logarithmiques plastiques $\boldsymbol{E}^p \in \mathbb{R}^{d\times d}_{\text{sym}}$, et un ensemble de variables internes $\underline{\alpha} := (\alpha_1, \cdots, \alpha_m) \in \mathbb{R}^m$. Par simplicité, nous notons $\underline{\chi}_{\log} := (\boldsymbol{E}^p, \underline{\alpha}) \in \underline{\mathcal{X}}_{\log}$ les variables internes généralisées, où l'espace des variables internes généralisées est

$$\underline{\mathcal{X}}_{\log} := \left\{ \underline{\chi}_{\log} = (\boldsymbol{E}^p, \underline{\alpha}) \in \mathbb{R}^{d\times d}_{\text{sym}} \times \mathbb{R}^m \mid \operatorname{trace}(\boldsymbol{E}^p) = 0 \right\}. \tag{1.39}$$

La formulation faible du problème de plasticité incrémentale en grandes déformations plastiques est: Pour tout $1 \le n \le N$ avec $\underline{u}^{n-1} \in \underline{V}_{\text{D}}^{n-1}$ et $\underline{\chi}_{\log}^{n-1} \in L^2(\Omega_0; \underline{\mathcal{X}}_{\log})$ donnés à partir du pas de pseudo-temps précédent ou de la condition initiale :

$$\left\{ \begin{array}{l} \text{Trouver } \underline{u}^n \in \underline{V}_{\text{D}}^n \text{ et } \underline{\chi}_{\log}^n \in L^2(\Omega_0; \underline{\mathcal{X}}_{\log}) \text{ tels que} \\ \displaystyle\int_{\Omega_0} \boldsymbol{P}^n : \boldsymbol{\nabla}\underline{v}\, d\Omega_0 = \int_{\Omega_0} \underline{f}^n \cdot \underline{v}\, d\Omega_0 + \int_{\Gamma_{\text{N}}} \underline{t}_{\text{N}}^n \cdot \underline{v}\, d\Gamma, \qquad \forall \underline{v} \in \underline{V}_0. \\ (\underline{\chi}_{\log}^n, \boldsymbol{P}^n) = \text{FINITE\_PLASTICITY}(\underline{\chi}_{\log}^{n-1}, \boldsymbol{F}(\underline{u}^{n-1}), \boldsymbol{F}(\underline{u}^n)). \end{array} \right. \tag{1.40}$$

où comme précédemment, les chargements extérieurs sont supposés morts (c'est à dire indépendants du champ de déplacement $\underline{u}^n$). La procédure FINITE_PLASTICITY permet de calculer les nouvelles valeurs des variables internes généralisées $\underline{\chi}_{\log}$ et du tenseur des contraintes de Piola–Kirchhoff $\boldsymbol{P}$ à partir des valeurs précédentes des variables internes généralisées $\underline{\chi}^{n-1}$ et du tenseur du gradient de déformations $\boldsymbol{F}^{n-1}$, et de la valeur actuelle du tenseur du gradient de déformations $\boldsymbol{F}^n$. Cette procédure réutilise la procédure SMALL_PLASTICITY en complément d'un pré- et d'un post-traitement géométriques. Les détails concernant le contenu de cette procédure et son calcul peuvent être trouvés dans Miehe, Apel & Lambrecht [167, Box 4].

1.4.5 Gestion numérique de l'incompressibilité

Comme évoqué précédemment, un problème de verrouillage numérique peut apparaître avec les éléments finis H^1-conformes (d'ordre bas) quand les déformations élastiques sont quasi-incompressibles et/ou les déformations plastiques sont incompressibles. Une raison pour l'apparition de ce verrouillage est que les éléments H^1-conformes (d'ordre bas) ne sont pas assez riches pour approcher correctement une telle solution. Pour résoudre cette difficulté numérique, de nombreuses méthodes ont été développées. Nous présentons ci-dessous les principales méthodes ainsi que leurs avantages et inconvénients. Nous commençons par les méthodes les plus anciennes.

- **Méthodes mixtes** : L'idée est d'introduire un ou plusieurs multiplicateurs de Lagrange pour imposer la condition d'incompressibilité. L'ajout de ces multiplicateurs augmente le coût de la construction et de la résolution du problème global. En outre, celui-ci est de type point-selle, ce qui peut compliquer la résolution avec une méthode itérative. De plus, la formulation des méthodes mixtes est dépendante de la loi de comportement utilisée et ces méthodes sont difficilement extensibles aux maillages polyédriques. Pour les grandes déformations hyperélastiques, nous mentionnons les travaux de Al Akhrass & al. [9], Brink & Stein [44], Dobrowolski [99], et Klass, Maniatty & Shephar [150],

et en ce qui concerne la plasticité, nous avons en petites déformations les travaux de Cervera & al. [53, 52, 51] et Chimumenti & al. [60, 59] et en grandes déformations les travaux de Al Akhrass & al. [9], Agelet de Saracibar & al. [6], Bargellini & al. [24], Le Tallec, Rahier & Kaiss [157], de Souza Neto & al. [82], et Simo, Taylor & Pister [196]. Plus récemment, une analyse de stabilité menée par Aurichhio & al. [16, 17, 15] a montré certaines limitations des méthodes mixtes pour les grandes déformations hyperélastiques.

- **Méthodes de Galerkin discontinu (dG)** : Les méthodes dG (Arnold & al. [12], Cockburn [73]) reposent sur une formulation primale comme les méthodes éléments finis H^1-conformes. En revanche, l'espace d'approximation n'est plus continu mais typiquement polynomial par morceaux. Un inconvénient de ses méthodes dG est qu'elles sont coûteuses car il y a beaucoup d'inconnues. En outre, dans le cas de la plasticité, le comportement doit être calculé sur les faces en plus des cellules et la matrice tangente de Newton n'est pas symétrique. Nous mentionnons pour les grandes déformations hyperélastique, les travaux de Eyck & Lew [117], Eyck, Celiker & Lew [116, 115], et Noels & Radovitzsky [174]. Les méthodes Interior penalty dG ont été développées pour la plasticité classique en petites déformations par Hansbo [131] et Liu & al. [162], et en grandes déformations par Liu, Wheeler & Yotov [163]; et en ce qui concerne la plasticité à gradient en petites déformations, nous mentionnons les travaux de Djoko & al. [98, 97] et en grandes déformations, ceux de McBride & Djoko [166].

- **Méthodes d'intégration réduite ou sélective** : La technique d'intégration réduite (Zienkiewicz, Taylor & Too, [217]) consiste à intégrer la matrice de rigidité associée aux éléments finis H^1-conformes en utilisant une règle d'intégration d'ordre plus faible que celui nécessaire pour une intégration exacte, alors que la méthode d'intégration sélective (Doherty, Wilson & Taylor, [100]) consiste à ne sous-intégrer que les termes de la matrice de rigidité liés à la contrainte d'incompressibilité. Ces deux méthodes permettent de réduire en partie les problèmes de verrouillage (cf. Ponthot [179]) mais présentent des difficultés pour les stabiliser (présence de modes à énergie nulle) et les étendre à des matériaux anisotropes (cf. les travaux de Hughes [145]). Un lien a pu être établi sous conditions avec certaines méthodes mixtes par Malkus & Hughes [165] et l'opérateur de stabilisation des méthodes dG par Reese & al. [27, 182]. En ce qui concerne les grandes déformations, nous mentionnons pour l'hyperélasticité, les travaux de Adam & al. [5] et Reese, Küssner & Reddy [5, 183], et pour la plasticité, les travaux de Reese [181].

- **Méthodes Enhanced Assumed Strain (EAS)** : Les méthodes EAS ont été introduites par Simo & Rifai [194] où l'idée est de venir enrichir le tenseur des déformations par l'ajout de variables additionnelles dont certaines peuvent être éliminées par condensation statique. Cependant, il est en général nécessaire de stabiliser ces méthodes. Pour les grandes déformations, ces méthodes ont été utilisées dans les travaux de Eyck & Lew [118] et Reese & Wriggers [184] en hyperélasticité et dans les travaux de Krysl [152, 153] et Simo & al. [191, 192] en plasticité.

Depuis quelques années, d'autres méthodes que celles présentées ci-dessus ont été développées pour résoudre entre autres le problème du verrouillage numérique.

- **Méthodes isogéométriques (IGA)** : L'idée des méthodes IGA est d'utiliser pour la discrétisation des fonctions de base qui sont plus régulières que les polynômes de Lagrange comme les NURBS. Un avantage sur les domaines à frontière courbe, la

représentation de la géométrie réelle est plus fine, ce qui permet de réduire l'erreur de discrétisation géométrique. De manière générale, le prix à payer est un stencil plus étendu et une forte dépendance entre le module géométrique et le solveur éléments finis. Ces méthodes ont été développées pour la plasticité en petites déformations par Elguedj & al. [112] et en grandes déformations par Elguedj & Hughes [113]. De plus, une adaptation de l'intégration sélective aux méthodes IGA a été proposée par Adam & al. [5].

- **Méthodes de type Virtual Element Method (VEM)** : Assez récemment, les méthodes VEM (Beirão da Veiga, Brezzi, Marini & Russo, [28, 29]) ont été développées afin d'étendre les éléments finis aux maillages polyédriques. Ces méthodes reposent sur une formulation primale et elles sont robustes dans la limite incompressible. Nous mentionnons en particulier la méthode VEM d'ordre bas pour les petites déformations plastiques par Beirão da Veiga, Lovadina & Mora [30] (et son extension bidimensionnelle d'ordre élevé par Artioli & al. [13]), alors que le cas des grandes déformations plastiques est traité par Wriggers & Hudobivnik [209] en 2D et Hudobivnik, Aldakheel & Wriggers [143] en 3D, toujours pour de l'ordre bas. Le cas hyperélastique est étudié par Chi, Beirão da Veiga & Paulino [58] et Wriggers & al. [210].

- **Méthodes hybrides** : Ces dernières années, de nombreuse méthodes hybrides ont été développées en plus de HHO. L'idée est de rajouter des variables globales pour rendre les autres locales et donc éliminables par condensation statique. Ces méthodes se différencient par le choix des variables globales et par le lien entre variables globales et locales. Les méthodes Hybridizable Discontinuous Galerkin (HDG) [76] ont été utilisées pour l'hyperélasticité par Kabaria, Lew & Cockburn [147] et Nguyen et Peraire [171], alors que les méthodes hybrid dG (d'ordre bas) avec traces conformes et hybridizable weakly conforming Galerkin avec traces non-conformes ont été étudiées dans le cadre de la mécanique des solides linéaire par Krämer & al. [151] et dans le cas non-linéaire par Bayat & al. [26] et Wulfinghoff & al. [212].

Nous terminons cette brève revue bibliographique en illustrant le phénomène de verrouillage numérique sur la simulation d'un essai de traction en grandes déformations plastiques, voir la Fig 1.11. Nous remarquons que la trace du tenseur des contraintes de Cauchy oscille pour les éléments finis H^1-conformes linéaires (a) et quadratiques (b) avec intégration complète, alors que pour les éléments finis quadratiques sous-intégrés (c) et mixtes à trois champs (d), le verrouillage est éliminé.

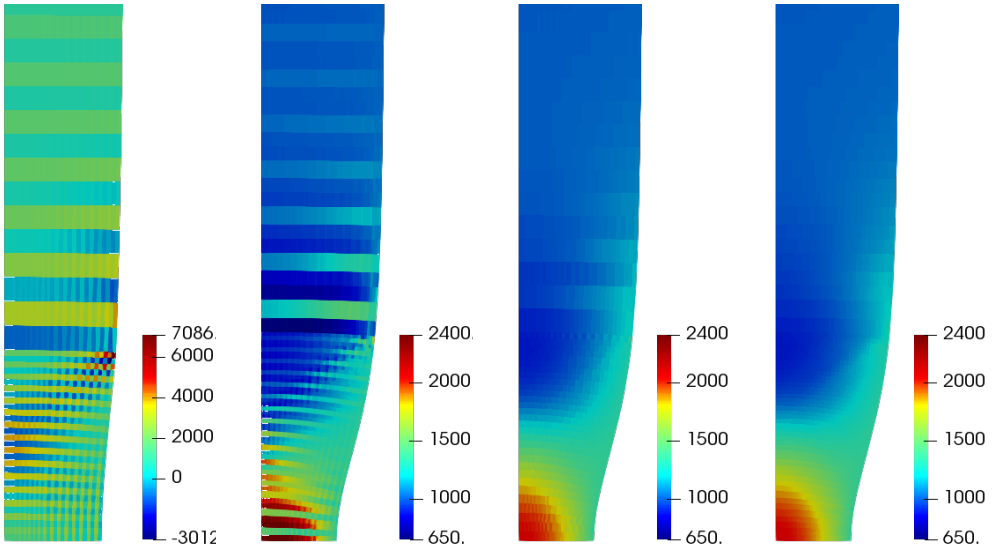

(a) Q1 (b) Q2 (c) Q2_RI (d) UPG

Figure 1.11: Gestion numérique de l'incompressibilité pour un essai de traction en grandes déformations plastiques: trace du tenseur des contraintes de Cauchy $\boldsymbol{\sigma}$ (en MPa) aux points de quadrature pour les méthodes éléments finis H^1-conformes linéaires (a) et quadratiques (b) avec intégration complète, quadratiques avec intégration réduite (c), et mixtes à trois champs (d).

1.5 Contact unilatéral de Signorini avec frottement de Tresca

Après les non-linéarités matérielle et géométrique vues précédemment, la non-linéarité de contact-frottement est l'autre non-linéarité qui est très souvent présente dans les simulations numériques en mécanique des solides (voir entre autres les travaux de Kikuchi & Oden [148], Haslinger, Hlaváček & Nečas [134], Han & Sofonea [129], Laursen [156], Wriggers [208], et Wohlmuth [207]). Cette non-linéarité pose en général un certain nombre de difficultés en particulier si les maillages sont non-coïncidents au niveau des surfaces de contact entre deux corps déformables (précision et robustesse). Nous nous limitons ici au problème initialement introduit par Signorini [188] d'un corps déformable élastique linéaire (petites déformations et pas de plasticité) qui entre en contact avec une fondation rigide.

1.5.1 Modèle continu

Nous considérons un corps élastique $\mathcal{B}_0$ qui est représenté dans sa configuration de référence par le domaine polygonal/polyédrique $\Omega_0 \subset \mathbb{R}^d$, $d \in \{2,3\}$ (voir la Fig 1.12). Le bord $\Gamma := \partial\Omega_0$ est partitionné en trois parties disjointes : le bord de Dirichlet Γ_{D}, le bord de Neumann Γ_{N} et le bord de contact-frottement Γ_{C}. Nous supposons que $\mathrm{mes}(\Gamma_{\mathrm{D}}) > 0$ pour bloquer les mouvements de corps rigide et $\mathrm{mes}(\Gamma_{\mathrm{C}}) > 0$ pour assurer la présence de contact. Pour simplifier, le bord de contact-frottement Γ_{C} est supposé être une ligne droite en 2D ou un polygone plan en 3D. Le corps $\mathcal{B}_0$ est encastré sur le bord de Dirichlet Γ_{D} et se déforme sous l'action d'un chargement volumique $\underline{f} \in L^2(\Omega_0;\mathbb{R}^d)$ et d'un chargement surfacique $\underline{t}_{\mathrm{N}} \in L^2(\Gamma_{\mathrm{N}};\mathbb{R}^d)$ sur le bord de Neumann. La normale sortante unitaire est notée $\underline{N}$.

Pour décrire les conditions de contact-frottement, nous adoptons la décomposition en partie normale et tangentielle du champ de déplacement $\underline{v}$ et du vecteur des forces surfaciques

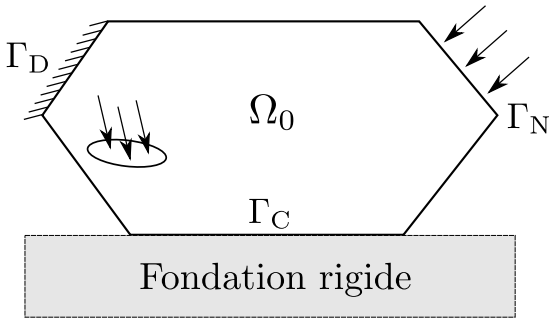

Figure 1.12: Géométrie du problème de contact avec une fondation rigide.

$\underline{\sigma}_N(\underline{v}) := \boldsymbol{\sigma}(\underline{v})\underline{N}$ défini sur $\partial\Omega_0$:

$$\underline{v} = v_N\underline{N} + \underline{v}_T \quad \text{et} \quad \underline{\sigma}_N(\underline{v}) = \sigma_N(\underline{v})\underline{N} + \underline{\sigma}_T(\underline{v}).$$

où $v_N := \underline{v}\cdot\underline{N}$ et $\sigma_N(\underline{v}) := \boldsymbol{\sigma}(\underline{v})\underline{N}\cdot\underline{N}$. Les conditions de contact unilatéral de Signorini [188] sur la surface de contact Γ_C sont données par

$$(i) \quad u_N \le 0, \qquad (ii) \quad \sigma_N(\underline{u}) \le 0, \qquad (iii) \quad \sigma_N(\underline{u})\, u_N = 0. \tag{1.41}$$

La première condition implique que le corps déformable ne peut pas pénétrer la fondation rigide. La deuxième condition indique que les efforts de contact sont des efforts de répulsion. La troisième est une condition de complémentarité qui implique qu'il y a du contact ($u_N = 0$) quand l'effort de contact est non nul et qu'il n'y a pas d'effort de contact quand il n'y a pas de contact ($u_N < 0$).

Dans les situations réalistes, la présence de contact induit souvent la présence de frottement entre les deux objets. Plusieurs modèles de frottement existent comme le frottement de Tresca ou de Coulomb. Par simplicité, nous nous limitons ici au frottement de Tresca qui se traduit par les conditions suivantes sur Γ_C :

$$\begin{cases} |\underline{\sigma}_T(\underline{u})| & \le s, & \text{si } \underline{u}_T = \underline{0}, & (iv) \\ \underline{\sigma}_T(\underline{u}) & = -\, s\, \dfrac{\underline{u}_T}{|\underline{u}_T|} & \text{sinon}, & (v) \end{cases} \tag{1.42}$$

où $s \ge 0$ est le seuil de glissement qui est donné. Notons que les conditions (iv) et (v) impliquent que $|\underline{\sigma}_T(\underline{u})| \le s$ dans tous les cas, et que si $|\underline{\sigma}_T(\underline{u})| < s$ alors $\underline{u}_T = \underline{0}$ (adhérence). Dans la situation $\underline{u}_T \neq \underline{0}$ (glissement), la contrainte tangentielle est de signe opposé au glissement et s'oppose à celui-ci. Ce modèle est assez réaliste dans le cas du contact bilatéral ($u_N = 0$ sur Γ_C), mais moins dans le cas général. Le frottement de Coulomb est alors plus approprié même si son traitement mathématique et numérique est plus compliqué. Le cas du contact sans frottement se retrouve en prenant $s = 0$ dans (1.42).

Le problème de contact unilatéral avec frottement de Tresca consiste à trouver un champ de déplacement $\underline{u} : \Omega_0 \to \mathbb{R}^d$ vérifiant les équations (1.26) avec $\underline{u}_D \equiv \underline{0}$, et les conditions de contact (1.41) et de frottement (1.42). Nous introduisons le cône convexe K des déplacements admissibles :

$$\underline{K} := \{\underline{v} \in \underline{V}_0 \ : \ v_N \le 0 \text{ sur } \Gamma_C\}.$$

Les éléments de $\underline{K}$ satisfont la condition de Dirichlet sur Γ_D et de non-interpénétration sur la zone de contact Γ_C. Posons

$$a(\underline{u},\underline{v}) := \int_{\Omega_0} \boldsymbol{\sigma}(\underline{u}) : \boldsymbol{\varepsilon}(\underline{v})\, d\Omega_0, \quad L(\underline{v}) := \int_{\Omega_0} \underline{f}\cdot\underline{v}\, d\Omega_0 + \int_{\Gamma_N} \underline{t}_N\cdot\underline{v}\, d\Gamma, \quad j(\underline{v}) := \int_{\Gamma_C} s|\underline{v}_t|\, d\Gamma,$$

pour tout $\underline{u}$ et $\underline{v}$ dans $\underline{V}_0$. La formulation faible du problème (1.26)–(1.41)–(1.42) comme une inéquation variationnelle de seconde espèce (voir [148, 123]) est la suivante :

$$\left\{ \begin{array}{l} \text{Trouver } \underline{u} \in \underline{K} \text{ tel que} \\ a(\underline{u}, \underline{v} - \underline{u}) + j(\underline{v}) - j(\underline{u}) \geq L(\underline{v} - \underline{u}), \qquad \forall\, \underline{v} \in \underline{K}. \end{array} \right. \tag{1.43}$$

Ce problème admet une unique solution, voir par exemple [148, Theorème 10.2, Chapitre 10]. Une difficulté supplémentaire pour les problèmes de contact-frottement est le manque de régularité de la solution. En effet, ce type de problème présente des singularités quelle que soit la régularité des données (voir [170]), et généralement la solution ne peut pas être plus régulière que $H^{\frac{5}{2}}(\Omega_0; \mathbb{R}^d)$.

1.5.2 Discrétisation par éléments finis

La discrétisation par éléments finis de l'inégalité variationnelle (1.43) est étudiée depuis de nombreuses années aussi bien d'un point de vue mathématique que numérique. Différentes stratégies de résolution ont été proposées pour imposer les conditions de Signorini au niveau discret :

- **Méthodes pénalisées** : L'idée est de remplacer les inéquations de contact-frottement par des équations non-linéaires en introduisant des coefficients de pénalisation. L'avantage de ces méthodes est qu'elles reposent sur une formulation primale et sont donc facilement implémentables. Cependant, les méthodes pénalisées sont en général inconsistantes et une pénétration non-physique ainsi qu'un problème de conditionnement peuvent apparaitre si les coefficients de pénalisation sont mal choisis. Ces méthodes ont été utilisées pour les problèmes de contact par Chernov, Maischak & Stephan [57], Chouly & Hild [65], Kikuchi & Oden [148], Kikuchi & Song [149], Oden & Kikuchi [175], et Oden & Kim [176].

- **Méthodes mixtes** : L'idée est d'introduire des multiplicateurs de Lagrange pour imposer les conditions de contact-frottement de manière consistante. Cependant, le problème à résoudre devient un problème de type point-selle et une condition de type inf-sup doit être vérifiée pour garantir la stabilité discrète. Nous mentionnons entre autres les travaux de Hild [139], Hild & Renard [140], Ben Belgacem & Renard [31], Hauret and Le Tallec [136], Laborde & Renard [155], Haslinger, Hlaváček & Nečas [134], Wohlmuth [207], et Abbas, Drouet & Hild [1].

- **Méthodes Nitsche-FEM** : La combinaison de l'approche Nitsche [173] avec les éléments finis H^1-conformes permet d'imposer les conditions de contact-frottement en les remplaçant par des équations non-linéaires. L'avantage est que ces méthodes reposent sur une formulation primale comme les méthodes pénalisées mais elles sont en outre consistantes. L'idée de ces méthodes est esquissée à la section 1.5.3 ci-dessous. L'application de ces méthodes pour le problème de Signorini a été étudiée par Chouly & Hild [64], Chouly [61], Chouly, Hild & Renard [67], Chouly & al. [63], et Chouly, Mlika & Renard [168, 68].

Pour la plupart des discrétisations, le frottement de Tresca crée des difficultés supplémentaires pour établir des taux de convergence optimaux en comparaison de ce qui peut être obtenu dans le cas sans frottement (voir, par exemple, les travaux de Hüeber & Wohlmuth [144], Wohlmuth [207], Hild & Renard [141], et Drouet & Hild [107] pour le contact sans frottement). En effet, les termes intégraux non-différentiables dus aux frottement introduisent dans les estimations d'erreur des quantités supplémentaires qui sont difficiles à majorer,

même quand des hypothèses supplémentaires sont faites (voir, par exemple, [134, 207]). Par conséquent, les résultats de convergence sont limités pour la plupart des discrétisations. Les premières estimations prouvées pour les méthodes mixtes et mortar sont sous-optimales (voir, par exemple, les travaux de Haslinger & Hlaváček [133], Hild [138], et Baillet & Sassi [19, 20]). Récemment, un taux de convergence en $\mathcal{O}(h^\nu)$ pour une régularité $H^{1+\nu}(\Omega_0;\mathbb{R}^d)$, $0 \leq \nu \leq 1$, a été obtenu par Wohlmuth [207, Theorème 4.9] dans le cas bidimensionnel pour une méthode mixte d'ordre bas avec des hypothèses techniques sur la zone de contact-frottement (c'est la première estimation optimale à notre connaissance). Dans le cas tridimensionnel, un taux en $O(h^{\min(\frac{1}{2},\nu)})$ a été prouvé sans hypothèse supplémentaire toujours par Wohlmuth dans [207, Théorème 4.10]. Pour la méthode pénalisée, un taux en $\mathcal{O}(h^{\frac{1}{2}+\frac{\nu}{2}+\nu^2})$ pour une régularité $H^{\frac{3}{2}+\nu}(\Omega_0;\mathbb{R}^d)$, $0 < \nu < \frac{1}{2}$, et le taux quasi-optimal en $\mathcal{O}(h|\log h|^{\frac{1}{2}})$ pour une régularité $H^2(\Omega_0;\mathbb{R}^d)$ ont été établis par Chouly & Hild dans [65], sans hypothèse supplémentaire sur la zone de contact-frottement. Ces résultats ont été améliorés récemment par Dione dans [96] où des taux optimaux ont été obtenus si le paramètre de pénalisation est suffisamment grand. Pour la discrétisation Nitsche-FEM, la convergence optimale d'ordre $\mathcal{O}(h^s)$ en norme $H^1(\Omega_0;\mathbb{R}^d)$ a été prouvée par Chouly dans [61] sous l'hypothèse de régularité $H^{1+s}(\Omega_0;\mathbb{R}^d)$ avec $s \in (\frac{1}{2}, k]$, où $k \geq 1$ est le degré polynomial des éléments finis de Lagrange (il est remarquable qu'aucune hypothèse supplémentaire ne soit nécessaire). De plus, l'estimation d'erreur reste valide en deux et trois dimensions d'espace, et pour tout degré polynomial $k \geq 1$.

Dans cette thèse, nous utilisons les méthodes de Nitsche pour imposer les conditions de contact et de frottement. Ce choix est motivé d'une part par le fait que les méthodes de Nitsche permettent de se passer de multiplicateurs de Lagrange, ce qui nous permettra de conserver une formulation primale en cohérence avec les développements précédents pour résoudre les problèmes de verrouillage numérique dû à l'incompressibilité. D'autre part, des méthodes Nitsche-HHO ont été développées dans [50] pour le problème de Signorini scalaire et des taux de convergence optimaux en $\mathcal{O}(h^{k+1})$ pour la norme de l'énergie ont été prouvés. Nous allons ici étendre cette analyse au problème de l'élasticité avec des conditions de contact et de frottement.

1.5.3 Formulation de Nitsche

La méthode de Nitsche a été développée initialement pour imposer faiblement les conditions aux limites de Dirichlet [173]. Depuis, cette méthode a été étendue aux traitements des conditions de contact et de frottement. L'idée est de reformuler les conditions de contact (1.41) et de frottement (1.42) en équations non-linéaires. Cela a été proposé pour la première fois dans [79] par Curnier & Alart (voir aussi [61] pour une preuve détaillée).

Proposition 1.8 *Soit γ une fonction à valeurs strictement positives sur Γ_C. Les conditions de contact avec frottement de Tresca (1.41)–(1.42) peuvent être reformulées comme suit :*

$$\sigma_N(\underline{u}) = [\sigma_N(\underline{u}) - \gamma\, u_N]_{\mathbb{R}^-} \tag{1.44a}$$

$$\underline{\sigma}_T(\underline{u}) = [\underline{\sigma}_T(\underline{u}) - \gamma\, \underline{u}_T]_s\,. \tag{1.44b}$$

où $[x]_{\mathbb{R}^-} := \min(x, 0)$ est la projection de x sur le sous-ensemble fermé convexe $\mathbb{R}^- = (-\infty, 0]$ et pour tout $\alpha \in \mathbb{R}^+$, $[\underline{x}]_\alpha$ est la projection orthogonale de $\underline{x}$ sur $\mathscr{B}(\underline{0}, \alpha) \subset \mathbb{R}^{d-1}$, où $\mathscr{B}(\underline{0}, \alpha)$ est la boule fermée centrée sur l'origine $\underline{0}$ et de rayon α. Cette projection est définie de manière analytique, pour tout $\underline{x} \in \mathbb{R}^{d-1}$, par

$$[\underline{x}]_\alpha = \begin{cases} \underline{x} & \text{si } |\underline{x}| \leq \alpha, \\ \alpha \dfrac{\underline{x}}{|\underline{x}|} & \text{sinon.} \end{cases} \tag{1.45}$$

Soit $\{\mathcal{T}_h\}_{h\geq 0}$ une famille d maillages simplicaux réguliers au sens habituel de Ciarlet [69] de Ω_0, et soit

$$\underline{V}_h := \{\underline{v}_h \in C^0(\overline{\Omega_0};\mathbb{R}^d) \,:\, \underline{v}_{h|T} \in \mathbb{P}^k(T;\mathbb{R}^d);\ \forall T \in \mathcal{T}_h\}$$

l'espace d'éléments finis de degré $k \geq 1$ sur $\mathcal{T}_h$. Nous considérons le sous-espace $\underline{V}_{h,0} := \{\underline{v}_h \in \underline{V}_h \,:\, \underline{v} = \underline{0} \text{ sur } \Gamma_D\}$. La discrétisation conforme Nitsche-FEM de la formulation faible (1.43) est la suivante (voir [63]) :

$$\begin{cases} \text{Trouver } \underline{u}_h \in \underline{V}_{h,0} \text{ tel que} \\ a_{\gamma\theta,h}(\underline{u}_h,\underline{v}_h) = \ell_{\gamma\theta,h}(\underline{v}_h) \qquad \forall \underline{v}_h \in \underline{V}_{h,0}, \end{cases} \tag{1.46}$$

où les formes semi-linéaire et linéaire introduites ci-dessus sont

$$\begin{aligned} a_{\gamma\theta,h}(\underline{v}_h,\underline{w}_h) :=& a(\underline{v}_h,\underline{w}_h) - \int_{\Gamma_C} \frac{\theta}{\gamma}\underline{\sigma}_N(\underline{v}_h)\cdot\underline{\sigma}_N(\underline{w}_h)\,d\Gamma \\ &+ \int_{\Gamma_C} \frac{1}{\gamma}\big[\phi^N_{\gamma,1}(\underline{v}_h)\big]_{\mathbb{R}^-}\phi^N_{\gamma,\theta}(\underline{w}_h)\,d\Gamma + \int_{\Gamma_C}\frac{1}{\gamma}\Big[\underline{\phi}^T_{\gamma,1}(\underline{v}_h)\Big]_s\cdot\underline{\phi}^T_{\gamma,\theta}(\underline{w}_h)\,d\Gamma, \quad (1.47a) \\ \ell_{\gamma\theta,h}(\underline{w}_h) :=& L(\underline{w}_h), \quad (1.47b) \end{aligned}$$

avec $\phi^N_{\gamma,\theta}(\underline{v}) := \theta\sigma_N(\underline{v}) - \gamma v_N$ et $\underline{\phi}^T_{\gamma,\theta}(\underline{v}) := \theta\underline{\sigma}_T(\underline{v}) - \gamma\underline{v}_T$. Notons que $a_{\gamma\theta,h}$ est non-linéaire par rapport à son premier argument. Ici, les paramètres utilisateur sont le paramètre de symétrie $\theta \in \{-1,0,1\}$ et le paramètre de pénalisation γ, tel que $\gamma = \gamma_0\, h^{-1}$ avec γ_0 choisi suffisamment grand pour assurer la coercivité pour $\theta \neq -1$ (la valeur minimum dépend d'une inégalité de trace discrète, voir, par exemple, les travaux de Nitsche [173], Hansbo [130]), et Stenberg [199]). Voir Chouly & al. [63] pour une discussion plus complète sur le choix de θ et γ_0, et ses implications.

1.6 Plan du manuscrit et contributions

Le manuscrit se compose de cinq chapitres et d'une annexe. Après cette introduction sur les problématiques rencontrées et les méthodes Hybrid High-Order (HH0) dans ce Chapitre 1, le Chapitre 2 est consacré à l'extension des méthodes HHO à la modélisation des grandes déformations hyperélastiques. Le problème discret est écrit comme résultant de la minimisation d'une énergie élastique non-linéaire où une reconstruction locale du gradient des déplacements est utilisée. Deux méthodes HHO sont considérées : une méthode stabilisée où le gradient discret est reconstruit dans l'espace des polynômes à valeurs matricielles d'ordre k et une stabilisation est ajoutée à la fonctionnelle d'énergie discrète, et une méthode non-stabilisée qui reconstruit un gradient discret stable d'ordre supérieur ce qui évite l'ajout d'un terme de stabilisation. Les deux méthodes vérifient localement le principe des travaux virtuels avec des tractions équilibrées. Nous présentons une étude numérique réalisée dans `disk++` des deux méthodes sur des solutions analytiques et sur des cas-tests tridimensionnels proches des applications industrielles visées où sont présents de fortes bandes de cisaillement et des phénomènes de cavitation. Les résultats obtenus sont comparés à ceux obtenus avec `code_aster` pour des méthodes conformes. De plus, les coûts numériques des deux méthodes HHO sont comparés et les deux méthodes présentent un comportement robuste à la limite incompressible. Ce chapitre est issu d'un article publié en 2018 chez Computational Mechanics intitulé "*Hybrid High-Order methods for finite deformations of hyperelastic materials*" [2].

Le Chapitre 3 se concentre sur le développement des méthodes HHO pour la plasticité associative en petites déformations. La méthode HHO développée supporte les maillages polyédriques avec des interfaces non-conformes, ne verrouille pas, l'intégration du comportement est réalisée seulement en des points de quadrature de la cellule, et la matrice tangente

de Newton est symétrique. La méthode vérifie localement le principe des travaux virtuels avec des tractions équilibrées. Plusieurs cas-tests bidimensionnels et tridimensionnels issus de la littérature sont présentés en utilisant la librairie `disk++`. Les résultats comprennent des comparaisons avec des solutions analytiques ou des résultats obtenus avec `code_aster` ainsi que des méthodes d'éléments finis H^1-conformes et mixtes. Ce travail peut en outre être vu comme la première extension des méthodes Hybridizable Discontinuous Galerkin (HDG) à la plasticité en petites déformations grâce au lien étroit entre HDG et HHO. Ce chapitre est issu d'un article publié en 2019 chez Computer Methods in Applied Mechanics and Engineering intitulé "*A Hybrid High-Order method for incremental associative plasticity with small deformations*" [3].

Le Chapitre 4 porte sur l'extension des méthodes HHO développées pour les petites déformations plastiques aux grandes déformations plastiques. Cette extension se fait grâce à l'utilisation du formalisme des déformations logarithmiques, ce qui permet de réutiliser les lois de comportement développées pour les petites déformations plastiques. Comme pour les petites déformations, la méthode HHO développée supporte les maillages polyédriques avec des interfaces non-conformes, ne verrouille pas, l'intégration du comportement est réalisée seulement en des points de quadrature de la cellule, et la matrice tangente de Newton est symétrique. Une étude numérique en utilisant les logiciels `disk++` et `code_aster` sur des cas-tests bidimensionnels et tridimensionnels issus de la littérature. Les comparaisons se font grâce à des solutions analytiques ou à des résultats obtenus avec `code_aster` et des méthodes d'éléments finis H^1-conformes et mixtes. Ce travail peut également être vu comme la première extension des méthodes HDG à la plasticité en grandes déformations. Ce chapitre est issu d'un article publié en ligne en 2019 chez International Journal for Numerical Methods in Engineering intitulé "*A Hybrid High-Order method for finite plasticity within a logarithmic strain framework*" [4].

Le Chapitre 5 présente le couplage entre les méthodes Nitsche et HHO pour gérer le contact unilatéral avec frottement de Tresca dans le cas de l'élasticité linéaire en petites déformations. L'imposition des conditions de contact et de frottement est réalisée sans ajout de multiplicateur de Lagrange grâce à l'approche de Nitsche. Des taux de convergence optimaux en h^{k+1} sont prouvés en norme de l'énergie ainsi que la robustesse à la limite incompressible. Comme précédemment, une implémentation dans `disk++` est réalisée ainsi que des comparaisons grâce à des solutions analytiques ou à des résultats obtenus avec `code_aster` pour des problème de contact (le frottement de Tresca n'étant pas disponible dans `code_aster`). Enfin, une extension de l'approche de type Nitsche aux problèmes de la plasticité en petites déformations est présentée. Ce Chapitre est issu d'une collaboration avec Franz Chouly et un article intitulé "*A Hybrid High-Order discretization combined with Nitsche's method for contact and Tresca friction in small strain elasticity*" [62] a été soumis.

Enfin, l'annexe A présente les principales idées pour l'implémentation dans `code_aster` des méthodes HHO pour la mécanique des solides.

CHAPTER 2

HYBRID HIGH-ORDER METHODS FOR FINITE DEFORMATIONS OF HYPERELASTIC MATERIALS

Abstract. We devise and evaluate numerically Hybrid High-Order (HHO) methods for hyperelastic materials undergoing finite deformations. The HHO methods use as discrete unknowns piecewise polynomials of order $k \geq 1$ on the mesh skeleton, together with cell-based polynomials that can be eliminated locally by static condensation. The discrete problem is written as the minimization of a broken nonlinear elastic energy where a local reconstruction of the displacement gradient is used. Two HHO methods are considered: a stabilized method where the gradient is reconstructed as a tensor-valued polynomial of order k and a stabilization is added to the discrete energy functional, and an unstabilized method which reconstructs a stable higher-order gradient and circumvents the need for stabilization. Both methods satisfy the principle of virtual work locally with equilibrated tractions. We present a numerical study of the two HHO methods on test cases with known solution and on more challenging three-dimensional test cases including finite deformations with strong shear layers and cavitating voids. We assess the computational efficiency of both methods, and we compare our results to those obtained with an industrial software using conforming finite elements and to results from the literature. The two HHO methods exhibit robust behavior in the quasi-incompressible regime.

This chapter is based on a publication in Computational Mechanics entitled "*Hybrid High-Order methods for finite deformations of hyperelastic materials*" [2].

Sommaire

2.1 Introduction

Hybrid-High Order (HHO) methods have been introduced a couple of years ago for linear elasticity problems in [89] and for diffusion problems in [91]. A review on diffusion problems can be found in [92], and a Péclet-robust analysis for advection-diffusion problems in [86]. Moreover, an open-source implementation of HHO methods using generic programming tools is available through the `Disk++` library described in [71]. Recent developments of HHO methods in computational mechanics include the incompressible Stokes equations (with possibly large irrotational forces) [93], the incompressible Navier–Stokes equations [94], Biot's consolidation problem [32], and nonlinear elasticity with small deformations [40]. The goal of the present work is to devise and evaluate numerically HHO methods for hyperelastic materials undergoing finite deformations. Such problems are particularly challenging since finite deformations induce an additional geometric nonlinearity on top of the one present in the stress-strain constitutive relation. Moreover, hyperelastic materials are often considered near the incompressible limit, so that robustness in this situation is important.

The discrete unknowns in HHO methods are face-based unknowns that are piecewise polynomials of some order $k \geq 1$ on the mesh skeleton ($k \geq 0$ for diffusion equations). Cell-based unknowns are also introduced in the discrete formulation. These additional unknowns are instrumental for the stability and approximation properties of the method and can be locally eliminated by using the well-known static condensation technique. In the present nonlinear context, this elimination is performed at each step of the nonlinear iterative solver (typically Newton's method). The devising of HHO methods hinges on two ideas: (i) a reconstruction operator that reconstructs locally from the local cell and face unknowns a displacement field or a tensor-valued field representing its gradient; (ii) a stabilization operator that enforces in a weak sense on each mesh face the consistency between the local face unknowns and the trace of the cell unknowns. A somewhat subtle design of the stabilization operator has been proposed in [89, 91] leading to $O(h^{k+1})$ energy-error estimates, where h is the mesh-size, for linear diffusion and elasticity problems and smooth solutions. HHO methods offer several advantages: (i) the construction is dimension-independent; (ii) general meshes (including fairly general polytopal mesh cells and non-matching interfaces) are supported; (iii) a local formulation using equilibrated fluxes is available, and (iv) HHO methods are computationally attractive owing to the static condensation of the cell unknowns and the higher-order convergence rates.

HHO methods have been bridged to Hybridizable Discontinuous Galerkin (HDG) methods in [74]. HDG methods, as originally devised in [76], are formulated in terms of a discrete triple which approximates the flux, the primal unknown, and its trace on the mesh skeleton. The HDG method is then specified by the discrete spaces for the above triple, and the stabilization operator that enters the discrete equations through the so-called numerical flux trace. The difference between HHO and HDG methods is twofold: (i) the HHO reconstruction operator replaces the discrete HDG flux (a similar rewriting of an HDG method for nonlinear elasticity can be found in [147]), and, more importantly, (ii) both HHO and HDG penalize in

a least-squares sense the difference between the discrete trace unknown and the trace of the discrete primal unknown (with a possibly mesh-dependent weight), but HHO uses a non-local operator over each mesh cell boundary that delivers one-order higher approximation than just penalizing pointwise the difference as in HDG.

Discretization methods for linear and nonlinear elasticity have undergone a vigorous development over the last decade. For discontinuous Galerkin (dG) methods, we mention in particular [160, 132, 78] for linear elasticity, and [117, 174] for nonlinear elasticity. HDG methods for linear elasticity have been coined in [198] (see also [77] for incompressible Stokes flows), and extensions to nonlinear elasticity can be found in [197, 171, 147]. Other recent developments in the last few years include, among others, Gradient Schemes for nonlinear elasticity with small deformations [106], the Virtual Element Method (VEM) for linear and nonlinear elasticity with small [30] and finite deformations [58, 210], the (low-order) hybrid dG method with conforming traces for nonlinear elasticity [212], the hybridizable weakly conforming Galerkin method with nonconforming traces for linear elasticity [151], the Weak Galerkin method for linear elasticity [204], and the discontinuous Petrov–Galerkin method for linear elasticity [48].

In the present work, we devise and evaluate numerically two HHO methods to approximate hyperelastic materials undergoing finite deformations. Following the ideas of [117, 147] developed in the context of dG and HDG methods, both HHO discrete solutions are formulated as stationary points of a discrete energy functional that is defined from the exact energy functional by replacing the displacement gradient in the Piola–Kirchhoff tensor by its reconstructed counterpart. In the first HHO method, called stabilized HHO (sHHO), a quadratic term associated with the HHO-stabilization operator is added to the discrete energy functional. For linear elasticity, one recovers the original HHO method from [89] if the displacement gradient is reconstructed locally in the tensor-valued polynomial space $\boldsymbol{\nabla}_X\mathbb{P}_d^{k+1}(T;\mathbb{R}^d)$ where k is the degree of the polynomials attached to the mesh skeleton and T is a generic mesh cell (and if the displacement divergence is reconstructed in $\mathbb{P}_d^k(T;\mathbb{R})$); the notation is defined more precisely in the following sections. In the present nonlinear context, the gradient is reconstructed in $\mathbb{P}_d^k(T;\mathbb{R}^{d\times d})$ (which is a strict superspace of $\boldsymbol{\nabla}_X\mathbb{P}_d^{k+1}(T;\mathbb{R}^d)$); the same reconstruction space is considered for HDG in [147] for nonlinear elasticity with finite deformations (where the stabilization operator is, however, different), and a similar choice with symmetric-valued reconstructions is considered for HHO in [40] for nonlinear elasticity with small deformations. The main reason for reconstructing the gradient in a larger space stems from the fact that the reconstructed gradient of a test function acts against a discrete Piola–Kirchhoff tensor which is not in gradient form. For a discussion and a numerical example in the context of the Leray–Lions problem, we refer the reader to [87, §4.1].

In nonlinear elasticity, the use of stabilization can lead to numerical difficulties since it is not clear beforehand how large the stabilization parameter ought to be and since a large value of this parameter can deteriorate the conditioning of the system and hamper the convergence of the iterative solvers; see [116, 115] for a related discussion on dG methods and [30, 58] for VEM. Moreover, [147, Section 4] presents an example where spurious solutions can appear in an HDG discretization if the stabilization parameter is not large enough. Motivated by these difficulties, we also consider a second method called unstabilized HHO (uHHO). Inspired by the recent ideas in [146] on stable dG methods without penalty parameters, we consider an HHO method where the gradient is reconstructed in a higher-order polynomial space, and no stabilization is added to the discrete energy. Focusing for simplicity on matching simplicial meshes, the reconstruction space can be (i) the Raviart–Thomas–Nédélec (RTN) space $\mathbb{RTN}_d^k(T;\mathbb{R}^{d\times d}) := \mathbb{P}_d^k(T;\mathbb{R}^{d\times d})\oplus(\mathbb{P}_d^{k,\mathrm{H}}(T;\mathbb{R}^d)\otimes\underline{X})$, where $\mathbb{P}_d^{k,\mathrm{H}}(T;\mathbb{R}^d)$ is the space composed of homogeneous polynomials of degree k, or (ii) the (larger) polynomial space $\mathbb{P}_d^{k+1}(T;\mathbb{R}^{d\times d})$.

For both choices, we prove, using the ideas in [146], that the reconstructed gradient is stable, thereby circumventing the need to introduce and tune any stabilization parameter. Reconstructing the gradient in $\mathbb{RTN}_d^k(T;\mathbb{R}^{d\times d})$ leads to optimal $O(h^{k+1})$-convergence rates for linear problems and smooth solutions, Instead, reconstructing the gradient in $\mathbb{P}_d^{k+1}(T;\mathbb{R}^{d\times d})$ leads to $O(h^k)$-convergence rates for linear problems and smooth solutions, i.e., the method still converges but at a suboptimal order in ideal situations. The advantage of reconstructing the gradient in $\mathbb{P}_d^{k+1}(T;\mathbb{R}^{d\times d})$ is, however, that our numerical results indicate that the method is more robust to handle strongly nonlinear problems.

This paper is organized as follows. In Section 2.2, we present the nonlinear hyperelasticity problem and we introduce some basic notation. The two HHO methods are presented in Section 2.3, where we also discuss some theoretical and implementation aspects. Section 2.4 then contains test cases with analytical (or computable) solution. We first consider three-dimensional traction test cases with manufactured solution to assess the convergence rates delivered by sHHO and uHHO in the nonlinear case. Then, we consider the dilatation of a quasi-incompressible annulus; in this test case, proposed in [147, Section 5.2], the exact solution can be approximated to a very high accuracy by solving an ordinary differential equation in the radial coordinate. We also compare the computational efficiency of both methods, and we consider a continuous Galerkin (cG) approximation based on H^1-conforming finite elements using the industrial software `code_aster` [111]. Section 2.5 considers three application-driven, three-dimensional examples: the indentation of a compressible and quasi-incompressible rectangular block (where we also provide a comparison with the industrial software `code_aster`), a hollow cylinder deforming under compression and shear, and a sphere expanding under traction with two cavitating voids. These last two examples are particularly challenging, and our results are compared to the HDG solutions reported in [147].

2.2 The nonlinear hyperelasticity problem

We are interested in finding the static equilibrium configuration of an elastic continuum body that occupies the domain Ω_0 in the reference configuration and that undergoes finite deformations under the action of a body force $\underline{f}$ in Ω_0, a traction force $\underline{t}_{\mathrm{N}}$ on the Neumann boundary Γ_{N}, and a prescribed displacement $\underline{u}_{\mathrm{D}}$ on the Dirichlet boundary Γ_{D} (the external forces $\underline{f}$ and $\underline{t}_{\mathrm{N}}$ are assumed dead, i.e. independent of the displacement). Here, $\Omega_0 \subset \mathbb{R}^d$, $d \in \{2,3\}$, is a bounded connected polytopal domain with unit outward normal $\underline{N}$ and with Lipschitz boundary $\Gamma := \partial\Omega_0$ decomposed in the two relatively open subsets Γ_{N} and Γ_{D} such that $\overline{\Gamma_{\mathrm{N}}} \cup \overline{\Gamma_{\mathrm{D}}} = \Gamma$, $\Gamma_{\mathrm{N}} \cap \Gamma_{\mathrm{D}} = \emptyset$, and Γ_{D} has positive Hausdorff-measure (so as to prevent rigid-body motions).

As is customary for elasticity problems with finite deformations, we adopt the Lagrangian description (cf, e.g, the textbooks [36, 70]). Due to the deformation, a point $\underline{X} \in \Omega_0$ is mapped to a point $\underline{x} = \underline{X} + \underline{u}(\underline{X})$ in the equilibrium configuration, where $\underline{u} : \Omega_0 \to \mathbb{R}^d$ is the displacement mapping. The model problem consists in finding a displacement mapping $\underline{u} : \Omega_0 \to \mathbb{R}^d$ satisfying the following equations:

$$-\underline{\mathrm{Div}}_X(\boldsymbol{P}) = \underline{f} \qquad \text{in } \Omega_0, \tag{2.1a}$$

$$\underline{u} = \underline{u}_{\mathrm{D}} \qquad \text{on } \Gamma_{\mathrm{D}}, \tag{2.1b}$$

$$\boldsymbol{P}\,\underline{N} = \underline{t}_{\mathrm{N}} \qquad \text{on } \Gamma_{\mathrm{N}}, \tag{2.1c}$$

where $\boldsymbol{P} := \boldsymbol{P}(\underline{X}, \boldsymbol{F}(\underline{u}))$ is the first Piola–Kirchhoff stress tensor and $\boldsymbol{F}(\underline{u}) = \boldsymbol{I} + \boldsymbol{\nabla}_X\,\underline{u}$ is the deformation gradient. The deformation gradient takes values in $\mathbb{R}^{d\times d}_+$ which is the set

of $d \times d$ matrices with positive determinant. The governing equations (2.1) are stated in Lagrangian form; in particular, the gradient and divergence operators are taken with respect to the coordinate $\underline{X}$ of the reference configuration (we use the subscript X to indicate it).

We restrict ourselves to bodies consisting of homogeneous hyperelastic materials for which there exists a strain energy density $\Psi(\boldsymbol{F})$ defined by a function $\Psi : \mathbb{R}_+^{d\times d} \to \mathbb{R}$. We assume that the first Piola–Kirchhoff stress tensor is defined as $\boldsymbol{P} = \partial_{\boldsymbol{F}}\Psi$ so that the associated elastic modulus is given by $\mathbb{A} = \partial^2_{\boldsymbol{F}\,\boldsymbol{F}}\Psi$. We denote by $\underline{V}_{\mathrm{D}}$ the set of all kinematically admissible displacements which satisfy the Dirichlet condition (2.1b), and we define the energy functional $\mathcal{E} : \underline{V}_{\mathrm{D}} \to \mathbb{R}$ such that

$$\mathcal{E}(\underline{v}) = \int_{\Omega_0} \Psi(\boldsymbol{F}(\underline{v}))\, d\Omega_0 - \int_{\Omega_0} \underline{f}\cdot\underline{v}\, d\Omega_0 - \int_{\Gamma_{\mathrm{N}}} \underline{t}_{\mathrm{N}}\cdot\underline{v}\, d\Gamma. \tag{2.2}$$

The static equilibrium problem (2.1) consists of seeking the stationary points of the energy functional $\mathcal{E}$ which satisfy the following weak form of the Euler–Lagrange equations:

$$0 = D\mathcal{E}(\underline{u})[\delta\underline{v}] = \int_{\Omega_0} \boldsymbol{P}(\boldsymbol{F}(\underline{u})) : \boldsymbol{\nabla}_X(\delta\underline{v})\, d\Omega_0 - \int_{\Omega_0} \underline{f}\cdot\delta\underline{v}\, d\Omega_0 - \int_{\Gamma_{\mathrm{N}}} \underline{t}_{\mathrm{N}}\cdot\delta\underline{v}\, d\Gamma, \tag{2.3}$$

for all virtual displacements $\delta\underline{v}$ satisfying a zero boundary condition on Γ_{D}. We assume that the strain energy density function Ψ is polyconvex (cf e.g. [21]) so that local minimizers of the energy functional exist. In the present work, we will mainly consider hyperelastic materials of Neohookean type extended to the compressible range such that

$$\Psi(\boldsymbol{F}) = \frac{\mu}{2}(\boldsymbol{F} : \boldsymbol{F} - d) - \mu \ln J + \frac{\lambda}{2}\Theta(J)^2, \tag{2.4}$$

where $J \in \mathbb{R}_{>0}$ is the determinant of $\boldsymbol{F}$, μ and λ are material constants, and $\Theta : \mathbb{R}_{>0} \to \mathbb{R}$ is a smooth function such that $\Theta(J) = 0 \Leftrightarrow J = 1$ and $\Theta'(1) \neq 0$. The function Θ represents the volumetric deformation energy, and the potential Ψ defined by (2.4) satisfies the principle of material frame indifference [70]. For further insight into the physical meaning, we refer the reader to [177, Chap.7]. For later use, it is convenient to derive directly from (2.4) the first Piola–Kirchhoff stress tensor

$$\boldsymbol{P}(\boldsymbol{F}) = \mu(\boldsymbol{F} - \boldsymbol{F}^{-T}) + \lambda J\Theta(J)\Theta'(J)\boldsymbol{F}^{-T}, \tag{2.5}$$

where we have used that $\partial_{\boldsymbol{F}} J = J\boldsymbol{F}^{-T}$, as well as the elastic modulus

$$\begin{aligned}\mathbb{A}(\boldsymbol{F}) =& \mu(\boldsymbol{I} \mathbin{\overline{\otimes}} \boldsymbol{I} + \boldsymbol{F}^{-T} \mathbin{\underline{\otimes}} \boldsymbol{F}^{-1}) - \lambda J\Theta(J)\Theta'(J)\boldsymbol{F}^{-T} \mathbin{\underline{\otimes}} \boldsymbol{F}^{-1} \\ &+ \lambda\left[J\Theta(J)(J\Theta''(J) + \Theta'(J)) + (J\Theta'(J))^2\right]\boldsymbol{F}^{-T} \otimes \boldsymbol{F}^{-T},\end{aligned} \tag{2.6}$$

where $\otimes$, $\mathbin{\underline{\otimes}}$ and $\mathbin{\overline{\otimes}}$ are defined such that $\{\circ \otimes \bullet\}_{ijkl} = \{\circ\}_{ij}\{\bullet\}_{kl}$, $\{\circ \mathbin{\underline{\otimes}} \bullet\}_{ijkl} = \{\circ\}_{il}\{\bullet\}_{jk}$ and $\{\circ \mathbin{\overline{\otimes}} \bullet\}_{ijkl} = \{\circ\}_{ik}\{\bullet\}_{jl}$, for all $1 \le i, j, k, l \le d$.

2.3 The Hybrid High-Order method

In this section, we present the unstabilized and stabilized HHO methods to be considered in our numerical tests.

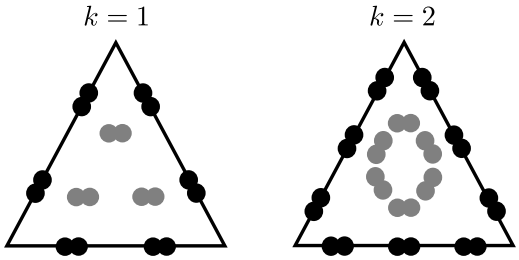

Figure 2.1: Face (black) and cell (gray) degrees of freedom in $\hat{\underline{U}}_T^k$ for $k=1$ and $k=2$ in the two-dimensional case (each dot represents a degree of freedom which is not necessarily a point evaluation).

2.3.1 Discrete setting

Let $(\mathcal{T}_h)_{h>0}$ be a shape-regular sequence of affine simplicial meshes with no hanging nodes of the domain Ω_0. A generic mesh cell in $\mathcal{T}_h$ is denoted $T \in \mathcal{T}_h$, its diameter h_T, and its unit outward normal $\underline{n}_T$. It is customary to define the global mesh-size as $h = \max_{T\in\mathcal{T}_h} h_T$. The mesh faces are collected in the set $\mathcal{F}_h$, and a generic mesh face is denoted $F \in \mathcal{F}_h$. The set $\mathcal{F}_h$ is further partitioned into the subset $\mathcal{F}_h^{\mathrm{i}}$ which is the collection of mesh interfaces and the subset $\mathcal{F}_h^{\mathrm{b}}$ which is the collection of mesh faces located at the boundary Γ. We assume that the mesh is compatible with the partition of the boundary Γ into Γ_{D} and Γ_{N}, and we further split the set $\mathcal{F}_h^{\mathrm{b}}$ into the disjoint subsets $\mathcal{F}_h^{\mathrm{b,D}}$ and $\mathcal{F}_h^{\mathrm{b,N}}$ with obvious notation. For all $T \in \mathcal{T}_h$, $\mathcal{F}_{\partial T}$ is the collection of the mesh faces that are subsets of ∂T.

Let $k \geq 1$ be a fixed polynomial degree. In each mesh cell $T \in \mathcal{T}_h$, the local HHO unknowns are a pair $(\underline{v}_T, \underline{v}_{\partial T})$, where the cell unknown $\underline{v}_T \in \mathbb{P}_d^k(T;\mathbb{R}^d)$ is a vector-valued d-variable polynomial of degree at most k in the mesh cell T, and $\underline{v}_{\partial T} \in \mathbb{P}_{d-1}^k(\mathcal{F}_{\partial T};\mathbb{R}^d) = \times_{F\in\mathcal{F}_{\partial T}} \mathbb{P}_{d-1}^k(F;\mathbb{R}^d)$ is a piecewise, vector-valued polynomial of degree at most k on each face $F \in \mathcal{F}_{\partial T}$. We write more concisely that

$$\hat{\underline{v}}_T := (\underline{v}_T, \underline{v}_{\partial T}) \in \hat{\underline{U}}_T^k := \mathbb{P}_d^k(T;\mathbb{R}^d) \times \mathbb{P}_{d-1}^k(\mathcal{F}_{\partial T};\mathbb{R}^d). \tag{2.7}$$

The degrees of freedom are illustrated in Fig. 2.1, where a dot indicates one degree of freedom (and is not necessarily computed as a point evaluation). More generally, the polynomial degree k of the face unknowns being fixed, HHO methods can be devised using cell unknowns that are polynomials of degree $l \in \{k-1, k, k+1\}$, see [74]; these variants are not further considered herein. We equip the space $\hat{\underline{U}}_T^k$ with the following local discrete strain semi-norm:

$$|\hat{\underline{v}}_T|_{1,T}^2 := \|\boldsymbol{\nabla}_X \underline{v}_T\|_{\boldsymbol{L}^2(T)}^2 + \|\eta_{\partial T}^{\frac{1}{2}}(\underline{v}_{\partial T} - \underline{v}_{T|\partial T})\|_{\underline{L}^2(\partial T)}^2, \tag{2.8}$$

with the piecewise constant function $\eta_{\partial T}$ such that $\eta_{\partial T|F} = h_F^{-1}$ for all $F \in \mathcal{F}_{\partial T}$ where h_F is the diameter of F. We notice that $|\hat{\underline{v}}_T|_{1,T} = 0$ implies that both functions $\underline{v}_T$ and $\underline{v}_{\partial T}$ are constant and take the same constant value.

2.3.2 Local gradient reconstruction

A crucial ingredient in the devising of the HHO method is a local gradient reconstruction in each mesh cell $T \in \mathcal{T}_h$. This reconstruction is materialized by an operator $\boldsymbol{G}_T : \hat{\underline{U}}_T^k \to \boldsymbol{R}(T;\mathbb{R}^{d\times d})$, where $\boldsymbol{R}(T;\mathbb{R}^{d\times d})$ is some finite-dimensional linear space typically composed of $\mathbb{R}^{d\times d}$-valued polynomials in T. For all $\hat{\underline{v}}_T \in \hat{\underline{U}}_T^k$, the reconstructed gradient $\boldsymbol{G}_T(\hat{\underline{v}}_T) \in \boldsymbol{R}(T;\mathbb{R}^{d\times d})$ is obtained by solving the following local problem: For all $\boldsymbol{\tau} \in \boldsymbol{R}(T;\mathbb{R}^{d\times d})$,

$$(\boldsymbol{G}_T(\hat{\underline{v}}_T), \boldsymbol{\tau})_{\boldsymbol{L}^2(T)} = (\boldsymbol{\nabla}_X \underline{v}_T, \boldsymbol{\tau})_{\boldsymbol{L}^2(T)} + (\underline{v}_{\partial T} - \underline{v}_{T|\partial T}, \boldsymbol{\tau}\,\underline{n}_T)_{\underline{L}^2(\partial T)}. \tag{2.9}$$

Solving this problem entails inverting the mass matrix associated with some basis of the polynomial space $\boldsymbol{R}(T;\mathbb{R}^{d\times d})$. In the present work, we consider three choices for the reconstruction space $\boldsymbol{R}(T;\mathbb{R}^{d\times d})$. The choice $\boldsymbol{R}(T;\mathbb{R}^{d\times d}) := \mathbb{P}_d^k(T;\mathbb{R}^{d\times d})$ is considered in the context of the stabilized HHO method which is further described in Section 2.3.4. The other two choices are $\boldsymbol{R}(T;\mathbb{R}^{d\times d}) = \mathbb{RTN}_d^k(T;\mathbb{R}^{d\times d})$ (that is, the RTN space of order k defined in the introduction) and the larger space $\boldsymbol{R}(T;\mathbb{R}^{d\times d}) = \mathbb{P}_d^{k+1}(T;\mathbb{R}^{d\times d})$. These choices are considered in the context of the unstabilized HHO method which is further described in Section 2.3.3.

Lemma 2.1 (Boundedness and stability) *The gradient reconstruction operator defined by (2.9) enjoys the following properties:* (i) *Boundedness: There is $\alpha_\sharp < +\infty$, uniform w.r.t. h, so that, for all $T \in \mathcal{T}_h$ and all $\hat{\underline{v}}_T \in \hat{\underline{U}}_T^k$,*

$$\|\boldsymbol{G}_T(\hat{\underline{v}}_T)\|_{\boldsymbol{L}^2(T)} \le \alpha_\sharp |\hat{\underline{v}}_T|_{1,T},. \tag{2.10}$$

(ii) *Stability: Provided $\mathbb{RTN}_d^k(T;\mathbb{R}^{d\times d}) \subseteq \boldsymbol{R}(T;\mathbb{R}^{d\times d})$, there is $\alpha_\flat > 0$, uniform w.r.t. h, so that, for all $T \in \mathcal{T}_h$ and all $\hat{\underline{v}}_T \in \hat{\underline{U}}_T^k$*

$$\alpha_\flat |\hat{\underline{v}}_T|_{1,T} \le \|\boldsymbol{G}_T(\hat{\underline{v}}_T)\|_{\boldsymbol{L}^2(T)}, \tag{2.11}$$

Proof. The boundedness property (2.10) follows by applying the Cauchy–Schwarz inequality to the right-hand side of (2.9) and a discrete trace inequality so as to bound $\|\boldsymbol{\tau}\,\underline{n}_T\|_{\underline{\boldsymbol{L}}^2(\partial T)}$ by $h_T^{-\frac{1}{2}}\|\boldsymbol{\tau}\|_{\boldsymbol{L}^2(T)}$. The proof of the stability property (2.11) is inspired from [146]; we sketch it for completeness. Let $\hat{\underline{v}}_T \in \hat{\underline{U}}_T^k$. We need to find a field $\boldsymbol{\tau} \in \boldsymbol{R}(T;\mathbb{R}^{d\times d})$ so that (i) $|\hat{\underline{v}}_T|_{1,T}^2 \le c(\boldsymbol{G}_T(\hat{\underline{v}}_T),\boldsymbol{\tau})_{\boldsymbol{L}^2(T)}$ and (ii) $\|\boldsymbol{\tau}\|_{\boldsymbol{L}^2(T)} \le c|\hat{\underline{v}}_T|_{1,T}$ for some constant c uniform w.r.t. h. Owing to our assumption $\mathbb{RTN}_d^k(T;\mathbb{R}^{d\times d}) \subseteq \boldsymbol{R}(T;\mathbb{R}^{d\times d})$, we can build $\boldsymbol{\tau} \in \mathbb{RTN}_d^k(T;\mathbb{R}^{d\times d})$, and we do so by prescribing its canonical degrees of freedom in T as follows:

$$\begin{aligned}
&(\boldsymbol{\tau},\boldsymbol{\phi})_{\boldsymbol{L}^2(T)} = (\boldsymbol{\nabla}_X \underline{v}_T,\boldsymbol{\phi})_{\boldsymbol{L}^2(T)}, && \forall \boldsymbol{\phi} \in \mathbb{P}_d^{k-1}(T;\mathbb{R}^{d\times d}),\\
&(\boldsymbol{\tau}\,\underline{n}_T,\underline{\varphi})_{\underline{L}^2(\partial T)} = (\eta_{\partial T}(\underline{v}_{\partial T} - \underline{v}_{T|\partial T}),\underline{\varphi})_{\underline{L}^2(\partial T)}, && \forall \underline{\varphi} \in \mathbb{P}_{d-1}^k(\mathcal{F}_{\partial T};\mathbb{R}^d).
\end{aligned}$$

With this choice, the above property (i) holds true since $(\boldsymbol{G}_T(\hat{\underline{v}}_T),\boldsymbol{\tau})_{\boldsymbol{L}^2(T)} = |\hat{\underline{v}}_T|_{1,T}^2$, whereas (ii) can be shown by using the classical stability of RTN functions in terms of their canonical degrees of freedom.

□

Remark 2.2 (General meshes) *The above stability proof exploits the properties of the RTN functions on simplicial meshes. If the meshes contain hanging nodes or cells with more general shapes, one possibility considered in the recent work [87] is to reconstruct the gradient using piecewise RTN functions on a simplicial submesh of the mesh cell $T \in \mathcal{T}_h$. Another construction has been recently devised in [121] for dG methods using a high-order lifting of the jumps on a simplicial submesh.*

2.3.3 The unstabilized HHO method

Let us set $\mathbb{P}_d^k(\mathcal{T}_h;\mathbb{R}^d) := \times_{T\in\mathcal{T}_h} \mathbb{P}_d^k(T;\mathbb{R}^d)$ and $\mathbb{P}_{d-1}^k(\mathcal{F}_h;\mathbb{R}^d) := \times_{F\in\mathcal{F}_h} \mathbb{P}_{d-1}^k(F;\mathbb{R}^d)$. The global space of discrete HHO unknowns is defined as

$$\hat{\underline{U}}_h^k := \mathbb{P}_d^k(\mathcal{T}_h;\mathbb{R}^d) \times \mathbb{P}_{d-1}^k(\mathcal{F}_h;\mathbb{R}^d). \tag{2.12}$$

For a generic element $\hat{\underline{v}}_h \in \hat{\underline{U}}_h^k$, we use the notation $\hat{\underline{v}}_h = ((\underline{v}_T)_{T\in\mathcal{T}_h}, (\underline{v}_F)_{F\in\mathcal{F}_h})$. For any mesh cell $T \in \mathcal{T}_h$, we denote by $\hat{\underline{v}}_T = (\underline{v}_T, \underline{v}_{\partial T}) \in \hat{\underline{U}}_T^k$ the local components of $\hat{\underline{v}}_h$ attached to the mesh cell T and the faces composing its boundary, and for any mesh face $F \in \mathcal{F}_h$, we denote by $\underline{v}_F$ the component attached to the face F. The Dirichlet boundary condition on the displacement field can be enforced explicitly on the discrete unknowns attached to the boundary faces in $\mathcal{F}_h^{\mathrm{b,D}}$. We set

$$\hat{\underline{U}}_{h,\mathrm{D}}^k := \left\{ \hat{\underline{v}}_h \in \hat{\underline{U}}_h^k \mid \underline{v}_F = \underline{\Pi}_F^k(\underline{u}_{\mathrm{D}}),\ \forall F \in \mathcal{F}_h^{\mathrm{b,D}} \right\}, \tag{2.13a}$$

$$\hat{\underline{U}}_{h,0}^k := \left\{ \hat{\underline{v}}_h \in \hat{\underline{U}}_h^k \mid \underline{v}_F = \underline{0},\ \forall F \in \mathcal{F}_h^{\mathrm{b,D}} \right\}, \tag{2.13b}$$

where $\underline{\Pi}_F^k$ denotes the L^2-orthogonal projector onto $\mathbb{P}_{d-1}^k(F;\mathbb{R}^d)$.

The discrete counterpart of the energy functional $\mathcal{E}$ defined by (2.2) is the discrete energy functional $\mathcal{E}_h^{\mathrm{u}} : \hat{\underline{U}}_{h,\mathrm{D}}^k \to \mathbb{R}$ defined by

$$\mathcal{E}_h^{\mathrm{u}}(\hat{\underline{v}}_h) = \sum_{T\in\mathcal{T}_h} \left\{ (\Psi(\boldsymbol{F}_T(\hat{\underline{v}}_T)), 1)_{L^2(T)} - (\underline{f}, \underline{v}_T)_{\underline{L}^2(T)} \right\} - \sum_{F\in\mathcal{F}_h^{\mathrm{b,N}}} (\underline{t}_{\mathrm{N}}, \underline{v}_F)_{\underline{L}^2(F)}, \tag{2.14}$$

for all $\hat{\underline{v}}_h \in \hat{\underline{U}}_{h,\mathrm{D}}^k$, with the local deformation gradient operator $\boldsymbol{F}_T : \hat{\underline{U}}_T^k \to \boldsymbol{R}(T;\mathbb{R}^{d\times d})$ such that $\boldsymbol{F}_T(\hat{\underline{v}}_T) := \boldsymbol{I} + \boldsymbol{G}_T(\hat{\underline{v}}_T)$ where the local gradient reconstruction space is $\boldsymbol{R}(T;\mathbb{R}^{d\times d}) = \mathbb{RTN}_d^k(T;\mathbb{R}^{d\times d})$ or $\boldsymbol{R}(T;\mathbb{R}^{d\times d}) = \mathbb{P}_d^{k+1}(T;\mathbb{R}^{d\times d})$.

The discrete problem consists in seeking the stationary points of the discrete energy functional $\mathcal{E}_h^{\mathrm{u}}$. This leads to the following discrete equations: Find $\hat{\underline{u}}_h \in \hat{\underline{U}}_{h,\mathrm{D}}^k$ such that

$$\sum_{T\in\mathcal{T}_h} (\boldsymbol{P}(\boldsymbol{F}_T(\hat{\underline{u}}_T)), \boldsymbol{G}_T(\delta\hat{\underline{v}}_T))_{\boldsymbol{L}^2(T)} = \sum_{T\in\mathcal{T}_h} (\underline{f}, \delta\underline{v}_T)_{\underline{L}^2(T)} + \sum_{F\in\mathcal{F}_h^{\mathrm{b,N}}} (\underline{t}_{\mathrm{N}}, \delta\underline{v}_F)_{\underline{L}^2(F)}, \tag{2.15}$$

for any generic virtual displacement $\delta\hat{\underline{v}}_h \in \hat{\underline{U}}_{h,0}^k$. The discrete problem (2.15) expresses the principle of virtual work at the global level. As is often the case with discrete formulations using face-based discrete unknowns, it is possible to devise a local principle of virtual work in terms of face-based discrete tractions that comply with the law of action and reaction. This has been shown in [74] for HHO methods applied to the diffusion equation, and the argument extends immediately to the present context. For all $T \in \mathcal{T}_h$, let us define the discrete traction:

$$\underline{T}_T = \boldsymbol{\Pi}_{\partial T}^k(\boldsymbol{\Pi}_T^R(\boldsymbol{P}(\boldsymbol{F}_T(\hat{\underline{u}}_T))))\,\underline{n}_T, \tag{2.16}$$

where $\boldsymbol{\Pi}_T^R$ denotes the L^2-orthogonal projector onto $\boldsymbol{R}(T;\mathbb{R}^{d\times d})$. (Note that the projector $\boldsymbol{\Pi}_{\partial T}^k$ is not needed if $\boldsymbol{R}(T;\mathbb{R}^{d\times d}) = \mathbb{RTN}_d^k(T;\mathbb{R}^{d\times d})$ since the normal component on ∂T of functions in $\mathbb{RTN}_d^k(T;\mathbb{R}^{d\times d})$ is in $\mathbb{P}_{d-1}^k(\partial T;\mathbb{R}^d)$.)

Lemma 2.3 (Equilibrated tractions) *The following local principle of virtual work holds true for all $T \in \mathcal{T}_h$: For all $\delta\underline{v}_T \in \mathbb{P}_d^k(T;\mathbb{R}^d)$,*

$$(\boldsymbol{P}(\boldsymbol{F}_T(\hat{\underline{u}}_T)), \boldsymbol{\nabla}_X \delta\underline{v}_T)_{\boldsymbol{L}^2(T)} - (\underline{T}_T, \delta\underline{v}_{T|\partial T})_{\underline{L}^2(\partial T)} = (\underline{f}, \delta\underline{v}_T)_{\underline{L}^2(T)}, \tag{2.17}$$

where the discrete tractions $\underline{T}_T \in \mathbb{P}_{d-1}^k(\mathcal{F}_{\partial T};\mathbb{R}^d)$ defined by (2.16) satisfy the following law of action and reaction for all $F \in \mathcal{F}_h^i \cup \mathcal{F}_h^{b,N}$:

$$\underline{T}_{T_-|F} + \underline{T}_{T_+|F} = \underline{0}, \quad \text{if } F \in \mathcal{F}_h^i \text{ with } \partial T_- \cap \partial T_+ = F, \tag{2.18a}$$

$$\underline{T}_{T|F} = \underline{\Pi}_F^k(\underline{t}_N), \qquad \text{if } F \in \mathcal{F}_h^{b,N} \text{ with } \partial T \cap \Gamma_N = F. \tag{2.18b}$$

Proof. We follow the ideas in [74]. The local principle of virtual work (2.17) follows by considering the virtual displacement $((\delta_{\underline{v}T}\delta_{T,T'})_{T'\in\mathcal{T}_h}, (\underline{0})_{F\in\mathcal{F}_h}) \in \underline{\hat{U}}_{h,0}^k$ in (2.15), with the Kronecker delta such that $\delta_{T,T'} = 1$ if $T = T'$ and $\delta_{T,T'} = 0$ otherwise, and observing that, owing to (2.9), we have

$$\begin{aligned}(\underline{f}, \delta_{\underline{v}T})_{\underline{L}^2(T)} &= (\boldsymbol{P}(\boldsymbol{F}_T(\hat{\underline{u}}_T)), \boldsymbol{G}_T(\delta_{\underline{v}T}, \underline{0}))_{\boldsymbol{L}^2(T)}\\ &= (\boldsymbol{\Pi}_T^R\boldsymbol{P}(\boldsymbol{F}_T(\hat{\underline{u}}_T)), \boldsymbol{G}_T(\delta_{\underline{v}T}, \underline{0}))_{\boldsymbol{L}^2(T)}\\ &= (\boldsymbol{\Pi}_T^R(\boldsymbol{P}(\boldsymbol{F}_T(\hat{\underline{u}}_T))), \boldsymbol{\nabla}_X\delta_{\underline{v}T})_{\boldsymbol{L}^2(T)} - (\boldsymbol{\Pi}_T^R(\boldsymbol{P}(\boldsymbol{F}_T(\hat{\underline{u}}_T)))\,\underline{n}_T, \delta_{\underline{v}T|\partial T})_{\underline{L}^2(\partial T)}\\ &= (\boldsymbol{P}(\boldsymbol{F}_T(\hat{\underline{u}}_T)), \boldsymbol{\nabla}_X\delta_{\underline{v}T})_{\boldsymbol{L}^2(T)} - (\underline{T}_T, \delta_{\underline{v}T|\partial T})_{\underline{L}^2(\partial T)}.\end{aligned}$$

Similarly, the balance property (2.18) follows by considering, for all $F \in \mathcal{F}_h^{\mathrm{i}} \cup \mathcal{F}_h^{\mathrm{b,N}}$, the virtual displacement $((\underline{0})_{T\in\mathcal{T}_h}, (\delta_{\underline{v}F}\delta_{F,F'})_{F'\in\mathcal{F}_h}) \in \underline{\hat{U}}_{h,0}^k$ in (2.15) (with obvious notation for the face-based Kronecker delta), and observing that both $\delta_{\underline{v}F}$ and $\underline{T}_{T_\pm|F}$ are in $\mathbb{P}_{d-1}^k(F;\mathbb{R}^d)$.

□

Let us now discuss the choice of the gradient reconstruction space where one can set either $\boldsymbol{R}(T;\mathbb{R}^{d\times d}) = \mathbb{RTN}_d^k(T;\mathbb{R}^{d\times d})$ or $\boldsymbol{R}(T;\mathbb{R}^{d\times d}) = \mathbb{P}_d^{k+1}(T;\mathbb{R}^{d\times d})$. The key property with $\boldsymbol{R}(T;\mathbb{R}^{d\times d}) = \mathbb{RTN}_d^k(T;\mathbb{R}^{d\times d})$ is that the normal component on ∂T of functions in $\mathbb{RTN}_d^k(T;\mathbb{R}^{d\times d})$ is in the space $\mathbb{P}_{d-1}^k(\partial T;\mathbb{R}^d)$ used for the face HHO unknowns (the normal components of such functions actually span $\mathbb{P}_{d-1}^k(\partial T;\mathbb{R}^d)$). Proceeding as in [89] then leads to the following important commuting property:

$$\boldsymbol{G}_T(\underline{\hat{I}}_T^k(\underline{v})) = \boldsymbol{\Pi}_T^R(\boldsymbol{\nabla}_X\underline{v}), \qquad \forall\underline{v}\in H^1(T;\mathbb{R}^d), \tag{2.19}$$

where the reduction operator $\underline{\hat{I}}_T^k : H^1(T;\mathbb{R}^d) \to \underline{\hat{U}}_T^k$ is defined so that $\underline{\hat{I}}_T^k(\underline{v}) = (\underline{\Pi}_T^k(\underline{v}), \underline{\Pi}_{\partial T}^k(\underline{v}))$, where $\underline{\Pi}_T^k$ is the L^2-orthogonal projector onto $\mathbb{P}_d^k(T;\mathbb{R}^d)$ and $\underline{\Pi}_{\partial T}^k$ is the L^2-orthogonal projector onto $\mathbb{P}_{d-1}^k(\mathcal{F}_{\partial T};\mathbb{R}^d)$. Proceeding as in [89, Thm. 8] and using the approximation properties of the RTN finite elements, one can show that for the linear elasticity problem and smooth solutions, the energy error measured as $\|\boldsymbol{\nabla}_X\underline{u} - \boldsymbol{G}_h(\hat{\underline{u}}_h)\|_{\boldsymbol{L}^2(\mathcal{T}_h)}$ converges as $h^{k+1}|\underline{u}|_{\underline{H}^{k+2}(\Omega_0)}$ (the subscript $\boldsymbol{L}^2(\mathcal{T}_h)$ means that the Hilbertian sum of $L^2(T;\mathbb{R}^{d\times d})$-norms over the mesh cells is considered). Concerning implementation, we observe that the reconstruction operator needs to select basis functions for the RTN space; however, the canonical basis functions are not needed, and one can use simple monomial bases.

Considering instead the choice $\boldsymbol{R}(T;\mathbb{R}^{d\times d}) = \mathbb{P}_d^{k+1}(T;\mathbb{R}^{d\times d})$ leads to a larger space for the local gradient reconstruction (for $d = 3$, the local space is of dimension 45 ($k = 1$) and 108 ($k = 2$) for RTN functions and of dimension 90 ($k = 1$) and 180 ($k = 2$) for $\mathbb{R}^{d\times d}$-valued polynomials of order $(k + 1)$). One benefit of considering a larger space is, according to our numerical experiments, an increased robustness of the method to handle strongly nonlinear cases. One disadvantage is that the above property on the normal component of functions in $\boldsymbol{R}(T;\mathbb{R}^{d\times d})$ no longer holds. Therefore, one no longer has (2.19); however, one can infer from (2.9) the weaker property

$$\boldsymbol{G}_T(\underline{\tilde{I}}_T^k(\underline{v})) = \boldsymbol{\nabla}_X(\underline{\Pi}_T^k(\underline{v})), \qquad \forall\underline{v}\in H^1(T;\mathbb{R}^d), \tag{2.20}$$

where the reduction operator $\underline{\tilde{I}}_T^k : H^1(T;\mathbb{R}^d) \to \underline{\hat{U}}_T^k$ is defined so that $\underline{\tilde{I}}_T^k(\underline{v}) = (\underline{\Pi}_T^k(\underline{v}), \underline{\Pi}_T^k(\underline{v})_{|\partial T})$. Proceeding as in [89, Thm. 8], one can show that for the linear elasticity problem and smooth solutions, the energy error $\|\boldsymbol{\nabla}_X\underline{u} - \boldsymbol{G}_h(\hat{\underline{u}}_h)\|_{\boldsymbol{L}^2(\mathcal{T}_h)}$ converges as $h^k|\underline{u}|_{\underline{H}^{k+1}(\Omega_0)}$. This convergence rate will be confirmed by the experiments reported in Section 2.4.1. Finally, regardless of the choice of $\boldsymbol{R}(T;\mathbb{R}^{d\times d})$, testing (2.9) with a function

$\boldsymbol{\tau} = q\boldsymbol{I} \in \mathbb{P}_d^k(T;\mathbb{R}^{d\times d})$ with q arbitrary in $\mathbb{P}_d^k(T;\mathbb{R})$, one can show that

$$\Pi_T^k(\mathrm{trace}(\boldsymbol{G}_T(\underline{\hat{I}}_T^k(\underline{v})))) = \Pi_T^k(\nabla\cdot\underline{v}), \qquad \forall \underline{v} \in H^1(T;\mathbb{R}^d). \tag{2.21}$$

The presence of the projector Π_T^k on the left-hand side indicates that $\mathrm{trace}(\boldsymbol{G}_T(\underline{\hat{I}}_T^k(\underline{v})))$ may be affected by a high-order perturbation hampering the argument of [89, Prop. 3] to prove robustness in the quasi-incompressible limit for linear elasticity. Nevertheless, we observe absence of locking in the numerical experiments performed in Sections 2.4.2 and 2.5.

2.3.4 The stabilized HHO method

The discrete unknowns in the stabilized HHO method are exactly the same as those in the unstabilized HHO method. The only difference is in the form of the discrete elastic energy. In the stabilized HHO method, the gradient is reconstructed locally in the polynomial space $\boldsymbol{R}(T;\mathbb{R}^{d\times d}) = \mathbb{P}_d^k(T;\mathbb{R}^{d\times d})$ for all $T \in \mathcal{T}_h$. Since the norm $\|\boldsymbol{G}_T(\underline{\hat{v}}_T)\|_{\boldsymbol{L}^2(T)}$ does not control the semi-norm $|\underline{\hat{v}}_T|_{1,T}$ for all $\underline{\hat{v}}_T \in \underline{\hat{U}}_T^k$ (as can be seen from a simple counting argument based on the dimension of the involved spaces), we need to augment the discrete elastic energy by a stabilization semi-norm. This semi-norm is based on the usual stabilization operator for HHO methods $\underline{S}_{\partial T}^k : \underline{\hat{U}}_T^k \to \mathbb{P}_{d-1}^k(\mathcal{F}_{\partial T};\mathbb{R}^d)$ such that, for all $\underline{\hat{v}}_T \in \underline{\hat{U}}_T^k$,

$$\underline{S}_{\partial T}^k(\underline{\hat{v}}_T) = \underline{\Pi}_{\partial T}^k\big(\underline{v}_{\partial T} - \underline{D}_T^{k+1}(\underline{\hat{v}}_T)_{|\partial T} - (\underline{v}_T - \underline{\Pi}_T^k(\underline{D}_T^{k+1}(\underline{\hat{v}}_T)))_{|\partial T}\big), \tag{2.22}$$

with the local displacement reconstruction operator $\underline{D}_T^{k+1} : \underline{\hat{U}}_T^k \to \mathbb{P}_d^{k+1}(T;\mathbb{R}^d)$ such that, for all $\underline{\hat{v}}_T \in \underline{\hat{U}}_T^k$, $\underline{D}_T^{k+1}(\underline{\hat{v}}_T) \in \mathbb{P}_d^{k+1}(T;\mathbb{R}^d)$ is obtained by solving the following Neumann problem in T: For all $\underline{w} \in \mathbb{P}_d^{k+1}(T;\mathbb{R}^d)$,

$$(\boldsymbol{\nabla}_X \underline{D}_T^{k+1}(\underline{\hat{v}}_T), \boldsymbol{\nabla}_X \underline{w})_{\boldsymbol{L}^2(T)} = (\boldsymbol{\nabla}_X \underline{v}_T, \boldsymbol{\nabla}_X \underline{w})_{\boldsymbol{L}^2(T)} + (\underline{v}_{\partial T} - \underline{v}_{T|\partial T}, \boldsymbol{\nabla}_X \underline{w}\, \underline{n}_T)_{\underline{L}^2(\partial T)}, \tag{2.23}$$

and additionally enforcing that $\int_T \underline{D}_T^{k+1}(\underline{\hat{v}}_T)\, dT = \int \underline{v}_T\, dT$. Comparing with (2.9), one readily sees that $\boldsymbol{\nabla}_X \underline{D}_T^{k+1}(\underline{\hat{v}}_T)$ is the L^2-orthogonal projection of $\boldsymbol{G}_T(\underline{\hat{v}}_T)$ onto the subspace $\boldsymbol{\nabla}_X \mathbb{P}_d^{k+1}(T;\mathbb{R}^d) \subsetneq \mathbb{P}_d^k(T;\mathbb{R}^{d\times d}) = \boldsymbol{R}(T;\mathbb{R}^{d\times d})$. Following [89, Lemma 4], it is straightforward to establish the following stability and boundedness properties (the proof is omitted for brevity).

Lemma 2.4 (Boundedness and stability) *Let the gradient reconstruction operator be defined by (2.9) with $\boldsymbol{R}(T;\mathbb{R}^{d\times d}) = \mathbb{P}_d^k(T;\mathbb{R}^{d\times d})$. Let the stabilization operator be defined by (2.22). Then, there exist real numbers $0 < \alpha_\flat < \alpha_\sharp < +\infty$, uniform w.r.t. h, so that*

$$\alpha_\flat |\underline{\hat{v}}_T|_{1,T} \le \left(\|\boldsymbol{G}_T(\underline{\hat{v}}_T)\|_{\boldsymbol{L}^2(T)}^2 + \|\eta_{\partial T}^{\frac{1}{2}} \underline{S}_{\partial T}^k(\underline{\hat{v}}_T)\|_{\underline{L}^2(\partial T)}^2\right)^{\frac{1}{2}} \le \alpha_\sharp |\underline{\hat{v}}_T|_{1,T}, \tag{2.24}$$

for all $T \in \mathcal{T}_h$ and all $\underline{\hat{v}}_T \in \underline{\hat{U}}_T^k$, with $\eta_{\partial T}$ defined below (2.8).

Remark 2.5 (HDG-type stabilization) *In general, HDG methods use the stabilization operator $\underline{\tilde{S}}_{\partial T}^k(\underline{\hat{v}}_T) = \underline{v}_{\partial T} - \underline{v}_{T|\partial T}$ in the equal-order case, or $\underline{\tilde{S}}_{\partial T}^k(\underline{\hat{v}}_T) = \underline{\Pi}_{\partial T}^k(\underline{v}_{\partial T} - \underline{v}_{T|\partial T})$ if the cell unknowns are taken to be polynomials of order $(k+1)$ (see [158]). The definition in Eq. (2.22), introduced in [89], enjoys, even in the equal-order case, the high-order approximation property $\|\eta_{\partial T}^{\frac{1}{2}} \underline{S}_{\partial T}^k(\underline{\hat{I}}_T^k(\underline{v}))\|_{\underline{L}^2(\partial T)} \le c h_T^{k+1} |\underline{v}|_{\underline{H}^{k+2}(T)}$ with the reduction operator $\underline{\hat{I}}_T^k : H^1(T;\mathbb{R}^d) \to \underline{\hat{U}}_T^k$ defined below (2.19) and c uniform w.r.t. h.*

In the stabilized HHO method, the discrete energy functional $\mathcal{E}_h^{\mathrm{s}} : \hat{\underline{U}}_{h,\mathrm{D}}^k \to \mathbb{R}$ is defined as

$$\mathcal{E}_h^{\mathrm{s}}(\hat{\underline{v}}_h) = \sum_{T\in\mathcal{T}_h} \Big\{ (\Psi(\boldsymbol{F}_T(\hat{\underline{v}}_T)),1)_{L^2(T)} - (\underline{f},\underline{v}_T)_{\underline{L}^2(T)} \Big\} - \sum_{F\in\mathcal{F}_h^{\mathrm{b,N}}} (\underline{t}_{\mathrm{N}},\underline{v}_F)_{\underline{L}^2(F)} + \sum_{T\in\mathcal{T}_h} \frac{\beta}{2} \|\eta_{\partial T}^{\frac{1}{2}} \underline{S}_{\partial T}^k(\hat{\underline{v}}_T)\|_{\underline{L}^2(\partial T)}^2, \tag{2.25}$$

with a user-dependent weight of the form $\beta = \beta_0\mu$ with typically $\beta_0 \geq 1$ (in the original HHO method for linear elasticity [89], the choice $\beta_0 = 2$ is considered). The discrete problem consists in seeking the stationary points of the discrete energy functional: Find $\hat{\underline{u}}_h \in \hat{\underline{U}}_{h,\mathrm{D}}^k$ such that

$$\begin{aligned} &\sum_{T\in\mathcal{T}_h} (\boldsymbol{P}(\boldsymbol{F}_T(\hat{\underline{u}}_T)), \boldsymbol{G}_T(\delta\hat{\underline{v}}_T))_{\boldsymbol{L}^2(T)} + \sum_{T\in\mathcal{T}_h} \beta(\eta_{\partial T}\underline{S}_{\partial T}^k(\hat{\underline{u}}_T), \underline{S}_{\partial T}^k(\delta\hat{\underline{v}}_T))_{\underline{L}^2(\partial T)} \\ &= \sum_{T\in\mathcal{T}_h} (\underline{f},\delta\underline{v}_T)_{\underline{L}^2(T)} + \sum_{F\in\mathcal{F}_h^{\mathrm{b,N}}} (\underline{t}_{\mathrm{N}},\delta\underline{v}_F)_{\underline{L}^2(F)}, \end{aligned} \tag{2.26}$$

for all $\delta\hat{\underline{v}}_h \in \hat{\underline{U}}_{h,0}^k$. As for the unstabilized HHO method, the discrete problem (2.26) expresses the principle of virtual work at the global level, and following [74], it is possible to devise a local principle of virtual work in terms of face-based discrete tractions that comply with the law of action and reaction. Let $\hat{\underline{S}}_{\partial T}^k : \mathbb{P}_{d-1}^k(\mathcal{F}_{\partial T};\mathbb{R}^d) \to \mathbb{P}_{d-1}^k(\mathcal{F}_{\partial T};\mathbb{R}^d)$ be defined such that

$$\hat{\underline{S}}_{\partial T}^k(\underline{\theta}) = \underline{\Pi}_{\partial T}^k\big(\underline{\theta} - (\boldsymbol{I} - \underline{\Pi}_T^k)\underline{D}_T^{k+1}(\underline{0},\underline{\theta})_{|\partial T}\big). \tag{2.27}$$

Comparing (2.22) with (2.27), we observe that $\underline{S}_{\partial T}^k(\hat{\underline{v}}_T) = \hat{\underline{S}}_{\partial T}^k(\underline{v}_{\partial T} - \underline{v}_{T|\partial T})$ for all $\hat{\underline{v}}_T \in \hat{\underline{U}}_T^k$. Let $\hat{\underline{S}}_{\partial T}^{k*} : \mathbb{P}_{d-1}^k(\mathcal{F}_{\partial T};\mathbb{R}^d) \to \mathbb{P}_{d-1}^k(\mathcal{F}_{\partial T};\mathbb{R}^d)$ be the adjoint operator of $\underline{S}_{\partial T}^k$ with respect to the $L^2(\partial T;\mathbb{R}^d)$-inner product. We observe that the stabilization-related term in (2.26) can be rewritten as

$$(\eta_{\partial T}\underline{S}_{\partial T}^k(\hat{\underline{u}}_T), \underline{S}_{\partial T}^k(\delta\hat{\underline{v}}_T))_{\underline{L}^2(\partial T)} = (\hat{\underline{S}}_{\partial T}^{k*}(\eta_{\partial T}\hat{\underline{S}}_{\partial T}^k(\underline{u}_{\partial T} - \underline{u}_{T|\partial T})), \delta\underline{v}_{\partial T} - \delta\underline{v}_{T|\partial T})_{\underline{L}^2(\partial T)}. \tag{2.28}$$

Finally, let us define the discrete traction

$$\underline{T}_T = \boldsymbol{\Pi}_T^k(\boldsymbol{P}(\boldsymbol{F}_T(\hat{\underline{u}}_T)))_{|\partial T}\,\underline{n}_T + \beta\hat{\underline{S}}_{\partial T}^{k*}(\eta_{\partial T}\hat{\underline{S}}_{\partial T}^k(\underline{u}_{\partial T} - \underline{u}_{T|\partial T})). \tag{2.29}$$

Lemma 2.6 (Equilibrated tractions) *The following local principle of virtual work holds true for all $T \in \mathcal{T}_h$: For all $\delta\underline{v}_T \in \mathbb{P}_d^k(T;\mathbb{R}^d)$,*

$$(\boldsymbol{P}(\boldsymbol{F}_T(\hat{\underline{u}}_T)), \boldsymbol{\nabla}_X\delta\underline{v}_T)_{\boldsymbol{L}^2(T)} - (\underline{T}_T,\delta\underline{v}_T)_{\underline{L}^2(\partial T)} = (\underline{f},\delta\underline{v}_T)_{\underline{L}^2(T)}, \tag{2.30}$$

where the discrete tractions $\underline{T}_T \in \mathbb{P}_{d-1}^k(\mathcal{F}_{\partial T};\mathbb{R}^d)$ defined by (2.29) satisfy the following law of action and reaction for all $F \in \mathcal{F}_h^i \cup \mathcal{F}_h^{b,N}$:

$$\underline{T}_{T_-|F} + \underline{T}_{T_+|F} = \underline{0}, \quad \text{if } F \in \mathcal{F}_h^i \text{ with } \partial T_- \cap \partial T_+ = F, \tag{2.31a}$$

$$\underline{T}_{T|F} = \underline{\Pi}_F^k(\underline{t}_N), \quad \text{if } F \in \mathcal{F}_h^{b,N} \text{ with } \partial T \cap \Gamma_N = F. \tag{2.31b}$$

Proof. Proceed as in the proof of Lemma 2.3; see also [74].

□

Let us briefly comment on the commuting properties of the reconstructed gradient in $\mathbb{P}_d^k(T;\mathbb{R}^{d\times d})$. Proceeding as above, one obtains

$$\boldsymbol{G}_T(\hat{\underline{I}}_T^k(\underline{v})) = \boldsymbol{\Pi}_T^k(\boldsymbol{\nabla}_X\underline{v}), \qquad \forall \underline{v}\in H^1(T;\mathbb{R}^d), \tag{2.32}$$

where the reduction operator $\hat{\underline{I}}_T^k : H^1(T;\mathbb{R}^d)\to\hat{\underline{U}}_T^k$ is defined below (2.19). Proceeding as in [89, Thm. 8], one can show that for the linear elasticity problem and smooth solutions, the energy error $\|\boldsymbol{\nabla}_X\underline{u}-\boldsymbol{G}_h(\hat{\underline{u}}_h)\|_{\boldsymbol{L}^2(\mathcal{T}_h)}$ converges as $h^{k+1}|\underline{u}|_{\underline{H}^{k+2}(\Omega_0)}$. This convergence rate will be confirmed by the experiments reported in Section 2.4.1. Moreover, taking the trace in (2.32), we infer that (compare with (2.21))

$$\mathrm{trace}(\boldsymbol{G}_T(\hat{\underline{I}}_T^k(\underline{v}))) = \Pi_T^k(\nabla\cdot\underline{v}), \qquad \forall \underline{v}\in H^1(T;\mathbb{R}^d), \tag{2.33}$$

which is the key commuting property used in [89] to prove robustness for quasi-incompressible linear elasticity. This absence of locking is confirmed in the numerical experiments performed in Sections 2.4.2 and 2.5 in the nonlinear regime. Finally, we refer the reader to [40] for further analytical results on symmetric-valued gradients reconstructed in the smaller space $\mathbb{P}_d^k(T;\mathbb{R}^{d\times d}_{\mathrm{sym}})$.

Remark 2.7 (Choice of β_0) *For the HHO method applied to linear elasticity, a natural choice for the stabilization parameter is $\beta_0 = 2$ [89]. To our knowledge, there is no general theory on the choice of β_0 in the case of finite deformations of hyperelastic materials. Following ideas developed in [116, 115] for dG and in [30] for VEM, one can consider to take (possibly in an adaptive fashion) the largest eigenvalue (in absolute value) of the elastic modulus $\mathbb{A}$. This choice introduces additional nonlinearities to be handled by Newton's method, and may require some relaxation. Another possibility discussed in [58] for VEM methods is based on the trace of the Hessian of the isochoric part of the strain-energy density Ψ. Such an approach bears similarities with the classic selective integration for FEM, and for the Neohookean materials considered herein, this choice implies to take $\beta_0 = 1$. Finally, let us mention that [147, Section 4] presents an example where spurious solutions can appear if the HDG stabilization parameter is not large enough; however, too large values of the parameter can also deteriorate the condition number of the stiffness matrix and can cause numerical instabilities in Newton's method.*

2.3.5 Nonlinear solver and static condensation

Both nonlinear problems (2.15) and (2.26) are solved using Newton's method. Let $i\geq 0$ be the index of the Newton's step. Given an initial discrete displacement $\hat{\underline{u}}_h^0\in\hat{\underline{U}}_{h,\mathrm{D}}^k$, one computes at each Newton's step the incremental displacement $\delta\hat{\underline{u}}_h^i\in\hat{\underline{U}}_{h,0}^k$ and updates the discrete displacement as $\hat{\underline{u}}_h^{i+1}=\hat{\underline{u}}_h^i+\delta\hat{\underline{u}}_h^i$. The linear system of equations to be solved is

$$\begin{aligned}&\sum_{T\in\mathcal{T}_h}(\mathbb{A}(\boldsymbol{F}_T(\hat{\underline{u}}_T^i)):\boldsymbol{G}_T(\delta\hat{\underline{u}}_T^i),\boldsymbol{G}_T(\delta\hat{\underline{v}}_T))_{\boldsymbol{L}^2(T)}\\ &+\sum_{T\in\mathcal{T}_h}\beta(\eta_{\partial T}\underline{S}_{\partial T}^k(\delta\hat{\underline{u}}_T^i),\underline{S}_{\partial T}^k(\delta\hat{\underline{v}}_T))_{\underline{L}^2(\partial T)} = -R_h^i(\delta\underline{\hat{v}}_h),\end{aligned}\tag{2.34}$$

for all $\delta\underline{\hat{v}}_h\in\hat{\underline{U}}_{h,0}^k$, with the residual term

$$\begin{aligned}R_h^i(\delta\underline{\hat{v}}_h) = &\sum_{T\in\mathcal{T}_h}(\boldsymbol{P}(\boldsymbol{F}_T(\hat{\underline{u}}_T^i)),\boldsymbol{G}_T(\delta\hat{\underline{v}}_T))_{\boldsymbol{L}^2(T)}+\sum_{T\in\mathcal{T}_h}\beta(\eta_{\partial T}\underline{S}_{\partial T}^k(\hat{\underline{u}}_T^i),\underline{S}_{\partial T}^k(\delta\hat{\underline{v}}_T))_{\underline{L}^2(\partial T)}\\ &-\sum_{T\in\mathcal{T}_h}(\underline{f},\delta\underline{v}_T)_{\underline{L}^2(T)}-\sum_{F\in\mathcal{F}_h^{\mathrm{b,N}}}(\underline{t}_{\mathrm{N}},\delta\underline{v}_F)_{\underline{L}^2(F)},\end{aligned}\tag{2.35}$$

where $\beta = 0$ in the unstabilized case and $\beta = \beta_0\mu$ in the stabilized case, the gradient being reconstructed in the corresponding polynomial space. It can be seen from (2.34) that the assembling of the stiffness matrix on the left-hand side is local (and thus fully parallelizable).

As is classical with HHO methods [89], and more generally with hybrid approximation methods, the cell unknowns $\delta\underline{u}^i_{\mathcal{T}_h}$ in (2.34) can be eliminated locally using a static condensation (or Schur complement) technique. Indeed, testing (2.34) against the function $((\delta\underline{v}_T\delta_{T,T'})_{T'\in\mathcal{T}_h}, (\underline{0})_{F\in\mathcal{F}_h})$ with Kronecker delta $\delta_{T,T'}$ and $\delta\underline{v}_T$ arbitrary in $\mathbb{P}^k_d(T;\mathbb{R}^d)$, one can express, for all $T\in\mathcal{T}_h$, the cell unknown $\delta\underline{u}^i_T$ in terms of the local face unknowns collected in $\delta\underline{u}^i_{\partial T}$. As a result, the static condensation technique allows one to reduce (2.34) to a linear system in terms of the face unknowns only. This reduced system is of size $N_{\mathcal{F}_h}\times\dim(\mathbb{P}^k_{d-1}(T;\mathbb{R}^d))$ where $N_{\mathcal{F}_h}$ denotes the number of mesh faces, and its stencil is such that each mesh face is connected to its neighbouring faces that share a mesh cell with the face in question.

The implementation of the HHO methods is realized using the open-source library `DiSk++` [71] which provides generic programming tools for the implementation of HHO methods and is available at the address `https://github.com/wareHHOuse/diskpp`. The data structure requires access to faces and cells as in standard dG or HDG codes. The gradient and stabilization operators are built locally at the cell level using scaled translated monomials to define the basis functions (see [71, Section 3.2.1] for more details). Finally, the Dirichlet boundary conditions are enforced strongly, and the linear systems are solved using the direct solver PardisoLU from the MKL library (alternatively, iterative solvers are also applicable). Dunavant quadratures [108] are used with order $2k$ for stabilized HHO methods, and with order $(2k+2)$ for unstabilized HHO methods.

2.4 Test cases with known solution

The goal of this section is to evaluate the stabilized and unstabilized HHO methods on some test cases with known solution. This allows us to compute errors on the displacement and the gradient as $\|\underline{u}-\underline{u}_{\mathcal{T}_h}\|_{\underline{L}^2(\Omega_0)}$ and $\|\boldsymbol{\nabla}_X\underline{u}-\boldsymbol{G}_h(\hat{\underline{u}}_h)\|_{\boldsymbol{L}^2(\mathcal{T}_h)}$ where $\underline{u}$ is the exact solution. We assess the convergence rates to smooth solutions and we study the behavior of the HHO methods in the quasi-incompressible regime. We consider two- and three-dimensional settings. We use the abridged notation uHHO(k) for the unstabilized method with $\boldsymbol{R}(T;\mathbb{R}^{d\times d}) = \mathbb{P}^{k+1}_d(T;\mathbb{R}^{d\times d})$ and sHHO(k) with $\boldsymbol{R}(T;\mathbb{R}^{d\times d}) = \mathbb{P}^k_d(T;\mathbb{R}^{d\times d})$ for the stabilized method; whenever the context is unambiguous, we drop the polynomial degree k. All the considered meshes are matching, simplicial affine meshes.

2.4.1 Three-dimensional manufactured solution

We first report convergence rates for a nonlinear problem with a manufactured solution in three space dimensions. We denote by $\underline{X} = (X,Y,Z)$ the Cartesian coordinates in $\mathbb{R}^3$. We set $\Gamma = \Gamma_{\mathrm{D}}$ and the value of $\underline{u}_{\mathrm{D}}$ is determined from the exact solution on Γ_{D}. Concerning the constitutive relation, we take $\mu = 1$, $\lambda = 10$ (which corresponds to a Poisson ratio of $\nu \simeq 0.455$), and $\Theta(J) = \ln J$. We consider the unit cube $\Omega_0 = (0,1)\times(0,1)\times(0,1)$ and the exact displacement solution is

$$u_X = \left(\frac{1}{\lambda}+\alpha\right)X + \vartheta(Y), \quad u_Y = -\left(\frac{1}{\lambda}+\frac{\alpha+\gamma+\alpha\gamma}{1+\alpha+\gamma+\alpha\gamma}\right)Y, \tag{2.36a}$$

$$u_Z = \left(\frac{1}{\lambda}+\gamma\right)Z + g(X) + h(Y), \tag{2.36b}$$

where α and γ are positive real numbers, and $\vartheta:\mathbb{R}\to\mathbb{R}$, $g:\mathbb{R}\to\mathbb{R}$, $h:\mathbb{R}\to\mathbb{R}$ are smooth functions. Choosing $\vartheta(Y) = \alpha\sin(\pi Y)$, $g(X) = \gamma\sin(\pi X)$, and $h(Y) = 0$, the corresponding

body forces are given by

$$f_X = \mu\alpha\pi^2 \sin(\pi X), \qquad f_Y = 0, \qquad f_Z = \mu\gamma\pi^2 \sin(\pi Y). \tag{2.37}$$

We set $\alpha = \gamma = 0.1$. The stabilization parameter is taken as $\beta_0 = 1$ for sHHO. The displacement and gradient errors are reported as a function of the average mesh size h for $k = 1$ in Tab. 2.1, for $k = 2$ in Tab. 2.2 and for $k = 3$ in Tab. 2.3. For all $k \in \{1, 2, 3\}$, the displacement and the gradient converge, respectively, with order $(k + 2)$ and $(k + 1)$ for sHHO and with order $(k + 1)$ and k for uHHO. These convergence rates are consistent with the discussion at the end of Sections 2.3.3 and 2.3.4 on the convergence rates to be expected for linear elasticity and smooth solutions.

2.4.2 Quasi-incompressible annulus

Our goal is now to evaluate the sHHO and uHHO methods in the quasi-incompressible case for finite deformations. We consider a test case from [147, Section 5.2] that consists of an annulus centered at the origin with inner radius $R_0 = 0.5$ and outer radius $R_1 = 1$. The annulus is deformed by imposing a displacement $\underline{u}_{\mathrm{D}}(\underline{X}) = \underline{X}(r_0 - R_0)/R_0$ on $\Gamma_{\mathrm{D}} = S_{R_0}$ where r_0 is a real positive parameter, and $\underline{t}_{\mathrm{N}} = \underline{0}$ on $\Gamma_{\mathrm{N}} = S_{R_1}$ (S_R is the sphere of radius R centered at the origin). An accurate reference solution can be computed by solving an ordinary differential equation along the radial coordinate, as detailed in [147]. We set $r_0 = 1.5$ and $\mu = 0.333$ (different values of λ are considered). Since we use meshes with planar faces, we only consider $k = 1$.

The reference and deformed configuration for sHHO(1) are shown in Fig. 2.2a for $\lambda = 1666.44$ (which corresponds to a Poisson ratio of $\nu \simeq 0.4999$). The stabilization parameter has to be of the order of $\beta_0 = 100$ to achieve convergence. In Fig. 2.2b, we display the discrete Jacobian J^h on the reference configuration (computed using sHHO(1)), and we observe that this quantity takes values very close to 1 everywhere in the annulus (as expected). Convergence rates for the displacement and the gradient are reported in Tab. 2.4 for $\lambda = 1666.44$ (similar convergence rates, not reported herein, are observed for lower values of λ). We observe that for sHHO, the displacement and the gradient converge with order 2, whereas for uHHO, the displacement converges with order 2 and the gradient with order 1. More importantly, the errors are uniform with respect to λ as shown Fig. 2.3. This result confirms numerically that in this case, sHHO and uHHO remain locking-free in quasi-incompressible finite deformations. Incidentally, we notice that sHHO produces slightly lower errors than uHHO which is consistent with the higher-order convergence for sHHO. Moreover, the displacement on the boundary is imposed by uniform load increments. For $\lambda = 1666.44$, sHHO requires 30 loading steps with a total of 125 Newton's iterations, whereas uHHO requires 33 loading steps with a total of 137 Newton's iterations, i.e., sHHO is about 10% more computationally-effective than uHHO in this example. Finally, the reference values of u_r, P_{rr} and $P_{\theta\theta}$ at the barycenter of each cell are plotted in Fig. 2.4 for $\lambda = 1666.44$, showing the pointwise convergence of the various discrete solutions. We observe that for both HHO methods, the error on P_{rr} is slightly more important near the inner boundary of the annulus (where the stress is maximal).

2.4.3 Efficiency

In this section, we compare the performance of sHHO, uHHO and that of a continuous Galerkin (cG) method in terms of efficiency when solving the three-dimensional manufactured solution from Section 2.4.1. The number of unknowns is the number of degrees of freedom attached to faces after static condensation for sHHO and uHHO and the number of degrees of

Mesh size h	sHHO(1)				uHHO(1)			
	Displacement		Gradient		Displacement		Gradient	
	Error	Order	Error	Order	Error	Order	Error	Order
4.75e-1	1.14e-3	-	9.40e-3	-	1.85e-3	-	6.64e-2	-
3.21e-1	4.27e-4	2.49	4.66e-3	1.78	7.76e-4	2.22	4.00e-2	1.25
2.19e-1	1.22e-4	3.28	2.24e-3	1.91	3.49e-4	2.10	2.95e-2	0.84
1.76e-1	6.36e-5	2.97	1.51e-3	1.79	2.19e-4	2.12	2.36e-2	1.01
1.39e-1	3.10e-5	3.05	9.16e-4	2.14	1.36e-4	2.01	1.88e-2	0.96
1.11e-1	1.56e-5	3.00	5.92e-4	1.91	8.79e-5	1.94	1.50e-2	1.00

Table 2.1: 3D manufactured solution: errors vs. h for $k = 1$.

Mesh size h	sHHO(2)				uHHO(2)			
	Displacement		Gradient		Displacement		Gradient	
	Error	Order	Error	Order	Error	Order	Error	Order
4.75e-1	1.04e-4	-	9.89e-4	-	1.96e-4	-	7.68e-3	-
3.21e-1	3.01e-5	3.16	3.18e-4	2.71	6.10e-5	2.96	3.51e-3	1.96
2.19e-1	4.54e-6	4.04	9.57e-5	3.01	1.68e-5	3.17	1.60e-3	2.02
1.76e-1	1.79e-6	4.23	4.78e-5	3.16	9.72e-6	2.49	1.10e-3	1.68
1.39e-1	7.23e-7	3.85	2.35e-5	3.01	4.30e-6	3.36	6.53e-4	2.24
1.11e-1	2.93e-7	3.96	1.21e-5	2.91	2.23e-6	2.88	4.20e-4	1.94

Table 2.2: 3D manufactured solution: errors vs. h for $k = 2$.

Mesh size h	sHHO(3)				uHHO(3)			
	Displacement		Gradient		Displacement		Gradient	
	Error	Order	Error	Order	Error	Order	Error	Order
4.75e-1	7.39e-6	-	6.42e-5	-	1.59e-5	-	7.79e-4	-
3.21e-1	9.88e-7	5.13	1.67e-5	3.41	2.80e-6	4.42	2.16e-4	3.26
2.19e-1	1.58e-7	4.79	2.98e-6	4.53	5.23e-7	4.40	6.55e-5	3.14
1.76e-1	5.54e-8	4.77	1.37e-6	3.52	2.07e-7	4.21	3.23e-5	3.19
1.39e-1	1.60e-8	5.29	4.86e-7	4.43	8.08e-8	4.01	1.61e-5	2.95
1.11e-1	5.01e-9	5.17	1.96E-7	4.03	3.25e-8	4.05	8.25E-6	2.97

Table 2.3: 3D manufactured solution: errors vs. h for $k = 3$.

Mesh size h	sHHO(1)				uHHO(1)			
	Displacement		Gradient		Displacement		Gradient	
	Error	Order	Error	Order	Error	Order	Error	Order
1.15e-1	5.98e-2	-	3.22e-1	-	4.00e-2	-	1.23e-1	-
5.77e-2	1.81e-2	1.72	8.23e-1	1.97	1.32e-2	1.62	1.01e-1	0.28
3.45e-2	6.30e-3	2.05	3.15e-2	1.86	3.80e-3	2.42	6.60e-2	0.83
2.52e-2	3.42e-3	1.95	1.83e-2	1.73	2.03e-3	2.05	5.11e-2	0.94
1.64e-2	1.49e-3	1.93	7.98e-3	1.93	9.76e-4	1.72	3.09e-2	1.08

Table 2.4: Quasi-incompressible annulus: errors vs. h for $k = 1$ and $\lambda = 1666.44$.

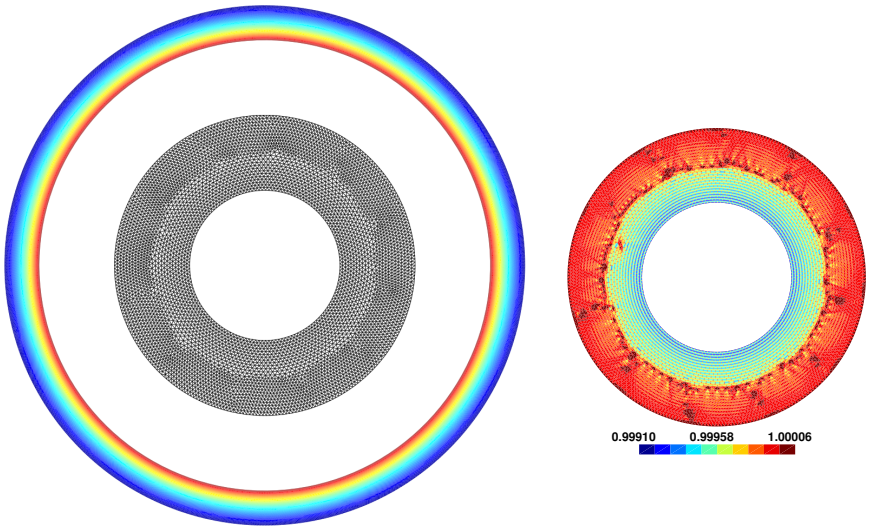

(a) Reference and deformed configuration

(b) Discrete Jacobian on the reference configuration

Figure 2.2: Quasi-incompressible annulus with $\lambda = 1666.44$: sHHO(1) solution on a mesh composed of 10161 triangles.

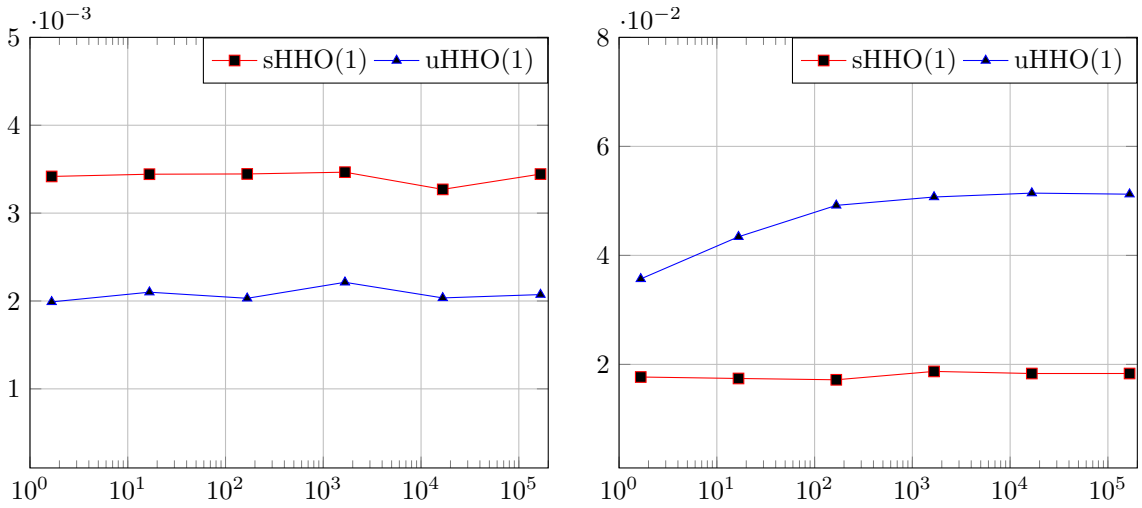

(a) Displacement error

(b) Gradient error

Figure 2.3: Quasi-incompressible annulus: errors vs. λ for $h = 2.52\text{e-}2$

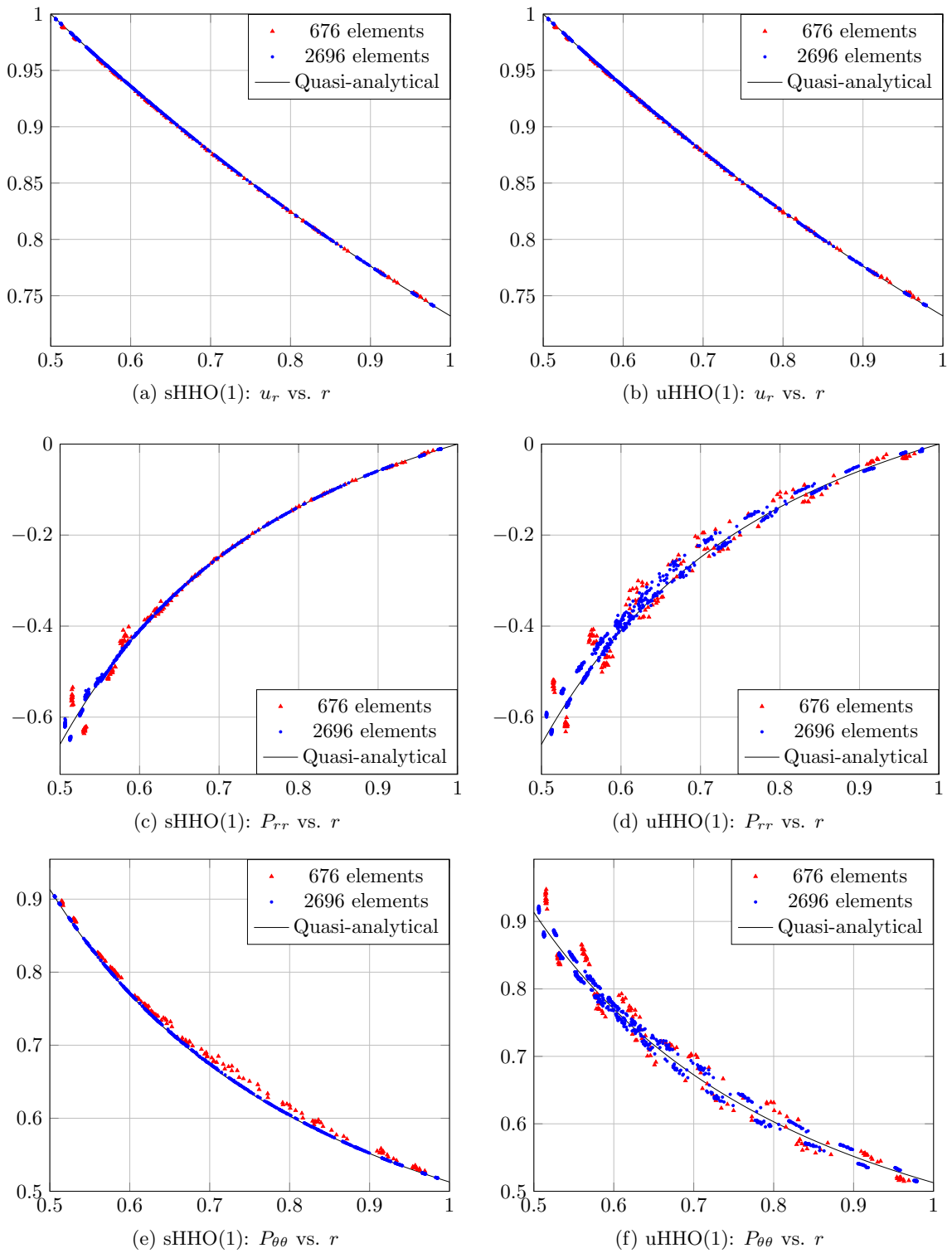

(a) sHHO(1): u_r vs. r

(b) uHHO(1): u_r vs. r

(c) sHHO(1): P_{rr} vs. r

(d) uHHO(1): P_{rr} vs. r

(e) sHHO(1): $P_{\theta\theta}$ vs. r

(f) uHHO(1): $P_{\theta\theta}$ vs. r

Figure 2.4: Quasi-incompressible annulus with $\lambda = 1666.44$: comparison of the reference and computed values of u_r, P_{rr} and $P_{\theta\theta}$ at the barycenter of the mesh cells (located in the upper quadrant) for two different meshes obtained with the sHHO and uHHO methods.

freedom attached to nodes for cG. The cG method is based on a primal formulation realized within the industrial open-source FEM software `code_aster` [111] interfaced with the open-source `mfront` code generator [137] to generate Neohookean laws.

We present the displacement error versus the number of degrees of freedom in Fig. 2.5a and versus the number of non-zero entries in the stiffness matrix in Fig. 2.5b. Owing to the static condensation, we observe that, for the same approximation order and the same number of degrees of freedom or non-zero entries in the stiffness matrix, the displacement error is smaller for sHHO than for cG and comparable between uHHO and cG. Let us now

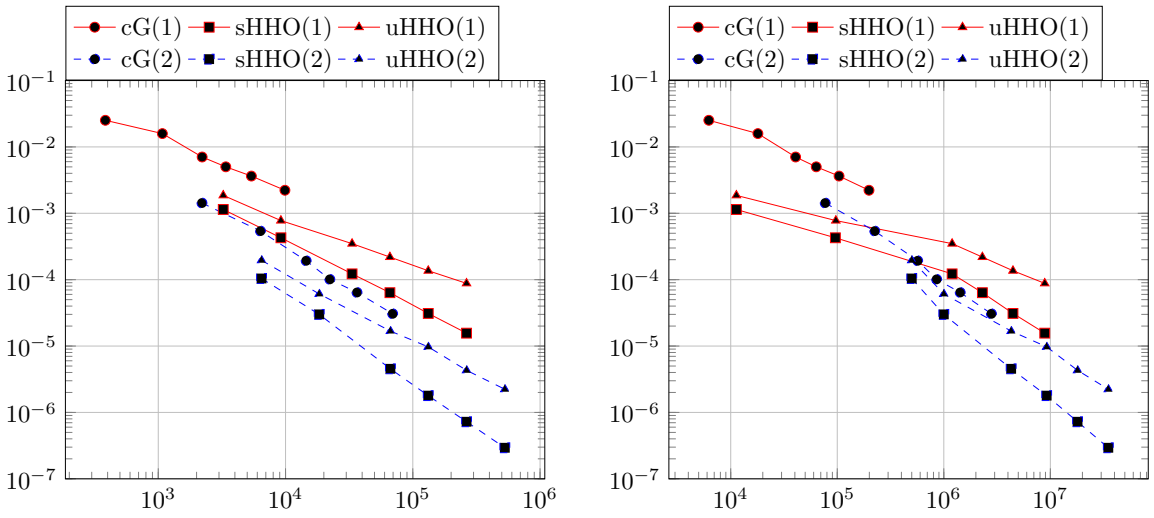

(a) Displacement error vs. number of degrees of freedom

(b) Displacement error vs number of non-zero entries in the stiffness matrix

Figure 2.5: 3D manufactured solution: comparison of the displacement error obtained with sHHO, uHHO, and cG.

compare the time spent to solve the non-linear problem when using sHHO(k) and uHHO(k) with $k \in \{1, 2\}$. For the present test case, the nonlinear problem is solved, for both methods, in four Newton's iterations. The codes are instrumented to measure the assembly time τ_{ass} to build the local contributions to the global stiffness matrix and the solver time τ_{sol} which corresponds to solving the global linear system (τ_{ass} and τ_{sol} are computed after summation over all the Newton's steps). In `DiSk++`, the linear algebra operations are realized using the Eigen library and the global linear system (involving face unknowns only) is solved with PardisoLU. The tests are run sequentially on a 3.4 Ghz Intel Xeon processor with 16 Gb of RAM. In Fig. 2.6a we plot the ratio $\tau_{\text{ass}}/\tau_{\text{sol}}$ versus the number of mesh faces, card($\mathcal{F}_h$). We can see that on the finer meshes, the cost of local computations becomes negligible compared to that of the linear solver; we notice that the situation is a bit less favorable than for the results on linear elasticity reported in [89] since the space to reconstruct the gradient is now larger. In Fig. 2.6b we provide a more detailed assessment of the cost on a fixed mesh with 31621 faces. More precisely, the time τ_{ass} spent in assembling the problem is now divided into two parts, one part, denoted `Gradrec`, to reconstruct the gradient and build the global system to solve (the part related to static condensation is not included and takes a marginal fraction of the cost), and another part, denoted `Stabilization`, to build the stabilization operator for the sHHO method (including the time to build the displacement reconstruction, see (2.23)). In addition, the time τ_{sol} spent in solving the system is now denoted `Solver`. We observe that the difference between sHHO(k) and uHHO(k) is not really important; in fact,

the time that uHHO(k) spends in reconstructing the gradient in a larger space is more or less equivalent to the time that sHHO(k) spends in building the stabilization operator. Moreover, if memory is not a limiting factor, the gradient and the stabilization can be computed once and for all, and re-used at each Newton's step.

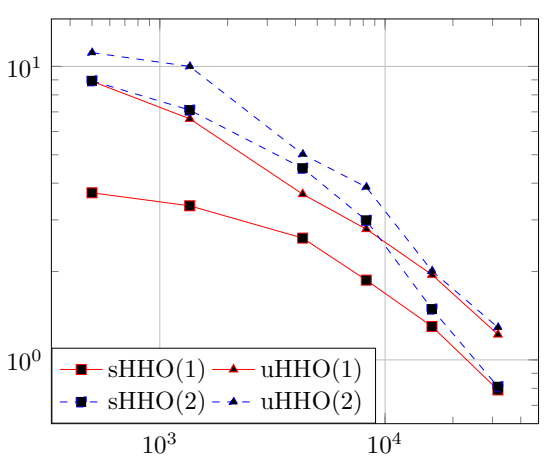

(a) τ_{ass} / τ_{sol} vs. card($\mathcal{F}_h$)

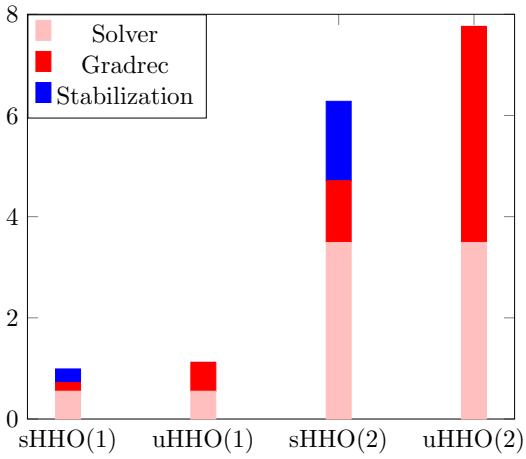

(b) Time for the different operations normalized by the total time for sHHO(1) for a mesh with 31621 faces

Figure 2.6: Comparison of CPU times for the sHHO and uHHO methods.

Another interesting observation is that the condition number of the global stiffness matrix for both methods is improved by static condensation, as shown in Fig. 2.7a where the ratio of the condition number without and with static condensation is displayed as a function of the number of face degrees of freedom. This positive effect is even increased as the mesh is refined, and it is also more pronounced when the polynomial degree k is higher. Finally, we assess the influence of the stabilization parameter β on the condition number of the stiffness matrix for sHHO(k) $k \in \{1, 2\}$. Fig. 2.7b reports the condition number for $\beta \in \{10^3, 10^6\}$ normalized by the condition number for $\beta = 1$, as a function of the total number of face degrees of freedom. We observe that the condition number is amplified by a factor of 10^2 when β goes from 1 to 10^3 and by a factor 10^3 when β goes from 10^3 to 10^6, independently of the polynomial degree k.

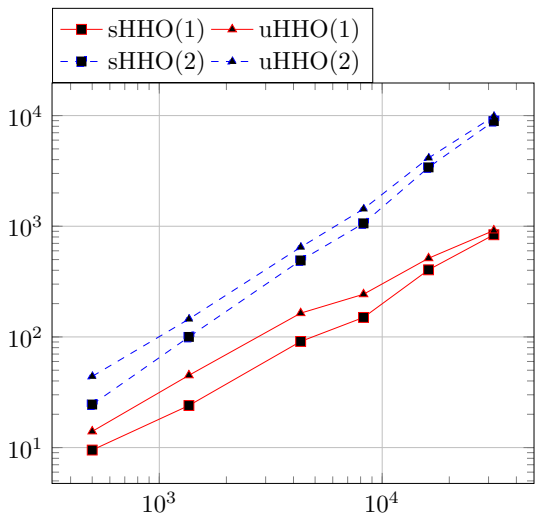

(a) Ratio of the condition number without and with static condensation vs. card($\mathcal{F}_h$)

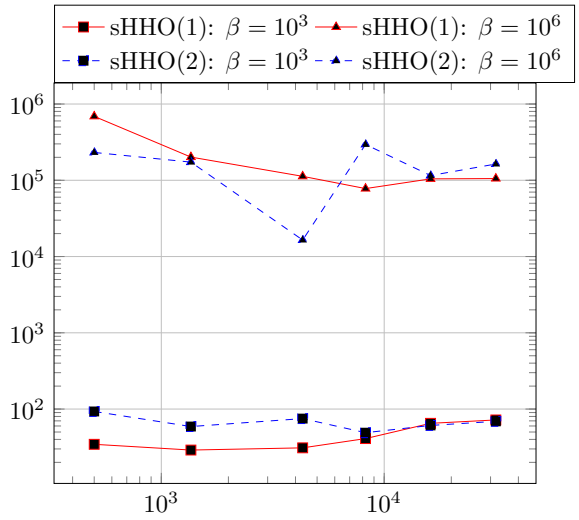

(b) Condition number normalized by that for sHHO(1) or sHHO(2) with $\beta = 1$ vs. card($\mathcal{F}_h$)

Figure 2.7: Condition number of the global stiffness matrix.

2.5 Application-driven three-dimensional examples

The goal of this section is to show that sHHO and uHHO are capable of dealing with challenging three-dimensional examples with finite deformations. For the first test case, we compare our results to those obtained with a cG method implemented in the industrial software `code_aster`. For the second and third test cases, we compare our results with the HDG solutions reported in [147]. In all cases, we choose $\Theta(J) = \ln J$.

2.5.1 Quasi-incompressible indented block

In this example, we model an indentation problem as a prototype for a contact problem. We consider the unit cube $(-1,1) \times (-1,1) \times (-1,1)$. To model the rigid indentor, the bottom surface is clamped, a vertical displacement of -0.8 is imposed on the subset $(-0.5,0.5) \times (-0.5,0.5) \times \{1\}$ of the top surface, and the other parts of the boundary are traction-free. We set $\mu = 1$ and $\lambda = 4999$ in the quasi-incompressible regime (which corresponds to a Poisson ratio of $\nu \simeq 0.4999$). The stabilization parameter needs to be taken of the order of $\beta_0 = 100$ for sHHO. Fig. 2.8c and Fig. 2.8d present the Euclidean displacement norm on the deformed configuration obtained with cG(1) and sHHO(1) respectively (the uHHO(1) solution is very close to the sHHO(1) solution). We observe the locking phenomenon affecting the cG solution. To better appreciate the influence of the parameter λ on the discrete solutions, we plot in Fig. 2.8a and Fig. 2.8b the Euclidean displacement norm on the deformed configuration in the compressible regime ($\lambda = 1$, which corresponds to a Poisson ratio of $\nu = 0.25$). We observe that in the compressible regime, the results produced by the various numerical methods are all very close, whereas the cG solutions depart from the the sHHO and uHHO solutions in the quasi-incompressible regime. Finally, the computed vertical component of the discrete traction integrated over the indented top surface is plotted in Fig. 2.9 for sHHO and uHHO as a function of the imposed vertical displacement. The two HHO methods produce very similar results and capture well the nonlinear response of the block.

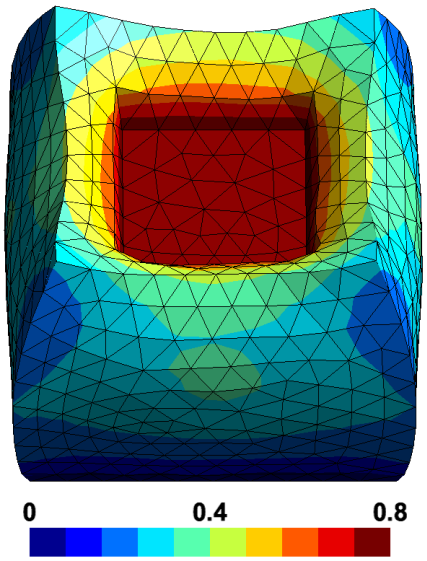

(a) Euclidean displacement norm for cG(1) in the compressible regime

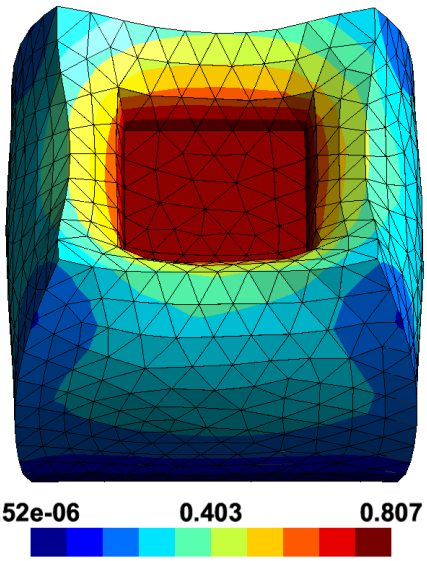

(b) Euclidean displacement norm for sHHO(1) in the compressible regime

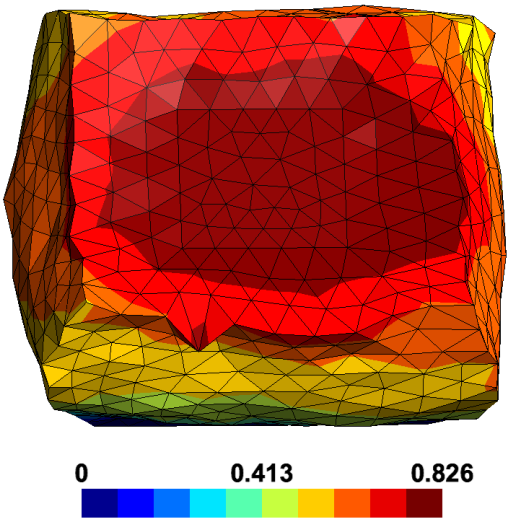

(c) Euclidean displacement norm for cG(1) in the quasi-incompressible regime

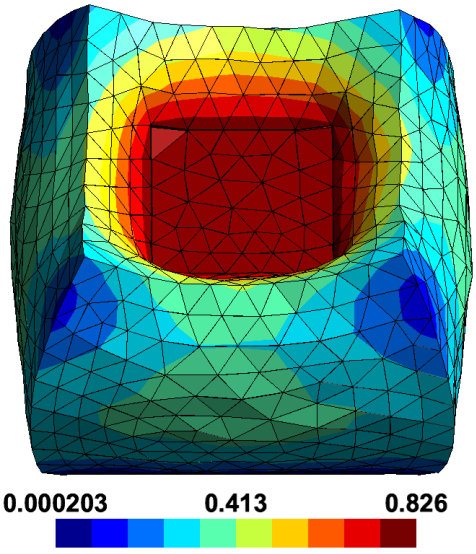

(d) Euclidean displacement norm for sHHO(1) in the quasi-incompressible regime

Figure 2.8: Indented block: compressible (top) and quasi-incompressible regime (bottom) with Euclidean displacement norm shown in color on a mesh composed of 5526 tetrahedra.

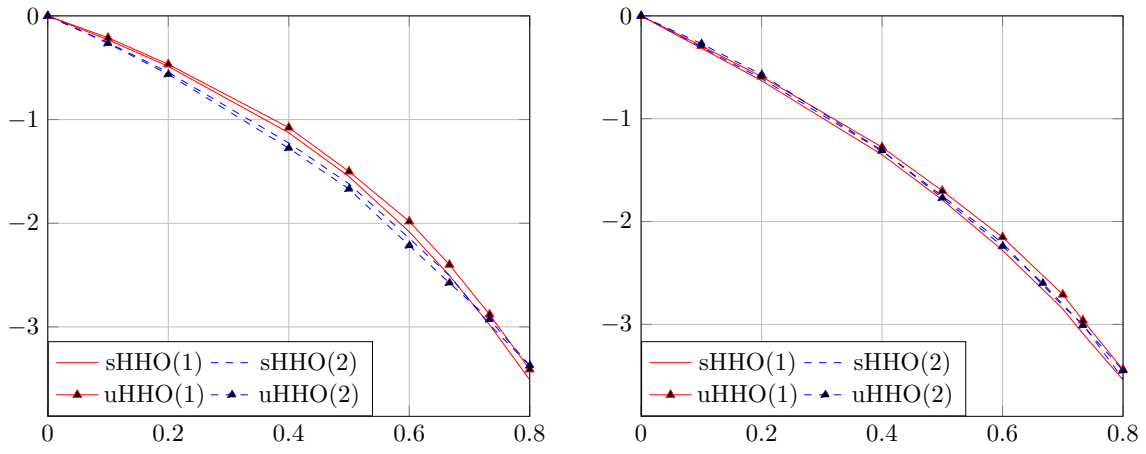

(a) Compressible block (b) Quasi-incompressible block

Figure 2.9: Indented block: vertical component of the computed discrete traction integrated over the indented surface versus the imposed vertical displacement using the sHHO and uHHO methods.

2.5.2 Cylinder under compression and shear

This test case, proposed in [147], simulates a hollow cylinder under important compression and shear (it can be seen as a controlled buckling). The cylinder in its reference configuration has a inner and outer radius of 0.75 and 1, and a height of 4. The bottom face is clamped, whereas the top face has an horizontally and vertically imposed displacement of -1 in both directions, and the lateral faces are traction-free. We set $\mu = 0.1$, $\lambda = 1$ (which corresponds to a Poisson ratio of $\nu \simeq 0.455$). For sHHO, the stabilization parameter has to be taken of the order of $\beta_0 = 100$. We notice that both sHHO and uHHO are robust and produce very close results, which compare very well with the results reported in [147]. The loading is applied in 30 steps for uHHO and in 37 steps for sHHO, leading respectively to a total of 152 and 187 Newton's iterations. This indicates that uHHO is up to 20% more effective for this test case. Some snapshots of the solution obtained with uHHO(1) on a mesh composed of 20382 tetrahedra are shown in Fig. 2.10 where the color indicates the Euclidean norm of the displacement. Fig. 2.11 displays the von Mises stress at different loading steps on the deformed configuration. This figure allows one to observe the emerging localization of the deformation field. Finally, the evolution during the loading of the vertical component of the discrete traction integrated over the top face of the cylinder is plotted in Fig. 2.12. The minimum is reached when the cylinder begins to bend at 75% of the loading; beyond this value, the cylinder becomes less rigid.

2.5.3 Sphere with cavitating voids

The last example simulates the problem of cavitation encountered for instance in elastomers, that is, the growth of cavities under large tensile stresses [22]. Simulations of cavitation phenomena present difficulties because the growth induces significant deformations near the cavities. For a review, we refer the reader to [213]. Some conforming [161], non-conforming [213], and HDG [147] methods have already been studied for this problem. For cavitation to take place, the strain energy density has to be changed, and we consider here, as in [147], the

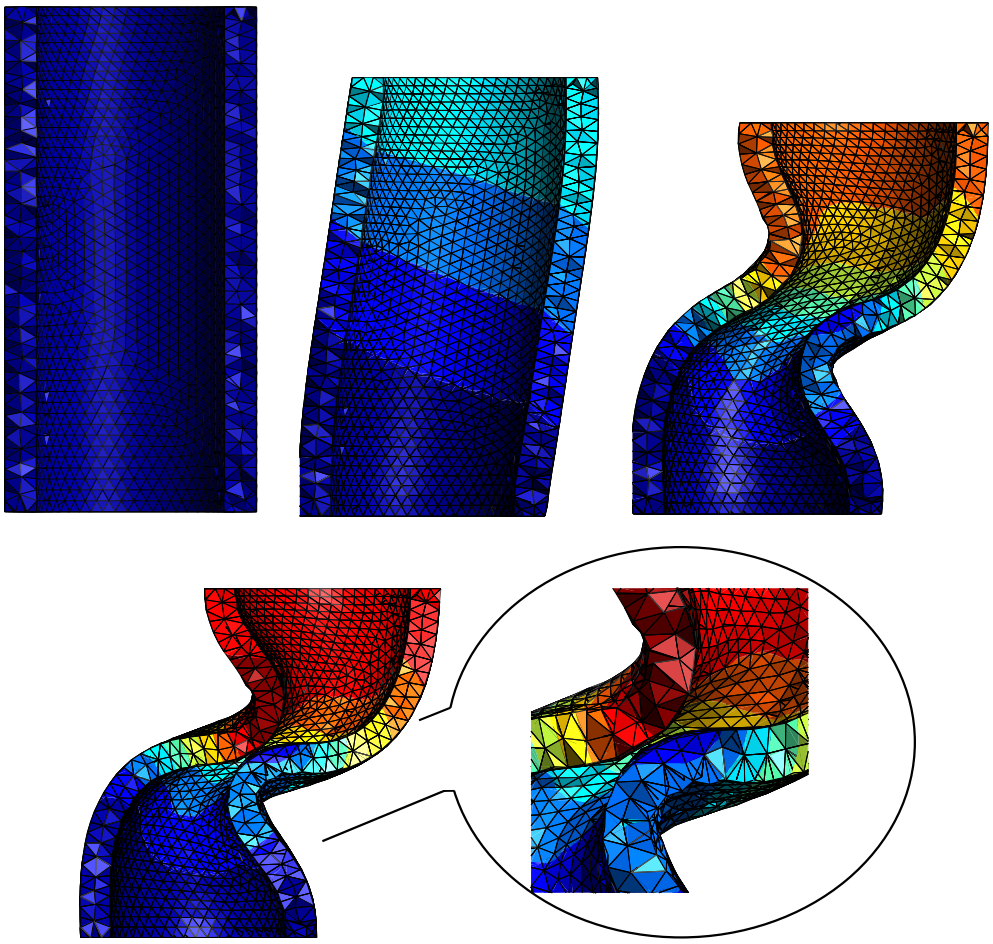

Figure 2.10: Sheared cylinder: snapshots of the Euclidean displacement norm on the deformed configuration at 0%, 40%, 80%, and 100% of loading, and a zoom where the deformations are the most important (uHHO(1) solution). The color scale goes from 0.0 (blue) to 1.8 (red).

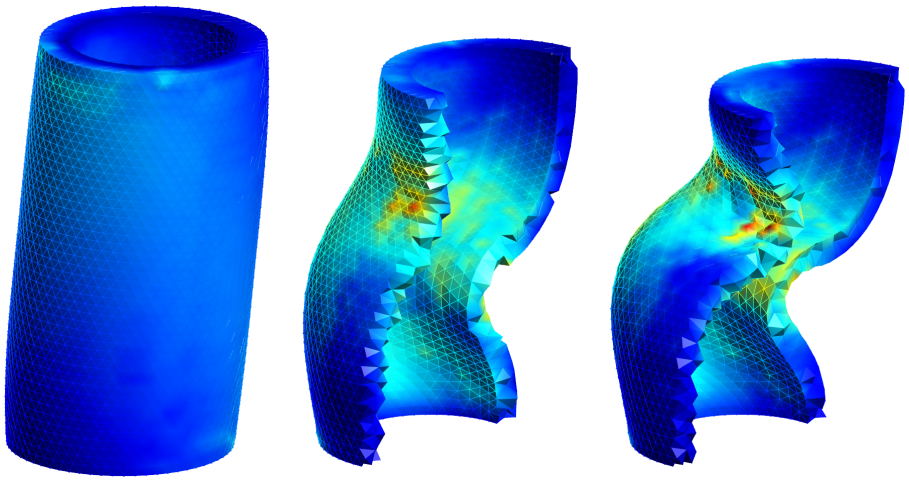

Figure 2.11: Sheared cylinder: von Mises stress on the deformed configuration at 40%, 80% and 100% of loading (uHHO(1) solution). The color scales goes from 0.0 (blue) to 0.275 (red).

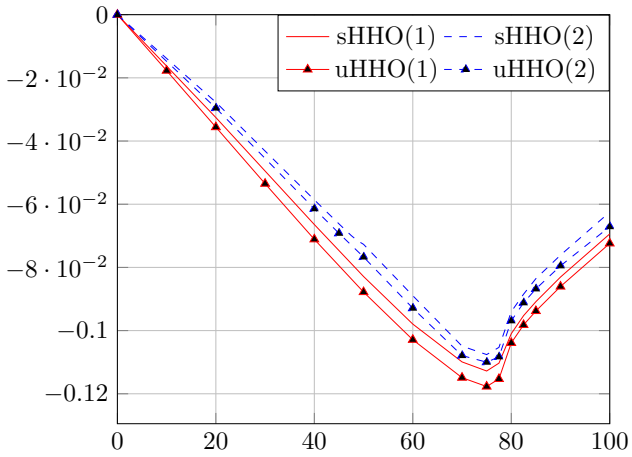

Figure 2.12: Sheared cylinder: evolution during the loading of the vertical component of the discrete traction integrated over the top of the cylinder for sHHO and uHHO.

following modified Neohookean law:

$$\Psi(\boldsymbol{F}) = \frac{2\mu}{3^{5/4}}\,(\boldsymbol{F} : \boldsymbol{F})^{3/4} - \mu \ln J + \frac{\lambda}{2}(\ln J)^2, \tag{2.38}$$

where μ and λ are constant parameters. We set $\mu = 1$, $\lambda = 1$ (which corresponds to a Poisson ratio of $\nu = 0.25$).

The reference configuration consists of a unit sphere of radius 1 with two spherical cavities. The origin of the Cartesian coordinate system is the center of the sphere. The first cavity has a radius of 0.15 and its center is the point of coordinates $(-0.7, -0.7, 0)$, and the second cavity has a radius of 0.2 and its center is the point of coordinates $(0.25, 0.25, 0.25)$. A displacement $\underline{u}(\underline{X}) = r\underline{X}$ with $r \geq 0$ is imposed on the outer surface ($|\underline{X}| = 1$) of the sphere. The stabilization parameter has to be taken of the order of $\beta_0 = 100$ for sHHO. The mesh is composed of 32288 tetrahedra, and the value of r is increased progressively until the moment where the Newton's method fails to converge. Some snapshots of the Euclidean displacement norm are shown in Fig. 2.13 on the deformed configuration for uHHO(2). We also present a zoom near the region where the two cavities are only separated by a thin layer. The reported solution compares very well with the HDG solution from [147]. Interestingly, the maximum value attained of r is larger for uHHO than for sHHO and is larger for $k = 2$ than for $k = 1$ (see Fig. 2.14). For $k = 2$, the maximum value of r is 2.52 for uHHO and 2.13 for sHHO, which indicates about 15% more robustness for uHHO than for sHHO to handle extreme loading situations in this case. Finally, Fig. 2.14 presents the radial component of the discrete traction integrated over the outer surface of the sphere versus the imposed radial displacement obtained with sHHO and uHHO.

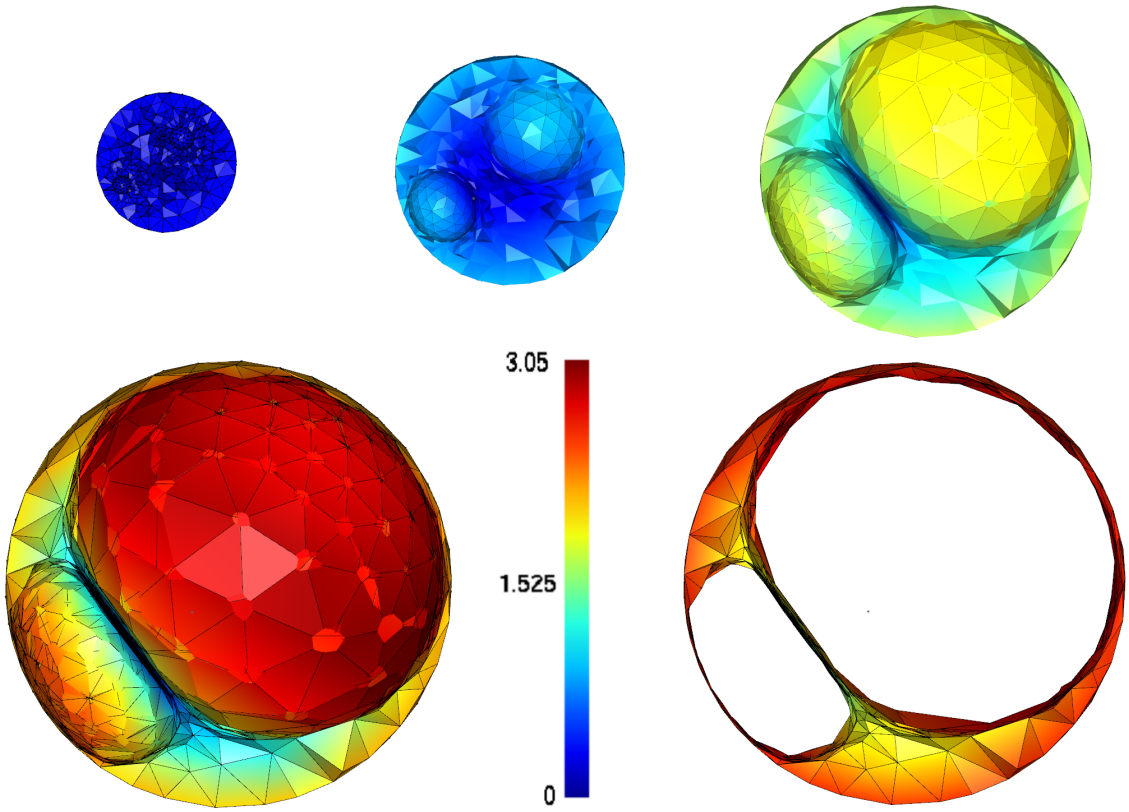

Figure 2.13: Sphere with cavitating voids: snaphots of the Euclidean displacement norm at $r = 0$, $r = 0.8$, $r = 1.6$ and $r = 2.52$ of loading (the sphere is cut along the Equatorial plane) for uHHO(2) on the deformed configuration. The bottom right plot shows a thin slice of the sphere (still along the Equatorial plane) for $r = 2.52$.

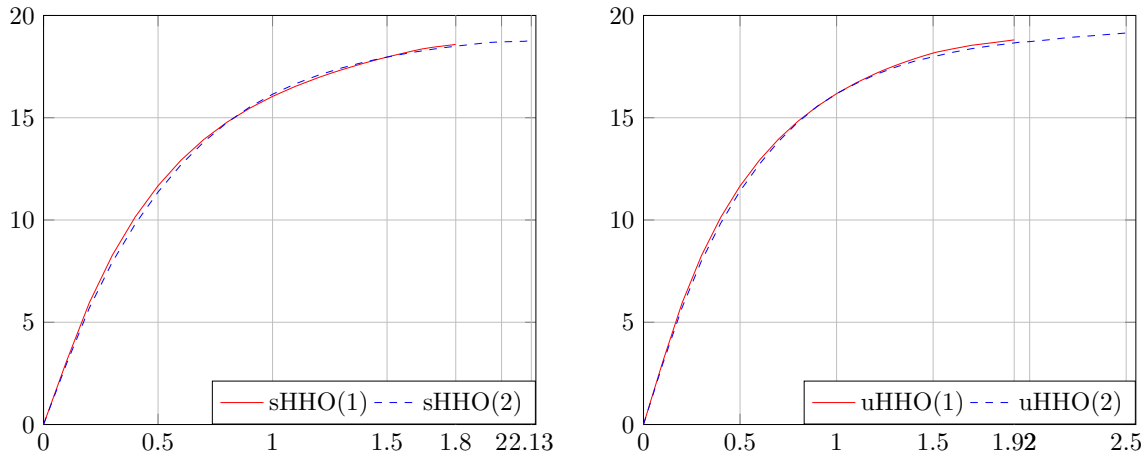

Figure 2.14: Sphere with cavitating voids: radial component of the discrete traction integrated over the outer surface versus the imposed radial displacement obtained with sHHO (left) and uHHO (right). Notice in both cases the larger value attained by r for $k = 2$.

2.6 Conclusion

We have proposed and evaluated numerically two HHO methods to approximate hyperelastic materials undergoing finite deformations. Both methods deliver solutions that compare well to the existing literature on challenging three-dimensional test cases, such as a hollow cylinder under compression and shear or a sphere under traction with two cavitating voids. In addition, both methods remain well-behaved in the quasi-incompressible limit, as observed numerically on an annulus under traction and on the indentation of a rectangular block. The test cases with analytical solution also show that both methods are competitive with respect to an industrial software using conforming finite elements. The stabilized HHO method rests on a firmer theoretical basis than the unstabilized method, but requires the introduction and tuning of a stabilization parameter that can become fairly large in the quasi-incompressible limit. The unstabilized HHO method avoids any stabilization by introducing a stable gradient reconstructed in the higher-order polynomial space $\mathbb{P}_d^{k+1}(T;\mathbb{R}^{d\times d})$, but for smooth solutions, the convergence rate is one order lower than with the stabilized method, i.e., the unstabilized method still converges, but in a suboptimal way. For compressible materials, the unstabilized method appears to be somewhat more competitive than the stabilized method since it requires less Newton's iterations and, at the same time, supports stronger loads, as observed in particular in the case of cavitating voids in the sphere.

We have also evaluated numerically the unstabilized HHO method using Raviart–Thomas–Nédélec reconstructions of the gradient (detailed results were not reported herein for brevity). We have retrieved the optimal-order convergence rates for smooth solutions, but the method seems to be somewhat less robust for strongly nonlinear problems. For example, in the case of the sphere with cavitating voids for $k = 1$, if the discrete gradient is reconstructed in $\mathbb{RTN}_d^k(T;\mathbb{R}^{d\times d})$, then the maximum value is $r = 1.12$ whereas, if the discrete gradient is reconstructed in $\mathbb{RTN}_d^{k+1}(T;\mathbb{R}^{d\times d})$ (which contains the space $\mathbb{P}_d^{k+1}(T;\mathbb{R}^{d\times d})$), then the maximum value for r is the same as for uHHO using $\mathbb{P}_d^{k+1}(T;\mathbb{R}^{d\times d})$ and $k = 1$ ($r = 1.92$).

Among possible perspectives of this work, we mention the devising of a reconstruction based on the ideas introduced in [121] for dG methods, and the use of different reconstructions for the isochoric and volumic parts of the energy density. The present methods can also be applied to approximate other nonlinear problems.

CHAPTER 3

A HYBRID HIGH-ORDER METHOD FOR INCREMENTAL ASSOCIATIVE PLASTICITY WITH SMALL DEFORMATIONS

Abstract. We devise and evaluate numerically a Hybrid High-Order (HHO) method for incremental associative plasticity with small deformations. The HHO method uses as discrete unknowns piecewise polynomials of order $k \geq 1$ on the mesh skeleton, together with cell-based polynomials that can be eliminated locally by static condensation. The HHO method supports polyhedral meshes with non-matching interfaces, is free of volumetric locking, and the integration of the constitutive law is performed only at cell-based quadrature nodes. Moreover, the principle of virtual work is satisfied locally with equilibrated tractions. Various two- and three-dimensional test cases from the literature are presented including comparison against known solutions and against results obtained with an industrial software using conforming and mixed finite elements.

This chapter is based on a publication in Computer Methods in Applied Mechanics and Engineering entitled "*A Hybrid High-Order method for incremental associative plasticity with small deformations*" [3].

Sommaire

3.1 Introduction

Hybrid High-Order (HHO) methods have been introduced a few years ago for diffusion problems in [91] and for linear elasticity problems in [89]. Recently, the development of HHO methods has received a vigorous interest. Examples include in solids mechanics Biot's problem [32], nonlinear elasticity with small deformations [40], and hyperelasticity with finite deformations [2], and in fluid mechanics, the incompressible Stokes equations [93], the steady incompressible Navier–Stokes equations [94], and viscoplastic flows with yield stress [49]. The discrete unknowns in HHO methods are face-based unknowns that are piecewise polynomials on the mesh skeleton. Cell-based unknowns are also introduced. These additional unknowns are instrumental for the stability and approximation properties of the method and can be locally eliminated by using the well-known static condensation technique (based on a local Schur complement). For nonlinear problems, this elimination is performed at each step of the nonlinear iterative solver (typically Newton's method).

The devising of HHO methods hinges on two key ideas: (i) a local higher-order reconstruction operator acting on the face and cell unknowns; (ii) a local stabilization operator that weakly enforces on each mesh face the consistency between the local face unknowns and the trace of the cell unknowns. A somewhat subtle design of the stabilization operator has been proposed in [89, 91] leading to $O(h^{k+1})$ energy-error estimates for linear model problems with smooth solutions, where h is the mesh-size and k is the polynomial order of the face unknowns. HHO methods offer several advantages: (i) the construction is dimension-independent; (ii) general meshes (including fairly general polyhedral mesh cells and non-matching interfaces) are supported; (iii) a local formulation using equilibrated fluxes is available, and (iv) computational benefits owing to the static condensation of the cell unknowns and the higher-order convergence rates. In computational mechanics, another salient feature of HHO methods is the absence of volumetric locking [89]. Furthermore, HHO methods have been bridged in [74] to Hybridizable Discontinuous Galerkin (HDG) methods [76] and to nonconforming Virtual Element Methods (ncVEM) [18]. The essential difference with HDG methods is that the HHO stabilization is different so as to deliver higher-order convergence rates on general meshes. Concerning ncVEM, the devising viewpoint is different (ncVEM considers the computable projection of virtual functions instead of a reconstruction operator), and the stabilization achieves similar convergence rates as HHO but is written differently. An open-source implementation of HHO methods, the `DiSk++` library, is available using generic programming tools [71].

In the present work, we devise and evaluate numerically a HHO method for incremental associative plasticity with small deformations. Modelling plasticity problems is particularly relevant in nonlinear solid mechanics since this is one of the main nonlinearities that can be encountered. Moreover, plasticity can have a major influence on the behavior of a mechanical structure. Plastic deformations are generally assumed to be incompressible, which can lead to serious volumetric-locking problems, particularly with a continuous Galerkin (cG) approximation based on (low-order) H^1-conforming finite elements, where only the displacement

field is approximated globally contrary to the plastic deformations and the variables associated with the plastic behavior which are defined and solved locally in each mesh cell. A way to circumvent volumetric locking is to consider mixed methods on simplicial or hexahedral meshes, as in [60, 196, 194]. However, mixed methods need additional global unknowns to impose the condition of plastic incompressibility that generally increase the cost of building and solving the global system (the variables associated with the plastic behavior are still solved locally). Moreover, devising mixed methods on polyhedral meshes with non-matching interfaces is a delicate question. Note that cG methods as well as mixed methods require to perform the integration of the constitutive law only at quadrature nodes in the mesh cells. Another class of methods free of volumetric locking are discontinuous Galerkin (dG) methods. We mention in particular [117, 116, 115, 174] for hyperelasticity and [169] for damage mechanics. Interior penalty dG methods have been developed for classical plasticity with small [131, 162] and finite [163] deformations, and for gradient plasticity with small [98, 97] and finite [166] deformations. However, dG methods from the literature generally require to perform the integration of the constitutive law also at additional quadrature nodes located at the mesh faces. Since the behavior integration can be the most expensive part of the computation during the assembling step [137], this additional integration on the mesh faces can lead to a substantial increase in the computational burden. Moreover, implementing the behavior integration on the mesh faces in an existing finite element code is not straightforward since the data structure for internal variables cannot be necessarily re-used. We also mention the lowest-order Virtual Element Method (VEM) for inelastic problems with small deformations devised in [30] using the maximum norm of the tangent modulus for stabilization (see also [13] for a two-dimensional higher-order extension), whereas the case of finite deformations is treated in [209], still in the lowest-order case, with a pseudo-energy based stabilization.

The HHO method devised in this work uses polynomials of arbitrary order $k \geq 1$ on the mesh faces, and as in [40, 2], the local reconstruction operator builds a symmetric gradient in the tensor-valued polynomial space $\mathbb{P}_d^k(T;\mathbb{R}^{d\times d}_{\rm sym})$, where T is a generic mesh cell and d is the space dimension. The present HHO method offers the above-mentioned benefits of HHO methods (dimension-independent construction, general meshes, local conservation, static condensation). In particular, equilibrated tractions satisfying the law of action and reaction while being in local balance with the external loads and the internal efforts are available. Moreover, in view of the above discussion on the literature, we observe that the present HHO method (i) hinges on a displacement-based formulation thus avoiding the need to introduce additional global unknowns; (ii) is free of volumetric locking; (iii) supports general meshes; and (iv) requires the integration of the constitutive law only at the cell level. Another attractive feature is that the linear system at each step of Newton's method is coercive for strain-hardening materials provided the stabilization parameter is simply positive. We also notice that, to our knowledge, HDG methods have not yet been devised for plasticity problems (for hyperelasticity problems, we mention [147, 171]). Owing to the close links between HHO and HDG methods, this work can thus be seen as the first HDG-like method for plasticity problems. Another follow-up of the HHO idea of local reconstruction is to pave the way for dG methods requiring only a cell-based integration of the constitutive law, by using discrete gradients as in [117, 88, 147]. We also mention the recent study of low-order hybrid dG method with conforming traces and the hybridizable weakly conforming Galerkin method with nonconforming traces in [26] in the context of nonlinear solid mechanics.

This paper is organized as follows: in Section 2, we present the incremental associative plasticity problem and the weak formulation of the governing equations. In Section 3, we devise the HHO method and highlight some of its theoretical aspects. In Section 4, we investigate numerically the HHO method on two- and three-dimensional test cases from

the literature, and we compare our results to analytical solutions whenever available and to numerical results obtained using established cG and mixed methods implemented in the open-source industrial software `code_aster` [111].

3.2 Plasticity model

In what follows, we write v for scalar-valued fields, $\underline{v}$ or $\underline{V}$ for vector-valued fields, $\boldsymbol{V}$ for second-order tensor-valued fields, and $\mathbb{V}$ for fourth-order tensor-valued fields. Contrary to the elastic model, the elastoplastic model is based on the assumption that the deformations are no longer reversible. We place ourselves within the framework of generalized standard materials initially introduced in [127] and further developed in [159]. Moreover, we consider the regime of small deformations and the plasticity model is assumed to be strain-hardening (or perfect) and rate-independent, i.e., the time and the speed of the deformations have no influence on the solution. For this reason, only the incremental plasticity problem is considered.

3.2.1 Helmholtz free energy and yield function

An important hypothesis for the modelling of plasticity under small deformations is that the (symmetric) total strain tensor $\boldsymbol{\varepsilon}$, which is equal to the symmetric gradient $\boldsymbol{\nabla}^s\underline{u}$ of the displacement field $\underline{u}$, can be decomposed into the sum of an elastic part and a plastic part, denoted by $\boldsymbol{\varepsilon}^e$ and $\boldsymbol{\varepsilon}^p$ respectively, so that $\boldsymbol{\varepsilon} = \boldsymbol{\varepsilon}^e + \boldsymbol{\varepsilon}^p$, which is rewritten as follows:

$$\boldsymbol{\varepsilon}^e = \boldsymbol{\varepsilon} - \boldsymbol{\varepsilon}^p. \tag{3.1}$$

Both tensors, $\boldsymbol{\varepsilon}^e$ and $\boldsymbol{\varepsilon}^p$, are symmetric, and the plastic deformations are assumed to be incompressible so that

$$\operatorname{trace}(\boldsymbol{\varepsilon}^p) = 0. \tag{3.2}$$

Since we consider generalized standard materials, the local material state is described by the total strain tensor $\boldsymbol{\varepsilon} \in \mathbb{R}^{d\times d}_{\mathrm{sym}}$, the plastic strain tensor $\boldsymbol{\varepsilon}^p \in \mathbb{R}^{d\times d}_{\mathrm{sym}}$, and a finite collection of internal variables $\underline{\alpha} := (\alpha_1, \cdots, \alpha_m) \in \mathbb{R}^m$. We assume that there exists a Helmholtz free energy $\Psi : \mathbb{R}^{d\times d}_{\mathrm{sym}} \times \mathbb{R}^m \to \mathbb{R}$ acting on the pair $(\boldsymbol{\varepsilon}^e, \underline{\alpha})$ and satisfying the following hypothesis.

Hypothesis 3.1 (Helmholtz free energy) *Ψ can be decomposed additively into an elastic and a plastic part as follows:*

$$\Psi(\boldsymbol{\varepsilon}^e, \underline{\alpha}) = \frac{1}{2}\,\boldsymbol{\varepsilon}^e : \mathbb{C} : \boldsymbol{\varepsilon}^e + \Psi^p(\underline{\alpha}) \tag{3.3}$$

where the function Ψ^p is strictly convex, and the elastic modulus is $\mathbb{C} = 2\mu\mathbb{I}^s + \lambda\boldsymbol{I}\otimes\boldsymbol{I}$, with $\mu > 0$, $3\lambda + 2\mu > 0$, $(\mathbb{I}^s)_{ij,kl} = \frac{1}{2}(\delta_{ik}\delta_{jl} + \delta_{il}\delta_{jk})$, and $(\boldsymbol{I}\otimes\boldsymbol{I})_{ij,kl} = \delta_{ij}\delta_{kl}$.

The elastic modulus $\mathbb{C}$ is isotropic, constant, and positive definite with $\boldsymbol{e} : \mathbb{C} : \boldsymbol{e} = 2\mu\,\boldsymbol{e} : \boldsymbol{e} + \lambda\operatorname{trace}(\boldsymbol{e})^2$, for all $\boldsymbol{e} \in \mathbb{R}^{d\times d}_{\mathrm{sym}}$.

As a consequence of the second principle of thermodynamics, the Cauchy stress tensor $\boldsymbol{\sigma} \in \mathbb{R}^{d\times d}_{\mathrm{sym}}$ and the thermodynamic forces $\underline{q} \in \mathbb{R}^m$ are derived from Ψ as follows:

$$\boldsymbol{\sigma} = \partial_{\boldsymbol{\varepsilon}^e}\Psi = \mathbb{C} : \boldsymbol{\varepsilon}^e \quad \text{and} \quad \underline{q} = \partial_{\underline{\alpha}}\Psi^p. \tag{3.4}$$

The criterion to determine whether the deformations are plastic hinges on the scalar yield function $\Phi : \mathbb{R}^{d\times d}_{\mathrm{sym}} \times \mathbb{R}^m \to \mathbb{R}$, which is a continuous and convex function of the stress tensor

$\boldsymbol{\sigma}$ and the thermodynamic forces $\underline{q}$. The set of stresses and thermodynamic forces that verify $\Phi(\boldsymbol{\sigma}, \underline{q}) \leq 0$ is the convex set of admissible states (or plasticity admissible domain):

$$\mathcal{A} := \left\{ (\boldsymbol{\sigma}, \underline{q}) \in \mathbb{R}^{d\times d}_{\text{sym}} \times \mathbb{R}^m \mid \Phi(\boldsymbol{\sigma}, \underline{q}) \leq 0 \right\}. \tag{3.5}$$

The set of admissible states is partitioned into two disjoint subsets, the elastic domain $\mathcal{A}^e$ which is the interior of the set $\mathcal{A}$ and the yield surface $\partial\mathcal{A}$ which is the boundary of the set $\mathcal{A}$, so that

$$\mathcal{A}^e := \left\{ (\boldsymbol{\sigma}, \underline{q}) \in \mathcal{A} \mid \Phi(\boldsymbol{\sigma}, \underline{q}) < 0 \right\}, \quad \partial\mathcal{A} := \left\{ (\boldsymbol{\sigma}, \underline{q}) \in \mathcal{A} \mid \Phi(\boldsymbol{\sigma}, \underline{q}) = 0 \right\}. \tag{3.6}$$

Hypothesis 3.2 (Yield function) *The yield function* $\Phi : \mathbb{R}^{d\times d}_{sym} \times \mathbb{R}^m \to \mathbb{R}$ *satisfies the following properties:* (i) Φ *is a piecewise analytical function;* (ii) *the point* $(\mathbf{0}, \underline{0})$ *lies in the elastic domain, i.e.,* $\Phi(\mathbf{0}, \underline{0}) < 0$*; and* (iii) Φ *is differentiable at all points on the yield surface* $\partial\mathcal{A}$.

3.2.2 Plasticity model problem in incremental form

We are interested in finding the quasi-static evolution in the pseudo-time interval $[0, t_F]$, $t_F > 0$, of an elastoplastic material body that occupies the domain Ω_0 in the reference configuration. Here, $\Omega_0 \subset \mathbb{R}^d$, $d \in \{2, 3\}$, is a bounded connected polyhedral domain with Lipschitz boundary $\Gamma := \partial\Omega_0$ decomposed in the two relatively open subsets Γ_{N} and Γ_{D}, where a Neumann and a Dirichlet condition are enforced respectively, and such that $\overline{\Gamma_{\text{N}}} \cup \overline{\Gamma_{\text{D}}} = \Gamma$, $\Gamma_{\text{N}} \cap \Gamma_{\text{D}} = \emptyset$, and Γ_{D} has positive Hausdorff-measure (so as to prevent rigid-body motions). The evolution occurs under the action of a body force $\underline{f} : \Omega_0 \times [0, t_F] \to \mathbb{R}^d$, a traction force $\underline{t}_{\text{N}} : \Gamma_{\text{N}} \times [0, t_F] \to \mathbb{R}^d$ on the Neumann boundary Γ_{N}, and a prescribed displacement $\underline{u}_{\text{D}} : \Gamma_{\text{D}} \times [0, t_F] \to \mathbb{R}^d$ on the Dirichlet boundary Γ_{D}: The pseudo-time interval $[0, t_F]$ is discretized into N subintervals such that $t^0 = 0 < t^1 < \cdots < t^N = t_F$. We denote by V, resp. $\underline{V}_0$, the set of all kinematically admissible displacements which satisfy the Dirichlet conditions, resp. homogeneous Dirichlet conditions on Γ_{D}

$$\underline{V}^n_{\text{D}} = \left\{ \underline{v} \in H^1(\Omega_0; \mathbb{R}^d) \mid \underline{v} = \underline{u}_{\text{D}}(t^n) \text{ on } \Gamma_{\text{D}} \right\}, \ \underline{V}_0 = \left\{ \underline{v} \in H^1(\Omega_0; \mathbb{R}^d) \mid \underline{v} = \underline{0} \text{ on } \Gamma_{\text{D}} \right\}. \tag{3.7}$$

Moreover, we denote $\underline{\chi} := (\boldsymbol{\varepsilon}^p, \underline{\alpha}) \in \underline{\mathcal{X}}$ the generalized internal variables, where the space of the generalized internal variables is

$$\underline{\mathcal{X}} := \left\{ \underline{\chi} = (\boldsymbol{\varepsilon}^p, \underline{\alpha}) \in \mathbb{R}^{d\times d}_{\text{sym}} \times \mathbb{R}^m \mid \text{trace}(\boldsymbol{\varepsilon}^p) = 0 \right\}. \tag{3.8}$$

Then the problem can be formulated as follows: For all $1 \leq n \leq N$, given $\underline{u}^{n-1} \in \underline{V}^{n-1}_{\text{D}}$ and $\underline{\chi}^{n-1} \in L^2(\Omega_0; \underline{\mathcal{X}})$ from the previous pseudo-time step or the initial condition, find $\underline{u}^n \in \underline{V}^n_{\text{D}}$ and $\underline{\chi}^n \in L^2(\Omega_0; \underline{\mathcal{X}})$ such that

$$\int_{\Omega_0} \boldsymbol{\sigma}^n : \boldsymbol{\varepsilon}(\underline{v})\, d\Omega_0 = \int_{\Omega_0} \underline{f}^n \cdot \underline{v}\, d\Omega_0 + \int_{\Gamma_{\text{N}}} \underline{t}^n_{\text{N}} \cdot \underline{v}\, d\Gamma \text{ for all } \underline{v} \in \underline{V}_0, \tag{3.9a}$$

and

$$(\underline{\chi}^n, \boldsymbol{\sigma}^n, \mathbb{C}^n_{ep}) = \text{SMALL\_PLASTICITY}(\underline{\chi}^{n-1}, \boldsymbol{\varepsilon}(\underline{u}^{n-1}), \boldsymbol{\varepsilon}(\underline{u}^n) - \boldsymbol{\varepsilon}(\underline{u}^{n-1})). \tag{3.9b}$$

The procedure SMALL_PLASTICITY allows one to compute the new values of the generalized internal variables $\underline{\chi}$, the stress tensor $\boldsymbol{\sigma}$ and the consistent elastoplastic tangent modulus $\mathbb{C}_{ep}$ at each pseudo-time step. This procedure is detailed in Section 3.2.3 below. The incremental problem (3.9) can be reformulated as an incremental variational inequality by introducing a dissipative function, see for example [97]. For strain-hardening plasticity, the weak formulation (3.9) is well-posed, see [128, Section 6.4]. For perfect plasticity, under additional hypotheses on the loads, the existence of a solution to (3.9) with bounded deformation is studied in [80].

3.2.3 Algorithmic aspects

Algorithm 1 presents the incremental associative elastoplasticity problem that has to be solved in order to find the new value, after incrementation, of the generalized internal variables $\underline{\chi}^{\text{new}} = (\boldsymbol{\varepsilon}^{\text{p,new}}, \underline{\alpha}^{\text{new}}) \in \underline{\mathcal{X}}$, the stress tensor $\boldsymbol{\sigma}^{\text{new}} \in \mathbb{R}^{d\times d}_{\text{sym}}$, and the consistent elastoplastic tangent modulus $\mathbb{C}^{\text{new}}_{ep}$, given the generalized internal variables $\underline{\chi} \in \underline{\mathcal{X}}$, the strain tensor $\boldsymbol{\varepsilon} \in \mathbb{R}^{d\times d}_{\text{sym}}$, and the incremental strain tensor $\mathrm{d}\boldsymbol{\varepsilon} \in \mathbb{R}^{d\times d}_{\text{sym}}$. Solving this problem is denoted as previously

$$(\underline{\chi}^{\text{new}}, \boldsymbol{\sigma}^{\text{new}}, \mathbb{C}^{\text{new}}_{ep}) = \text{SMALL\_PLASTICITY}(\underline{\chi}, \boldsymbol{\varepsilon}, \mathrm{d}\boldsymbol{\varepsilon}). \tag{3.10}$$

The procedure to compute $(\underline{\chi}^{\text{new}}, \boldsymbol{\sigma}^{\text{new}}, \mathbb{C}^{\text{new}}_{ep})$ is described in Algorithm 1. First, an elastic trial state $(\boldsymbol{\sigma}^{\text{trial}}, \underline{q}^{\text{trial}})$ is computed. If $(\boldsymbol{\sigma}^{\text{trial}}, \underline{q}^{\text{trial}}) \in \mathcal{A}^e$, then the evolution is elastic, the trial state is accepted, and the internal variables are not modified. Otherwise, the evolution is plastic and the normal and flow rules are used to correct the elastic trial state $(\boldsymbol{\sigma}^{\text{trial}}, \underline{q}^{\text{trial}})$. Specifically, we introduce (see line 9 of Algorithm 1) the plastic multiplier (or consistency parameter) which depends on the yet-unknown pair $(\boldsymbol{\sigma}^{\text{new}}, \underline{q}^{\text{new}})$,

$$\Lambda(\boldsymbol{\sigma}^{\text{new}}, \underline{q}^{\text{new}}) = \frac{\partial_{\boldsymbol{\sigma}}\Phi(\boldsymbol{\sigma}^{\text{new}}, \underline{q}^{\text{new}}) : \mathbb{C} : \mathrm{d}\boldsymbol{\varepsilon}}{\partial_{\boldsymbol{\sigma}}\Phi(\boldsymbol{\sigma}^{\text{new}}, \underline{q}^{\text{new}}) : \mathbb{C} : \partial_{\boldsymbol{\sigma}}\Phi(\boldsymbol{\sigma}^{\text{new}}, \underline{q}^{\text{new}}) + \overline{H}(\boldsymbol{\sigma}^{\text{new}}, \underline{q}^{\text{new}})} \geq 0, \tag{3.11}$$

where $\overline{H}(\boldsymbol{\sigma}^{\text{new}}, \underline{q}^{\text{new}}) := \partial_{\underline{q}}\Phi(\boldsymbol{\sigma}^{\text{new}}, \underline{q}^{\text{new}}) : \partial^2_{\underline{\alpha},\underline{\alpha}}\Psi^p(\underline{\alpha}^{\text{new}}) : \partial_{\underline{q}}\Phi(\boldsymbol{\sigma}^{\text{new}}, \underline{q}^{\text{new}}) \geq 0$ is the generalized hardening modulus. For strain-hardening plasticity (resp. perfect plasticity), we have $\overline{H} > 0$ (resp. $\overline{H} = 0$). The normal and flow rules then state that the pair $(\boldsymbol{\sigma}^{\text{new}}, \underline{q}^{\text{new}}) \in \mathcal{A}$ must be such that $\mathrm{d}\boldsymbol{\varepsilon}^p = \Lambda\, \partial_{\boldsymbol{\sigma}}\Phi$ and $\mathrm{d}\underline{\alpha} = -\Lambda\, \partial_{\underline{q}}\Phi$, where the dependencies in $(\boldsymbol{\sigma}^{\text{new}}, \underline{q}^{\text{new}})$ are omitted for simplicity and where the multiplier Λ verifies in addition the complementary conditions

$$\Lambda \geq 0, \quad \Lambda\, \Phi = 0, \tag{3.12}$$

and the consistency condition

$$\Lambda\, \mathrm{d}\Phi = 0 \quad \text{if } (\boldsymbol{\sigma}^{\text{new}}, \underline{q}^{\text{new}}) \in \partial\mathcal{A}. \tag{3.13}$$

For strain-hardening plasticity, one can show (see [142]) that there exists a unique solution to the constrained nonlinear system considered in lines 7-9 of Algorithm 1.

Algorithm 1 Computation of $(\underline{\chi}^{\text{new}}, \boldsymbol{\sigma}^{\text{new}}, \mathbb{C}_{ep}^{\text{new}})$

1: **procedure** $SMALL\_PLASTICITY(\underline{\chi}, \boldsymbol{\varepsilon}, \mathrm{d}\boldsymbol{\varepsilon})$
2: Set $\boldsymbol{\sigma}^{\text{trial}} = \mathbb{C} : (\boldsymbol{\varepsilon}^e + \mathrm{d}\boldsymbol{\varepsilon})$ and $\underline{q}^{\text{trial}} = \partial_{\underline{\alpha}} \Psi^p(\underline{\alpha})$
3: **if** $(\boldsymbol{\sigma}^{\text{trial}}, \underline{q}^{\text{trial}}) \in \mathcal{A}^e$ **or if** $(\boldsymbol{\sigma}^{\text{trial}}, \underline{q}^{\text{trial}}) \in \partial\mathcal{A}$ and $\partial_{\boldsymbol{\sigma}} \Phi(\boldsymbol{\sigma}^{\text{trial}}, \underline{q}^{\text{trial}}) : \mathbb{C} : \mathrm{d}\boldsymbol{\varepsilon} \leq 0$ **then**
4: $\mathrm{d}\underline{\chi} = (\mathrm{d}\boldsymbol{\varepsilon}^p, \mathrm{d}\underline{\alpha}) = (\mathbf{0}, \underline{0})$, $\boldsymbol{\sigma}^{\text{new}} = \boldsymbol{\sigma}^{\text{trial}}$, $\mathbb{C}_{ep}^{\text{new}} = \mathbb{C}$
5: **else**
6: Solve the following constrained nonlinear system in $(\boldsymbol{\sigma}^{\text{new}}, \underline{q}^{\text{new}}, \mathrm{d}\boldsymbol{\varepsilon}^p, \mathrm{d}\underline{\alpha})$:
7: $\Phi(\boldsymbol{\sigma}^{\text{new}}, \underline{q}^{\text{new}}) = 0, \quad \partial_{\boldsymbol{\sigma}} \Phi(\boldsymbol{\sigma}^{\text{new}}, \underline{q}^{\text{new}}) : \mathbb{C} : (\mathrm{d}\boldsymbol{\varepsilon} - \mathrm{d}\boldsymbol{\varepsilon}^p) \leq 0$
8: $\boldsymbol{\sigma}^{\text{new}} = \mathbb{C} : (\boldsymbol{\varepsilon}^e + \mathrm{d}\boldsymbol{\varepsilon} - \mathrm{d}\boldsymbol{\varepsilon}^p), \quad \underline{q}^{\text{new}} = \partial_{\underline{\alpha}} \Psi^p(\underline{\alpha} + \mathrm{d}\underline{\alpha})$
9: $\mathrm{d}\boldsymbol{\varepsilon}^p = \Lambda(\boldsymbol{\sigma}^{\text{new}}, \underline{q}^{\text{new}})\, \partial_{\boldsymbol{\sigma}} \Phi(\boldsymbol{\sigma}^{\text{new}}, \underline{q}^{\text{new}}), \quad \mathrm{d}\underline{\alpha} = -\Lambda(\boldsymbol{\sigma}^{\text{new}}, \underline{q}^{\text{new}})\, \partial_{\underline{q}} \Phi(\boldsymbol{\sigma}^{\text{new}}, \underline{q}^{\text{new}})$
10: and set $\mathbb{C}_{ep}^{\text{new}} = \mathbb{C} - \dfrac{(\mathbb{C} : \partial_{\boldsymbol{\sigma}} \Phi(\boldsymbol{\sigma}^{\text{new}}, \underline{q}^{\text{new}})) \otimes (\mathbb{C} : \partial_{\boldsymbol{\sigma}} \Phi(\boldsymbol{\sigma}^{\text{new}}, \underline{q}^{\text{new}}))}{\partial_{\boldsymbol{\sigma}} \Phi(\boldsymbol{\sigma}^{\text{new}}, \underline{q}^{\text{new}}) : \mathbb{C} : \partial_{\boldsymbol{\sigma}} \Phi(\boldsymbol{\sigma}^{\text{new}}, \underline{q}^{\text{new}}) + \overline{H}(\boldsymbol{\sigma}^{\text{new}}, \underline{q}^{\text{new}})}$
11: **end if**
12: $\underline{\chi}^{\text{new}} = (\boldsymbol{\varepsilon}^{p,\text{new}}, \underline{\alpha}^{\text{new}}) = \underline{\chi} + \mathrm{d}\underline{\chi}$
13: **return** $(\underline{\chi}^{\text{new}}, \boldsymbol{\sigma}^{\text{new}}, \mathbb{C}_{ep}^{\text{new}})$
14: **end procedure**

Line 8 of Algorithm 1 shows that the increment in the stress tensor is given by $\mathrm{d}\boldsymbol{\sigma} = \mathbb{C} : (\mathrm{d}\boldsymbol{\varepsilon} - \mathrm{d}\boldsymbol{\varepsilon}^p)$, and one then introduces the so-called consistent elastoplastic tangent modulus $\mathbb{C}_{ep}^{\text{new}}$ such that $\mathrm{d}\boldsymbol{\sigma} = \mathbb{C}_{ep}^{\text{new}} : \mathrm{d}\boldsymbol{\varepsilon}$; $\mathbb{C}_{ep}^{\text{new}}$ is a fourth-order tensor having minor and major symmetries. If the evolution is elastic, then $\mathbb{C}_{ep}^{\text{new}} = \mathbb{C}$, and the consistent elastoplastic tangent modulus has two eigenvalues: 2μ with multiplicity five and $3\lambda + 2\mu$ with multiplicity one. Instead, if the evolution is plastic, then $\mathbb{C}_{ep}^{\text{new}} \neq \mathbb{C}$, and the eigenvalues of $\mathbb{C}_{ep}^{\text{new}}$, which are positive for strain-hardening plasticity (and non-negative for perfect plasticity) depend on the Helmholtz free energy Ψ and the yield function Φ (see [200] for details). For a finite incremental strain, the consistent elastoplastic tangent modulus generally differs from the so-called continuous elastoplastic tangent modulus which is obtained by letting the incremental strain tend to zero [195].

3.2.4 Example: combined linear isotropic and kinematic hardening with a von Mises yield criterion

An illustration of the plasticity model defined above is the combined linear isotropic and kinematic hardening model. The internal variables are $\underline{\alpha} := (\boldsymbol{\varepsilon}^p, p)$, where $p \geq 0$ is the equivalent plastic strain. We assume that the plastic part of the free energy is fully decoupled so that

$$\Psi^p(\underline{\alpha}) = \frac{K}{2} \boldsymbol{\varepsilon}^p : \boldsymbol{\varepsilon}^p + \frac{H}{2} p^2. \tag{3.14}$$

where $H \geq 0$, resp. $K \geq 0$, is the isotropic, resp. kinematic, hardening modulus. The associated thermodynamic forces $\underline{q} := (\boldsymbol{\beta}, r)$ are the back-stress tensor $\boldsymbol{\beta} = K\boldsymbol{\varepsilon}^p$ and the internal stress $r = Hp$. Note that $\boldsymbol{\beta}$ is a deviatoric tensor since $\mathrm{trace}(\boldsymbol{\beta}) = 0$. The perfect plastic model is retrieved by taking $H = K = 0$. Concerning the yield function, we consider a J_2-plasticity model with a von Mises criterion:

$$\Phi(\boldsymbol{\sigma}, \underline{q}) = \sqrt{\frac{3}{2}} \| \mathrm{dev}(\boldsymbol{\sigma} - \boldsymbol{\beta}) \|_{\boldsymbol{\ell}^2} - \sigma_{y,0} - r, \tag{3.15}$$

where $\sigma_{y,0}$ is the initial yield stress, $\mathrm{dev}(\boldsymbol{\tau}) := \boldsymbol{\tau} - \frac{1}{d} \mathrm{trace}(\boldsymbol{\tau}) \boldsymbol{I}$ is the deviatoric operator, and the Frobenius norm is defined as $\|\boldsymbol{\tau}\|_{\boldsymbol{\ell}^2} = \sqrt{\boldsymbol{\tau} : \boldsymbol{\tau}}$, for all $\boldsymbol{\tau} \in \mathbb{R}^{d \times d}$. The above model describes with a reasonable accuracy the behaviour of metals (see [159]).

3.3 The Hybrid High-Order method

3.3.1 Discrete setting

We consider a mesh sequence $(\mathcal{T}_h)_{h>0}$, where for each $h > 0$, the mesh $\mathcal{T}_h$ is composed of nonempty disjoint open polyhedra with planar faces such that $\overline{\Omega}_0 = \bigcup_{T\in\mathcal{T}_h} \overline{T}$. The mesh-size is $h = \max_{T\in\mathcal{T}_h} h_T$, where h_T stands for the diameter of the cell T. A closed subset F of $\overline{\Omega}_0$ is called a mesh face if it is a subset with nonempty relative interior of some affine hyperplane H_F and (i) if either there exist two distinct mesh cells T_-, $T_+ \in \mathcal{T}_h$ such that $F = \partial T_- \cap \partial T_+ \cap H_F$ (and F is called an interface) or (ii) there exists one mesh cell $T \in \mathcal{T}_h$ such that $F = \partial T \cap \Gamma \cap H_F$ (and F is called a boundary face). The mesh faces are collected in the set $\mathcal{F}_h$ which is further partitioned into the subset $\mathcal{F}_h^{\mathrm{i}}$ which is the collection of the interfaces and the subset $\mathcal{F}_h^{\mathrm{b}}$ which is the collection of the boundary faces. We assume that the mesh is compatible with the partition of the boundary Γ into Γ_{D} and Γ_{N}, so that we can further split the set $\mathcal{F}_h^{\mathrm{b}}$ into the disjoint subsets $\mathcal{F}_h^{\mathrm{b,D}}$ and $\mathcal{F}_h^{\mathrm{b,N}}$ with obvious notation. For all $T \in \mathcal{T}_h$, $\mathcal{F}_{\partial T}$ is the collection of the mesh faces that are subsets of ∂T and $\underline{n}_T$ is the unit outward normal to T. We assume that the mesh sequence $(\mathcal{T}_h)_{h>0}$ is shape-regular in the sense specified in [89], i.e., there is a matching simplicial submesh of $\mathcal{T}_h$ that belongs to a shape-regular family of simplicial meshes in the usual sense of Ciarlet [69] and such that each mesh cell $T \in \mathcal{T}_h$ (resp., mesh face $F \in \mathcal{F}_h$) can be decomposed in a finite number of sub-cells (resp., sub-faces) which belong to only one mesh cell (resp., to only one mesh face or to the interior of a mesh cell) with uniformly comparable diameter.

Let $k \geq 1$ be a fixed polynomial degree. In each mesh cell $T \in \mathcal{T}_h$, the local HHO unknowns consist of a pair $(\underline{v}_T, \underline{v}_{\partial T})$, where the cell unknown $\underline{v}_T \in \mathbb{P}_d^k(T;\mathbb{R}^d)$ is a vector-valued d-variate polynomial of degree at most k in the mesh cell T, and $\underline{v}_{\partial T} \in \mathbb{P}_{d-1}^k(\mathcal{F}_{\partial T};\mathbb{R}^d) = \times_{F\in\mathcal{F}_{\partial T}} \mathbb{P}_{d-1}^k(F;\mathbb{R}^d)$ is a piecewise, vector-valued $(d-1)$-variate polynomial of degree at most k on each face $F \in \mathcal{F}_{\partial T}$. We write more concisely that

$$\hat{\underline{v}}_T := (\underline{v}_T, \underline{v}_{\partial T}) \in \hat{\underline{U}}_T^k := \mathbb{P}_d^k(T;\mathbb{R}^d) \times \mathbb{P}_{d-1}^k(\mathcal{F}_{\partial T};\mathbb{R}^d). \tag{3.16}$$

The degrees of freedom are illustrated in Fig. 3.1, where a dot indicates one degree of freedom (which is not necessarily computed as a point evaluation). More generally, the polynomial degree k of the face unknowns being fixed, HHO methods can be devised using cell unknowns that are polynomials of degree $l \in \{k-1, k, k+1\} \cap \mathbb{N}^\star$, (see [74]); these variants are briefly investigated numerically in Section 3.4.6. We equip the space $\hat{\underline{U}}_T^k$ with the following local discrete strain semi-norm:

$$|\hat{\underline{v}}_T|_{1,T}^2 := \|\boldsymbol{\nabla}^s \underline{v}_T\|_{\boldsymbol{L}^2(T)}^2 + \|\eta_{\partial T}^{\frac{1}{2}}(\underline{v}_{\partial T} - \underline{v}_{T|\partial T})\|_{\underline{L}^2(\partial T)}^2, \tag{3.17}$$

with the piecewise constant function $\eta_{\partial T}$ such that $\eta_{\partial T|F} = h_F^{-1}$ for all $F \in \mathcal{F}_{\partial T}$, where h_F is the diameter of F. We notice that $|\hat{\underline{v}}_T|_{1,T} = 0$ implies that $\underline{v}_T$ is a rigid-body motion and that $\underline{v}_{\partial T}$ is the trace of $\underline{v}_T$ on ∂T.

3.3.2 Local symmetric strain reconstruction and stabilization

The first key ingredient in the devising of the HHO method is a local symmetric strain reconstruction in each mesh cell $T \in \mathcal{T}_h$. This reconstruction is materialized by an operator $\boldsymbol{E}_T^k : \hat{\underline{U}}_T^k \to \mathbb{P}_d^k(T;\mathbb{R}_{\mathrm{sym}}^{d\times d})$ mapping onto the space composed of symmetric $\mathbb{R}^{d\times d}$-valued polynomials in T. The main reason for reconstructing the symmetric strain tensor in a larger space than the space $\boldsymbol{\nabla}^s\mathbb{P}_d^{k+1}(T;\mathbb{R}^d)$ originally introduced in [89] for the linear elasticity problem is that the reconstructed symmetric gradient of a test function acts against a discrete

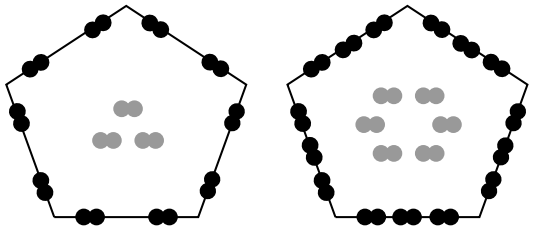

(a) $k = 1$ (b) $k = 2$

Figure 3.1: Face (black) and cell (gray) degrees of freedom in $\hat{\underline{U}}_T^k$ for $k = 1$ and $k = 2$ in the two-dimensional case (each dot represents a degree of freedom which is not necessarily a point evaluation).

Cauchy stress tensor which is not in symmetric gradient form, see [87, Section 4] for further insight. For all $\hat{\underline{v}}_T \in \hat{\underline{U}}_T^k$, the reconstructed symmetric strain tensor $\boldsymbol{E}_T^k(\hat{\underline{v}}_T) \in \mathbb{P}_d^k(T;\mathbb{R}_{\rm sym}^{d\times d})$ is obtained by solving the following local problem: For all $\boldsymbol{\tau} \in \mathbb{P}_d^k(T;\mathbb{R}_{\rm sym}^{d\times d})$,

$$(\boldsymbol{E}_T^k(\hat{\underline{v}}_T),\boldsymbol{\tau})_{\boldsymbol{L}^2(T)} = (\boldsymbol{\nabla}^s\underline{v}_T,\boldsymbol{\tau})_{\boldsymbol{L}^2(T)} + (\underline{v}_{\partial T} - \underline{v}_{T|\partial T}, \boldsymbol{\tau}\,\underline{n}_T)_{\underline{L}^2(\partial T)}. \tag{3.18}$$

Solving this problem entails choosing a basis of the polynomial space $\mathbb{P}_d^k(T;\mathbb{R})$ and inverting the associated mass matrix for each component of the tensor $\boldsymbol{E}_T^k(\hat{\underline{v}}_T)$. The second key ingredient in the HHO method is a local stabilization operator that enforces weakly the matching between the faces unknowns and the trace of the cell unknowns. Following [91, 89], the local stabilization operator $\underline{S}_{\partial T}^k : \hat{\underline{U}}_T^k \to \mathbb{P}_{d-1}^k(\mathcal{F}_{\partial T};\mathbb{R}^d)$ is used to penalize the difference between the face unknown $\underline{v}_{\partial T}$ and the trace of the cell unknown $\underline{v}_{T|\partial T}$ in a least-squares sense. The stabilization operator $\underline{S}_{\partial T}^k$ is defined such that, for all $\hat{\underline{v}}_T \in \hat{\underline{U}}_T^k$,

$$\underline{S}_{\partial T}^k(\hat{\underline{v}}_T) = \underline{\Pi}_{\partial T}^k\big(\underline{v}_{\partial T} - \underline{D}_T^{k+1}(\hat{\underline{v}}_T)_{|\partial T} - (\underline{v}_T - \underline{\Pi}_T^k(\underline{D}_T^{k+1}(\hat{\underline{v}}_T)))_{|\partial T}\big), \tag{3.19}$$

where $\underline{\Pi}_T^k$ and $\underline{\Pi}_{\partial T}^k$ denote, respectively, the L^2-orthogonal projectors onto $\mathbb{P}_d^k(T;\mathbb{R}^d)$ and $\mathbb{P}_{d-1}^k(\mathcal{F}_{\partial T};\mathbb{R}^d)$. The local displacement reconstruction operator $\underline{D}_T^{k+1} : \hat{\underline{U}}_T^k \to \mathbb{P}_d^{k+1}(T;\mathbb{R}^d)$ is such that, for all $\hat{\underline{v}}_T \in \hat{\underline{U}}_T^k$, $\underline{D}_T^{k+1}(\hat{\underline{v}}_T) \in \mathbb{P}_d^{k+1}(T;\mathbb{R}^d)$ is obtained by solving the following local Neumann problem: For all $\underline{w} \in \mathbb{P}_d^{k+1}(T;\mathbb{R}^d)$,

$$(\boldsymbol{\nabla}^s\underline{D}_T^{k+1}(\hat{\underline{v}}_T),\boldsymbol{\nabla}^s\underline{w})_{\boldsymbol{L}^2(T)} = (\boldsymbol{\nabla}^s\underline{v}_T,\boldsymbol{\nabla}^s\underline{w})_{\boldsymbol{L}^2(T)} + (\underline{v}_{\partial T} - \underline{v}_{T|\partial T}, \boldsymbol{\nabla}^s\underline{w}\,\underline{n}_T)_{\underline{L}^2(\partial T)}, \tag{3.20}$$

together with the mean-value conditions $\int_T \underline{D}_T^{k+1}(\hat{\underline{v}}_T)\,dT = \int_T \underline{v}_T\,dT$ and $\int_T \boldsymbol{\nabla}^{ss}\underline{D}_T^{k+1}(\hat{\underline{v}}_T)\,dT = \int_{\partial T} \frac{1}{2}(\underline{v}_{\partial T}\otimes\underline{n}_T - \underline{n}_T\otimes\underline{v}_{\partial T})\,d\partial T$, where $\boldsymbol{\nabla}^{ss}$ is the skew-symmetric part of the gradient operator. Comparing with (3.18), one readily sees that $\boldsymbol{\nabla}^s\underline{D}_T^{k+1}(\hat{\underline{v}}_T)$ is the L^2-orthogonal projection of $\boldsymbol{E}_T^k(\hat{\underline{v}}_T)$ onto the subspace $\boldsymbol{\nabla}^s\mathbb{P}_d^{k+1}(T;\mathbb{R}^d)$. Following [89, Lemma 4], it is straightforward to establish the following stability and boundedness properties (the proof is omitted for brevity).

Lemma 3.3 (Boundedness and stability) *Let the symmetric strain reconstruction operator be defined by (3.18) and the stabilization operator be defined by (3.19). Let $\eta_{\partial T}$ be defined below (3.17). Then, we have the following properties: (i) Boundedness: there exists $\alpha_\sharp < +\infty$, uniform w.r.t. h, so that, for all $T \in \mathcal{T}_h$ and all $\hat{\underline{v}}_T \in \hat{\underline{U}}_T^k$,*

$$\left(\|\boldsymbol{E}_T^k(\hat{\underline{v}}_T)\|_{\boldsymbol{L}^2(T)}^2 + \|\eta_{\partial T}^{\frac{1}{2}}\underline{S}_{\partial T}^k(\hat{\underline{v}}_T)\|_{\underline{L}^2(\partial T)}^2\right)^{\frac{1}{2}} \le \alpha_\sharp|\hat{\underline{v}}_T|_{1,T}. \tag{3.21}$$

(ii) Stability: there exists $\alpha_\flat > 0$*, uniform w.r.t.* h*, so that, for all* $T \in \mathcal{T}_h$ *and all* $\hat{\underline{v}}_T \in \hat{\underline{U}}_T^k$*,*

$$\alpha_\flat |\hat{\underline{v}}_T|_{1,T} \le \left(\|\boldsymbol{E}_T^k(\hat{\underline{v}}_T)\|_{\boldsymbol{L}^2(T)}^2 + \|\eta_{\partial T}^{\frac{1}{2}} \underline{S}_{\partial T}^k(\hat{\underline{v}}_T)\|_{\underline{L}^2(\partial T)}^2 \right)^{\frac{1}{2}}. \tag{3.22}$$

As shown in [89], the following important commuting property holds true:

$$\boldsymbol{E}_T^k(\hat{\underline{I}}_T^k(\underline{v})) = \boldsymbol{\Pi}_T^k(\boldsymbol{\nabla}^s \underline{v}), \qquad \forall \underline{v} \in H^1(T;\mathbb{R}^d), \tag{3.23}$$

where the reduction operator $\hat{\underline{I}}_T^k : H^1(T;\mathbb{R}^d) \to \hat{\underline{U}}_T^k$ is defined so that $\hat{\underline{I}}_T^k(\underline{v}) = (\underline{\Pi}_T^k(\underline{v}), \underline{\Pi}_{\partial T}^k(\underline{v}_{|\partial T}))$. Proceeding as in [89, Thm. 8], one can show that for the linear elasticity problem and smooth solutions, the energy error converges as $h^{k+1}|\underline{u}|_{\underline{H}^{k+2}(\Omega_0)}$. Finally, taking the trace in (3.23), we infer that

$$\operatorname{trace}\left(\boldsymbol{E}_T^k(\hat{\underline{I}}_T^k(\underline{v}))\right) = \Pi_T^k(\nabla \cdot \underline{v}), \qquad \forall \underline{v} \in H^1(T;\mathbb{R}^d), \tag{3.24}$$

which is the key commuting property used in [89] to prove robustness for quasi-incompressible linear elasticity. This absence of volumetric locking is confirmed in the numerical experiments performed in Section 3.4 in the nonlinear setting of incremental associative plasticity.

3.3.3 Global discrete problem

Let us now devise the global discrete problem. We set $\mathbb{P}_d^k(\mathcal{T}_h;\mathbb{R}^d) := \times_{T\in\mathcal{T}_h} \mathbb{P}_d^k(T;\mathbb{R}^d)$ and $\mathbb{P}_{d-1}^k(\mathcal{F}_h;\mathbb{R}^d) := \times_{F\in\mathcal{F}_h} \mathbb{P}_{d-1}^k(F;\mathbb{R}^d)$. The global space of discrete HHO unknowns is defined as

$$\hat{\underline{U}}_h^k := \mathbb{P}_d^k(\mathcal{T}_h;\mathbb{R}^d) \times \mathbb{P}_{d-1}^k(\mathcal{F}_h;\mathbb{R}^d). \tag{3.25}$$

For a generic element $\hat{\underline{v}}_h \in \hat{\underline{U}}_h^k$, we use the notation $\hat{\underline{v}}_h = ((\underline{v}_T)_{T\in\mathcal{T}_h}, (\underline{v}_F)_{F\in\mathcal{F}_h})$. For any mesh cell $T \in \mathcal{T}_h$, we denote by $\hat{\underline{v}}_T = (\underline{v}_T, \underline{v}_{\partial T}) \in \hat{\underline{U}}_T^k$ the local components of $\hat{\underline{v}}_h$ attached to the mesh cell T and the faces composing its boundary, and for any mesh face $F \in \mathcal{F}_h$, we denote by $\underline{v}_F$ the component attached to the face F. The Dirichlet boundary condition on the displacement field can be enforced explicitly on the discrete unknowns attached to the boundary faces in $\mathcal{F}_h^{\mathrm{b,D}}$. Letting $\underline{\Pi}_F^k$ denote the L^2-orthogonal projector onto $\mathbb{P}_{d-1}^k(F;\mathbb{R}^d)$, we set

$$\hat{\underline{U}}_{h,\mathrm{D}}^{k,n} := \left\{ \hat{\underline{v}}_h \in \hat{\underline{U}}_h^k \mid \underline{v}_F = \underline{\Pi}_F^k(\underline{u}_{\mathrm{D}}(t^n)),\ \forall F \in \mathcal{F}_h^{\mathrm{b,D}} \right\}, \tag{3.26a}$$

$$\hat{\underline{U}}_{h,0}^k := \left\{ \hat{\underline{v}}_h \in \hat{\underline{U}}_h^k \mid \underline{v}_F = \underline{0},\ \forall F \in \mathcal{F}_h^{\mathrm{b,D}} \right\}. \tag{3.26b}$$

Note that the map $\hat{\underline{v}}_h \mapsto (\sum_{T\in\mathcal{T}_h} |\hat{\underline{v}}_T|_{1,T}^2)^{\frac{1}{2}}$ defines a norm on $\hat{\underline{U}}_{h,0}^k$ (see [89, Prop. 5]).

A key feature of the present HHO method is that the discrete generalized internal variables are computed only at the quadrature points in each mesh cell. We introduce for all $T \in \mathcal{T}_h$, the quadrature points $\underline{\xi}_T = (\underline{\xi}_{T,j})_{1\le j\le m_Q}$, with $\underline{\xi}_{T,j} \in T$ for all $1 \le j \le m_Q$, and the quadrature weights $\underline{\omega}_T = (\omega_{T,j})_{1\le j\le m_Q}$, with $\omega_{T,j} \in \mathbb{R}$ for all $1 \le j \le m_Q$. We denote by k_Q the order of the quadrature. Then, the discrete internal variables are sought in the space

$$\tilde{\underline{\mathcal{X}}}_{\mathcal{T}_h}^{m_Q} := \bigtimes_{T\in\mathcal{T}_h} \underline{\mathcal{X}}^{m_Q}, \tag{3.27}$$

that is, for all $T \in \mathcal{T}_h$, the internal variables attached to T form a vector $\underline{\chi}_T = (\underline{\chi}_T(\underline{\xi}_{T,j}))_{1\le j\le m_Q}$ with $\underline{\chi}_T(\underline{\xi}_{T,j}) \in \underline{\mathcal{X}}$ for all $1 \le j \le m_Q$.

We can now formulate the global discrete problem. We use the following notation for two tensor-valued functions defined on T:

$$(\boldsymbol{s},\boldsymbol{e})_{\boldsymbol{L}^2_Q(T)} := \sum_{j=1}^{m_Q} \omega_{T,j}\, \boldsymbol{s}(\underline{\xi}_{T,j}) : \boldsymbol{e}(\underline{\xi}_{T,j}). \tag{3.28}$$

We also need to consider the case where we know the tensor $\tilde{\boldsymbol{s}}$ only at the Gauss nodes (we use a tilde to indicate this situation), i.e., we have $\tilde{\boldsymbol{s}} = (\tilde{\boldsymbol{s}}(\underline{\xi}_{T,j}))_{1\le j\le m_Q} \in (\mathbb{R}^{d\times d})^{m_Q}$. In this case, we slightly abuse the notation by denoting again by $(\tilde{\boldsymbol{s}},\boldsymbol{e})_{\boldsymbol{L}^2_Q(T)}$ the quantity equal to the right-hand side of (3.28) with $\tilde{\boldsymbol{s}}$ replacing $\boldsymbol{s}$. The global discrete problem consists in finding for any pseudo-time step $1 \le n \le N$, the pair of discrete displacements $\underline{\hat{u}}_h^n \in \underline{\hat{U}}_{h,\mathrm{D}}^{k,n}$ and the discrete internal variables $\underline{\tilde{\chi}}_{\mathcal{T}_h}^n \in \underline{\tilde{\mathcal{X}}}_{\mathcal{T}_h}^{m_Q}$ such that, for all $\delta\underline{\hat{v}}_h \in \underline{\hat{U}}_{h,0}^k$,

$$\begin{aligned}
&\sum_{T\in\mathcal{T}_h} (\tilde{\boldsymbol{\sigma}}^n, \boldsymbol{E}_T^k(\delta\underline{\hat{v}}_T))_{\boldsymbol{L}^2_Q(T)} + \sum_{T\in\mathcal{T}_h} \beta(\eta_{\partial T}\underline{S}_{\partial T}^k(\underline{\hat{u}}_T^n), \underline{S}_{\partial T}^k(\delta\underline{\hat{v}}_T))_{\underline{L}^2(\partial T)}\\
&= \sum_{T\in\mathcal{T}_h} (\underline{f}^n, \delta\underline{v}_T)_{\underline{L}^2(T)} + \sum_{F\in\mathcal{F}_h^{\mathrm{b,N}}} (\underline{t}_{\mathrm{N}}^n, \delta\underline{v}_F)_{\underline{L}^2(F)},
\end{aligned} \tag{3.29}$$

where for all $T \in \mathcal{T}_h$ and all $1 \le j \le m_Q$,

$$\begin{aligned}
&(\underline{\tilde{\chi}}_T^n(\underline{\xi}_{T,j}), \tilde{\boldsymbol{\sigma}}^n(\underline{\xi}_{T,j}), \tilde{\mathbb{C}}_{ep}^n(\underline{\xi}_{T,j})) =\\
&\quad \mathrm{SMALL_PLASTICITY}(\underline{\tilde{\chi}}_T^{n-1}(\underline{\xi}_{T,j}), \boldsymbol{E}_T^k(\underline{\hat{u}}_T^{n-1})(\underline{\xi}_{T,j}), \boldsymbol{E}_T^k(\underline{\hat{u}}_T^n)(\underline{\xi}_{T,j}) - \boldsymbol{E}_T^k(\underline{\hat{u}}_T^{n-1})(\underline{\xi}_{T,j})),
\end{aligned} \tag{3.30}$$

with $\underline{\hat{u}}_h^{n-1} \in \underline{\hat{U}}_{h,\mathrm{D}}^{k,n-1}$ and $\underline{\tilde{\chi}}_{\mathcal{T}_h}^{n-1} \in \underline{\tilde{\mathcal{X}}}_{\mathcal{T}_h}^{m_Q}$ given either from the previous pseudo-time step or the initial condition. Moreover, in the second line of (3.29), the stabilization employs a weight of the form $\beta = 2\mu\beta_0$ with $\beta_0 > 0$. In the original HHO method for linear elasticity [89], the choice $\beta_0 = 1$ is considered. In the present setting, the choice for β_0 is further discussed in Section 3.3.5 and in Section 3.4.6.

Remark 3.4 (Unstabilized HHO method) *An unstabilized HHO (uHHO) method has been considered in [2] on affine simplicial meshes without hanging nodes for hyperelastic materials in finite deformations inspired by the stable dG methods without penalty parameters devised in [146]; a more comprehensive treatment of unstabilized gradient reconstructions including polyhedral meshes can be found in [87]. In the uHHO method from [2], the symmetric gradient is reconstructed in a larger space than $\mathbb{P}_d^k(T;\mathbb{R}_{sym}^{d\times d})$, typically $\mathbb{P}_d^{k+1}(T;\mathbb{R}_{sym}^{d\times d})$, to achieve stability as in Lemma 3.3 with $\underline{S}_{\partial T}^k \equiv \underline{0}$. The price to be paid is a convergence rate of order k for smooth solutions. In the present setting of elastoplasticity with small deformations, our numerical tests (not shown for brevity) indicate for $k = 1$ less accurate results for uHHO than for HHO with stabilization, and for $k = 2$, the results are of comparable accuracy. The CPU costs are more or less comparable since the time saved by avoiding the stabilization for uHHO is compensated by the need to reconstruct the strain in a larger space.*

3.3.4 Discrete principle of virtual work

The discrete problem (3.29) expresses the principle of virtual work at the global level, and following the ideas introduced in [74] (see also [40, 2]), it is possible to infer a local principle

of virtual work in terms of face-based discrete tractions that comply with the law of action and reaction. Let $\underline{\hat{S}}^k_{\partial T} : \mathbb{P}^k_{d-1}(\mathcal{F}_{\partial T};\mathbb{R}^d) \to \mathbb{P}^k_{d-1}(\mathcal{F}_{\partial T};\mathbb{R}^d)$ be defined such that

$$\underline{\hat{S}}^k_{\partial T}(\underline{\theta}) = \underline{\Pi}^k_{\partial T}\big(\underline{\theta} - (\boldsymbol{I} - \underline{\Pi}^k_T)\underline{D}^{k+1}_T(\underline{0},\underline{\theta})_{|\partial T}\big). \tag{3.31}$$

Comparing (3.19) with (3.31), we observe that $\underline{S}^k_{\partial T}(\underline{\hat{v}}_T) = \underline{\hat{S}}^k_{\partial T}(\underline{v}_{\partial T} - \underline{v}_{T|\partial T})$ for all $\underline{\hat{v}}_T \in \underline{\hat{U}}^k_T$. Let $\underline{\hat{S}}^{k*}_{\partial T} : \mathbb{P}^k_{d-1}(\mathcal{F}_{\partial T};\mathbb{R}^d) \to \mathbb{P}^k_{d-1}(\mathcal{F}_{\partial T};\mathbb{R}^d)$ be the adjoint operator of $\underline{\hat{S}}^k_{\partial T}$ with respect to the $\underline{L}^2(\partial T)$-inner product so that we have $(\eta_{\partial T}\underline{\hat{S}}^k_{\partial T}(\underline{\theta}), \underline{\hat{S}}^k_{\partial T}(\underline{\zeta}))_{\underline{L}^2(\partial T)} = (\underline{\hat{S}}^{k*}_{\partial T}(\eta_{\partial T}\underline{\hat{S}}^k_{\partial T}(\underline{\theta})), \underline{\zeta})_{\underline{L}^2(\partial T)}$ (recall that the weight $\eta_{\partial T}$ is piecewise constant on ∂T). Let $\boldsymbol{\Pi}^k_{Q,T} : (\mathbb{R}^{d\times d})^{m_Q} \to \mathbb{P}^k_d(T;\mathbb{R}^{d\times d})$ denote the L^2_Q-orthogonal projector such that for all $\tilde{\boldsymbol{s}} \in (\mathbb{R}^{d\times d})^{m_Q}$, $(\boldsymbol{\Pi}^k_{Q,T}(\tilde{\boldsymbol{s}}), \boldsymbol{e})_{\boldsymbol{L}^2(T)} = (\tilde{\boldsymbol{s}}, \boldsymbol{e})_{\boldsymbol{L}^2_Q(T)}$ for all $\boldsymbol{e} \in \mathbb{P}^k_d(T;\mathbb{R}^{d\times d})$. Finally, for any pseudo-time step $1 \le n \le N$ and all $T \in \mathcal{T}_h$, let us define the discrete traction:

$$\underline{T}^n_T := \boldsymbol{\Pi}^k_{Q,T}(\tilde{\boldsymbol{\sigma}}^n_T)\,\underline{n}_T + \beta\underline{\hat{S}}^{k*}_{\partial T}(\eta_{\partial T}\underline{\hat{S}}^k_{\partial T}(\underline{u}^n_{\partial T} - \underline{u}^n_{T|\partial T})) \in \mathbb{P}^k_{d-1}(\mathcal{F}_{\partial T};\mathbb{R}^d), \tag{3.32}$$

where $\tilde{\boldsymbol{\sigma}}^n_T = (\tilde{\boldsymbol{\sigma}}^n_T(\underline{\xi}_{T,j}))_{1\le j\le m_Q} \in (\mathbb{R}^{d\times d}_{\rm sym})^{m_Q}$ with $\tilde{\boldsymbol{\sigma}}^n_T(\underline{\xi}_{T,j}) = \mathbb{C} : (\boldsymbol{E}^k_T(\hat{\underline{u}}^n_T)(\underline{\xi}_{T,j}) - \tilde{\boldsymbol{\varepsilon}}^{p,n}_T(\underline{\xi}_{T,j}))$ for all $1 \le j \le m_Q$.

Lemma 3.5 (Equilibrated tractions) *Assume that $k_Q \ge 2k$. Then, for any pseudo-time step $1 \le n \le N$, the following local principle of virtual work holds true for all $T \in \mathcal{T}_h$:*

$$(\tilde{\boldsymbol{\sigma}}^n_T, \boldsymbol{\nabla}^s\delta\underline{v}_T)_{\boldsymbol{L}^2_Q(T)} - (\underline{T}^n_T, \delta\underline{v}_T)_{\underline{L}^2(\partial T)} = (\underline{f}^n, \delta\underline{v}_T)_{\underline{L}^2(T)}, \qquad \forall\delta\underline{v}_T \in \mathbb{P}^k_d(T;\mathbb{R}^d), \tag{3.33}$$

where the discrete tractions $\underline{T}^n_T$ defined by (3.32) satisfy the following law of action and reaction for all $F \in \mathcal{F}^i_h \cup \mathcal{F}^{b,N}_h$:

$$\underline{T}^n_{T_-|F} + \underline{T}^n_{T_+|F} = \underline{0}, \quad \text{if } F \in \mathcal{F}^i_h \text{ with } F = \partial T_- \cap \partial T_+ \cap H_F, \tag{3.34a}$$

$$\underline{T}^n_{T|F} = \underline{\Pi}^k_F(\underline{t}^n_N), \qquad \text{if } F \in \mathcal{F}^{b,N}_h \text{ with } F = \partial T \cap \Gamma_N \cap H_F. \tag{3.34b}$$

Proof. Recall the notation $\tilde{\boldsymbol{\sigma}}^n_T = (\tilde{\boldsymbol{\sigma}}^n_T(\underline{\xi}_{T,j}))_{1\le j\le m_Q}$ with $\tilde{\boldsymbol{\sigma}}^n_T(\underline{\xi}_{T,j}) = \mathbb{C} : (\boldsymbol{E}^k_T(\hat{\underline{u}}^n_T)(\underline{\xi}_{T,j}) - \tilde{\boldsymbol{\varepsilon}}^{p,n}_T(\underline{\xi}_{T,j}))$ for all $1 \le j \le m_Q$. Let us consider the virtual displacement $((\delta\underline{v}_T\delta_{T,T'})_{T'\in\mathcal{T}_h}, (\underline{0})_{F\in\mathcal{F}_h}) \in \underline{\hat{U}}^k_{h,0}$ in (3.29), with the Kronecker delta such that $\delta_{T,T'} = 1$ if $T = T'$ and $\delta_{T,T'} = 0$ otherwise. Owing to (3.18), and since the quadrature is by assumption at least of order $2k$, we have

$$\begin{aligned}
(\underline{f}^n, \delta\underline{v}_T)_{\underline{L}^2(T)} &= (\tilde{\boldsymbol{\sigma}}^n_T, \boldsymbol{E}^k_T(\delta\underline{v}_T, \underline{0}))_{\boldsymbol{L}^2_Q(T)} + \beta(\eta_{\partial T}\underline{\hat{S}}^k_{\partial T}(\underline{u}^n_{\partial T} - \underline{u}^n_{T|\partial T}), \underline{\hat{S}}^k_{\partial T}(-\delta\underline{v}_{T|\partial T}))_{\underline{L}^2(\partial T)}\\
&= (\boldsymbol{\Pi}^k_{Q,T}(\tilde{\boldsymbol{\sigma}}^n_T), \boldsymbol{E}^k_T(\delta\underline{v}_T, \underline{0}))_{\boldsymbol{L}^2(T)} - \beta(\underline{\hat{S}}^{k*}_{\partial T}(\eta_{\partial T}\underline{\hat{S}}^k_{\partial T}(\underline{u}^n_{\partial T} - \underline{u}^n_{T|\partial T})), \delta\underline{v}_{T|\partial T})_{\underline{L}^2(\partial T)}\\
&= (\boldsymbol{\Pi}^k_{Q,T}(\tilde{\boldsymbol{\sigma}}^n_T), \boldsymbol{\nabla}^s\delta\underline{v}_T)_{\boldsymbol{L}^2(T)} - (\boldsymbol{\Pi}^k_{Q,T}(\tilde{\boldsymbol{\sigma}}^n_T)\,\underline{n}_T, \delta\underline{v}_T)_{\underline{L}^2(\partial T)}\\
&\quad - \beta(\underline{\hat{S}}^{k*}_{\partial T}(\eta_{\partial T}\underline{\hat{S}}^k_{\partial T}(\underline{u}^n_{\partial T} - \underline{u}^n_{T|\partial T})), \delta\underline{v}_{T|\partial T})_{\underline{L}^2(\partial T)}\\
&= (\tilde{\boldsymbol{\sigma}}^n_T, \boldsymbol{\nabla}^s\delta\underline{v}_T)_{\boldsymbol{L}^2_Q(T)} - (\underline{T}^n_T, \delta\underline{v}_T)_{\underline{L}^2(\partial T)}.
\end{aligned}$$

This establishes the local principle of virtual work (3.33). Similarly, the law of action and reaction (3.34) follows by considering, for all $F \in \mathcal{F}^{\rm i}_h \cup \mathcal{F}^{\rm b,N}_h$, the virtual displacement $((\underline{0})_{T\in\mathcal{T}_h}, (\delta\underline{v}_F\delta_{F,F'})_{F'\in\mathcal{F}_h}) \in \underline{\hat{U}}^k_{h,0}$ in (3.29) (with obvious notation for the face-based Kronecker delta), and observing that both $\delta\underline{v}_F$ and $\underline{T}_{T_\pm|F}$ are in $\mathbb{P}^k_{d-1}(F;\mathbb{R}^d)$. If $F \in \mathcal{F}^{\rm b,N}_h$ with

$F = \partial T \cap \Gamma_{\mathrm{N}} \cap H_F$, we have

$$\begin{aligned}
(\underline{t}_{\mathrm{N}}^n, \delta\underline{v}_F)_{\underline{L}^2(F)} &= (\underline{\Pi}_F^k(\underline{t}_{\mathrm{N}}^n), \delta\underline{v}_F)_{\underline{L}^2(F)} \\
&= (\tilde{\boldsymbol{\sigma}}_T^n, \boldsymbol{E}_T^k(\underline{0}, \delta\underline{v}_F))_{\boldsymbol{L}_Q^2(T)} + \beta(\eta_{\partial T}\underline{\hat{S}}_{\partial T}^k(\underline{u}_{\partial T}^n - \underline{u}_{T|\partial T}^n), \underline{\hat{S}}_{\partial T}^k(\delta\underline{v}_F))_{\underline{L}^2(F)} \\
&= (\boldsymbol{\Pi}_{Q,T}^k(\tilde{\boldsymbol{\sigma}}_T^n), \boldsymbol{E}_T^k(\underline{0}, \delta\underline{v}_F))_{\boldsymbol{L}^2(T)} + \beta(\eta_{\partial T}\underline{\hat{S}}_{\partial T}^k(\underline{u}_{\partial T}^n - \underline{u}_{T|\partial T}^n), \underline{\hat{S}}_{\partial T}^k(\delta\underline{v}_F))_{\underline{L}^2(\partial T)} \\
&= (\boldsymbol{\Pi}_{Q,T}^k(\tilde{\boldsymbol{\sigma}}_T^n)\,\underline{n}_T, \delta\underline{v}_F)_{\underline{L}^2(F)} + \beta(\underline{\hat{S}}_{\partial T}^{k*}(\eta_{\partial T}\underline{\hat{S}}_{\partial T}^k(\underline{u}_{\partial T}^n - \underline{u}_{T|\partial T}^n)), \delta\underline{v}_F)_{\underline{L}^2(\partial T)} \\
&= (\underline{T}_{T|F}^n, \delta\underline{v}_F)_{\underline{L}^2(F)},
\end{aligned}$$

whereas if $F \in \mathcal{F}_h^{\mathrm{i}}$ with $F = \partial T_- \cap \partial T_+ \cap H_F$, we have

$$\begin{aligned}
0 &= (\tilde{\boldsymbol{\sigma}}_{T_+}^n, \boldsymbol{E}_{T_+}^k(\underline{0}, \delta\underline{v}_F))_{\boldsymbol{L}_Q^2(T_+)} + \beta(\gamma_{\partial T_+}\underline{\hat{S}}_{\partial T_+}^k(\underline{u}_{\partial T_+}^n - \underline{u}_{T_+|\partial T_+}^n), \underline{\hat{S}}_{\partial T_+}^k(\delta\underline{v}_F))_{\underline{L}^2(\partial T_+)} \\
&\quad + (\tilde{\boldsymbol{\sigma}}_{T_-}^n, \boldsymbol{E}_{T_-}^k(\underline{0}, \delta\underline{v}_F))_{\boldsymbol{L}_Q^2(T_-)} + \beta(\gamma_{\partial T_-}\underline{\hat{S}}_{\partial T_-}^k(\underline{u}_{\partial T_-}^n - \underline{u}_{T_-|\partial T_-}^n), \underline{\hat{S}}_{\partial T_-}^k(\delta\underline{v}_F))_{\underline{L}^2(\partial T_-)} \\
&= (\boldsymbol{\Pi}_{Q,T_+}^k(\tilde{\boldsymbol{\sigma}}_{T_+}^n)\,\underline{n}_{T_+}, \delta\underline{v}_F)_{\underline{L}^2(\partial T_+)} + \beta(\underline{\hat{S}}_{\partial T_+}^{k*}(\gamma_{\partial T_+}\underline{\hat{S}}_{\partial T_+}^k(\underline{u}_{\partial T_+}^n - \underline{u}_{T_+|\partial T_+}^n)), \delta\underline{v}_F)_{\underline{L}^2(\partial T_+)} \\
&\quad + (\boldsymbol{\Pi}_{Q,T_-}^k(\tilde{\boldsymbol{\sigma}}_{T_-}^n)\,\underline{n}_{T_-}, \delta\underline{v}_F)_{\underline{L}^2(\partial T_-)} + \beta(\underline{\hat{S}}_{\partial T_-}^{k*}(\gamma_{\partial T_-}\underline{\hat{S}}_{\partial T_-}^k(\underline{u}_{\partial T_-}^n - \underline{u}_{T_-|\partial T_-}^n)), \delta\underline{v}_F)_{\underline{L}^2(\partial T_-)} \\
&= (\underline{T}_{T_+|F}^n + \underline{T}_{T_-|F}^n, \delta\underline{v}_F)_{\underline{L}^2(F)}.
\end{aligned}$$

□

3.3.5 Nonlinear solver

The nonlinear problem (3.29)-(3.30) arising at any pseudo-time step $1 \le n \le N$ is solved using a Newton's method. Given $\underline{\hat{u}}_h^{n-1} \in \underline{\hat{U}}_{h,\mathrm{D}}^{k,n-1}$ and $\underline{\tilde{\chi}}_{\mathcal{T}_h}^{n-1} \in \underline{\tilde{\mathcal{X}}}_{\mathcal{T}_h}^{m_Q}$ from the previous pseudo-time step or the initial condition, the Newton's method is initialized by setting $\underline{\hat{u}}_h^{n,0} = \underline{\hat{u}}_h^{n-1}$ up to the update of the Dirichlet condition and $\underline{\tilde{\chi}}_{\mathcal{T}_h}^{n,0} = \underline{\tilde{\chi}}_{\mathcal{T}_h}^{n-1}$. Then, at each Newton's step $i \ge 0$, one computes the incremental displacement $\delta\underline{\hat{u}}_h^{n,i} \in \underline{\hat{U}}_{h,0}^k$ and updates the discrete displacement as $\underline{\hat{u}}_h^{n,i+1} = \underline{\hat{u}}_h^{n,i} + \delta\underline{\hat{u}}_h^{n,i}$. The linear system of equations to be solved is

$$\sum_{T\in\mathcal{T}_h}(\tilde{\mathbb{C}}_{ep}^{n,i} : \boldsymbol{E}_T^k(\delta\underline{\hat{u}}_T^{n,i}), \boldsymbol{E}_T^k(\delta\underline{\hat{v}}_T))_{\boldsymbol{L}_Q^2(T)} + \sum_{T\in\mathcal{T}_h}\beta(\eta_{\partial T}\underline{S}_{\partial T}^k(\delta\underline{\hat{u}}_T^{n,i}), \underline{S}_{\partial T}^k(\delta\underline{\hat{v}}_T))_{\underline{L}^2(\partial T)} = -R_h^{n,i}(\delta\underline{\hat{v}}_h), \tag{3.35}$$

for all $\delta\underline{\hat{v}}_h \in \underline{\hat{U}}_{h,0}^k$, where for all $T \in \mathcal{T}_h$ and all $1 \le j \le m_Q$,

$$(\underline{\tilde{\chi}}_{T,j}^{n,i}(\underline{\xi}_{T,j}), \tilde{\boldsymbol{\sigma}}^{n,i}(\underline{\xi}_{T,j}), \tilde{\mathbb{C}}_{ep}^{n,i}(\underline{\xi}_{T,j})) = \mathrm{SMALL\_PLASTICITY}(\underline{\chi}_{T,j}^{n-1}, \boldsymbol{e}_{T,j}^{n-1}, \boldsymbol{e}_{T,j}^{n,i} - \boldsymbol{e}_{T,j}^{n-1}), \tag{3.36}$$

with $\underline{\chi}_{T,j}^{n-1} = \underline{\tilde{\chi}}_T^{n-1}(\underline{\xi}_{T,j})$, $\boldsymbol{e}_{T,j}^{n,i} = \boldsymbol{E}_T^k(\underline{\hat{u}}_T^{n,i})(\underline{\xi}_{T,j})$, $\boldsymbol{e}_{T,j}^{n-1} = \boldsymbol{E}_T^k(\underline{\hat{u}}_T^{n-1})(\underline{\xi}_{T,j})$, and the residual term

$$\begin{aligned}
R_h^{n,i}(\delta\underline{\hat{v}}_h) &= \sum_{T\in\mathcal{T}_h}(\tilde{\boldsymbol{\sigma}}^{n,i}, \boldsymbol{E}_T^k(\delta\underline{\hat{v}}_T)_{\boldsymbol{L}_Q^2(T)} + \sum_{T\in\mathcal{T}_h}\beta(\eta_{\partial T}\underline{S}_{\partial T}^k(\underline{\hat{u}}_T^{n,i}), \underline{S}_{\partial T}^k(\delta\underline{\hat{v}}_T))_{\underline{L}^2(\partial T)} \\
&\quad - \sum_{T\in\mathcal{T}_h}(\underline{f}^n, \delta\underline{v}_T)_{\underline{L}^2(T)} - \sum_{F\in\mathcal{F}_h^{\mathrm{b,N}}}(\underline{t}_{\mathrm{N}}^n, \delta\underline{v}_F)_{\underline{L}^2(F)}.
\end{aligned} \tag{3.37}$$

The assembling of the stiffness matrix resulting from the left-hand side of (3.35) is local (and thus fully parallelizable). The discrete internal variables $\underline{\tilde{\chi}}_{\mathcal{T}_h}^n \in \underline{\tilde{\mathcal{X}}}_{\mathcal{T}_h}^{m_Q}$ are updated at the end of each pseudo-time step.

For strain-hardening plasticity, the consistent elastoplastic tangent modulus $\mathbb{C}_{ep}$ is symmetric positive-definite. Let us set $\theta_{\mathcal{T}_h,Q} := \min_{(T,j)\in\mathcal{T}_h\times\{1,\ldots,m_Q\}} \theta^{\min}(\tilde{\mathbb{C}}_{ep}(\underline{\xi}_{T,j}))$, where $\theta^{\min}(\mathbb{M})$ denotes the smallest eigenvalue of the symmetric fourth-order tensor $\mathbb{M}$. The following result shows that the linear system (3.35) arising at each Newton's step is coercive under the simple choice $\beta_0 > 0$ on the stabilization parameter for strain-hardening plasticity.

Theorem 3.6 (Coercivity) *Assume that $k_Q \geq 2k$ and that all the quadrature weights are positive. Moreover, assume that the plastic model is strain-hardening. Then, the linear system (3.35) in each Newton's step is coercive for all $\beta_0 > 0$, i.e., there exists $C_{\rm ell} > 0$, independent of h, such that for all $\underline{\hat{v}}_h \in \underline{\hat{U}}_{h,0}^k$,*

$$\sum_{T\in\mathcal{T}_h} (\tilde{\mathbb{C}}_{ep} : \boldsymbol{E}_T^k(\underline{\hat{v}}_T), \boldsymbol{E}_T^k(\underline{\hat{v}}_T))_{\boldsymbol{L}_Q^2(T)} + \sum_{T\in\mathcal{T}_h} \beta(\eta_{\partial T}\underline{S}_{\partial T}^k(\underline{\hat{v}}_T), \underline{S}_{\partial T}^k(\underline{\hat{v}}_T))_{\underline{L}^2(\partial T)}$$
$$\geq C_{\rm ell} \min\left(\beta_0, \frac{\theta_{\mathcal{T}_h,Q}}{2\mu}\right) 2\mu \sum_{T\in\mathcal{T}_h} |\underline{\hat{v}}_T|_{1,T}^2. \quad (3.38)$$

Proof. Since the material is strain-hardening, the consistent elastoplastic tangent modulus is symmetric positive-definite (see line 10 of Algorithm 1). Hence, its smallest eigenvalue is real and positive, so that $\theta_{\mathcal{T}_h,Q} > 0$. Observing that $\boldsymbol{E}_T^k(\underline{\hat{v}}_T) \in \mathbb{P}_d^k(T, \mathbb{R}^{d\times d})$ for all $\underline{\hat{v}}_h \in \underline{\hat{U}}_{h,0}^k$ and that all the quadrature weights are by assumption positive, we infer that

$$\begin{aligned}
&\sum_{T\in\mathcal{T}_h} (\tilde{\mathbb{C}}_{ep} : \boldsymbol{E}_T^k(\underline{\hat{v}}_T), \boldsymbol{E}_T^k(\underline{\hat{v}}_T))_{\boldsymbol{L}_Q^2(T)} \\
&\quad + \sum_{T\in\mathcal{T}_h} \beta(\eta_{\partial T}\underline{S}_{\partial T}^k(\underline{\hat{v}}_T), \underline{S}_{\partial T}^k(\underline{\hat{v}}_T))_{\underline{L}^2(\partial T)} \\
&= \sum_{T\in\mathcal{T}_h} \sum_{j=1}^{m_Q} \omega_{T,j} \boldsymbol{E}_T^k(\underline{\hat{v}}_T)(\underline{\xi}_{T,j}) : \tilde{\mathbb{C}}_{ep}(\underline{\xi}_{T,j}) : \boldsymbol{E}_T^k(\underline{\hat{v}}_T)(\underline{\xi}_{T,j}) \\
&\quad + \sum_{T\in\mathcal{T}_h} \beta(\eta_{\partial T}\underline{S}_{\partial T}^k(\underline{\hat{v}}_T), \underline{S}_{\partial T}^k(\underline{\hat{v}}_T))_{\underline{L}^2(\partial T)} \\
&\geq \sum_{T\in\mathcal{T}_h} \left\{ \theta_{\mathcal{T}_h,Q} \sum_{j=1}^{m_Q} \omega_{T,j} \boldsymbol{E}_T^k(\underline{\hat{v}}_T)(\underline{\xi}_{T,j}) : \boldsymbol{E}_T^k(\underline{\hat{v}}_T)(\underline{\xi}_{T,j}) \right\} \\
&\quad + \sum_{T\in\mathcal{T}_h} \beta(\eta_{\partial T}\underline{S}_{\partial T}^k(\underline{\hat{v}}_T), \underline{S}_{\partial T}^k(\underline{\hat{v}}_T))_{\underline{L}^2(\partial T)} \\
&\geq \min(\theta_{\mathcal{T}_h,Q}, \beta) \sum_{T\in\mathcal{T}_h} \left\{ \|\boldsymbol{E}_T^k(\underline{\hat{v}}_T)\|_{\boldsymbol{L}_Q^2(T)}^2 + \|\eta_{\partial T}^{\frac{1}{2}}\underline{S}_{\partial T}^k(\underline{\hat{v}}_T)\|_{\underline{L}^2(\partial T)}^2 \right\} \\
&= \min(\theta_{\mathcal{T}_h,Q}, \beta) \sum_{T\in\mathcal{T}_h} \left\{ \|\boldsymbol{E}_T^k(\underline{\hat{v}}_T)\|_{\boldsymbol{L}^2(T)}^2 + \|\eta_{\partial T}^{\frac{1}{2}}\underline{S}_{\partial T}^k(\underline{\hat{v}}_T)\|_{\underline{L}^2(\partial T)}^2 \right\}.
\end{aligned}$$

We conclude by using the stability result from Lemma 3.3 and recalling that $\beta = 2\mu\beta_0$.

□

Remark 3.7 *Theorem 3.6 remains valid if the assumption on the strain-hardening plasticity model is replaced by the weaker assumption that $\theta_{\mathcal{T}_h,Q} > 0$ which is verified if the consistent elastoplastic tangent modulus is symmetric positive-definite.*

A reasonable choice of the stabilization parameter appears to be $\beta_0 \geq \max(1, \frac{\theta_{\mathcal{T}_h,Q}}{2\mu})$ because $\beta_0 = 1$ is a natural choice for the linear elasticity problem (see [89]) and the choice $\beta_0 \geq \frac{\theta_{\mathcal{T}_h,Q}}{2\mu}$ allows one to adjust the stabilization parameter if the evolution is plastic. We investigate numerically the choice of β_0 in Section 3.4.6. For the combined linear isotropic and kinematic plasticity model with a von Mises yield criterion, the suggested choice leads to $\beta_0 \geq 1$ since the smallest eigenvalue $\theta_{\mathcal{T}_h,Q}$ is such that $\frac{\theta_{\mathcal{T}_h,Q}}{2\mu} = \frac{\overline{H}}{\mu+\overline{H}} < 1$ for the continuous elastoplastic tangent modulus.

3.3.6 Implementation and static condensation

As is classical with HHO methods [89, 91], and more generally with hybrid approximation methods, the cell unknowns $\delta\underline{u}_T^{n,i}$ in (3.35) can be eliminated locally by using a static condensation (or Schur complement) technique. Indeed, testing (3.35) against the function $((\delta\underline{v}_T\delta_{T,T'})_{T'\in\mathcal{T}_h}, (\underline{0})_{F\in\mathcal{F}_h})$ with Kronecker delta $\delta_{T,T'}$ and $\delta\underline{v}_T$ arbitrary in $\mathbb{P}_d^k(T;\mathbb{R}^d)$, one can express, for all $T \in \mathcal{T}_h$, the cell unknown $\delta\underline{u}_T^{n,i}$ in terms of the local face unknowns collected in $\delta\underline{u}_{\partial T}^{n,i}$. As a result, the static condensation technique allows one to reduce (3.35) to a linear system in terms of the face unknowns only. The reduced system is of size $N_{\mathcal{F}_h} \times d\binom{k+d-1}{d-1}$, where $N_{\mathcal{F}_h}$ denotes the number of mesh faces (Dirichlet boundary faces can be eliminated by enforcing the boundary condition explicitly). In the reduced system, each mesh face is connected to neighbouring faces that share a mesh cell with the face in question. Note that static condensation can improve the condition number of the global stiffness matrix; we refer the reader to [2, Section 4.3] for numerical results in the case of HHO methods for hyperelastic materials. Since the behavior integration is performed at the cell level, the same procedure as for cG methods can be used to deal with a large variety of constitutive laws. One salient example is the standard radial return mapping [193] (see also [14, 201]) that will be used in the numerical examples of Section 3.4 to solve the nonlinear problem in Algorithm 1.

The implementation of HHO methods is realized using the open-source library `DiSk++` [71] which provides generic programming tools for the implementation of HHO methods and is available online[1]. The data structure requires access to faces and cells as in standard dG or HDG codes. The reconstruction and stabilization operators are built locally at the cell level using scaled translated monomials to define the basis functions (see [71, Section 3.2.1] for more details). If memory is not a limiting factor, it is computationally effective to compute these operators once and for all in all the mesh cells, and to re-use them at each Newton's step. The `DiSk++` library employs different quadratures depending on the type of the mesh cells. On segments, standard Gauss quadrature is used. On quadrilaterals and hexahedra, the quadrature is obtained by tensorizing the one-dimensional Gauss quadrature. On triangles and tetrahedra, the Dunavant [108] and Grundmann–Moeller [124] quadratures are used, respectively. Polyhedral cells are split into sub-simplices, and the integration is performed in each sub-simplex separately. The linear algebra operations are realized using the Eigen library and the global linear system (involving face unknowns only) is solved with PardisoLU from the MKL library (alternatively, iterative solvers are also applicable). Finally, the Dirichlet boundary conditions are enforced strongly on the face unknowns as described above.

[1] `https://github.com/wareHHOuse/diskpp`

3.4 Numerical examples

The goal of this section is to evaluate the proposed HHO method on two- and three-dimensional test cases from the literature: a sphere under internal pressure, a quasi-incompressible Cook's membrane, a perforated strip subjected to uniaxial extension, and a cube under compression. We compare the results produced by the HHO method to the analytical solution whenever available or to numerical results obtained using the industrial open-source FEM code `code_aster`[111]. In this case, we consider a quadratic cG formulation, referred to as T2 or Q2 depending on the mesh, and a three-field formulation in which the unknowns are the displacement, the pressure and the volumetric strain fields referred to as UPG [9]; in the UPG method, the displacement field is quadratic, whereas both the pressure and the volumetric strain fields are linear. The T2 and Q2 methods are known to present volumetric locking due to plastic incompressibility, whereas the UPG method is known to be robust but costly. Numerical results obtained using the UPG method on a very fine grid are used as a reference solution whenever an analytical solution is not available. Moreover, we also investigate the behavior of the HHO method on general meshes. The combined linear isotropic and kinematic plasticity model with a von Mises yield criterion described in Section 3.2.4 is used for all the test cases. Strain-hardening plasticity is considered for the two-dimensional cases, i.e., the quasi-incompressible Cook's membrane and the perforated strip under uniaxial traction, whereas perfect plasticity is considered for the three-dimensional cases, i.e., the sphere under internal pressure and the cube under compression. Moreover, for the two-dimensional test cases, we assume additionally a plane strain condition. In the numerical experiments reported in this section, the stabilization parameter is taken to be $\beta = 2\mu$ ($\beta_0 = 1$), and all the quadratures use positive weights. We employ the notation HHO(k) when using face (and cell) polynomials of order k. All the tests are run sequentially on a 3.4 Ghz Intel Xeon processor with 16 Gb of RAM.

3.4.1 Sphere under internal pressure

This first benchmark consists of a sphere under internal pressure for which an analytical solution is known (see [83, Section 7.5.2]). The sphere has an inner radius $R_{in} = 100$ mm and an outer radius $R_{out} = 200$ mm. An internal radial pressure P is imposed. The material parameters adopted are those of [83]: a Young modulus $E = 210$ GPa, a Poisson ratio $\nu = 0.3$, and an initial yield stress $\sigma_{y,0} = 240$ MPa. For symmetry reasons, only one-eighth of the sphere is discretized, and the mesh is composed of 506 tetrahedra, see Fig. 3.2a. The simulation is performed until the limit load corresponding to an internal pressure $P_{lim} \simeq 332.71$ MPa is reached. Numerically, this limit load is reached when the Newton solver stops converging. The load-deflection curves are plotted for HHO methods in Fig. 3.2b showing that both HHO(1) and HHO(2) produce numerical results in very good agreement with the analytical solution. For this test case, we do not expect that HHO(2) will deliver much more accurate solutions than HHO(1) since the geometry is discretized using tetrahedra with planar faces. The computed radial (σ_{rr}) and hoop ($\sigma_{\theta\theta}$) components of the stress tensor are shown in Fig. 3.3 at all the quadrature points for $P = 300$ MPa. For both HHO(1) and HHO(2), the computed stresses are very close to the analytical solution. The error on the stresses is slightly larger for HHO(1) than for HHO(2) near the transition between the elastic zone and the plastic zone (indicated by a dashed line at the radius $R_p = 157.56$ mm). Finally, the trace of the stress tensor is compared for HHO, UPG and cG methods in Fig. 3.4 at all the quadrature points for the limit load. A sign of locking is the presence of strong oscillations of the trace of the stress tensor. Thus, we notice that the quadratic element T2 locks, whereas HHO and UPG do not present any sign of locking and produce results that

are very close to the analytical solution.

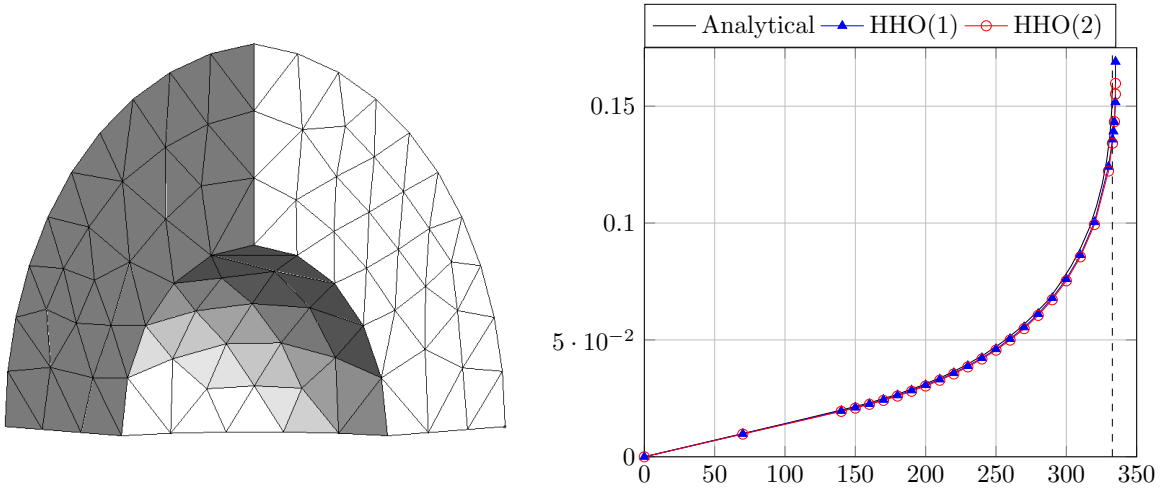

(a) (b)

Figure 3.2: Sphere under internal pressure: (a) Mesh in the reference configuration composed of 506 tetrahedra. (b) Average radial displacement at the outer surface (mm) vs. applied pressure (MPa); the dashed line indicates the theoretical limit load.

3.4.2 Quasi-incompressible Cook's membrane

We consider the quasi-incompressible Cook's membrane problem which is a well known bending-dominated test case (see for example [194, Section 6.2.3] or [60]). It consists of a tapered panel, clamped on one side, and subjected to a vertical load $F_y = 1.8$ N on the opposite side, as shown in Fig. 3.5a. The material parameters are a Young modulus $E = 70$ MPa, a Poisson ratio $\nu = 0.4999$, an initial yield stress $\sigma_{y,0} = 0.243$ MPa, an isotropic hardening modulus $H = 0.135$ MPa and a kinematic hardening modulus $K = 0$ MPa. The simulation is performed in twenty uniform increments of the load and with a sequence of refined quadrangular meshes such that each side contains 2^N edges, $1 \leq N \leq 7$. The vertical displacement of the point A is plotted in Fig. 3.5b for the HHO(1), HHO(2), cG, and UPG methods. As expected when comparing the number of degrees of freedom, the quadratic cG formulation Q2 has the slower convergence, HHO(1) converges slightly faster than UPG, and HHO(2) outperforms all the other methods. Moreover, we show in Fig. 3.6 the trace of the stress tensor. The cG formulation Q2 presents strong oscillations that confirm the presence of volumetric locking, contrary to the HHO and UPG methods which deliver similar and smooth results.

3.4.3 Perforated strip subjected to uniaxial extension

We consider a strip of width $2L = 200$ mm and height $2H = 360$ mm. The strip is perforated in its middle by a circular hole of radius $R = 50$ mm, and is subjected to a uniaxial extension $\delta = 5$ mm at its top and bottom ends. For symmetry reasons, only a quarter of the strip is discretized. The geometry and the boundary conditions are presented in Fig. 3.7a. This problem is frequently used in the literature, see for example [30, 13, 14, 201]. The material parameters are a Young modulus $E = 70$ MPa, a Poisson ratio $\nu = 0.3$, an initial yield stress $\sigma_{y,0} = 0.8$ MPa, an isotropic hardening modulus $H = 10$ MPa, and a kinematic hardening

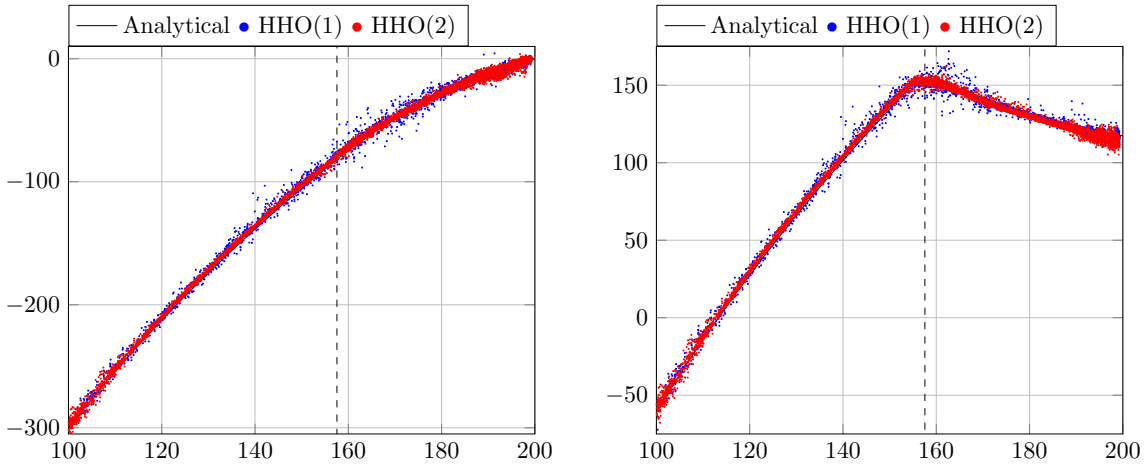

(a) σ_{rr} (MPa) vs. r (mm) (b) $\sigma_{\theta\theta}$ (MPa) vs. r (mm)

Figure 3.3: Sphere under internal pressure: radial (left) and hoop (right) components of the stress tensor (MPa) vs. r (mm) for HHO(1) and HHO(2) at all the quadrature points and for $P = 300$ MPa (the dashed line corresponds to the transition between the plastic zone and the elastic zone).

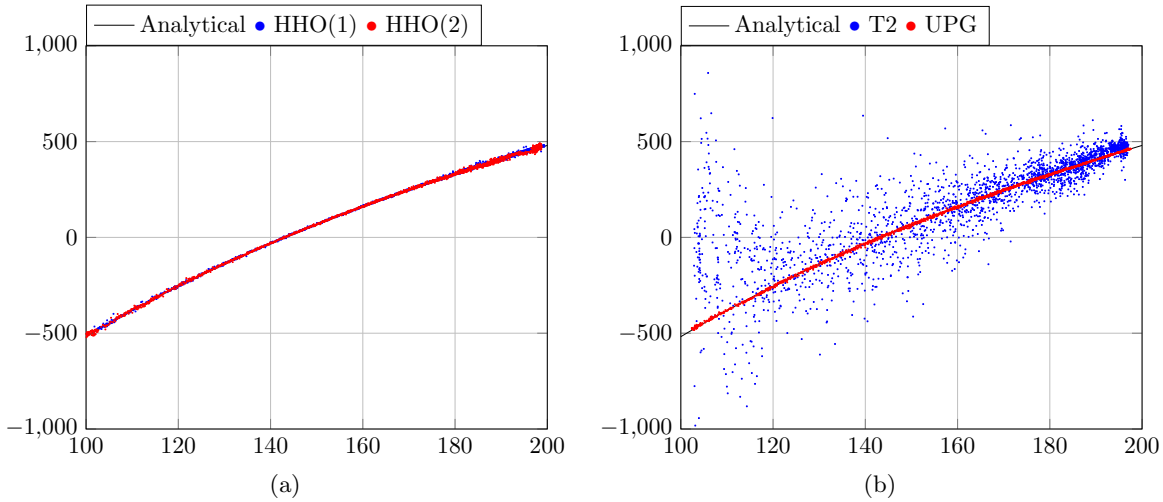

(a) (b)

Figure 3.4: Sphere under internal pressure: trace of the stress tensor (MPa) vs. r (mm) at all the quadrature points and for the limit load; (a) HHO(1) and HHO(2), (b) T2 and UPG.

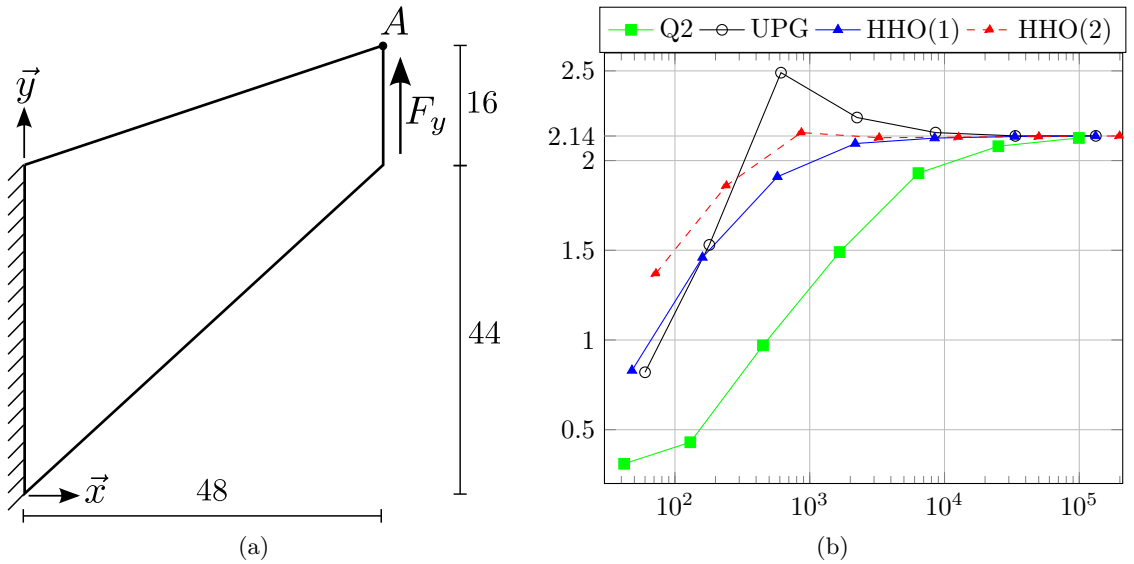

Figure 3.5: Quasi-incompressible Cook's membrane: (a) Geometry and boundary conditions (dimensions in mm). (b) Convergence of the vertical displacement of the point A (in mm) vs. the number of degrees of freedom for Q2, UPG, HHO(1), and HHO(2).

modulus $K = 5$ MPa. The relative displacement errors $err = (u - u_{\text{ref}})/u_{\text{ref}}$ versus the number of degrees of freedom are plotted for the points A and B (indicated in Fig. 3.7a), and for different triangular meshes in Fig. 3.8 (the reference solution u_{ref} is computed with the UPG method and a mesh composed of 37,032 triangles leading to 149,206 degrees of freedom). The relative errors are similar for UPG and HHO(1), and the errors are lower for HHO(2) for the same number of degrees of freedom. Finally, the equivalent plastic strain p is shown in Fig. 3.7b for UPG and HHO(2) on a triangular mesh. We remark that the results are similar and that there is no sign of locking.

3.4.4 Compression of a cube

This benchmark comes from [9, Section 5.2]. It consists of a rectangular block of length and width $2L = 20$ mm and height $H =$ 10mm. The lateral faces are free and the bottom face is clamped. Only one quarter is discretized owing to symmetries, see Fig. 3.9a. The material parameters are a Young modulus $E = 200$ GPa, a Poisson ratio $\nu = 0.3$, and an initial yield stress $\sigma_{y,0} = 150$ MPa. A vertical pressure $P = 350$ MPa is applied in 30 uniform increments in the part of the upper surface indicated in Fig. 3.9a. The trace of the stress tensor is plotted in Fig. 3.9b for UPG and HHO(1) on a tetrahedral mesh. Both methods do not present oscillations, contrary to the cG formulation (not shown for brevity).

3.4.5 Polyhedral meshes

In the previous sections, the proposed HHO method has been tested on simplicial and hexahedral meshes so as to be able to compare it to the UPG method which only supports these types of meshes. Our goal now is to illustrate the fact that the HHO method supports general meshes with possibly non-matching interfaces. For our test cases, the polyhedral meshes are generated from quadrangular or hexahedral meshes by removing the common face for some pairs of neighbouring cells and then merging the two cells in question (about 30% of the cells are merged) thereby producing non-matching interfaces materialized by hanging nodes for a

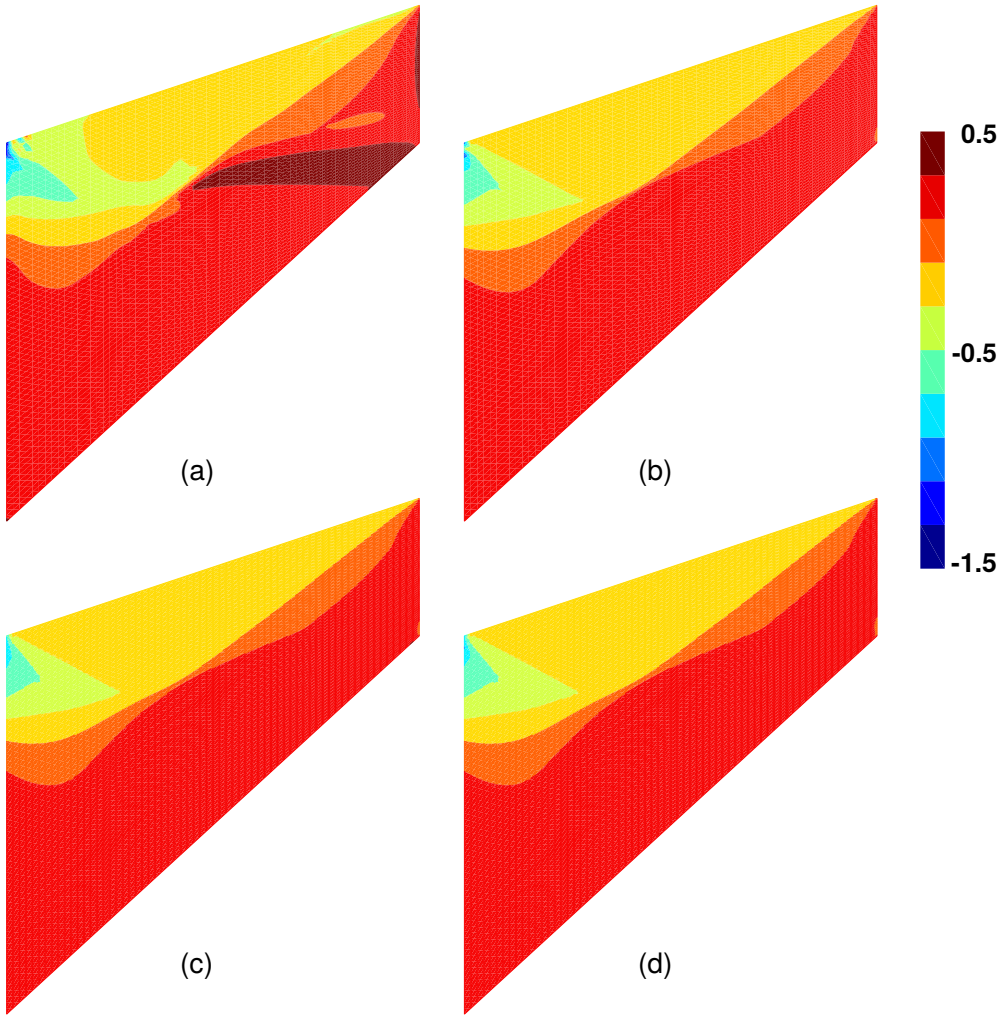

Figure 3.6: Quasi-incompressible Cook's membrane: trace of the stress tensor (MPa) on the reference configuration for a 64×64 quadrangular mesh; (a) Q2 (b) UPG (c) HHO(1) (d) HHO(2).

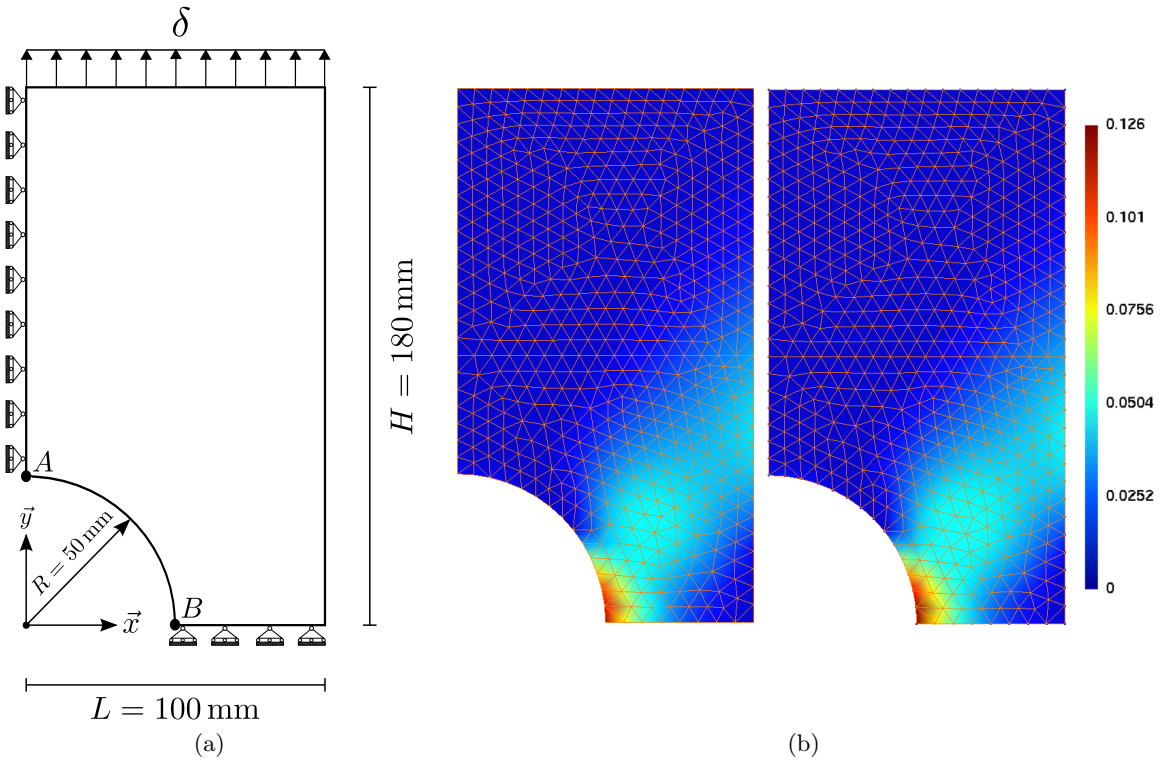

(a) (b)

Figure 3.7: Perforated strip: (a) Geometry. (b) Equivalent plastic strain p for a triangular mesh with UPG (left) and HHO(2) (right); there are 5,542 degrees of freedom for UPG and 9,750 for HHO(2).

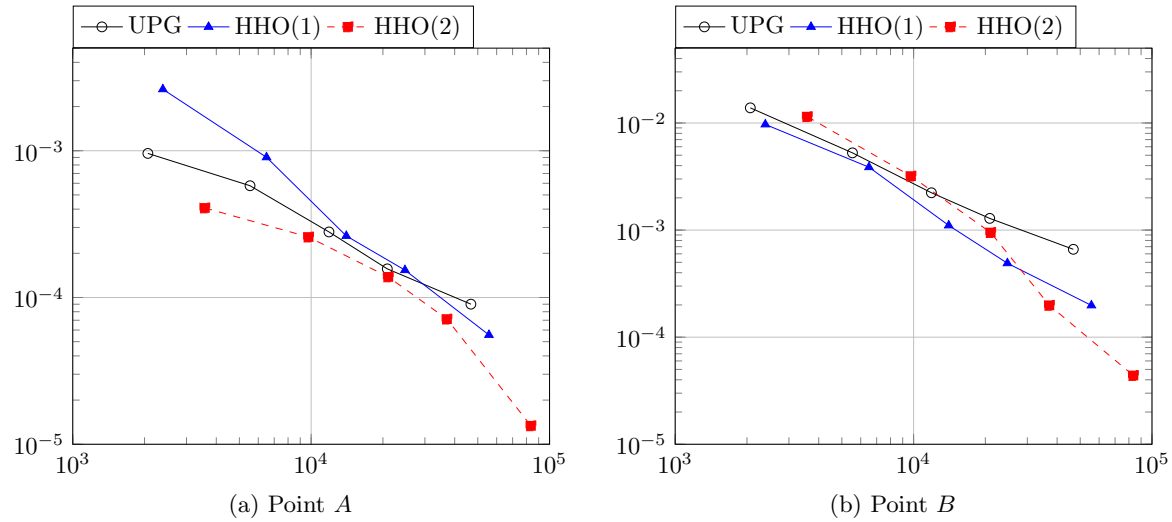

(a) Point A (b) Point B

Figure 3.8: Perforated strip: Relative displacement error at the points A (left) and B (right) vs. the number of degrees of freedom for UPG, HHO(1) and HHO(2).

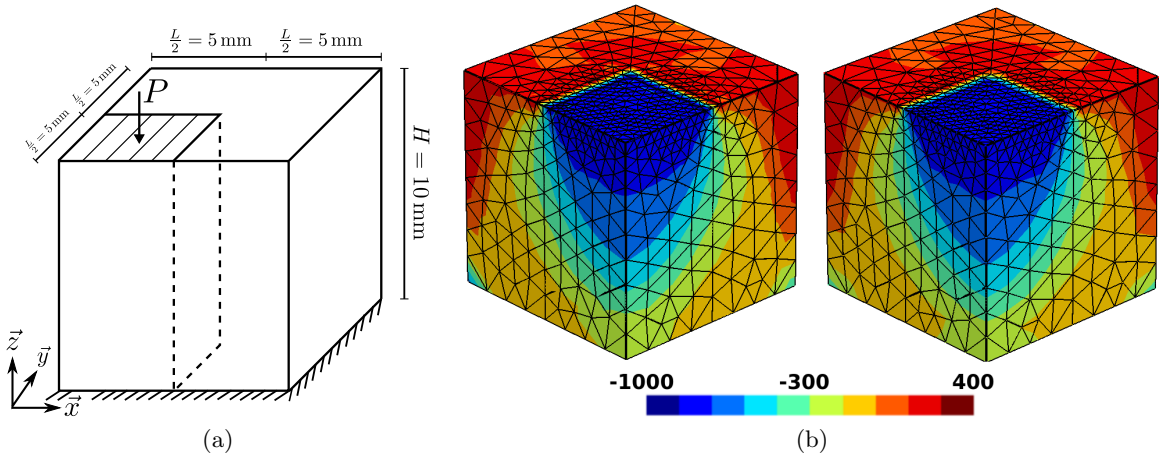

(a) (b)

Figure 3.9: Compression of a cube: (a) Geometry. (b) Trace of the stress tensor on the reference configuration (MPa) with UPG (left) and HHO(1) (right) on a tetrahedral mesh; there are 25,556 degrees of freedom for UPG and 15,947 for HHO(1).

significant portion of the mesh cells. In two dimensions, a random moving of the internal nodes is additionally applied in such a way that the cells remain star-shaped with respect to their barycenter. We consider the last two benchmarks presented above, i.e., the perforated strip (see Section 3.4.3) and the compressed cube (see Section 3.4.4). Concerning the perforated strip, we show an example of a polyhedral mesh in Fig. 3.10a and the equivalent plastic strain for HHO(2) on a triangular mesh and the polygonal mesh in Fig. 3.10b. The results agree very well on the two meshes. For the compression of the cube, we use a polyhedral mesh which is generated as above from a hexahedral mesh by removing the common face for some pairs of neighboring cells (see Fig. 3.11a for the mesh; note that a random moving of the internal nodes is not applied here to avoid nonplanar faces). We compare in Fig. 3.11b the trace of stress tensor for HHO(1) on a tetrahedral mesh and the polyhedral mesh. The results agree very well on the two meshes, and there is no sign of volumetric locking. These numerical experiments indicate that, as predicted by the theory, the HHO method supports general meshes both in two and three dimensions.

3.4.6 Variants of the HHO method

Once the polynomial degree k attached to faces has been fixed, there are three different possibilities for the polynomial degree l attached to cells, namely $l \in \{k-1, k, k+1\} \cap \mathbb{N}$ (see [74] for diffusive problems). Nevertheless, for $k = 1$, the choice $l = 0$ is not possible for linear elasticity because of the rigid body motions. In this appendix, we focus on the case $k = 2$ and we compare the variants $l \in \{1, 2, 3\}$ for the cell degrees of freedom. We use the notation HHO(2;l) and observe that the choice $l = 2$ corresponds to the results presented above. For the local operators $\boldsymbol{E}_T^k, \underline{D}_T^{k+1}$, and $\underline{S}_{\partial T}^k$, the only difference is that we replace $\hat{\underline{v}}_T \in \hat{\underline{U}}_T^k$ by $\hat{\underline{v}}_T \in \hat{\underline{U}}_T^{k,l} := \mathbb{P}_d^l(T;\mathbb{R}^d) \times \mathbb{P}_{d-1}^k(\mathcal{F}_{\partial T};\mathbb{R}^d)$. Moreover, for $l = k+1$, we consider the simpler expression for $\underline{S}_{\partial T}^k : \hat{\underline{U}}_T^{k,k+1} \to \mathbb{P}_{d-1}^k(\mathcal{F}_{\partial T},\mathbb{R}^d)$ such that for all $\hat{\underline{v}}_T \in \hat{\underline{U}}_T^{k,k+1}$, $\underline{S}_{\partial T}^k(\hat{\underline{v}}_T) = \underline{\Pi}_{\partial T}^k(\underline{v}_{\partial T} - \underline{v}_{T|\partial T})$. Lemma 3.3, Lemma 3.5, and Theorem 3.6 remain true (up to minor adaptations).

We compare these HHO variants on the first two benchmarks: the sphere under internal pressure (see Section 3.4.1) and the quasi-incompressible Cook's membrane (see Section 3.4.2). For the sphere benchmark, the computed radial (σ_{rr}) and hoop ($\sigma_{\theta\theta}$) components

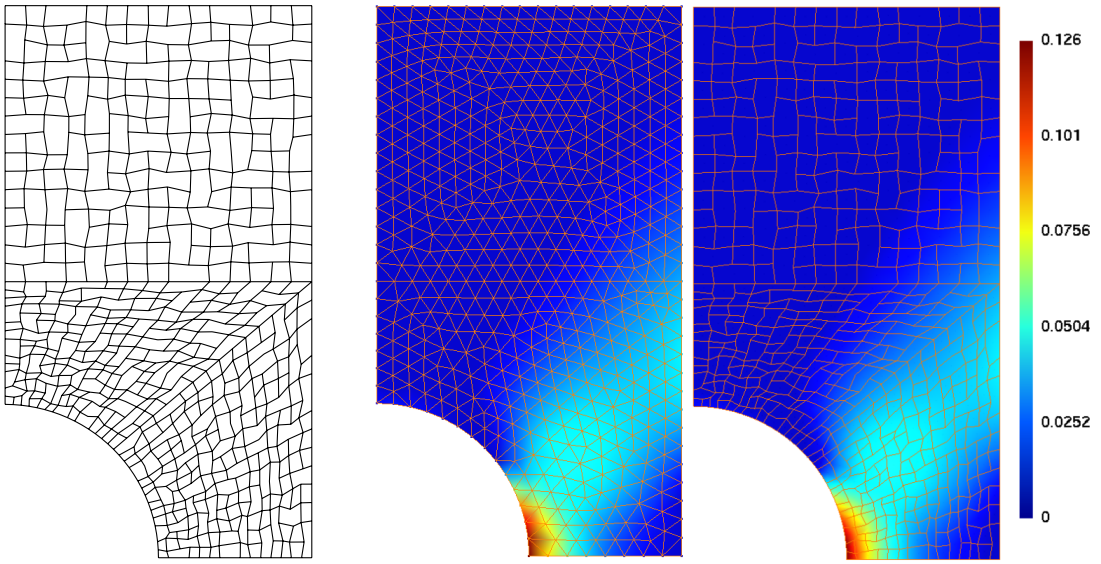

(a) (b)

Figure 3.10: Perforated strip: (a) Example of a polygonal mesh composed of 536 cells. (b) Equivalent plastic strain p with HHO(2) for a triangular mesh (left) and a polygonal mesh (right); there are 9,750 dofs for the triangular mesh and 7,590 dofs for the polygonal mesh.

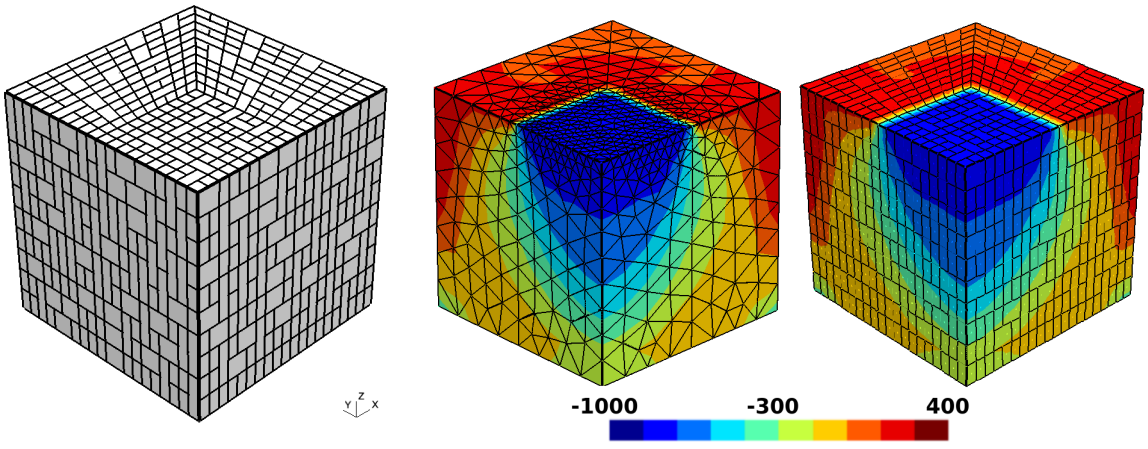

(a) (b)

Figure 3.11: Compression of a cube: (a) Example of a polyhedral mesh composed of 2,243 cells. (b) Trace of the stress tensor on the initial configuration (in MPa) for HHO(1) on a tetrahedral mesh (left) and on the polyhedral mesh (right); there are 31,941 dofs for the tetrahedral mesh and 75,261 dofs for the polyhedral mesh.

of the stress tensor are shown in Fig. 3.12 at all the quadrature points for $P = 300$ MPa for HHO(2;1) and HHO(2;3). The results are in agreement with those obtained with HHO(2;2). Let us now compare the time spent to solve the non-linear problem when using HHO(2,l)

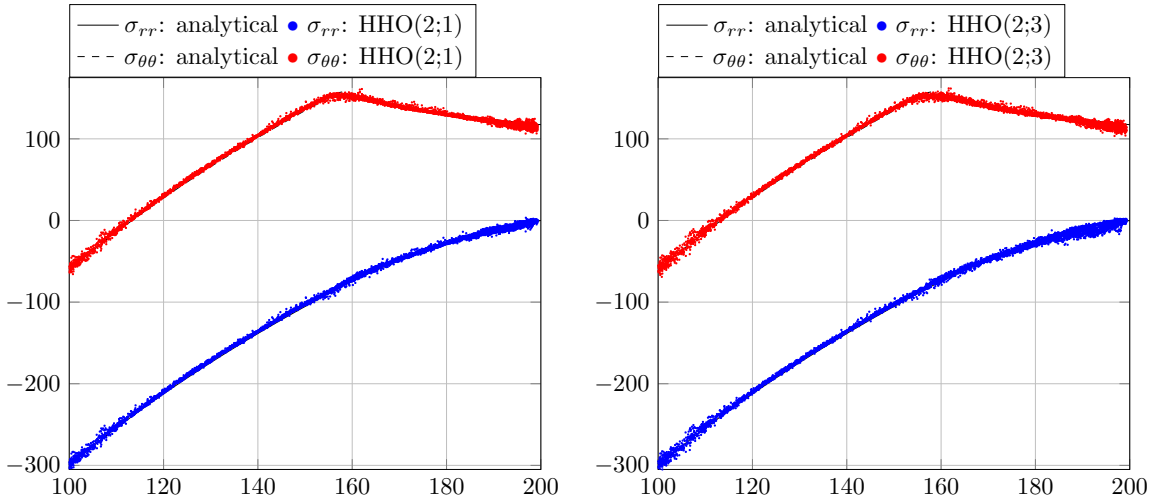

(a) HHO(2;1) (b) HHO(2;3)

Figure 3.12: Sphere under internal pressure: σ_{rr} (MPa) and $\sigma_{\theta\theta}$ (MPa) vs. r (mm) for HHO(2;1) and HHO(2;3) methods at all the quadrature points for $P = 300$ MPa.

with $l \in \{1, 2, 3\}$ and $\beta = 2\mu$ ($\beta_0 = 1$). The assembly time to build the local contributions to the global stiffness matrix is divided into three parts: one part, denoted `Gradrec`, to reconstruct the strain and build the global system; a second part, denoted `Stabilization`, to build the stabilization operator (including the time to build the displacement reconstruction, see (3.20)); and a last part, denoted `Static Condensation`, to perform the static condensation. The solver time, which corresponds to solving the global linear system, is denoted `Solver`. These times are computed after summation over all the Newton's iterations and are normalized by the total cost associated with HHO(2;2). In Fig. 3.13a, we provide an assessment of the cost on a fixed mesh with 506 tetrahedra. We observe that the difference between HHO(2;2) and HHO(2;3) is not really important; in fact, the time that HHO(2;3) spends to reconstruct the less expensive stabilization is compensated by a larger number of Newton's iterations. The HHO(2;1) variant turns out to be the most efficient (around 20% less CPU time than HHO(2;2)); indeed it needs less Newton's iterations and the cost of a single Newton's iteration is the cheapest. In Fig. 3.13b, we report the total number of Newton's iterations normalized by the result for HHO(2;2) and $\beta_0 = 1$ versus β_0. On the one hand, we remark that β_0 has a significant influence on the number of Newton's iterations if $\beta_0 \lesssim 1$ and on the other hand, the different variants need the same number of Newton's iterations to converge if $\beta_0 \gtrsim 10$. Note that this experiment is particularly challenging since we are considering here perfect plasticity for which the stability result from Theorem 3.6 is not applicable.

We repeat the above experiments with the Cook's membrane problem with strain hardening plasticity so that the stability result of Theorem 3.6 holds true with $\theta_{\mathcal{T}_h,Q} \approx 0.25$. In Fig. 3.14a, the CPU times on a 64×64 quadrangular mesh are reported. Here, HHO(2;3) turns out to be the most efficient variant (around 22% less CPU time than HHO(2,2)); indeed it needs the same number of Newton's iterations and the computation of the stabilization operator is faster than for the other variants. Nevertheless, these differences in terms of total

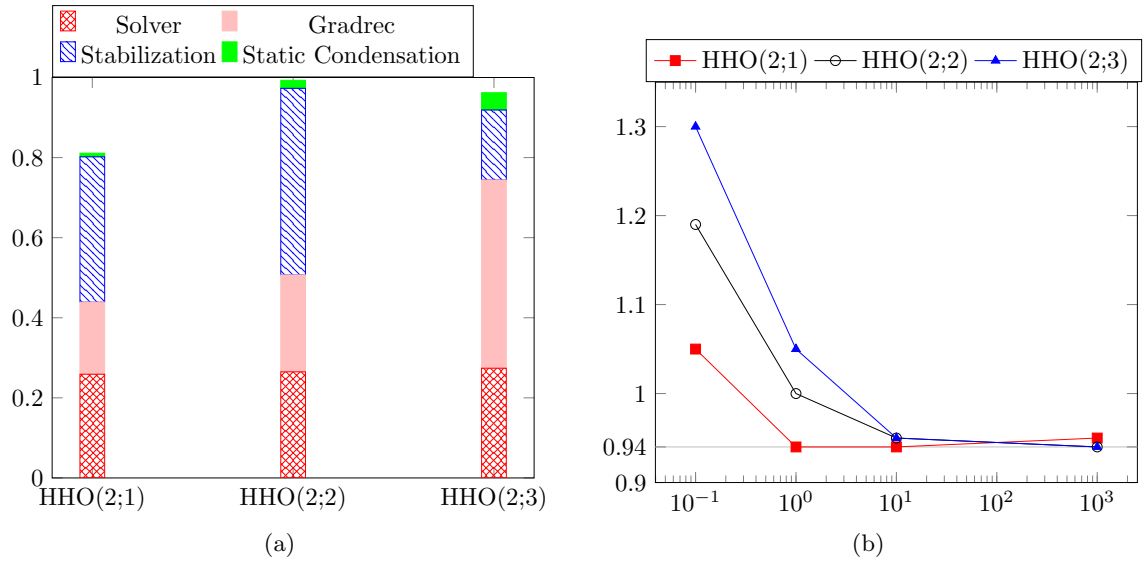

Figure 3.13: Sphere under internal pressure: (a) Comparison of normalized CPU times for HHO(2;l), $l \in \{1, 2, 3\}$. (b) Total number of Newton's iterations versus β_0 normalized by the result for HHO(2;2) and $\beta_0 = 1$.

CPU times are less noticeable in two dimensions than in three dimensions since the computations are less intensive. In Fig. 3.14b, we plot the number of Newton's iterations normalized by the result for HHO(2;2) and $\beta_0 = 1$ versus β_0. As above, HHO(2;1) is the variant that depends the least on β_0 but this behavior is less pronounced than for the sphere benchmark. In addition, whatever variant is used, if we take $\beta_0 = \frac{\theta_{\mathcal{T}_h,Q}}{2\mu} \approx 0.005$, the Newton's method needs more than 500 iterations to converge (compared to 108 iterations for HHO(2;2) and $\beta_0 = 1$). A first conclusion is that it seems reasonable to take $\beta_0 \in [1, 100]$ since the number of Newton's iterations is lower and the condition number does not increase too much. A second conclusion is that it seems preferable to use HHO(2;1) than HHO(2;2) or HHO(2;3) since HHO(2;1) is less sensitive to the choice of β_0.

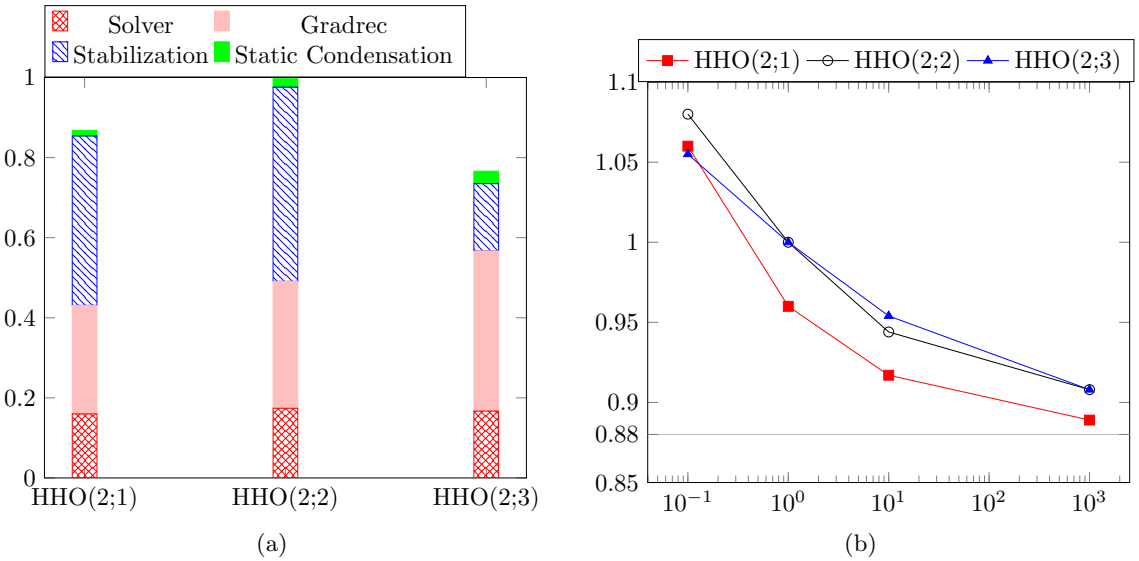

Figure 3.14: Quasi-incompressible Cook's membrane: (a) Comparison of normalized CPU times for HHO(2;l), $l \in \{1, 2, 3\}$. (b) Number of Newton's iteration versus β_0 normalized by the result for HHO(2;2) and $\beta_0 = 1$.

3.5 Conclusion

We have devised and evaluated numerically a Hybrid High-Order method to approximate associative plasticity problems in the small deformation regime. The method shows a robust behavior for the perfect plasticity model as well as for the combined linear isotropic and kinematic hardening model and produces accurate solutions with a moderate number of degrees of freedom. In particular, as mixed methods, the HHO method prevents volumetric locking due to plastic incompressiblity, but with less unknowns than mixed methods for the same accuracy. Moreover, the HHO method supports general meshes with possibly non-matching interfaces. This work can be pursued in several directions. One could use a non-local plasticity model, as for example a strain-gradient plasticity model, to take into account scale-dependent effects as in [97]. Furthermore, error estimates can be investigated, possibly by taking inspiration from [11, 97], where other discretization methods are analyzed for plasticity problems. Finally, the extension of the present HHO method to elastoplasticity in finite deformations is the subject of following chapter.

CHAPTER 4

A HYBRID HIGH-ORDER METHOD FOR FINITE ELASTOPLASTIC DEFORMATIONS WITHIN A LOGARITHMIC STRAIN FRAMEWORK

Abstract. We devise and evaluate numerically a Hybrid High-Order (HHO) method for finite plasticity within a logarithmic strain framework. The HHO method uses as discrete unknowns piecewise polynomials of order $k \geq 1$ on the mesh skeleton, together with cell-based polynomials that can be eliminated locally by static condensation. The HHO method leads to a primal formulation, supports polyhedral meshes with non-matching interfaces, is free of volumetric locking, the integration of the constitutive law is performed only at cell-based quadrature nodes, and the tangent matrix in Newton's method is symmetric. Moreover, the principle of virtual work is satisfied locally with equilibrated tractions. Various two- and three-dimensional benchmarks are presented, as well as comparisons against known solutions obtained with an industrial software using conforming and mixed finite elements.

This chapter is based on a paper published online in International Journal for Numerical Methods in Engineering entitled "*A Hybrid High-Order method for finite plasticity within a logarithmic strain framework*" [4].

Sommaire

4.1 Introduction

Modelling plasticity, particularly in the regime of finite deformations, is of a major importance in industrial applications since this is one of the main nonlinearites that can be encountered in nonlinear solid mechanics. Moreover, finite elastoplastic deformations have a major influence on the life time of a mechanical structure. The present contribution is an extension to the finite strain regime of the Hybrid High-Order (HHO) method for incremental associative plasticity with small deformations [3]. This extension hinges on a logarithmic strain framework [167] for anisotropic finite elastoplasticity. This framework provides a natural extension of small elastoplastic deformations to finite elastoplastic deformations by means of purely geometric transformations. Indeed, the weak form of the plasticity problem is derived from the minimization of an energy functional based on an incremental pseudo-energy density.

The present work aims at addressing the following important issues. Firstly, the incompressibility of the plastic deformations generally leads to volumetric locking when employing a continuous Galerkin (cG) approximation based on low-order H^1-conforming finite elements. In these methods, only the displacement field is approximated globally, whereas the variables associated with the plastic behavior are computed locally in each mesh cell (typically at quadrature nodes). A way to circumvent the volumetric locking is to use high-order H^1-conforming finite elements or NURBS for small [113] and finite [112] elastoplastic deformations. Therein, the displacement is still the only field which is approximated globally. However, the resulting discrete problem is more costly to solve because of the larger support of the basis functions. Another possible way to prevent volumetric locking is to introduce additional global unknowns as in the Enhanced Assumed Strain (EAS) methods [191] and in mixed methods [9, 6, 82, 196] on simplicial or hexahedral meshes (the variables associated with the plastic behavior are still computed locally). However, the introduction of additional globally coupled unknowns generally increases the cost of building and solving the discrete problem. Moreover, devising mixed methods on polyhedral meshes with non-matching interfaces is a delicate question. On the positive side, cG methods as well as EAS and mixed methods require to perform the integration of the constitutive law only at the quadrature nodes in the mesh cells. Another class of methods free of volumetric locking are discontinuous Galerkin (dG) methods. We mention in particular [117, 116, 115, 174] for hyperelasticity. Interior penalty dG methods have been developed for classical plasticity with small [131, 162] and finite [163] deformations, and for gradient plasticity with small [98, 97] and finite [166] deformations. However, dG methods from the literature generally require to perform the integration of the constitutive law also at additional quadrature nodes located at the mesh faces. Moreover, if the plasticity problem is solved using a Newton's method, which is often

the case, the tangent matrix from the dG formulation is generally non-symmetric owing to the nonlinear nature of the consistency term. Thus, the solving cost can increase significantly, particularly with iterative solvers (the memory requirement can become important for direct solvers). We also mention the lowest-order Virtual Element Method (VEM) for inelastic problems with small deformations [30] (and its two-dimensional higher-order extension [13]), whereas the case of finite deformations is treated in [209, 143], still in the lowest-order case. We also mention the recent study of low-order hybrid dG methods with conforming traces [212] and the hybridizable weakly conforming Galerkin method with nonconforming traces in the context of linear [151] and nonlinear [26] solid mechanics. Moreover, finite volume methods for plasticity problems have been developped for small deformations [202] and for large deformations [25, 47].

In the present work, we devise and evaluate numerically a HHO method for finite plasticity within a logarithmic strain framework. HHO methods have been introduced a few years ago for diffusion problems [91] and for linear elasticity problems [89]. Since then, the development of HHO methods has received a vigorous interest. Examples include in solids mechanics Biot's problem [32], nonlinear elasticity [40] and associative plasticity [3] with small deformations, and hyperelasticity with finite deformations [2], and in fluid mechanics, the incompressible Stokes equations [93], the steady incompressible Navier–Stokes equations [94], and viscoplatic flows with yield stress [49]. The discrete unknowns in HHO methods in computational mechanics are face-based vector-valued polynomials of arbitrary order $k \geq 1$ on the mesh skeleton. Cell-based vector-valued polynomials are also introduced for the stability and approximation properties of the method. These cell-based vector-valued polynomials are eliminated locally by using the well-known static condensation technique (based on a local Schur complement).

The devising of HHO methods hinges on two key ideas: (i) a local reconstruction operator acting on the face and cell unknowns that builds a tensor-valued polynomial representing the displacement gradient in the polynomial space $\mathbb{P}_d^k(T;\mathbb{R}^{d\times d})$, where T is a generic mesh cell and d is the space dimension [40, 2]; (ii) a local stabilization operator that weakly enforces on each mesh face the consistency between the local face unknowns and the trace of the cell unknowns [91, 89]. HHO methods offer several advantages: (i) general meshes (including fairly general polyhedral mesh cells and non-matching interfaces) are supported; (ii) a local formulation using equilibrated fluxes is available; (iii) computational benefits owing to the static condensation of the cell unknowns and the higher-order convergence rates, and (iv) the construction is dimension-independent. Moreover, an open-source implementation of HHO methods, the `DiSk++` library, is available using generic programming tools [71]. In computational mechanics, other salient features of HHO methods are: (i) a displacement-based formulation avoiding the need to introduce additional globally coupled unknowns; (ii) absence of volumetric locking; (iii) the integration of the constitutive law only at the cell quadrature nodes; and (iv) the tangent matrix arising in the Newton's method is symmetric. Furthermore, HHO methods have been bridged [74] to Hybridizable Discontinuous Galerkin (HDG) methods [76] and to nonconforming Virtual Element Methods (ncVEM) [18]. The essential difference with HDG methods is that the HHO stabilization is different so as to deliver $O(h^{k+1})$ energy-error estimates for linear model problems with smooth solutions on general meshes, where h is the mesh-size. Concerning ncVEM, the devising viewpoint is different (ncVEM considers the computable projection of virtual functions instead of a reconstruction operator), whereas the stabilization achieves similar convergence rates as HHO but is written differently. We also notice that, to our knowledge, HDG methods have not yet been devised for finite elastoplasticity problems (in contrast to hyperelasticity problems [147, 171]). Owing to the close links between HHO and HDG methods, this work can thus be seen as the first

HDG-like method for plasticity problems in finite deformations.

This paper is organized as follows: in Section 2, we present the plasticity model within a logarithmic strain framework and the weak formulation of the governing equations. In Section 3, we devise the HHO method and highlight some of its theoretical aspects. In Section 4, we investigate numerically the HHO method on two- and three-dimensional benchmarks from the literature, and we compare our results to analytical solutions whenever available and to numerical results obtained using established cG and mixed methods implemented in the open-source industrial software `code_aster`[111].

4.2 Plasticity model

In what follows, we write v or V for scalar-valued fields, $\underline{v}$ or $\underline{V}$ for vector-valued fields, $\boldsymbol{v}$ or $\boldsymbol{V}$ for second-order tensor-valued fields, and $\mathbb{V}$ for fourth-order tensor-valued fields. Contrary to the hyperelastic model, the elastoplastic model is based on the assumption that the deformations are no longer reversible.

4.2.1 Kinematics

Let $\mathcal{B}_0$ be an elastoplastic material body that occupies the domain Ω_0 in the reference configuration. Here, $\Omega_0 \subset \mathbb{R}^d$, $d \in \{2,3\}$, is a bounded connected polyhedral domain with Lipschitz boundary $\Gamma := \partial\Omega_0$ decomposed in the two relatively open subsets Γ_{N} and Γ_{D}, where a Neumann and a Dirichlet condition is enforced respectively, and such that $\overline{\Gamma_{\mathrm{N}}} \cup \overline{\Gamma_{\mathrm{D}}} = \Gamma$, $\Gamma_{\mathrm{N}} \cap \Gamma_{\mathrm{D}} = \emptyset$, and Γ_{D} has positive Hausdorff-measure (so as to prevent rigid-body motions). Due to the deformation, a point $\underline{X} \in \Omega_0$ is mapped to a point $\underline{x}(t) = \underline{X} + \underline{u}(\underline{X}, t)$ in the equilibrium configuration, where $\underline{u} : \Omega_0 \times I \to \mathbb{R}^d$ is the displacement mapping. The deformation gradient $\boldsymbol{F}(\underline{u}) = \boldsymbol{I} + \boldsymbol{\nabla}_X \underline{u}$ takes values in $\mathbb{R}^{d\times d}_+$ which is the set of $\mathbb{R}^{d\times d}$-matrices with positive determinant. In what follows, the gradient and divergence operators are taken with respect to the coordinate $\underline{X}$ of the reference configuration (we use the subscript X to indicate it).

We use the logarithmic strain framework [167] developed for anisotropic finite elastoplasticity. Hence, it allows us to define the logarithmic strain tensor $\boldsymbol{E} \in \mathbb{R}^{d\times d}_{\mathrm{sym}}$ as

$$\boldsymbol{E} := \frac{1}{2}\ln(\boldsymbol{F}^T\boldsymbol{F}). \tag{4.1}$$

This measure of the deformations $\boldsymbol{E}$ is objective. Moreover, if the eigenvectors of $\boldsymbol{E}$ do not change with time (the eigenvalues may change in time), then $\dot{\boldsymbol{E}} = \dot{\boldsymbol{U}}\boldsymbol{U}^{-1}$, where $\boldsymbol{U} \in \mathbb{R}^{d\times d}_{\mathrm{sym}}$ is the right stretch tensor from the polar decomposition $\boldsymbol{F} = \boldsymbol{R}\boldsymbol{U}$. The plastic deformations are measured by means of the plastic logarithmic strain tensor $\boldsymbol{E}^p \in \mathbb{R}^{d\times d}_{\mathrm{sym}}$. We assume the following additive decomposition of the logarithmic strain tensor $\boldsymbol{E}$:

$$\boldsymbol{E}^e := \boldsymbol{E} - \boldsymbol{E}^p, \tag{4.2}$$

where $\boldsymbol{E}^e \in \mathbb{R}^{d\times d}_{\mathrm{sym}}$ is the elastic logarithmic strain tensor. Finally, the plastic strains are assumed to be incompressible, i.e.

$$\operatorname{trace} \boldsymbol{E}^p = 0. \tag{4.3}$$

4.2.2 Constitutive logarithmic strain model

In what follows, we place ourselves within the framework of generalized standard materials initially introduced in [127] and further developed in [159]. Moreover, the plasticity model is

assumed to be strain-hardening (or perfect) and rate-independent, i.e., the time and the speed of the deformations have no influence on the strains. For this reason, only the incremental plasticity problem is considered. The local material state is described by the logarithmic strain tensor $\boldsymbol{E} \in \mathbb{R}^{d\times d}_{\text{sym}}$, the plastic logarithmic strain tensor $\boldsymbol{E}^p \in \mathbb{R}^{d\times d}_{\text{sym}}$, and a finite collection of internal variables $\underline{\alpha} := (\alpha_1, \cdots, \alpha_m) \in \mathbb{R}^m$, which contain typically at least the equivalent plastic strain p, see Sect. 4.2.5 for a simple example or [159] for more detailed examples. For simplicity, we denote $\underline{\chi} := (\boldsymbol{E}^p, \underline{\alpha}) \in \underline{\mathcal{X}}$ the generalized internal variables, where the space of the generalized internal variables is

$$\underline{\mathcal{X}} := \left\{ \underline{\chi} = (\boldsymbol{E}^p, \underline{\alpha}) \in \mathbb{R}^{d\times d}_{\text{sym}} \times \mathbb{R}^m \mid \operatorname{trace}(\boldsymbol{E}^p) = 0 \right\}. \tag{4.4}$$

Moreover, we assume that there exists a Helmholtz free energy $\psi : \mathbb{R}^{d\times d}_{\text{sym}} \times \mathbb{R}^m \to \mathbb{R}$ acting on the pair $(\boldsymbol{E}^e, \underline{\alpha})$ and satisfying the following hypothesis.

Hypothesis 4.1 (Helmholtz free energy) *ψ can be decomposed additively into an elastic and a plastic part as follows:*

$$\psi(\boldsymbol{E}^e, \underline{\alpha}) = \psi^e(\boldsymbol{E}^e) + \psi^p(\underline{\alpha}). \tag{4.5}$$

where the function ψ^p is strictly convex and the function ψ^e is polyconvex.

Following the second principle of thermodynamics, the logarithmic stress tensor $\boldsymbol{T} \in \mathbb{R}^{d\times d}_{\text{sym}}$ and the thermodynamic forces $\underline{q} \in \mathbb{R}^m$ are derived from ψ as follows:

$$\boldsymbol{T} = \partial_{\boldsymbol{E}^e} \psi^e(\boldsymbol{E}^e) \quad \text{and} \quad \underline{q} = \partial_{\underline{\alpha}} \psi^p(\underline{\alpha}). \tag{4.6}$$

The criterion to determine whether the deformations become plastic hinges on the scalar-valued yield function $\Phi : \mathbb{R}^{d\times d}_{\text{sym}} \times \mathbb{R}^m \to \mathbb{R}$, which is a continuous and convex function of the logarithmic stress tensor $\boldsymbol{T}$ and the thermodynamic forces $\underline{q}$. Letting $\mathcal{A} := \left\{ (\boldsymbol{T}, \underline{q}) \in \mathbb{R}^{d\times d}_{\text{sym}} \times \mathbb{R}^m \mid \Phi(\boldsymbol{T}, \underline{q}) \leq 0 \right\}$ be the convex set of admissible states, the elastic domain $\mathcal{A}^e$ is composed of all the pairs $(\boldsymbol{T}, \underline{q})$ such that $\Phi(\boldsymbol{T}, \underline{q}) < 0$, and the yield surface $\partial\mathcal{A}$ of all the pairs $(\boldsymbol{T}, \underline{q})$ such that $\Phi(\boldsymbol{T}, \underline{q}) = 0$.

Hypothesis 4.2 (Yield function) *The yield function $\Phi : \mathbb{R}^{d\times d}_{sym} \times \mathbb{R}^m \to \mathbb{R}$ satisfies the following properties:* (i) *Φ is a piecewise analytical function;* (ii) *the point $(\boldsymbol{0}, \underline{0})$ lies in the elastic domain, i.e., $\Phi(\boldsymbol{0}, \underline{0}) < 0$; and* (iii) *$\Phi$ is differentiable at all points on the yield surface $\partial\mathcal{A}$.*

Finally, the incremental dissipation function $D : \underline{\mathcal{X}} \to \mathbb{R}$ is a convex function which is positively homogeneous of degree one and is defined as follows:

$$D(\mathrm{d}\underline{\chi}) = \sup_{(\boldsymbol{T}, \underline{q}) \in \mathcal{A}} \left(\boldsymbol{T} : \mathrm{d}\boldsymbol{E}^p - \underline{q} \cdot \mathrm{d}\underline{\alpha} \right), \tag{4.7}$$

where $\mathrm{d}\underline{\chi}, \mathrm{d}\boldsymbol{E}^p$, and $\mathrm{d}\underline{\alpha}$ are the finite increments of $\underline{\chi}, \boldsymbol{E}^p$, and $\underline{\alpha}$, respectively.

4.2.3 Finite elastoplasticity model problem in incremental form

We are interested in finding the quasi-static evolution in the pseudo-time interval $I = [0, t_F]$, $t_F > 0$, of the elastoplastic material body $\mathcal{B}_0$. The pseudo-time interval I is discretized into N subintervals such that $t^0 = 0 < t^1 < \cdots < t^N = t_F$. The evolution occurs under the action of a body force $\underline{f} : \Omega_0 \times I \to \mathbb{R}^d$, a traction force $\underline{t}_{\text{N}} : \Gamma_{\text{N}} \times I \to \mathbb{R}^d$ exerted on the Neumann boundary Γ_{N}, and a displacement $\underline{u}_{\text{D}} : \Gamma_{\text{D}} \times I \to \mathbb{R}^d$ imposed on the Dirichlet boundary

Γ_{D}. Note that the external forces $\underline{f}$ and $\underline{t}_{\mathrm{N}}$ are assumed dead, i.e. independent of the displacement. We denote by $\underline{V}$ the set of all displacements with weak gradient and by $\underline{\mathfrak{X}}$ the set of generalized internal variables such that the integrals below are well defined. Moreover, we denote by $\underline{V}_{\mathrm{D}}^n$, resp. $\underline{V}_0$, the subspace of $\underline{V}$ which satisfies the Dirichlet conditions, resp. homogeneous Dirichlet conditions on Γ_{D} and :

$$\underline{V}_{\mathrm{D}}^n = \{\underline{v} \in \underline{V} \,|\, \underline{v} = \underline{u}_{\mathrm{D}}(t^n) \ \text{ on } \Gamma_{\mathrm{D}}\}\,, \ \underline{V}_0 = \{\underline{v} \in \underline{V} \,|\, \underline{v} = \underline{0} \ \text{ on } \Gamma_{\mathrm{D}}\}\,. \tag{4.8}$$

Following [167], we define for any pseudo-time step $1 \leq n \leq N$, the incremental pseudo-energy density $\Psi : \mathbb{R}_+^{d\times d} \times \underline{\mathcal{X}} \to \mathbb{R}$ acting on the pair $(\boldsymbol{F}, \underline{\chi})$ such that

$$\Psi(\boldsymbol{F}, \underline{\chi}) = \big\{\big(\psi^e(\boldsymbol{E}^e) + \psi^p(\underline{\alpha})\big) - \big(\psi^e(\boldsymbol{E}^e(\underline{u}^{n-1})) + \psi^p(\underline{\alpha}^{n-1})\big)\big\} + D(\underline{\chi} - \underline{\chi}^{n-1}), \tag{4.9}$$

where $\underline{u}^{n-1} \in \underline{V}_{\mathrm{D}}^{n-1}$ and $\underline{\chi}^{n-1} \in \underline{\mathfrak{X}}$ are given from the previous pseudo-time step or the initial condition. Note that the second term in (4.9), which is evaluated at t^{n-1}, is irrelevant for minimization purposes. It is added so that the pseudo-energy is in a time-incremental form. This allows us to define the energy functional $\mathcal{E}^n : \underline{V}_{\mathrm{D}}^n \times \underline{\mathfrak{X}} \to \mathbb{R}$ such that, for all kinematically admissible displacement fields $\underline{v} \in \underline{V}_{\mathrm{D}}^n$ and all generalized internal variables $\underline{\chi} \in \underline{\mathfrak{X}}$.

$$\mathcal{E}^n(\underline{v}, \underline{\chi}) = \int_{\Omega_0} \Psi(\boldsymbol{F}(\underline{v}), \underline{\chi})\, d\Omega_0 - \int_{\Omega_0} \underline{f}^n \cdot \underline{v}\, d\Omega_0 - \int_{\Gamma_{\mathrm{N}}} \underline{t}_{\mathrm{N}}^n \cdot \underline{v}\, d\Gamma. \tag{4.10}$$

The quasi-static equilibrium of the elastoplastic body $\mathcal{B}_0$ is determined at each pseudo-time step $1 \leq n \leq N$ by finding a displacement field $\underline{u}^n \in \underline{V}_{\mathrm{D}}^n$ and generalized internal variables $\underline{\chi}^n \in \underline{\mathfrak{X}}$ which minimize the energy functional $\mathcal{E}^n$ in (4.10), i.e.,

$$(\underline{u}^n, \underline{\chi}^n) \in \underset{\underline{v}\in\underline{V}_{\mathrm{D}}^n,\, \underline{\chi}\in\underline{\mathfrak{X}}}{\arg\min}\ \mathcal{E}^n(\underline{v}, \underline{\chi}). \tag{4.11}$$

On the one hand, the first variation of $\mathcal{E}^n$ with respect to the displacement field leads to:

$$0 = D\mathcal{E}^n(\underline{u}^n, \underline{\chi}^n)[\underline{v}] = \int_{\Omega_0} \boldsymbol{P}^n : \boldsymbol{\nabla}_X \underline{v}\, d\Omega_0 - \int_{\Omega_0} \underline{f}^n \cdot \underline{v}\, d\Omega_0 - \int_{\Gamma_{\mathrm{N}}} \underline{t}_{\mathrm{N}}^n \cdot \underline{v}\, d\Gamma, \quad \text{for all } \underline{v} \in \underline{V}_0, \tag{4.12}$$

where $\boldsymbol{P}^n := \partial_{\boldsymbol{F}} \Psi(\boldsymbol{F}(\underline{u}^n), \underline{\chi}^n)$ is the first Piola–Kirchhoff stress tensor. On the other hand, the first variation of $\mathcal{E}^n$ with respect to the generalized internal variables leads to the following incremental nonlinear equations (see [167, 190] for example):

$$\boldsymbol{E}^{p,n} - \boldsymbol{E}^{p,n-1} = \Lambda(\boldsymbol{T}^n, \underline{q}^n)\, \partial_{\boldsymbol{T}} \Phi(\boldsymbol{T}^n, \underline{q}^n), \quad \text{and} \quad \underline{\alpha}^n - \underline{\alpha}^{n-1} = -\Lambda(\boldsymbol{T}^n, \underline{q}^n)\, \partial_{\underline{q}} \Phi(\boldsymbol{T}^n, \underline{q}^n), \tag{4.13}$$

where the plastic multiplier $\Lambda(\boldsymbol{T}^n, \underline{q}^n)$ verifies the Kuhn–Tucker conditions

$$\Lambda(\boldsymbol{T}^n, \underline{q}^n) \geq 0, \quad \Phi(\boldsymbol{T}^n, \underline{q}^n) \leq 0, \quad \text{and} \quad \Lambda(\boldsymbol{T}^n, \underline{q}^n)\, \Phi(\boldsymbol{T}^n, \underline{q}^n) = 0. \tag{4.14}$$

We assume additionally that the incremental pseudo-energy density Ψ is polyconvex so that local minimizers of the energy functional (4.10) exist (cf. e.g [167, 21]). Thus, the minimization problem (4.11) can be reformulated, in a more classical way as follows: For all $1 \leq n \leq N$, given $\underline{u}^{n-1} \in \underline{V}_{\mathrm{D}}^{n-1}$ and $\underline{\chi}^{n-1} \in \underline{\mathfrak{X}}$ from the previous pseudo-time step or the initial condition, find $\underline{u}^n \in \underline{V}_{\mathrm{D}}^n$ and $\underline{\chi}^n \in \underline{\mathfrak{X}}$ such that

$$\int_{\Omega_0} \boldsymbol{P}^n : \boldsymbol{\nabla}_X \underline{v}\, d\Omega_0 = \int_{\Omega_0} \underline{f}^n \cdot \underline{v}\, d\Omega_0 + \int_{\Gamma_{\mathrm{N}}} \underline{t}_{\mathrm{N}}^n \cdot \underline{v}\, d\Gamma, \quad \text{for all } \underline{v} \in \underline{V}_0, \tag{4.15a}$$

and

$$(\underline{\chi}^n, \boldsymbol{P}^n, \mathbb{A}_{ep}^n) = \text{FINITE\_PLASTICITY}(\underline{\chi}^{n-1}, \boldsymbol{F}(\underline{u}^{n-1}), \boldsymbol{F}(\underline{u}^n)). \tag{4.15b}$$

The procedure FINITE_PLASTICITY allows one to compute the new values of the generalized internal variables $\underline{\chi}$, the first Piola–Kirchhoff stress tensor $\boldsymbol{P}$ and the consistent nominal elastoplastic tangent modulus $\mathbb{A}_{ep}$ at each pseudo-time step. This procedure is detailed in Section 4.2.4.

4.2.4 Algorithmic aspects

The incremental elastoplasticity problem that has to be solved is to find the new value, after incrementation, of the generalized internal variables $\underline{\chi}^{\text{new}} = (\boldsymbol{E}^{p,\text{new}}, \underline{\alpha}^{\text{new}}) \in \underline{\mathcal{X}}$, the first Piola–Kirchhoff stress tensor $\boldsymbol{P}^{\text{new}} \in \mathbb{R}^{d\times d}_{\text{sym}}$, and the consistent nominal elastoplastic tangent modulus $\mathbb{A}_{ep}^{new}$, given the generalized internal variables $\underline{\chi} \in \underline{\mathcal{X}}$, the deformation gradient $\boldsymbol{F} \in \mathbb{R}^{d\times d}_{+}$, and the new value of the deformation gradient $\boldsymbol{F}^{\text{new}} \in \mathbb{R}^{d\times d}_{+}$. Solving this problem is denoted as previously

$$(\underline{\chi}^{\text{new}}, \boldsymbol{P}^{\text{new}}, \mathbb{A}_{ep}^{new}) = \text{FINITE\_PLASTICITY}(\underline{\chi}, \boldsymbol{F}, \boldsymbol{F}^{\text{new}}). \tag{4.16}$$

The procedure to compute $(\underline{\chi}^{\text{new}}, \boldsymbol{P}^{\text{new}}, \mathbb{A}_{ep}^{new})$ is described in Algorithm 2 and is composed of three different steps. Firstly, a geometric pre-processing is applied in order to compute the logarithmic strain tensors $\boldsymbol{E}$ and $\boldsymbol{E}^{\text{new}}$. Secondly, the procedure SMALL_PLASTICITY is used to solve the nonlinear incremental problem (4.13)-(4.14) so as to compute $(\underline{\chi}^{\text{new}}, \boldsymbol{T}^{\text{new}}, \mathbb{E}_{ep}^{new})$. The resolution of (4.13)-(4.14) inside the procedure SMALL_PLASTICITY requires to solve a constrained nonlinear problem which is the same as in the case of plasticity with small deformations and thus makes it possible to extend the procedures already developed for small deformations to finite deformations without modifications (further details about the procedure SMALL_PLASTICITY can be found in [3, Sect. 2.3]). One significant example of such a procedure is the standard radial return mapping [190, 193]. Finally, a geometric post-processing step is applied to compute the new values of the first Piola–Kirchhoff stress tensor $\boldsymbol{P}^{\text{new}}$ and the consistent nominal elastoplastic tangent modulus $\mathbb{A}_{ep}^{new}$ from the logarithmic stress tensor $\boldsymbol{T}^{\text{new}}$ and the consistent logarithmic elastoplastic tangent modulus $\mathbb{E}_{ep}^{new}$. Detailed explanations to compute the pre- and post-processing steps are given in [167, Box. 4]. Note that $\mathbb{A}_{ep}^{new} := \partial_{\boldsymbol{F}\boldsymbol{F}}\Psi(\boldsymbol{F}^{\text{new}}, \underline{\chi}^{\text{new}})$ is the consistent elastoplastic tangent modulus and is a

Algorithm 2 Computation of $(\underline{\chi}^{\text{new}}, \boldsymbol{P}^{\text{new}}, \mathbb{A}_{ep}^{new})$

1: **procedure** FINITE_PLASTICITY$(\underline{\chi}, \boldsymbol{F}, \boldsymbol{F}^{\text{new}})$
2: Set $\boldsymbol{E} = \frac{1}{2}\ln(\boldsymbol{F}^T\boldsymbol{F})$, $\boldsymbol{E}^{\text{new}} = \frac{1}{2}\ln(\boldsymbol{F}^{\text{new},T}\boldsymbol{F}^{\text{new}})$ and $\mathrm{d}\boldsymbol{E} := \boldsymbol{E}^{\text{new}} - \boldsymbol{E}$
3: Compute $(\underline{\chi}^{\text{new}}, \boldsymbol{T}^{\text{new}}, \mathbb{E}_{ep}^{new}) = \text{SMALL\_PLASTICITY}(\underline{\chi}, \boldsymbol{E}, \mathrm{d}\boldsymbol{E})$.
4: Compute $\boldsymbol{P}^{\text{new}} = \boldsymbol{T}^{\text{new}} : (\partial_{\boldsymbol{F}}\boldsymbol{E})^{\text{new}}$ and $\mathbb{A}_{ep}^{new} = (\partial_{\boldsymbol{F}}\boldsymbol{E})^{\text{new},T} : \mathbb{E}_{ep}^{new} : (\partial_{\boldsymbol{F}}\boldsymbol{E})^{\text{new}} + \boldsymbol{T}^{\text{new}} : (\partial_{\boldsymbol{F}\boldsymbol{F}}\boldsymbol{E})^{\text{new}}$
5: **return** $(\underline{\chi}^{\text{new}}, \boldsymbol{P}^{\text{new}}, \mathbb{A}_{ep}^{new})$
6: **end procedure**

fourth-order tensor having only the major symmetries contrary to $\mathbb{E}_{ep}^{new}$ which has the major and minor symmetries. For a finite incremental strain, the consistent elastoplastic tangent modulus generally differs from the so-called continuous elastoplastic tangent modulus which is obtained by letting the incremental strain tend to zero [195].

4.2.5 Example: nonlinear isotropic hardening with a von Mises yield criterion

An illustration of the plasticity model defined above is the nonlinear isotropic hardening model with a von Mises criterion. The elastic part of the free energy is such that

$$\psi^e(\boldsymbol{E}^e) = \frac{1}{2}\boldsymbol{E}^e : \mathbb{C} : \boldsymbol{E}^e, \tag{4.17}$$

where the elastic modulus is $\mathbb{C} = 2\mu\mathbb{I}^s + \lambda \boldsymbol{I} \otimes \boldsymbol{I}$, with $\mu > 0$, $3\lambda + 2\mu > 0$, $(\mathbb{I}^s)_{ij,kl} = \frac{1}{2}(\delta_{ik}\delta_{jl} + \delta_{il}\delta_{jk})$, and $(\boldsymbol{I} \otimes \boldsymbol{I})_{ij,kl} = \delta_{ij}\delta_{kl}$. The internal variable is $\underline{\alpha} := p$, where $p \geq 0$ is the equivalent plastic strain. The plastic part of the free energy is such that

$$\psi^p(\underline{\alpha}) = \sigma_{y,0}p + \frac{H}{2}p^2 + (\sigma_{y,\infty} - \sigma_{y,0})(p - \frac{1 - e^{-\delta p}}{\delta}), \tag{4.18}$$

where $H \geq 0$ is the isotropic hardening modulus, $\sigma_{y,0} > 0$, resp. $\sigma_{y,\infty} \geq 0$, is the initial, resp. infinite, yield stress and $\delta \geq 0$ is the saturation parameter. The associated thermodynamic force $\underline{q} = \sigma_{y,0} + Hp + (\sigma_{y,\infty} - \sigma_{y,0})(1 - e^{-\delta p})$ is called the internal stress. Concerning the yield function, we consider a J_2-plasticity model with a von Mises criterion:

$$\Phi(\boldsymbol{T}, \underline{q}) = \sqrt{\frac{3}{2}}\|\operatorname{dev}(\boldsymbol{T})\|_{\ell^2} - \underline{q}, \tag{4.19}$$

where $\operatorname{dev}(\boldsymbol{\tau}) := \boldsymbol{\tau} - \frac{1}{d}\operatorname{trace}(\boldsymbol{\tau})\boldsymbol{I}$ is the deviatoric operator, and the Frobenius norm is defined as $\|\boldsymbol{\tau}\|_{\ell^2} = \sqrt{\boldsymbol{\tau} : \boldsymbol{\tau}}$, for all $\boldsymbol{\tau} \in \mathbb{R}^{d\times d}$. Moreover, the above model describes with a reasonable accuracy the behaviour of metals [159]. This model is used for the numerical examples presented in Section 4.4.

4.3 The Hybrid High-Order method

4.3.1 Discrete setting

We consider a mesh sequence $(\mathcal{T}_h)_{h>0}$, where for each $h > 0$, the mesh $\mathcal{T}_h$ is composed of nonempty disjoint open polyhedra with planar faces such that $\overline{\Omega}_0 = \bigcup_{T\in\mathcal{T}_h} \overline{T}$. The mesh-size is $h = \max_{T\in\mathcal{T}_h} h_T$, where h_T stands for the diameter of the cell T. A closed subset F of $\overline{\Omega}_0$ is called a mesh face if it is a subset with nonempty relative interior of some affine hyperplane H_F and (i) if either there exist two distinct mesh cells T_-, $T_+ \in \mathcal{T}_h$ such that $F = \partial T_- \cap \partial T_+ \cap H_F$ (and F is called an interface) or (ii) there exists one mesh cell $T \in \mathcal{T}_h$ such that $F = \partial T \cap \Gamma \cap H_F$ (and F is called a boundary face). The mesh faces are collected in the set $\mathcal{F}_h$ which is further partitioned into the subset $\mathcal{F}_h^{\mathrm{i}}$ which is the collection of the interfaces and the subset $\mathcal{F}_h^{\mathrm{b}}$ which is the collection of the boundary faces. We assume that the mesh is compatible with the partition of the boundary Γ into Γ_{D} and Γ_{N}, so that we can further split the set $\mathcal{F}_h^{\mathrm{b}}$ into the disjoint subsets $\mathcal{F}_h^{\mathrm{b,D}}$ and $\mathcal{F}_h^{\mathrm{b,N}}$ with obvious notation. For all $T \in \mathcal{T}_h$, $\mathcal{F}_{\partial T}$ is the collection of the mesh faces that are subsets of ∂T and $\underline{n}_T$ is the unit outward normal to T. We assume that the mesh sequence $(\mathcal{T}_h)_{h>0}$ is shape-regular in the sense specified in [89], i.e., there is a matching simplicial submesh of $\mathcal{T}_h$ that belongs to a shape-regular family of simplicial meshes in the usual sense of Ciarlet [69] and such that each mesh cell $T \in \mathcal{T}_h$ (resp., mesh face $F \in \mathcal{F}_h$) can be decomposed in a finite number of sub-cells (resp., sub-faces) which belong to only one mesh cell (resp., to only one mesh face or to the interior of a mesh cell) with uniformly comparable diameter.

Let $k \geq 1$ be a fixed polynomial degree and $l \in \{k, k+1\}$. In each mesh cell $T \in \mathcal{T}_h$, the local HHO unknowns consist of a pair $(\underline{v}_T, \underline{v}_{\partial T})$, where the cell unknown $\underline{v}_T \in \mathbb{P}_d^l(T;\mathbb{R}^d)$

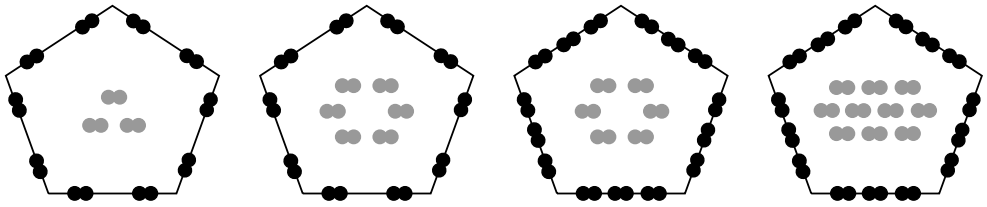

(a) $(k,l)=(1,1)$ (b) $(k,l)=(1,2)$ (c) $(k,l)=(2,2)$ (d) $(k,l)=(2,3)$

Figure 4.1: Face (black) and cell (gray) degrees of freedom in $\hat{\underline{U}}_T^{k,l}$ for different values of the pair (k,l) in the two-dimensional case (each dot represents a degree of freedom which is not necessarily a point evaluation).

is a vector-valued d-variate polynomial of degree at most l in the mesh cell T, and $\underline{v}_{\partial T} \in \mathbb{P}_{d-1}^k(\mathcal{F}_{\partial T};\mathbb{R}^d) = \times_{F\in\mathcal{F}_{\partial T}} \mathbb{P}_{d-1}^k(F;\mathbb{R}^d)$ is a piecewise, vector-valued $(d-1)$-variate polynomial of degree at most k on each face $F \in \mathcal{F}_{\partial T}$. We write more concisely that

$$\hat{\underline{v}}_T := (\underline{v}_T, \underline{v}_{\partial T}) \in \hat{\underline{U}}_T^{k,l} := \mathbb{P}_d^l(T;\mathbb{R}^d) \times \mathbb{P}_{d-1}^k(\mathcal{F}_{\partial T};\mathbb{R}^d). \tag{4.20}$$

We write the superscript k first since k is the value that determines the convergence rates of the approximation. The degrees of freedom are illustrated in Fig. 4.1, where a dot indicates one degree of freedom (which is not necessarily computed as a point evaluation) and the geometric shape of the cell is only illustrative. We equip the space $\hat{\underline{U}}_T^{k,l}$ with the following local discrete strain semi-norm:

$$|\hat{\underline{v}}_T|_{1,T}^2 := \|\boldsymbol{\nabla}_X \underline{v}_T\|_{\boldsymbol{L}^2(T)}^2 + \|\eta_{\partial T}^{\frac{1}{2}}(\underline{v}_{T|\partial T} - \underline{v}_{\partial T})\|_{\underline{L}^2(\partial T)}^2, \tag{4.21}$$

with the piecewise constant function $\eta_{\partial T}$ such that $\eta_{\partial T|F} = h_F^{-1}$ for all $F \in \mathcal{F}_{\partial T}$, where h_F is the diameter of F. We notice that $|\hat{\underline{v}}_T|_{1,T} = 0$ implies that $\underline{v}_T$ is a constant and that $\underline{v}_{\partial T}$ is the trace of $\underline{v}_T$ on ∂T.

4.3.2 Local gradient reconstruction and stabilization

The first key ingredient in the devising of the HHO method is a local gradient reconstruction in each mesh cell $T \in \mathcal{T}_h$. This reconstruction is materialized by an operator $\boldsymbol{G}_T^k : \hat{\underline{U}}_T^{k,l} \to \mathbb{P}_d^k(T;\mathbb{R}^{d\times d})$ mapping onto the space composed of $\mathbb{R}^{d\times d}$-valued polynomials in T. The main reason for reconstructing the gradient in a larger space than the space $\boldsymbol{\nabla}_X \mathbb{P}_d^{k+1}(T;\mathbb{R}^d)$ (as for the linear elasticity problem [89]) is that the reconstructed gradient of a test function acts against a discrete stress tensor which is not in gradient form, see [87, Section 4] for further insight. For all $\hat{\underline{v}}_T \in \hat{\underline{U}}_T^{k,l}$, the reconstructed gradient $\boldsymbol{G}_T^k(\hat{\underline{v}}_T) \in \mathbb{P}_d^k(T;\mathbb{R}^{d\times d})$ is obtained by solving the following local problem: For all $\boldsymbol{\tau} \in \mathbb{P}_d^k(T;\mathbb{R}^{d\times d})$,

$$(\boldsymbol{G}_T^k(\hat{\underline{v}}_T), \boldsymbol{\tau})_{\boldsymbol{L}^2(T)} = (\boldsymbol{\nabla}_X \underline{v}_T, \boldsymbol{\tau})_{\boldsymbol{L}^2(T)} + (\underline{v}_{\partial T} - \underline{v}_{T|\partial T}, \boldsymbol{\tau}\underline{n}_T)_{\underline{L}^2(\partial T)}. \tag{4.22}$$

Solving this problem entails choosing a basis of the polynomial space $\mathbb{P}_d^k(T;\mathbb{R})$ and inverting the associated mass matrix for each component of the tensor $\boldsymbol{G}_T^k(\hat{\underline{v}}_T)$. The second key ingredient in the HHO method is a local stabilization operator that enforces weakly the matching between the faces unknowns and the trace of the cell unknowns. Following [91, 89], the stabilization operator $\underline{S}_{\partial T}^k : \mathbb{P}_{d-1}^l(\mathcal{F}_{\partial T};\mathbb{R}^d) \to \mathbb{P}_{d-1}^k(\mathcal{F}_{\partial T};\mathbb{R}^d)$ acts on the difference $\underline{\theta} = \underline{v}_{\partial T} - \underline{v}_{T|\partial T} \in \mathbb{P}_{d-1}^l(\mathcal{F}_{\partial T};\mathbb{R}^d)$, and in the mixed-order case $l = k+1$ is such that, for all $\underline{\theta} \in \mathbb{P}_{d-1}^{k+1}(\mathcal{F}_{\partial T};\mathbb{R}^d)$,

$$\underline{S}_{\partial T}^k(\underline{\theta}) = \underline{\Pi}_{\partial T}^k(\underline{\theta}), \tag{4.23}$$

where $\underline{\Pi}^k_{\partial T}$ denotes the L^2-orthogonal projectors onto $\mathbb{P}^k_{d-1}(\mathcal{F}_{\partial T};\mathbb{R}^d)$, and in the equal-order case $l=k$ is such that, for all $\underline{\theta}\in\mathbb{P}^k_{d-1}(\mathcal{F}_{\partial T};\mathbb{R}^d)$,

$$\underline{S}^k_{\partial T}(\underline{\theta}) = \underline{\Pi}^k_{\partial T}\big(\underline{\theta} - (\boldsymbol{I}-\underline{\Pi}^k_T)\underline{D}^{k+1}_T(\underline{0},\underline{\theta})_{|\partial T}\big), \tag{4.24}$$

where $\underline{\Pi}^k_T$ denotes the L^2-orthogonal projectors onto $\mathbb{P}^k_d(T;\mathbb{R}^d)$. The local displacement reconstruction operator $\underline{D}^{k+1}_T : \hat{\underline{U}}^{k,l}_T \to \mathbb{P}^{k+1}_d(T;\mathbb{R}^d)$ is such that, for all $\hat{\underline{v}}_T\in\hat{\underline{U}}^{k,l}_T$, $\underline{D}^{k+1}_T(\hat{\underline{v}}_T)\in\mathbb{P}^{k+1}_d(T;\mathbb{R}^d)$ is obtained by solving the following local Neumann problem: For all $\underline{w}\in\mathbb{P}^{k+1}_d(T;\mathbb{R}^d)$,

$$(\boldsymbol{\nabla}_X\underline{D}^{k+1}_T(\hat{\underline{v}}_T),\boldsymbol{\nabla}_X\underline{w})_{\boldsymbol{L}^2(T)} = (\boldsymbol{\nabla}_X\underline{v}_T,\boldsymbol{\nabla}_X\underline{w})_{\boldsymbol{L}^2(T)} + (\underline{v}_{\partial T}-\underline{v}_{T|\partial T},\boldsymbol{\nabla}_X\underline{w}\,\underline{n}_T)_{\underline{L}^2(\partial T)}. \tag{4.25}$$

together with the mean-value conditions $\int_T \underline{D}^{k+1}_T(\hat{\underline{v}}_T)\,dT = \int_T \underline{v}_T\,dT$. Comparing with (4.22), one readily sees that $\boldsymbol{\nabla}_X\underline{D}^{k+1}_T(\hat{\underline{v}}_T)$ is the L^2-orthogonal projection of $\boldsymbol{G}^k_T(\hat{\underline{v}}_T)$ onto the subspace $\boldsymbol{\nabla}_X\mathbb{P}^{k+1}_d(T;\mathbb{R}^d)$. Note also that the right-hand side of (4.24) can be rewritten as $\underline{\Pi}^k_{\partial T}(\underline{v}_{\partial T}-\underline{v}_{T|\partial T}-(\boldsymbol{I}-\underline{\Pi}^k_T)\underline{D}^{k+1}_T(\hat{\underline{v}}_T)_{|\partial T})$. Adapting [89, Lemma 4], it is straightforward to establish the following stability and boundedness properties (the proof is omitted for brevity).

Lemma 4.3 (Boundedness and stability) *Let the gradient reconstruction operator be defined by (4.22) and the stabilization operator be defined by (4.23) or (4.24). Let $\eta_{\partial T}$ be defined below (4.21). Then, we have the following properties: (i) Boundedness: there exists $\alpha_\sharp<+\infty$, uniform w.r.t. h, such that, for all $T\in\mathcal{T}_h$ and for $\hat{\underline{v}}_T\in\hat{\underline{U}}^{k,l}_T$,*

$$\left(\|\boldsymbol{G}^k_T(\hat{\underline{v}}_T)\|^2_{\boldsymbol{L}^2(T)} + \|\eta^{\frac12}_{\partial T}\underline{S}^k_{\partial T}(\underline{v}_{\partial T}-\underline{v}_{T|\partial T})\|^2_{\underline{L}^2(\partial T)}\right)^{\frac12} \le \alpha_\sharp|\hat{\underline{v}}_T|_{1,T}. \tag{4.26}$$

(ii) Stability: there exists $\alpha_\flat>0$, uniform w.r.t. h, such that, for all $T\in\mathcal{T}_h$ and all $\hat{\underline{v}}_T\in\hat{\underline{U}}^{k,l}_T$,

$$\alpha_\flat|\hat{\underline{v}}_T|_{1,T} \le \left(\|\boldsymbol{G}^k_T(\hat{\underline{v}}_T)\|^2_{\boldsymbol{L}^2(T)} + \|\eta^{\frac12}_{\partial T}\underline{S}^k_{\partial T}(\underline{v}_{\partial T}-\underline{v}_{T|\partial T})\|^2_{\underline{L}^2(\partial T)}\right)^{\frac12}. \tag{4.27}$$

As shown in [89], the following important commuting property holds true:

$$\boldsymbol{G}^k_T(\hat{\underline{I}}^k_T(\underline{v})) = \boldsymbol{\Pi}^k_T(\boldsymbol{\nabla}_X\underline{v}), \qquad \forall\underline{v}\in H^1(T;\mathbb{R}^d), \tag{4.28}$$

with the reduction operator $\hat{\underline{I}}^k_T : H^1(T;\mathbb{R}^d)\to\hat{\underline{U}}^{k,l}_T$ defined as $\hat{\underline{I}}^k_T(\underline{v}) = (\underline{\Pi}^l_T(\underline{v}),\underline{\Pi}^k_{\partial T}(\underline{v}_{|\partial T}))$. Taking the trace in (4.28), we infer that

$$\mathrm{trace}\left(\boldsymbol{G}^k_T(\hat{\underline{I}}^k_T(\underline{v}))\right) = \Pi^k_T(\nabla_X\cdot\underline{v}), \qquad \forall\underline{v}\in H^1(T;\mathbb{R}^d), \tag{4.29}$$

which is the key commuting property to prove robustness for quasi-incompressible linear elasticity, see [89]. This absence of volumetric locking is confirmed in the numerical experiments performed in Section 4.4 in the nonlinear setting of finite elastoplasticity. Finally, proceeding as in [89, Thm. 8], one can show that for the linear elasticity problem and smooth solutions, the energy error converges as $h^{k+1}|\underline{u}|_{\underline{H}^{k+2}(\Omega_0)}$.

Remark 4.4 (HDG-type stabilization) *The stabilization operator (4.24) is essential to prove the above mentioned convergence rates in the equal-order case for linear problems and smooth solutions on general meshes. In general, HDG methods use the stabilization operator $\underline{S}^k_{\partial T}(\underline{\theta})=\underline{\theta}$ in the equal-order case which differs from the stabilization operator (4.24) and allows one to show only that the energy error converges as $h^k|\underline{u}|_{\underline{H}^{k+1}(\Omega_0)}$ for linear problems and smooth solutions on general meshes. In the mixed-order case, the stabilization operator (4.23) has been initially introduced in [158] and the same convergence rates as for the HHO method are obtained.*

4.3.3 Global discrete problem

Let us now devise the global discrete problem. We set $\mathbb{P}_d^l(\mathcal{T}_h;\mathbb{R}^d) := \times_{T\in\mathcal{T}_h}\mathbb{P}_d^l(T;\mathbb{R}^d)$ and $\mathbb{P}_{d-1}^k(\mathcal{F}_h;\mathbb{R}^d) := \times_{F\in\mathcal{F}_h}\mathbb{P}_{d-1}^k(F;\mathbb{R}^d)$. The global space of discrete HHO unknowns is defined as

$$\underline{\hat{U}}_h^{k,l} := \mathbb{P}_d^l(\mathcal{T}_h;\mathbb{R}^d)\times\mathbb{P}_{d-1}^k(\mathcal{F}_h;\mathbb{R}^d). \tag{4.30}$$

For an element $\underline{\hat{v}}_h \in \underline{\hat{U}}_h^{k,l}$, we use the generic notation $\underline{\hat{v}}_h = (\underline{v}_{\mathcal{T}_h}, \underline{v}_{\mathcal{F}_h})$. For any mesh cell $T\in\mathcal{T}_h$, we denote by $\underline{\hat{v}}_T \in \underline{\hat{U}}_T^{k,l}$ the local components of $\underline{\hat{v}}_h$ attached to the mesh cell T and to the faces composing its boundary ∂T, and for any mesh face $F\in\mathcal{F}_h$, we denote by $\underline{v}_F$ the component of $\underline{\hat{v}}_h$ attached to the face F. The Dirichlet boundary condition on the displacement field can be enforced explicitly on the discrete unknowns attached to the boundary faces in $\mathcal{F}_h^{\mathrm{b,D}}$. Letting $\underline{\Pi}_F^k$ denote the L^2-orthogonal projector onto $\mathbb{P}_{d-1}^k(F;\mathbb{R}^d)$, we set

$$\underline{\hat{U}}_{h,\mathrm{D}}^{k,l,n} := \left\{\underline{\hat{v}}_h\in\underline{\hat{U}}_h^{k,l} \mid \underline{v}_F = \underline{\Pi}_F^k(\underline{u}_{\mathrm{D}}(t^n)),\ \forall F\in\mathcal{F}_h^{\mathrm{b,D}}\right\}, \tag{4.31a}$$

$$\underline{\hat{U}}_{h,0}^{k,l} := \left\{\underline{\hat{v}}_h\in\underline{\hat{U}}_h^{k,l} \mid \underline{v}_F = \underline{0},\ \forall F\in\mathcal{F}_h^{\mathrm{b,D}}\right\}. \tag{4.31b}$$

Note that the map $\underline{\hat{v}}_h\mapsto(\sum_{T\in\mathcal{T}_h}|\underline{\hat{v}}_T|_{1,T}^2)^{\frac12}$ defines a norm on $\underline{\hat{U}}_{h,0}^{k,l}$.

A key feature of the present HHO method is that the discrete generalized internal variables are computed only at the quadrature points in each mesh cell. We introduce for all $T\in\mathcal{T}_h$, the quadrature points $\underline{\xi}_T = (\underline{\xi}_{T,j})_{1\le j\le m_Q}$, with $\underline{\xi}_{T,j}\in T$ for all $1\le j\le m_Q$, and the quadrature weights $\omega_T = (\omega_{T,j})_{1\le j\le m_Q}$, with $\omega_{T,j}\in\mathbb{R}$ for all $1\le j\le m_Q$. We denote by k_Q the order of the quadrature. Then, the discrete internal variables are sought in the space

$$\underline{\tilde{\mathcal{X}}}_{\mathcal{T}_h}^{m_Q} := \bigtimes_{T\in\mathcal{T}_h}\underline{\mathcal{X}}^{m_Q}, \tag{4.32}$$

that is, for all $T\in\mathcal{T}_h$, the internal variables attached to T form a vector $\underline{\tilde{\chi}}_T = (\underline{\tilde{\chi}}_T(\underline{\xi}_{T,j}))_{1\le j\le m_Q}$ with $\underline{\tilde{\chi}}_T(\underline{\xi}_{T,j})\in\underline{\mathcal{X}}$ for all $1\le j\le m_Q$.

We can now formulate the global discrete problem. We use the following notation for two tensor-valued functions $(\boldsymbol{p},\boldsymbol{q})$ defined on T:

$$(\boldsymbol{p},\boldsymbol{q})_{\boldsymbol{L}_Q^2(T)} := \sum_{j=1}^{m_Q}\omega_{T,j}\,\boldsymbol{p}(\underline{\xi}_{T,j}):\boldsymbol{q}(\underline{\xi}_{T,j}). \tag{4.33}$$

We also need to consider the case where we know the tensor $\tilde{\boldsymbol{p}}$ only at the quadrature nodes (we use a tilde to indicate this situation), i.e., we have $\tilde{\boldsymbol{p}} = (\tilde{\boldsymbol{p}}(\underline{\xi}_{T,j}))_{1\le j\le m_Q}\in(\mathbb{R}^{d\times d})^{m_Q}$. In this case, we slightly abuse the notation by denoting again by $(\tilde{\boldsymbol{p}},\boldsymbol{q})_{\boldsymbol{L}_Q^2(T)}$ the quantity equal to the right-hand side of (4.33). The discrete energy functional $\mathcal{E}_h^n : \underline{\hat{U}}_{h,\mathrm{D}}^{k,l,n}\times\underline{\tilde{\mathcal{X}}}_{\mathcal{T}_h}^{m_Q}\to\mathbb{R}$ is defined for any pseudo-time step $1\le n\le N$ by

$$\begin{aligned}\mathcal{E}_h^n(\underline{\hat{v}}_h,\underline{\tilde{\chi}}_{\mathcal{T}_h}) = \sum_{T\in\mathcal{T}_h}\left\{(\tilde\Psi(\boldsymbol{F}_T^k(\underline{\hat{v}}_T),\underline{\tilde{\chi}}_T),1)_{L_Q^2(T)} - (\underline{f}^n,\underline{v}_T)_{\underline{L}^2(T)}\right\} - \sum_{F\in\mathcal{F}_h^{\mathrm{b,N}}}(\underline{t}_{\mathrm{N}}^n,\underline{v}_F)_{\underline{L}^2(F)}\\ + \sum_{T\in\mathcal{T}_h}\frac{\beta}{2}\|\eta_{\partial T}^{\frac12}\underline{S}_{\partial T}^k(\underline{v}_{\partial T}-\underline{v}_{T|\partial T})\|_{\underline{L}^2(\partial T)}^2,\end{aligned} \tag{4.34}$$

for all $\underline{\hat{v}}_h\in\underline{\hat{U}}_{h,\mathrm{D}}^{k,l,n}$ and $\underline{\tilde{\chi}}_{\mathcal{T}_h}\in\underline{\tilde{\mathcal{X}}}_{\mathcal{T}_h}^{m_Q}$, with the local deformation gradient operator $\boldsymbol{F}_T^k : \underline{\hat{U}}_T^{k,l}\to\mathbb{P}_d^k(T;\mathbb{R}^{d\times d})$ such that $\boldsymbol{F}_T^k(\underline{\hat{v}}_T) := \boldsymbol{I} + \boldsymbol{G}_T^k(\underline{\hat{v}}_T)$. Moreover, in the second line of (4.34), the

stabilization employs a weight of the form $\beta = 2\mu\beta_0$ with $\beta_0 > 0$. In the original HHO method for linear elasticity [89], the choice $\beta_0 = 1$ is considered. In the present setting, the choice for β_0 is further discussed in Section 4.3.5 and in Section 4.5.3. The global discrete problem consists in seeking for any pseudo-time step $1 \le n \le N$, a stationary point of the discrete energy functional: Find the pair of discrete displacements $\hat{\underline{u}}_h^n \in \hat{\underline{U}}_{h,\mathrm{D}}^{k,l,n}$ and the discrete internal variables $\tilde{\underline{\chi}}_{\mathcal{T}_h}^n \in \tilde{\underline{\mathcal{X}}}_{\mathcal{T}_h}^{m_Q}$ such that, for all $\delta\hat{\underline{v}}_h \in \hat{\underline{U}}_{h,0}^{k,l}$,

$$\begin{aligned}&\sum_{T\in\mathcal{T}_h}(\tilde{\boldsymbol{P}}^n, \boldsymbol{G}_T^k(\delta\hat{\underline{v}}_T))_{\boldsymbol{L}_Q^2(T)} + \sum_{T\in\mathcal{T}_h}\beta(\eta_{\partial T}\underline{S}_{\partial T}^k(\underline{u}_{\partial T}^n - \underline{u}_{T|\partial T}^n), \underline{S}_{\partial T}^k(\delta\underline{v}_{\partial T} - \delta\underline{v}_{T|\partial T}))_{\underline{L}^2(\partial T)}\\ &= \sum_{T\in\mathcal{T}_h}(\underline{f}^n, \delta\underline{v}_T)_{\underline{L}^2(T)} + \sum_{F\in\mathcal{F}_h^{\mathrm{b,N}}}(\underline{t}_{\mathrm{N}}^n, \delta\underline{v}_F)_{\underline{L}^2(F)},\end{aligned} \tag{4.35}$$

where for all $T \in \mathcal{T}_h$ and all $1 \le j \le m_Q$,

$$\begin{aligned}&(\tilde{\underline{\chi}}_T^n(\underline{\xi}_{T,j}), \tilde{\boldsymbol{P}}^n(\underline{\xi}_{T,j}), \tilde{\mathbb{A}}_{ep}^n(\underline{\xi}_{T,j})) =\\ &\qquad \mathrm{FINITE\_PLASTICITY}(\tilde{\underline{\chi}}_T^{n-1}(\underline{\xi}_{T,j}), \boldsymbol{F}_T^k(\hat{\underline{u}}_T^{n-1})(\underline{\xi}_{T,j}), \boldsymbol{F}_T^k(\hat{\underline{u}}_T^n)(\underline{\xi}_{T,j})),\end{aligned} \tag{4.36}$$

with $\hat{\underline{u}}_h^{n-1} \in \hat{\underline{U}}_{h,\mathrm{D}}^{k,l,n-1}$ and $\tilde{\underline{\chi}}_{\mathcal{T}_h}^{n-1} \in \tilde{\underline{\mathcal{X}}}_{\mathcal{T}_h}^{m_Q}$ given either from the previous pseudo-time step or the initial condition.

4.3.4 Discrete principle of virtual work

The discrete problem (4.35) expresses the principle of virtual work at the global level, and adapting the ideas introduced in [74] (see also [3, 40]), it is possible to infer a local principle of virtual work in terms of face-based discrete tractions that comply with the law of action and reaction.

Let $\underline{S}_{\partial T}^{k*} : \mathbb{P}_{d-1}^k(\mathcal{F}_{\partial T};\mathbb{R}^d) \to \mathbb{P}_{d-1}^k(\mathcal{F}_{\partial T};\mathbb{R}^d)$ be the adjoint operator of $\underline{S}_{\partial T}^k$ with respect to the $L^2(\partial T;\mathbb{R}^d)$-inner product so that we have $(\eta_{\partial T}\underline{S}_{\partial T}^k(\underline{\theta}), \underline{S}_{\partial T}^k(\underline{\zeta}))_{\underline{L}^2(\partial T)} = (\underline{S}_{\partial T}^{k*}(\eta_{\partial T}\underline{S}_{\partial T}^k(\underline{\theta})), \underline{\zeta})_{\underline{L}^2(\partial T)}$ (recall that the weight $\eta_{\partial T}$ is piecewise constant on ∂T). Let $\boldsymbol{\Pi}_{Q,T}^k : (\mathbb{R}^{d\times d})^{m_Q} \to \mathbb{P}_d^k(T;\mathbb{R}^{d\times d})$ denote the L_Q^2-orthogonal projector such that for all $\tilde{\boldsymbol{p}} \in (\mathbb{R}^{d\times d})^{m_Q}$, $(\boldsymbol{\Pi}_{Q,T}^k(\tilde{\boldsymbol{p}}), \boldsymbol{q})_{\boldsymbol{L}^2(T)} = (\tilde{\boldsymbol{p}}, \boldsymbol{q})_{\boldsymbol{L}_Q^2(T)}$ for all $\boldsymbol{q} \in \mathbb{P}_d^k(T;\mathbb{R}^{d\times d})$. Finally, for any pseudo-time step $1 \le n \le N$ and all $T \in \mathcal{T}_h$, let us define the discrete traction:

$$\underline{T}_T^n := \boldsymbol{\Pi}_{Q,T}^k(\tilde{\boldsymbol{P}}_T^n)\cdot\underline{n}_T + \beta\underline{S}_{\partial T}^{k*}(\eta_{\partial T}\underline{S}_{\partial T}^k(\underline{u}_{\partial T}^n - \underline{u}_{T|\partial T}^n)) \in \mathbb{P}_{d-1}^k(\mathcal{F}_{\partial T};\mathbb{R}^d), \tag{4.37}$$

where $\tilde{\boldsymbol{P}}_T^n = (\tilde{\boldsymbol{P}}_T^n(\underline{\xi}_{T,j}))_{1\le j\le m_Q} \in (\mathbb{R}^{d\times d})^{m_Q}$ and $\hat{\underline{u}}_T^n \in \hat{\underline{U}}_T^{k,l}$.

Lemma 4.5 (Equilibrated tractions) *Assume that $k_Q \ge 2k$. Then, for any pseudo-time step $1 \le n \le N$, the following local principle of virtual work holds true for all $T \in \mathcal{T}_h$:*

$$(\tilde{\boldsymbol{P}}_T^n, \boldsymbol{\nabla}_X\delta\underline{v}_T)_{\boldsymbol{L}_Q^2(T)} - (\underline{T}_T^n, \delta\underline{v}_{T|\partial T})_{\underline{L}^2(\partial T)} = (\underline{f}^n, \delta\underline{v}_T)_{\underline{L}^2(T)}, \qquad \forall\delta\underline{v}_T \in \mathbb{P}_d^l(T;\mathbb{R}^d), \tag{4.38}$$

where the discrete tractions $\underline{T}_T^n$ defined by (4.37) satisfy the following law of action and reaction for all $F \in \mathcal{F}_h^i \cup \mathcal{F}_h^{b,N}$:

$$\underline{T}_{T_-|F}^n + \underline{T}_{T_+|F}^n = \underline{0}, \quad \text{if } F \in \mathcal{F}_h^i \text{ with } F = \partial T_- \cap \partial T_+ \cap H_F, \tag{4.39a}$$

$$\underline{T}_{T|F}^n = \underline{\Pi}_F^k(\underline{t}_N^n), \qquad \text{if } F \in \mathcal{F}_h^{b,N} \text{ with } F = \partial T \cap \Gamma_N \cap H_F. \tag{4.39b}$$

4.3.5 Nonlinear solver and implementation

The nonlinear problem (4.35)-(4.36) arising at any pseudo-time step $1 \le n \le N$ is solved using a Newton's method. Given $\underline{\hat{u}}_h^{n-1} \in \underline{\hat{U}}_{h,\mathrm{D}}^{k,l,n-1}$ and $\underline{\tilde{\chi}}_{\mathcal{T}_h}^{n-1} \in \underline{\tilde{\mathcal{X}}}_{\mathcal{T}_h}^{m_Q}$ from the previous pseudo-time step or the initial condition, the Newton's method is initialized by setting $\underline{\hat{u}}_h^{n,0} = \underline{\hat{u}}_h^{n-1}$, up to the update of the Dirichlet condition, and $\underline{\tilde{\chi}}_{\mathcal{T}_h}^{n,0} = \underline{\tilde{\chi}}_{\mathcal{T}_h}^{n-1}$. Then, at each Newton's step $i \ge 0$, one computes the incremental displacement $\delta\underline{\hat{u}}_h^{n,i} \in \underline{\hat{U}}_{h,0}^{k,l}$ and updates the discrete displacement as $\underline{\hat{u}}_h^{n,i+1} = \underline{\hat{u}}_h^{n,i} + \delta\underline{\hat{u}}_h^{n,i}$. The linear system of equations to be solved is

$$\begin{aligned}
&\sum_{T\in\mathcal{T}_h} (\tilde{\mathbb{A}}_{ep}^{n,i} : \boldsymbol{G}_T^k(\delta\underline{\hat{u}}_T^{n,i}), \boldsymbol{G}_T^k(\delta\underline{\hat{v}}_T))_{\boldsymbol{L}_Q^2(T)} \\
&+ \sum_{T\in\mathcal{T}_h} \beta(\eta_{\partial T}\underline{S}_{\partial T}^k(\delta\underline{u}_{\partial T}^{n,i} - \delta\underline{u}_T^{n,i}|_{\partial T}), \underline{S}_{\partial T}^k(\delta\underline{v}_{\partial T} - \delta\underline{v}_{T|\partial T}))_{\underline{L}^2(\partial T)} \\
&= -R_h^{n,i}(\delta\underline{v}_{\mathcal{T}_h}, \delta\underline{v}_{\mathcal{F}_h}),
\end{aligned} \tag{4.40}$$

for all $\underline{\delta\hat{v}}_T \in \underline{\hat{U}}_{h,0}^{k,l}$, where for all $T \in \mathcal{T}_h$ and all $1 \le j \le m_Q$,

$$(\underline{\tilde{\chi}}_T^{n,i}(\underline{\xi}_{T,j}), \tilde{\boldsymbol{P}}^{n,i}(\underline{\xi}_{T,j}), \tilde{\mathbb{A}}_{ep}^{n,i}(\underline{\xi}_{T,j})) = \mathrm{FINITE\_PLASTICITY}(\underline{\chi}_{T,j}^{n-1}, \boldsymbol{F}_{T,j}^{n-1}, \boldsymbol{F}_{T,j}^{n,i}), \tag{4.41}$$

with $\underline{\chi}_{T,j}^{n-1} := \underline{\tilde{\chi}}_T^{n-1}(\underline{\xi}_{T,j})$, $\boldsymbol{F}_{T,j}^{n,i} := \boldsymbol{F}_T^k(\underline{\hat{u}}_T^{n,i})(\underline{\xi}_{T,j})$, $\boldsymbol{F}_{T,j}^{n-1} := \boldsymbol{F}_T^k(\underline{\hat{u}}_T^{n-1})(\underline{\xi}_{T,j})$, and the residual term

$$\begin{aligned}
R_h^{n,i}(\underline{\delta\hat{v}}_h) = &\sum_{T\in\mathcal{T}_h} (\tilde{\boldsymbol{P}}^{n,i}, \boldsymbol{G}_T^k(\underline{\delta\hat{v}}_T))_{\boldsymbol{L}_Q^2(T)} - \sum_{T\in\mathcal{T}_h} (\underline{f}^n, \delta\underline{v}_T)_{\underline{L}^2(T)} - \sum_{F\in\mathcal{F}_h^{\mathrm{b,N}}} (\underline{t}_{\mathrm{N}}^n, \delta\underline{v}_F)_{\underline{L}^2(F)} \\
&+ \sum_{T\in\mathcal{T}_h} \beta(\eta_{\partial T}\underline{S}_{\partial T}^k(\underline{u}_{\partial T}^{n,i} - \underline{u}_T^{n,i}|_{\partial T}), \underline{S}_{\partial T}^k(\delta\underline{v}_{\partial T} - \delta\underline{v}_{T|\partial T}))_{\underline{L}^2(\partial T)}.
\end{aligned} \tag{4.42}$$

The assembling of the stiffness matrix resulting from the left-hand side of (4.40) is local (and thus fully parallelizable). The discrete internal variables $\underline{\tilde{\chi}}_{\mathcal{T}_h}^n \in \underline{\tilde{\mathcal{X}}}_{\mathcal{T}_h}^{m_Q}$ are updated at the end of each pseudo-time step. Moreover, since the consistent elastoplastic tangent modulus $\mathbb{A}_{ep}$ has major symmetries, its eigenvalues are real. Let us set $\theta_{\mathcal{T}_h,Q} := \min_{(T,j)\in\mathcal{T}_h\times\{1,\ldots,m_Q\}} \theta^{\min}(\tilde{\mathbb{A}}_{ep}(\underline{\xi}_{T,j}))$, where $\theta^{\min}(\mathbb{M})$ denotes the smallest eigenvalue of a symmetric fourth-order tensor $\mathbb{M}$. The following result shows that the linear system (4.40) arising at each Newton's step is coercive under the simple choice $\beta_0 > 0$ on the stabilization parameter if $\tilde{\mathbb{A}}_{ep}$ is positive-definite. Notice that strain-hardening plasticity is not a sufficient condition for positive-definiteness of $\tilde{\mathbb{A}}_{ep}$ (only for $\tilde{\mathbb{E}}_{ep}$) since in finite elastoplasticity, geometrical nonlinearities also exist.

Theorem 4.6 (Coercivity) *Assume that $k_Q \ge 2k$ and that all the quadrature weights are positive. Moreover, assume that the consistent elastoplastic tangent modulus $\mathbb{A}_{ep}$ is positive-definite, i.e., $\theta_{\mathcal{T}_h,Q} > 0$. Then, the linear system (4.40) in each Newton's step is coercive for all $\beta_0 > 0$, i.e., there exists $C_{\mathrm{ell}} > 0$, independent of h, such that for all $\underline{\hat{v}}_h \in \underline{\hat{U}}_{h,0}^{k,l}$,*

$$\begin{aligned}
&\sum_{T\in\mathcal{T}_h} (\tilde{\mathbb{A}}_{ep} : \boldsymbol{G}_T^k(\underline{\hat{v}}_T), \boldsymbol{G}_T^k(\underline{\hat{v}}_T))_{\boldsymbol{L}_Q^2(T)} + \sum_{T\in\mathcal{T}_h} \beta\|\eta_{\partial T}^{\frac{1}{2}}\underline{S}_{\partial T}^k(\underline{v}_{\partial T} - \underline{v}_{T|\partial T})\|_{\underline{L}^2(\partial T)}^2 \\
&\qquad \ge C_{\mathrm{ell}} \min\left(\beta_0, \frac{\theta_{\mathcal{T}_h,Q}}{2\mu}\right) 2\mu \sum_{T\in\mathcal{T}_h} |\underline{\hat{v}}_T|_{1,T}^2.
\end{aligned} \tag{4.43}$$

The proof follows directly from [3, Theorem 6]. Note that Theorem 4.6 states that one iteration of the Newton's process is stable under a positive-definiteness assumption but does not state that a solution to the whole Newton's process exists. The existence of such a solution has been showed in the context of nonlinear elliptic equations for dG methods [214]. Moreover, if the consistent elastoplastic tangent modulus $\mathbb{A}_{ep}$ is no longer positive-definite for at least one quadrature point which is a possibility in finite elastoplasticity since geometrical nonlinearities also exist, then Theorem 4.6 is no longer valid (even if $\tilde{\mathbb{E}}_{ep}$ remains positive-definite). Moreover, a reasonable choice of the stabilization parameter appears to be $\beta_0 \geq \max(1, \frac{\theta_{\mathcal{T}_h,Q}}{2\mu})$ because $\beta_0 = 1$ is a natural choice for linear elasticity [89] and the choice $\beta_0 \geq \frac{\theta_{\mathcal{T}_h,Q}}{2\mu}$ allows one to adjust the stabilization parameter if the evolution is plastic. We investigate numerically the choice of β_0 in Section 4.5.3.

From a numerical point of view, as is classical with HHO methods [89, 91], and more generally with hybrid approximation methods, the cell unknowns $\delta\underline{\boldsymbol{u}}_T^{n,i}$ in (4.40) can be eliminated locally by using a static condensation (or Schur complement) technique. This allows one to reduce (4.40) to a linear system in terms of the face unknowns only. The reduced system is of size $N_{\mathcal{F}_h} \times d\binom{k+d-1}{d-1}$, where $N_{\mathcal{F}_h}$ denotes the number of mesh faces (unknowns attached to Dirichlet boundary faces can be eliminated by enforcing the boundary condition explicitly). The implementation of HHO methods is realized using the open-source library `DiSk++` which provides generic programming tools for the implementation of HHO methods and is available online[1]. We refer the reader to [71] and [3, Section 3.6] for further aspects about the implementation.

4.4 Numerical examples

The goal of this section is to evaluate the proposed HHO method on two- and three-dimensional benchmarks from the literature: (*i*) a necking of a 2D rectangular bar subjected to uniaxial extension, (*ii*) a Cook's membrane subjected to bending, (*iii*) a torsion of a square-section bar, and (*iv*) a quasi-incompressible sphere under internal radial force. We compare our results to the analytical solution whenever available or to numerical results obtained using the industrial open-source FEM software `code_aster`[111]. In this case, we consider a linear, resp. quadratic, cG formulation, referred to as Q1, resp. T2 or Q2 when full integration is used, or, Q2_RI when reduced integration is used, depending on the mesh, and a three-field mixed formulation in which the unknowns are the displacement, the pressure and the volumetric strain fields referred to as UPG [9]; in the UPG method, the displacement field is quadratic, whereas both the pressure and the volumetric strain fields are linear. The conforming Q1, T2 and Q2 methods with full integration, contrary to Q2_RI method with reduced integration in most of the situations, are known to present volumetric locking due to plastic incompressibility, whereas the UPG method is known to be robust but costly. Numerical results obtained using the UPG method are used as a reference solution whenever an analytical solution is not available.

The nonlinear isotropic plasticity model with a von Mises yield criterion described in Section 4.2.5 is used for the test cases. For the first three test cases, strain-hardening plasticity is considered with the following material parameters: Young modulus $E = 206.9$ GPa, Poisson ratio $\nu = 0.29$, hardening parameter $H = 129.2$ MPa, initial yield stress $\sigma_{y,0} = 450$ MPa, infinite yield stress $\sigma_{y,\infty} = 715$ MPa, and saturation parameter $\delta = 16.93$. For the fourth case, perfect plasticity is considered with the following material parameters: Young modulus $E = 28.85$ MPa, Poisson ratio $\nu = 0.499$, hardening parameter $H = 0$ MPa, initial and

[1] `https://github.com/wareHHOuse/diskpp`

Method	Number of dofs	Number of QPs
Q1	884	1600
Q2	2566	3600
Q2_RI	2566	1600
UPG	3450	3600
HHO(1;1)	3364	1600
HHO(1;2)	3364	1600
HHO(2;2)	5046	3600
HHO(2;3)	5046	3600

Table 4.1: Necking of a 2D rectangular bar: number of globally coupled degrees of freedom (dofs) and quadrature points (QPs) for the different methods.

infinite yield stresses $\sigma_{y,0} = \sigma_{y,\infty} = 6$ MPa, and saturation parameter $\delta = 0$. Moreover, for the two-dimensional test cases (i) and (ii), we assume additionally a plane strain condition. In the numerical experiments reported in this section, the stabilization parameter is taken to be $\beta = 2\mu$ ($\beta_0 = 1$), and all the quadratures use positive weights. In particular, for the HHO method, we employ a quadrature of order $k_Q = 2k$ for the behavior cell integration. We employ the notation HHO(k, l) when using face polynomials of order k and cell polynomials of order l.

In Section 4.5, we perform further numerical investigations to test other aspects of HHO methods such as the support of general meshes with possibly non-conforming interfaces, the possibility of considering the lowest-order case $k = 0$, and the dependence on the stabilization parameter β.

4.4.1 Necking of a 2D rectangular bar

In this first benchmark, we consider a 2D rectangular bar with an initial imperfection. The bar is subjected to uniaxial extension. This example has been studied previously by many authors as a necking problem [113, 191, 82, 6, 209] and can be used to test the robustness of the different methods. The bar has a length of 53.334 mm and a variable width from an initial width value of 12.826 mm at the top to a width of 12.595 mm at the center of the bar to create a geometric imperfection. A vertical displacement $u_y = 5$ mm is imposed at both ends, as shown in Fig. 4.2a. For symmetry reasons, only one-quarter of the bar is discretized, and the mesh is composed of 400 quadrangles, see Fig. 4.2b. The load-displacement curve is plotted in Fig. 4.2c. We observe that except for Q1, all the other methods give very similar results. Moreover, the equivalent plastic strain p, respectively the trace of the Cauchy stress tensor $\boldsymbol{\sigma}$, are shown in Fig. 4.3, resp. in Fig. 4.4, at the quadrature points on the final configuration. A sign of locking is the presence of strong oscillations in the trace of the Cauchy stress tensor $\boldsymbol{\sigma}$. We notice that the cG formulations Q1 and Q2 lock, contrary to the HHO, Q2_RI, and UPG methods which deliver similar results. We remark however that the results for HHO(1;1), HHO(1;2), and Q2_RI are slightly less smooth than for HHO(2;2), HHO(2;3), and UPG. The reason is that on a fixed mesh, the three former methods have less quadrature points than the three latter ones, see Table 4.1 (HHO(2;2), HHO(2;3), and UPG have the same number of quadrature points). Therefore, the stress is evaluated using less points in HHO(1;1), HHO(1;2), and Q2_RI. It is sufficient to refine the mesh or to increase the order of the quadrature by two in HHO(1;1) and HHO(1;2) to retrieve similar results to those for the three other methods (not shown for brevity).

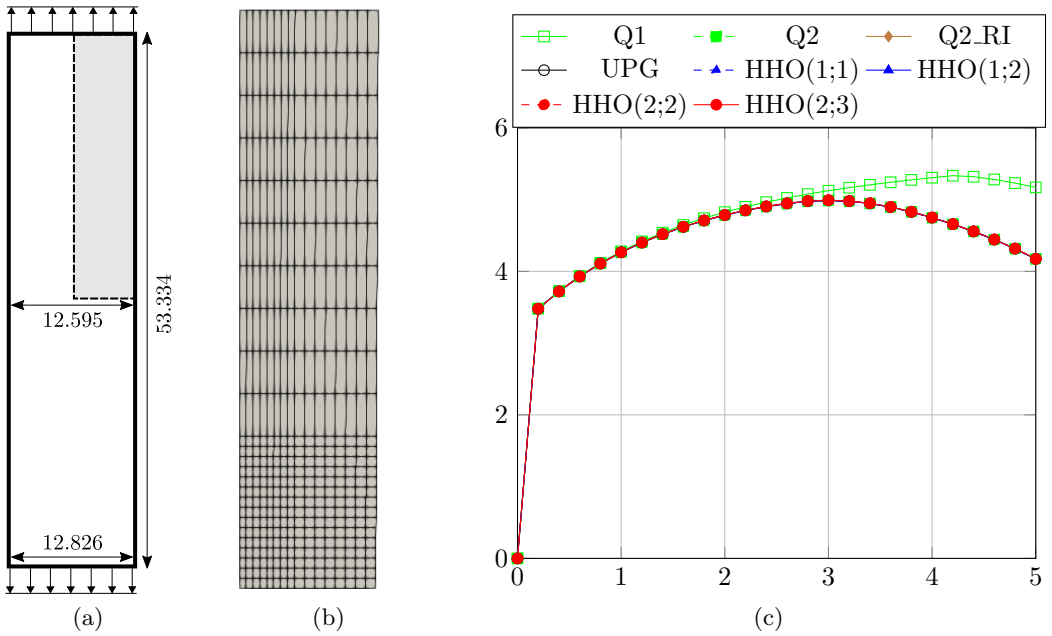

Figure 4.2: Necking of a 2D rectangular bar: (a) Geometry and boundary conditions (dimensions in mm). For symmetry reasons only the upper right-quarter of the bar is considered (b) Mesh composed of 400 quadrangles used for the computations. (c) Vertical reaction versus imposed displacement for the different methods (all the curves overlap except that for Q1) .

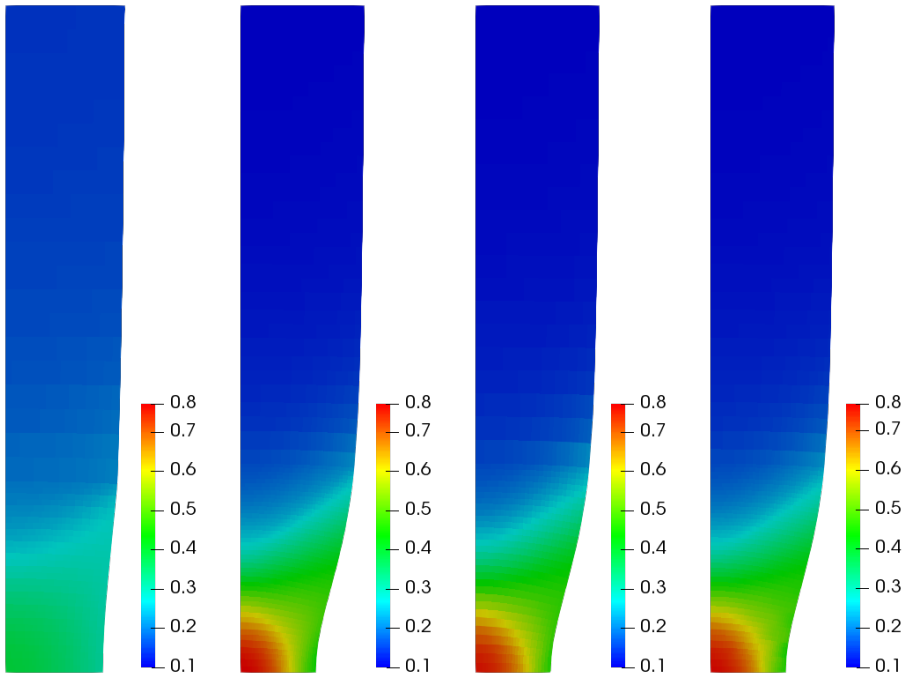

(a) Q1 (b) Q2 (c) Q2_RI (d) UPG

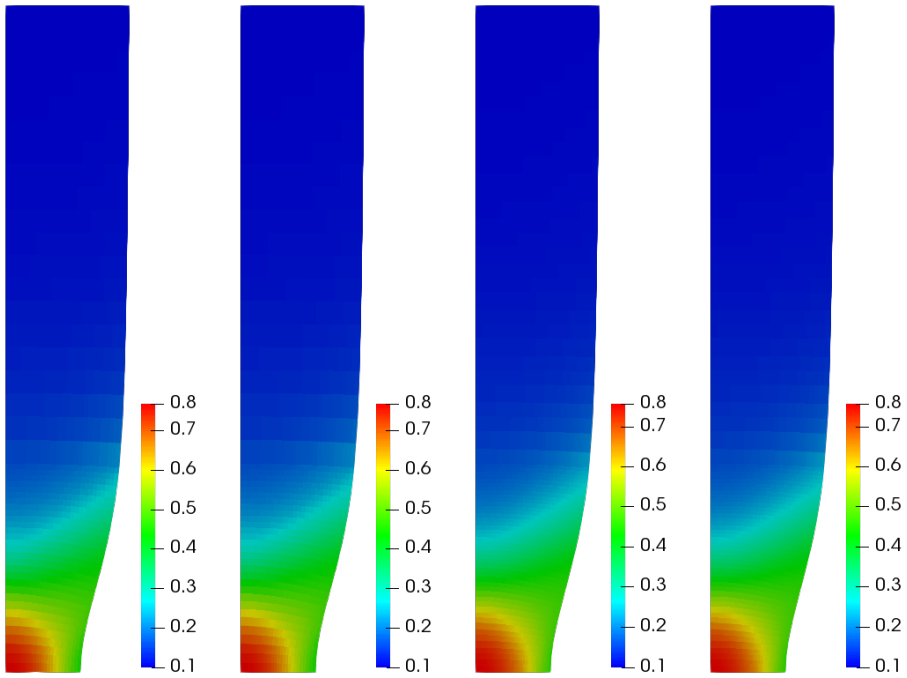

(e) HHO(1;1) (f) HHO(1;2) (g) HHO(2;2) (h) HHO(2;3)

Figure 4.3: Necking of a 2D rectangular bar: Equivalent plastic strain p at the quadrature points on the final configuration for the different methods.

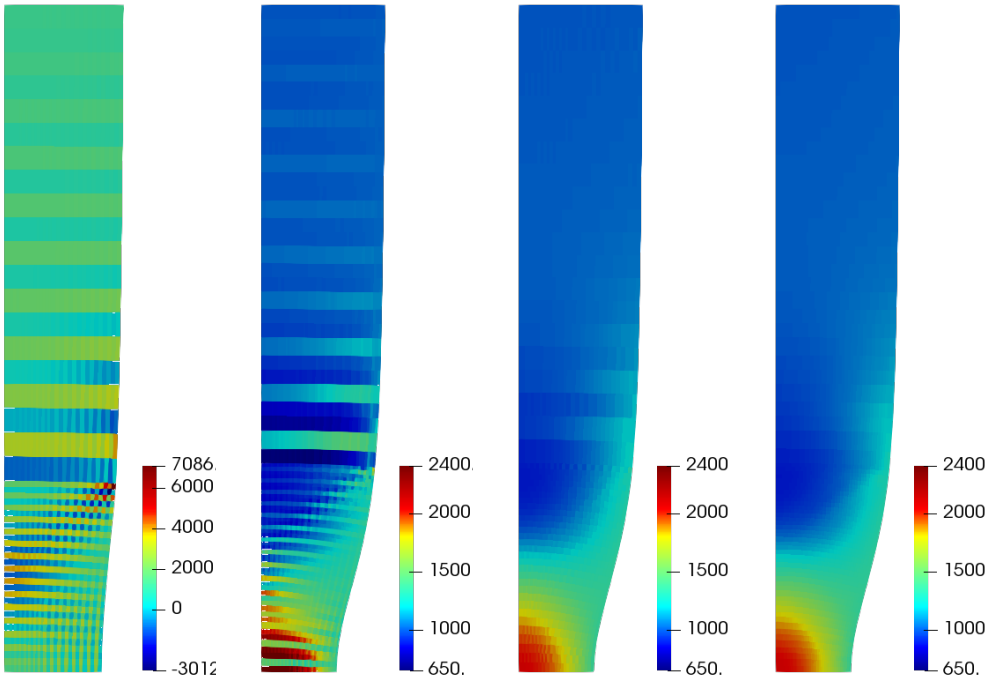

(a) Q1 (b) Q2 (c) Q2_RI (d) UPG

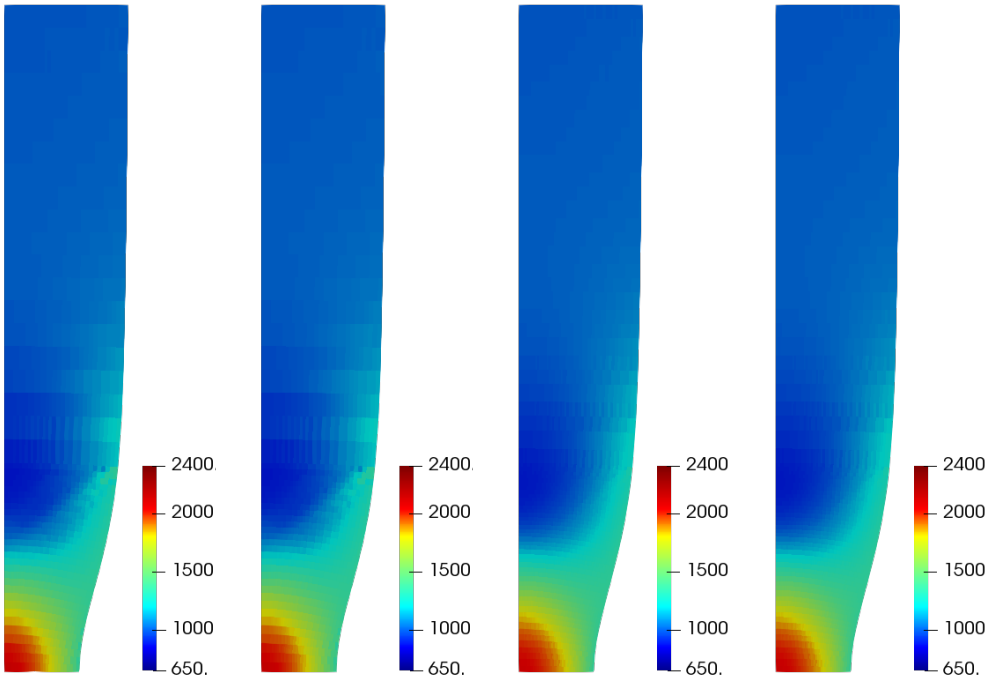

(e) HHO(1;1) (f) HHO(1;2) (g) HHO(2;2) (h) HHO(2;3)

Figure 4.4: Necking of a 2D rectangular bar: trace of the Cauchy stress tensor $\boldsymbol{\sigma}$ (in MPa) at the quadrature points on the final configuration for the different methods.

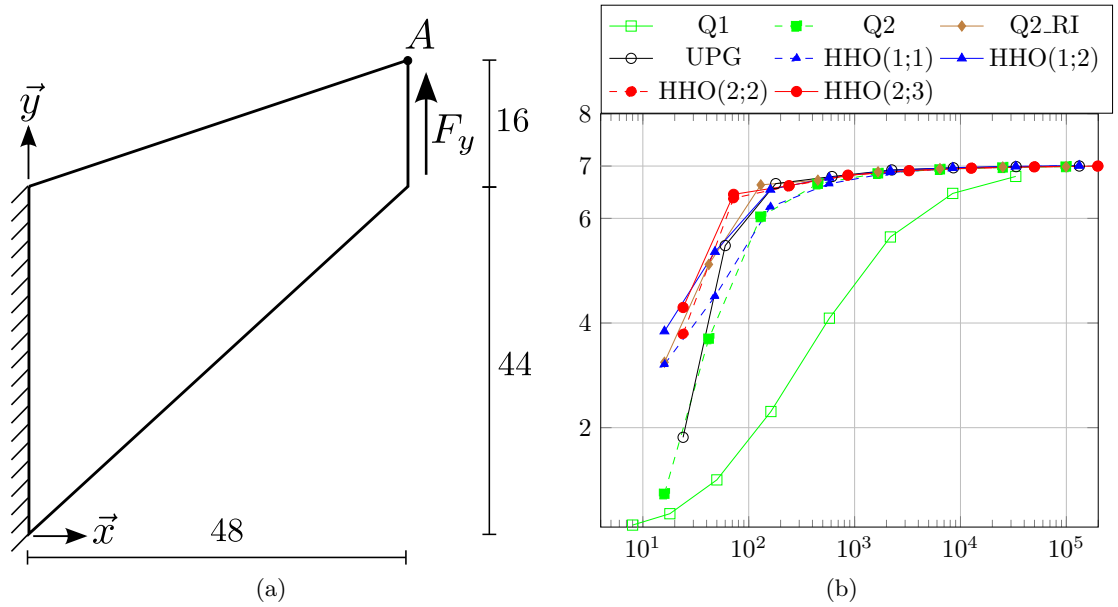

Figure 4.5: Cook's membrane: (a) Geometry and boundary conditions (dimensions in mm). (b) Convergence of the vertical displacement of the point A (in mm) vs. the number of degrees of freedom for Q1, Q2, Q2_RI, UPG, and HHO methods.

4.4.2 Cook's membrane

We consider the Cook's membrane problem which is a well known bending-dominated test case [191, 9, 112]. It consists of a tapered panel, clamped on one side, and subjected to a total vertical load $F_y = 5$ kN applied uniformly along all the opposite side, as shown in Fig. 4.5a. The simulation is performed on a sequence of refined quadrangular meshes such that each side contains 2^N edges with $0 \leq N \leq 6$. The vertical displacement of the point A versus the number of degrees of freedom is plotted in Fig. 4.5b for the different methods. As expected when comparing the number of degrees of freedom, the linear cG formulation Q1 has the slower convergence, HHO(1;2), Q2_RI, and UPG converge slightly faster than HHO(1;1), Q2, whereas HHO(2;2) and HHO(2;3) outperform all the other methods and give almost the same results. Moreover, we show in Fig. 4.6 the trace of the Cauchy stress tensor $\boldsymbol{\sigma}$ at the quadrature points on the final configuration. The cG formulations Q1 and Q2 present oscillations that confirm the presence of volumetric locking, contrary to the HHO, Q2_RI, and UPG methods which deliver similar and smooth results (even if the cG formulations Q1 and Q2 present volumetric locking in terms of stress, they converge in terms of displacement with mesh refinement). However, if we compare the trace of the Cauchy stress tensor $\boldsymbol{\sigma}$ for HHO(1;1) and HHO(1;2), we remark that the trace is slightly smoother near the upper-right corner for HHO(1;2) than for HHO(1;1). This can be explained by the presence of non-physical vertical localization bands of plastic deformations for HHO(1;1) and not for HHO(1;2). Localization bands constitute a well-known problem when the plasticity model is local. Computational practice with cG approximations indicates that increasing the order of the finite elements mitigates this issue. The same effect is observed here by increasing the degree of the cell unknowns (further numerical investigations are performed in Sect. 4.5.1 for HHO methods). An alternative is to use a non-local plasticity model [166].

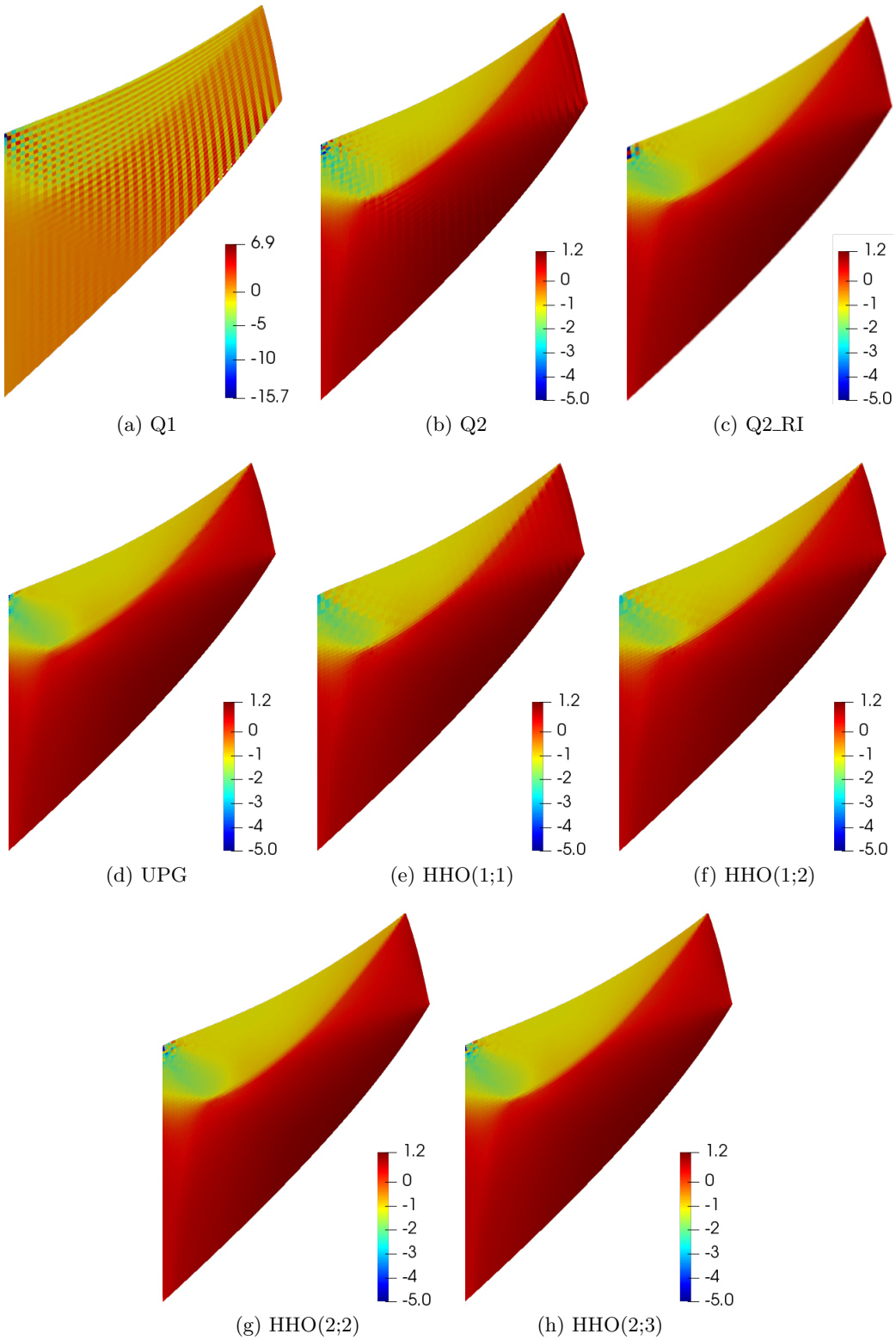

(a) Q1 (b) Q2 (c) Q2_RI

(d) UPG (e) HHO(1;1) (f) HHO(1;2)

(g) HHO(2;2) (h) HHO(2;3)

Figure 4.6: Cook's membrane: trace of the Cauchy stress tensor $\boldsymbol{\sigma}$ (in GPa) at the quadrature points on the final configuration for a 32×32 quadrangular mesh and for the different methods.

4.4.3 Torsion of a square-section bar

This third benchmark [143] allows one to test the robustness of HHO methods under large torsion. The bar has a square-section of length $L = 1$ mm and a height of $H = 5$ mm along the z-direction. The bottom end is clamped and the top end is subjected to a planar rotation of an angle Θ around its center along the z-direction and remains plane (the displacement of the top end along the z-direction is blocked), see Fig. 4.7a. The mesh is composed of 1900 hexahedra, see Fig. 4.7b. The equivalent plastic strain p is plotted in Fig. 4.8 for HHO(1;1) and for different rotation angles Θ. There is no sign of localization of the plastic deformations even for large rotations whatever the HHO variant is used. Moreover, the trace of the Cauchy stress tensor $\boldsymbol{\sigma}$ is plotted on the final configuration for $\Theta = 360°$ and for the Q2, UPG, and HHO methods in Fig. 4.9. As expected, there is no sign of volumetric locking for the HHO and UPG methods which give similar results contrary to Q2. The small oscillations observed at both ends are due to the imposed conditions on the displacement.

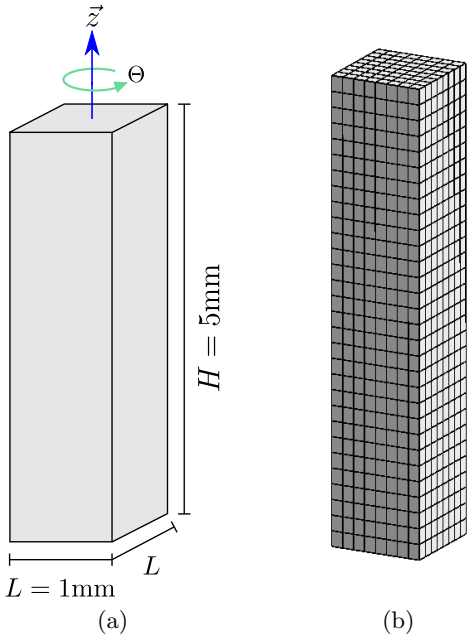

Figure 4.7: Torsion test of a square-section bar: (a) Geometry and boundary conditions (dimensions in mm) (b) Mesh in the reference configuration composed of 1920 hexahedra.

4.4.4 Quasi-incompressible sphere under internal radial force

This last benchmark [9] consists of a quasi-incompressible sphere under internal radial forces for which an analytical solution is known when the entire sphere has reached a plastic state. This benchmark is particularly challenging compared to the previous ones since we consider here perfect plasticity. The sphere has an inner radius $R_{in} = 0.8$ mm and an outer radius $R_{out} = 1$ mm. An internal radial force P is imposed. For symmetry reasons, only one-eighth of the sphere is discretized, and the mesh is composed of 1580 tetrahedra, see Fig. 4.10a. The simulation is performed until the limit load corresponding to an internal radial force $P_{lim} \simeq 20.43$ N is reached. The equivalent plastic strain p is plotted for HHO(1;2) in Fig. 4.10b, and the trace of the Cauchy stress tensor $\boldsymbol{\sigma}$ is compared for HHO, UPG and T2 methods in Fig. 4.11 at all the quadrature points on the final configuration for the limit load. We notice that the quadratic element T2 locks, whereas HHO and UPG do not present any sign

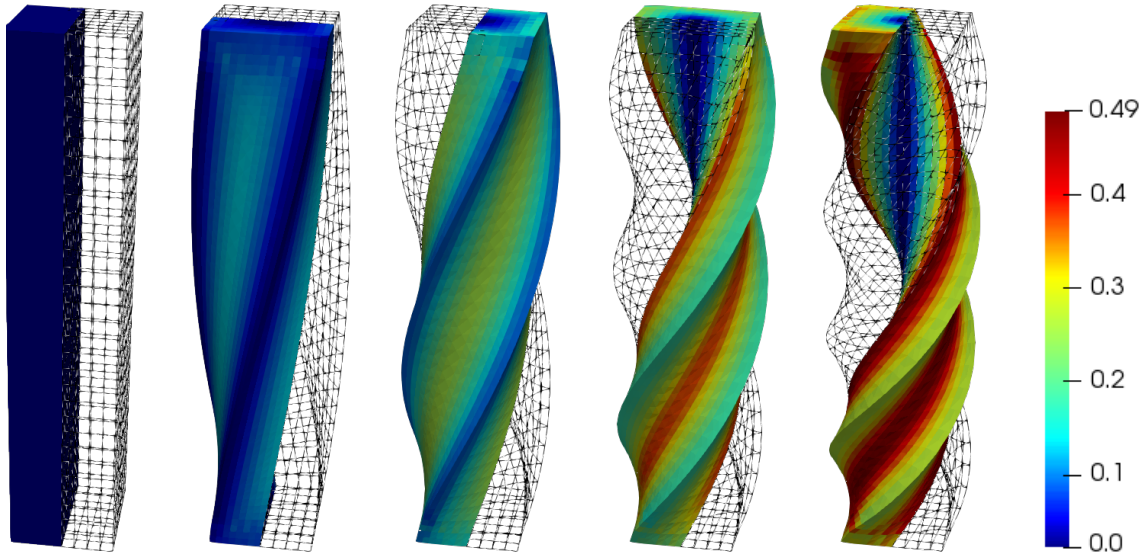

(a) $\Theta = 0°$ (b) $\Theta = 90°$ (c) $\Theta = 180°$ (d) $\Theta = 270°$ (e) $\Theta = 360°$

Figure 4.8: Torsion of a square-section bar: Equivalent plastic strain p for HHO(1;1) at the quadrature points for different rotation angles Θ.

of locking and produce results that are very close to the analytical solution. However, the trace of the Cauchy stress tensor $\boldsymbol{\sigma}$ is slightly more dispersed around the analytical solution for HHO(2;2) and HHO(2;3) than for HHO(1;1) and HHO(1;2) near the outer boundary. For this test case, we do not expect that HHO(2;2) and HHO(2;3) will deliver more accurate solutions than HHO(1;1) and HHO(1;2) since the geometry is discretized using tetrahedra with planar faces.

We next investigate the influence of the quadrature order k_Q on the accuracy of the solution. The trace of the Cauchy stress tensor $\boldsymbol{\sigma}$ is compared for HHO(1;1), HHO(2;2), and UPG methods in Fig. 4.12 at all the quadrature points on the final configuration for the limit load, and for a quadrature order k_Q higher than the one employed in Fig. 4.11 (HHO(1;2) and HHO(2;3) give similar results and are not shown for brevity). We remark that when we increase the quadrature order, UPG locks for quasi-incompressible finite deformations, whereas HHO does not lock, and the results are (only) a bit more dispersed around the analytical solution. Moreover, HHO(2;2) is less sensitive than HHO(1;1) to the choice of the quadrature order k_Q. Note that this problem is not present for HHO methods with small deformations [3]. Furthermore, this sensitivity to the quadrature order seems to be absent for finite deformations when the elastic deformations are compressible (the plastic deformations are still incompressible). To illustrate this claim, we perform the same simulations as before but for a compressible material. The Poisson ratio is taken now as $\nu = 0.3$ (recall that we used $\nu = 0.499$ in the quasi-incompressible case) whereas the other material parameters are unchanged. Unfortunately, an analytical solution is no longer available in the compressible case. We compare again the trace of the Cauchy stress tensor $\boldsymbol{\sigma}$ for HHO(1;1), HHO(2;2), and UPG methods in Fig. 4.13 at all the quadrature points on the final configuration and for different quadrature orders k_Q. We observe a quite marginal dependence on the quadrature order for HHO methods (as in the quasi-incompressible case); whereas the UPG method still locks if the order of the quadrature is increased. Moreover, in the compressible case, HHO(2;2) gives a more accurate solution than HHO(1;1).

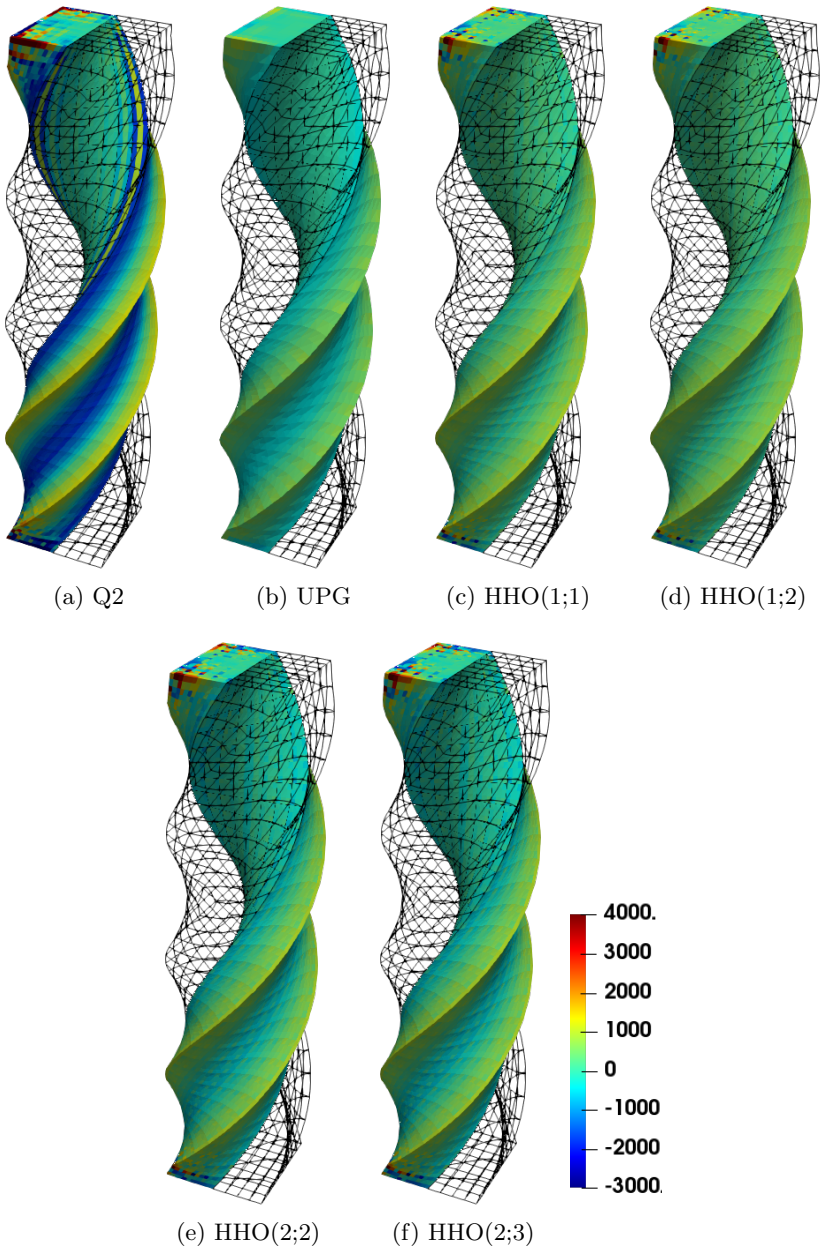

(a) Q2 (b) UPG (c) HHO(1;1) (d) HHO(1;2)

(e) HHO(2;2) (f) HHO(2;3)

Figure 4.9: Torsion of a square-section bar: trace of the Cauchy stress tensor $\boldsymbol{\sigma}$ (in MPa) at the quadrature points for $\Theta = 360°$ and for the HHO, UPG, and Q2 methods .

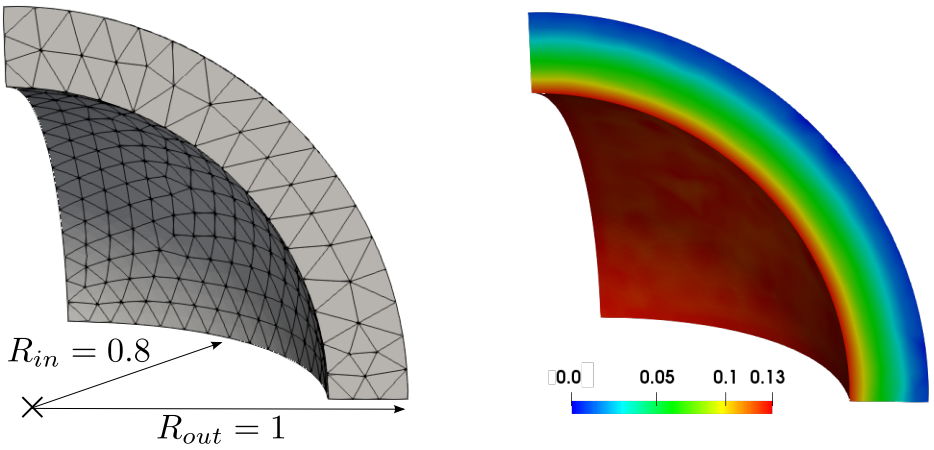

(a) (b)

Figure 4.10: Quasi-incompressible sphere under internal radial forces: (a) Mesh in the reference configuration composed of 1580 tetrahedra (dimensions in mm). (b) Equivalent plastic strain p for HHO(1;2) on the final configuration.

4.4.5 Summary of the above results

The proposed HHO method has been tested successfully on four benchmarks in two and three dimensions. A first conclusion is that the proposed HHO method is robust for large elastoplastic deformations and is locking-free as mixed methods but without the need to introduce additional globally coupled unknowns. HHO(2;2) and HHO(2;3) give generally more accurate results both for the displacement and the Cauchy stress tensor than HHO(1;1), HHO(1;2), and UPG on a fixed mesh (cG methods lock). Moreover, contrary to the UPG method, HHO methods are not very sensitive to the choice of the quadrature order (particularly for $k = 2$). Finally, HHO(1;1) appears to be more prone to the localization of the plastic deformations, contrary to the other variants HHO(1;2), HHO(2;2), and HHO(2;3).

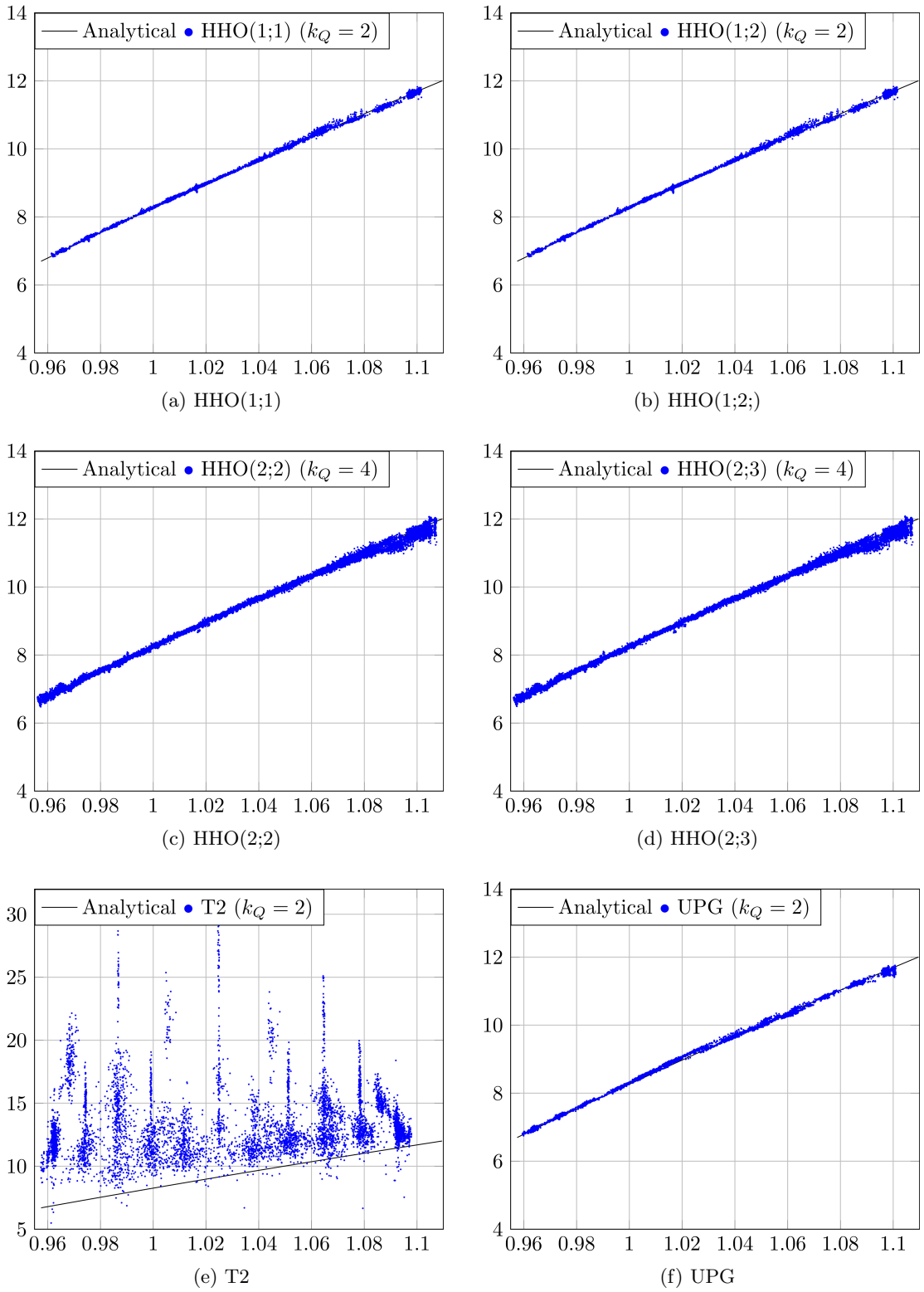

(a) HHO(1;1) (b) HHO(1;2;)

(c) HHO(2;2) (d) HHO(2;3)

(e) T2 (f) UPG

Figure 4.11: Quasi-incompressible sphere under internal radial force: trace of the Cauchy stress tensor $\boldsymbol{\sigma}$ (in MPa) vs. deformed radius r (in mm) for the different methods at all the quadrature points and for the limit load.

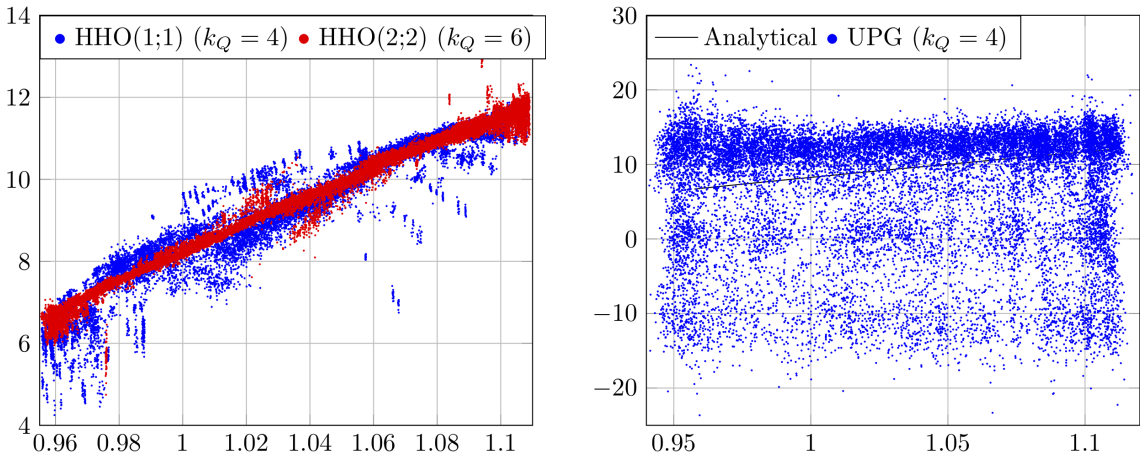

(a) HHO (b) UPG

Figure 4.12: Quasi-incompressible sphere under internal radial force: trace of the Cauchy stress tensor $\boldsymbol{\sigma}$ (in MPa) vs. deformed radius r (in mm) for HHO(1;1), HHO(2;2) and UPG at all the quadrature points for the limit load and for a higher quadrature order k_Q.

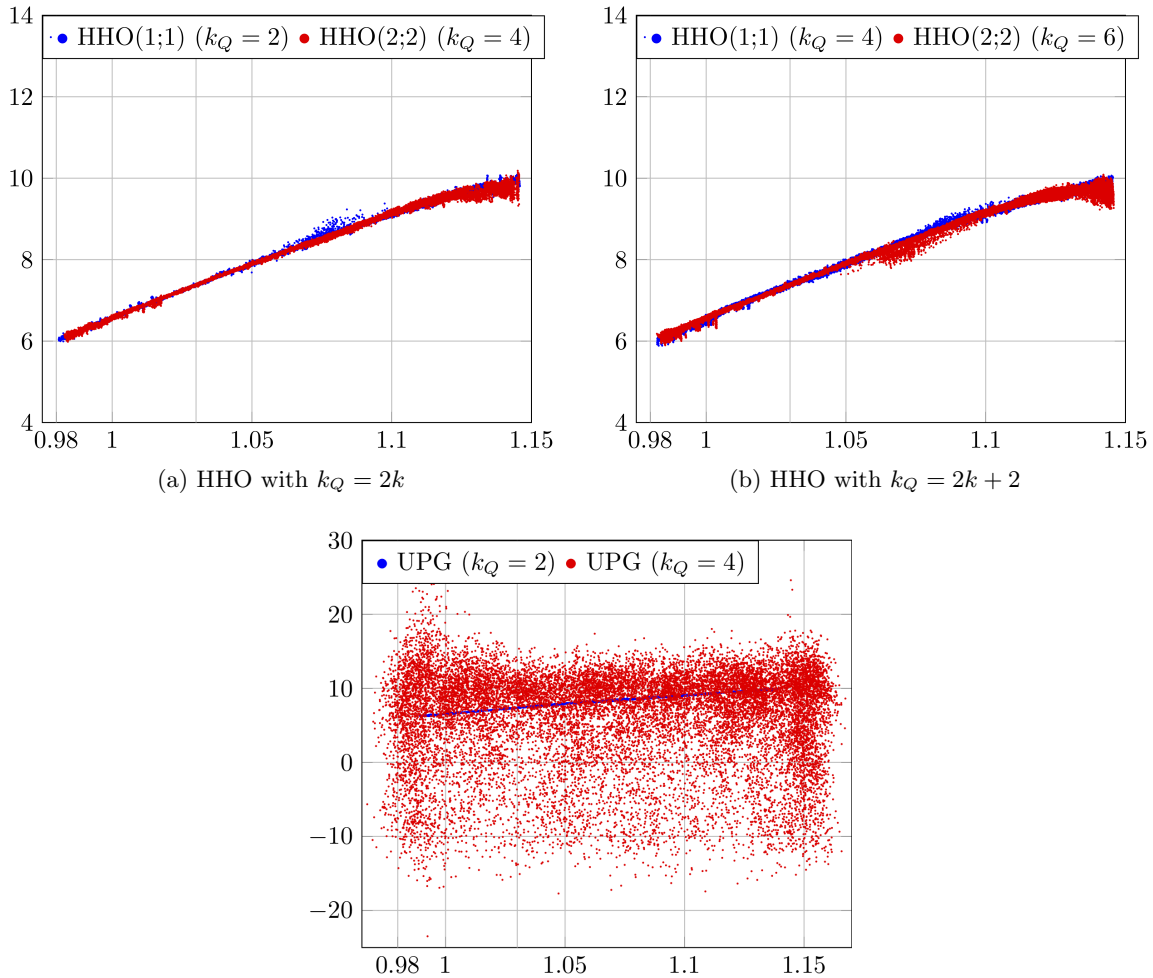

(a) HHO with $k_Q = 2k$

(b) HHO with $k_Q = 2k + 2$

(c) UPG

Figure 4.13: Compressible sphere ($\nu = 0.3$) under internal radial force: trace of the Cauchy stress tensor $\boldsymbol{\sigma}$ (in MPa) vs. deformed radius r (in mm) for the different methods at all the quadrature points and for the limit load.

4.5 Further numerical investigations

In this section, we perform further numerical investigations to test other capacities of HHO methods such as the support of general meshes with possibly non-conforming interfaces, the possibility of considering the lowest-order case $k = 0$, the dependence on the stabilization parameter β, and the application to an industrial study.

4.5.1 Polygonal meshes

In the previous sections, the proposed HHO method has been tested on simplicial and hexahedral meshes so as to be able to compare it to the UPG method which only supports this type of meshes. Our goal is now to illustrate that the HHO method supports general meshes with possibly non-matching interfaces. For our test cases, the polygonal meshes are generated from quadrangular meshes by removing the common face for some pairs of neighbouring cells and then merging the two cells in question (about 30% of the cells are merged) thereby producing non-matching interfaces materialized by hanging nodes for a significant portion of the mesh cells. We consider the Cook's membrane problem from Section 4.4.2 and we use a mesh composed of 719 polygonal cells including quads, pentagons (quads with one hanging node) and hexagons (quads with two hanging nodes). The trace of the Cauchy stress tensor $\boldsymbol{\sigma}$ is shown in Fig. 4.14 at the quadrature points on the reference configuration; and we compare the results with a reference solution computed with HHO(2;3) on a 32×32 quadrangular mesh. The results agree very well except for HHO(1;1) where the trace is not smooth due to the localization of the plastic deformations (as for the quadrangular mesh, see Section 4.4.2). A reason for the localization of the plastic deformations is the loss of coercivity of the consistent elastoplastic tangent modulus $\tilde{\mathbb{A}}_{ep}$. The evolution of the magnitude of the smallest eigenvalue $\theta_{\mathcal{T}_h,Q}$ of $\tilde{\mathbb{A}}_{ep}$ during the loading is plotted in Fig. 4.15. We remark that the magnitude of $\theta_{\mathcal{T}_h,Q}$ decreases quickly when the plastic evolution begins (around $F_y = 1$ kN), then $\theta_{\mathcal{T}_h,Q}$ continues to decrease more slowly and remains positive for all HHO methods except for HHO(1;1) where it decreases more quickly and becomes negative (so that Theorem 4.6 is no longer valid). As mentioned above, this loss of positive-definiteness of $\tilde{\mathbb{A}}_{ep}$ for HHO(1;1) can explain the presence of nonphysical plastic localization. Moreover, the distribution of the smallest eigenvalue $\theta^{\min}(\tilde{\mathbb{A}}_{ep})$ of $\tilde{\mathbb{A}}_{ep}$ at the quadrature points at the end of the loading $F_y = 5$ kN for the different HHO methods is summarized in Table 4.2. Only HHO(1;1) has negative eigenvalues. We remark that the number of quadrature points where $\tilde{\mathbb{A}}_{ep}$ has negative eigenvalues for HHO(1;1) or close to 0 (<0.5) for the others HHO methods is small compared to the total number of quadrature points. This confirms that the loss of positive-definiteness and the presence of plastic localization are local and confined to few quadrature points. Note that for a total vertical load $F_y > 6.1$ kN, $\theta_{\mathcal{T}_h,Q}$ is negative for all HHO methods.

4.5.2 Lowest-order variant

The main reason to take $k \geq 1$ in the HHO method applied to the linear elasticity problem is that the rigid-body motions $\underline{RM}(T)$ are then a subset of $\underline{U}_T^{1,1}$. The lowest-order case $k = 0$ and $l = 1$ is interesting since there are only d unknowns per face, i.e, two in 2D and three in 3D; and we could expect that the energy error, resp. the L^2-error, converges as $h|\underline{u}|_{\underline{H}^2(\Omega_0)}$, resp. as $h^2|\underline{u}|_{\underline{H}^2(\Omega_0)}$, for the linear elasticity problem. The difficulty with this lowest-order case is to deal with the rigid-body motions on the faces since unfortunately $\underline{RM}(T)_{|\partial T} \nsubseteq \mathbb{P}^0_{d-1}(\mathcal{F}_{\partial T};\mathbb{R}^d)$. Therefore, at the theoretical level, it is not clear that Lemma 4.3 still holds true. Nevertheless, we observed numerically that for the linear elasticity problem,

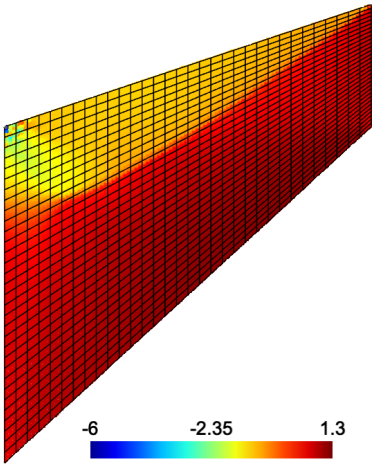

(a) Reference solution with HHO(2;3) on a quadrangular mesh

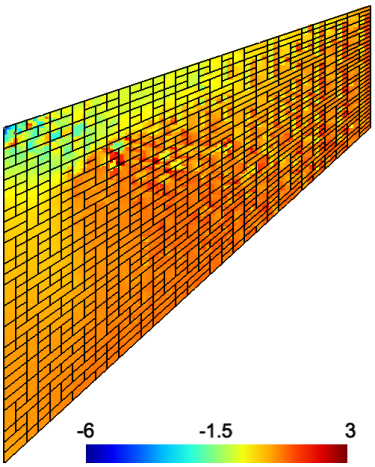

(b) HHO(1;1)

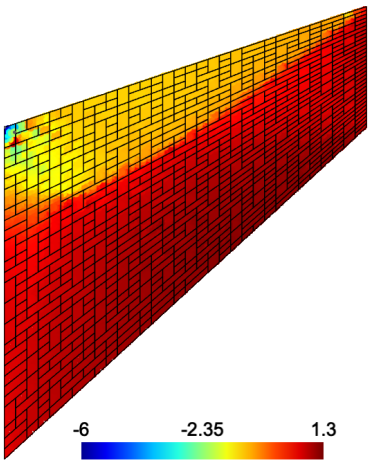

(c) HHO(1;2)

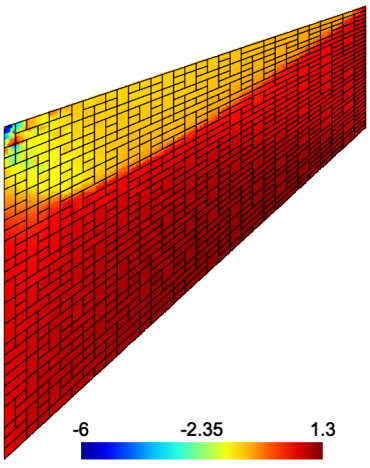

(d) HHO(2;2)

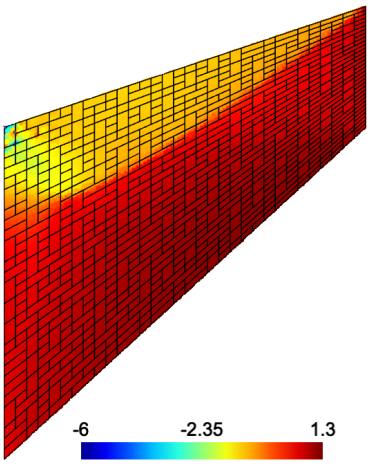

(e) HHO(2;3)

Figure 4.14: Cook's membrane: trace of the Cauchy stress tensor $\boldsymbol{\sigma}$ (in GPa) at the quadrature points on the reference configuration (a) Reference solution with HHO(2;3) on a 32×32 quadrangular mesh composed of 1024 cells. (b)-(e) Results for the different HHO variants on a mesh with hanging nodes composed of 719 polygonal cells.

Method	$\theta_{\mathcal{T}_h,Q}$ (in MPa)	Total number of eigenvalues by sub-interval over [-6; 170] (in MPa)							Total
		[-6; -1]	(-1; -0.5]	(-0.5; 0]	(0; 0.5]	(0.5; 1]	(1; 5]	(5; 150]	(150; 170]	
HHO(1;1)	-5.83	5	2	5	10	92	5435	1	546	6096
HHO(1;2)	0.46	0	0	0	3	968	4735	0	390	6096
HHO(2;2)	0.30	0	0	0	7	2073	9731	0	1005	12816
HHO(2;3)	0.29	0	0	0	8	2073	9729	0	1006	12816

Table 4.2: Cook's membrane: distribution of the smallest eigenvalue $\theta^{\min}(\tilde{\mathbb{A}}_{ep})$ (in MPa) of the consistent elastoplastic tangent modulus $\tilde{\mathbb{A}}_{ep}$ at the quadrature points at the end of the loading $F_y = 5$ kN for the different HHO methods on a mesh with hanging nodes composed of 719 polygonal cells.

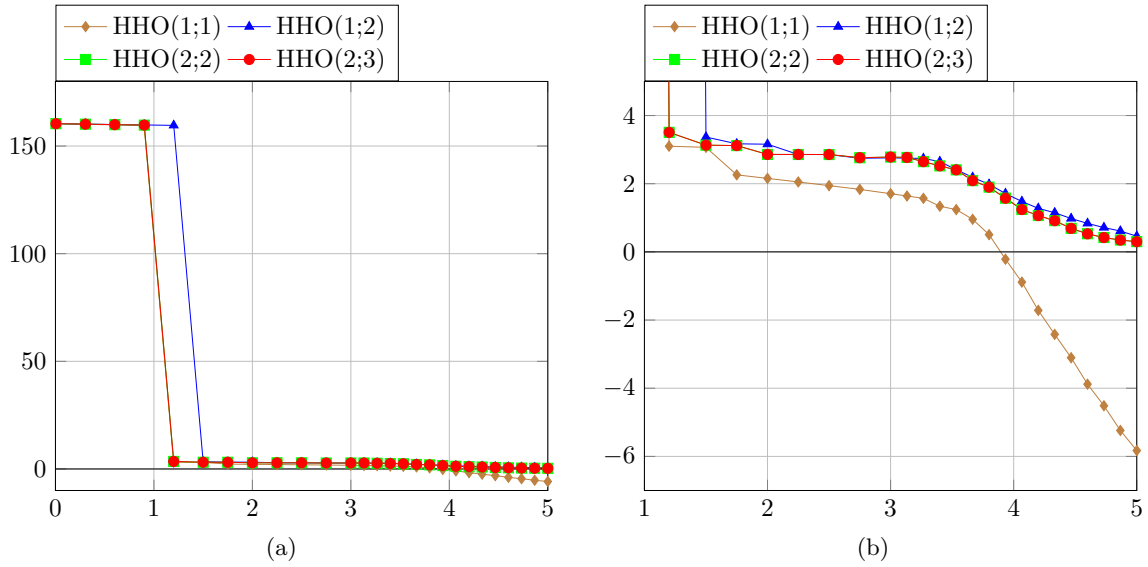

Figure 4.15: Cook's membrane: evolution of the magnitude of the smallest eigenvalue $\theta_{\mathcal{T}_h,Q}$ (in MPa) vs. vertical load applied F_y (in kN) for the different HHO methods on a non-conforming mesh with hanging nodes composed of 719 polygonal cells (a) during the complete loading (b) a zoom when the plastic evolution occurs.

the energy error, resp. the L^2-error, converges as $h|\underline{u}|_{\underline{H}^2(\Omega_0)}$, resp. as $h^2|\underline{u}|_{\underline{H}^2(\Omega_0)}$, (the expected optimal rates) if all the cells have at least $2d$ faces, i.e, four faces in 2D and six faces in 3D. This observation seems to be confirmed for small elastoplasticity. However, the conclusions are less clear for finite elastoplasticity. The equivalent plastic strain p and the trace of the Cauchy stress tensor $\boldsymbol{\sigma}$ are plotted in Fig. 4.16 at the quadrature points on the final configuration for the necking of a rectangular bar (see Section 4.4.1) approximated using the HHO(0;1) variant. We observe the absence of volumetric locking and that the results are close to those obtained for $k \geq 1$ (see Fig. 4.3 and Fig. 4.4). However, for the Cook's membrane problem (see Section 4.4.2), the displacement is not correct (not shown for brevity).

Remark 4.7 *In[122], a theoretical study of an HDG method for the linear elasticity problem in the equal-order case $k = 0$ is performed where the main difference with the present HHO method is the stabilization weight which is of the form $O(1)$ and no longer $O(h^{-1})$ as here. In this case, for the linear elasticity problem, the the energy error, the L^2-error, and the stress error converge as $h|\underline{u}|_{\underline{H}^2(\Omega_0)}$, $h|\underline{u}|_{\underline{H}^2(\Omega_0)}$, as $h^{\frac{1}{2}}|\underline{u}|_{\underline{H}^2(\Omega_0)}$, respectively, on general meshes. Moreover, recent numerical results still for the linear elasticity problem [187] indicate that the stress error can converge as $h|\underline{u}|_{\underline{H}^2(\Omega_0)}$. Nevertheless, the L^2-error converges slower for this HDG variant than what we could expect for the lowest-order HHO method.*

4.5.3 Influence of the stabilization parameter

To evaluate the influence of the stabilization parameter β_0, we compare the total number of Newton's iterations needed to solve the nonlinear problem (4.35) versus the magnitude of the stabilization parameter β_0. The Newton's iterations are stopped under the relative criterion $\|R_h(\delta\underline{\hat{v}}_h)\|_{\mathcal{T}_h} \leq 10^{-6}\|F_{\text{int}}(\delta\underline{\hat{v}}_h)\|_{\mathcal{T}_h}$ where F_{int} are the internal forces. We perform this comparison on two of the previous benchmarks, the Cook's membrane problem (see Section 4.4.2) and the quasi-incompressible sphere under internal radial force (see Section 4.4.4).

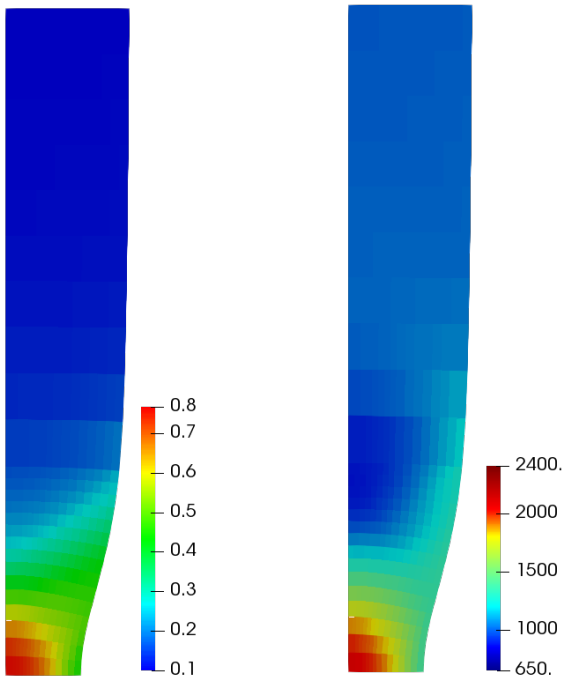

(a) Equivalent plastic strain p (b) Trace of the Cauchy stress tensor $\boldsymbol{\sigma}$

Figure 4.16: Necking of a 2D rectangular bar with low-order variant HHO(0;1): (a) equivalent plastic strain p and (b) trace of the Cauchy stress tensor $\boldsymbol{\sigma}$ (in MPa) at the quadrature points on the final configuration.

In Fig. 4.17a, we report the total number of Newton's iterations for the Cook's membrane problem with strain-hardening plasticity. We use a 32×32 quadrangular mesh, and 15 load increments of equal size are considered. On the one hand, we remark that the different HHO variants need almost the same total number of Newton's iterations (around 78 compared to 75 for UPG) if $\beta_0 \geq 0.1$; On the other hand, if $\beta_0 < 0.01$, the Newton's method stops converging whatever the HHO variant and the number of load increments. For the quasi-incompressible sphere under internal radial forces, the force is applied in 15 increments of equal size. Recall that this experiment is particularly challenging since we are considering here perfect plasticity for which the stability result from Theorem 4.6 is not applicable. In Fig. 4.17b, we plot the total number of Newton's iterations to perform the simulation. On the one hand, if $\beta_0 \geq 10$, all the HHO variants need almost to the same total number of Newton's iterations (around 57 compared to 55 for UPG). On the other hand, if $\beta_0 \leq 1$, the HHO variants with $k = 2$ need more Newton's iterations than the HHO variants with $k = 1$. As previously, if $\beta_0 < 0.1$, the Newton's method stops converging.

A first conclusion is therefore that the proposed HHO methods are stable for a large range of values of the stabilization parameter β_0. A second conclusion is that it seems reasonable to take $\beta_0 \in [1, 100]$ since the number of Newton's iterations is lower and close to the value for UPG, and the condition number does not increase too much. Note that for extremely large values of β_0, HHO methods reduce to H^1-conforming methods due to the matching of the face unknowns with the trace of the cell unknowns, and volumetric-locking can appear (not shown here for brevity).

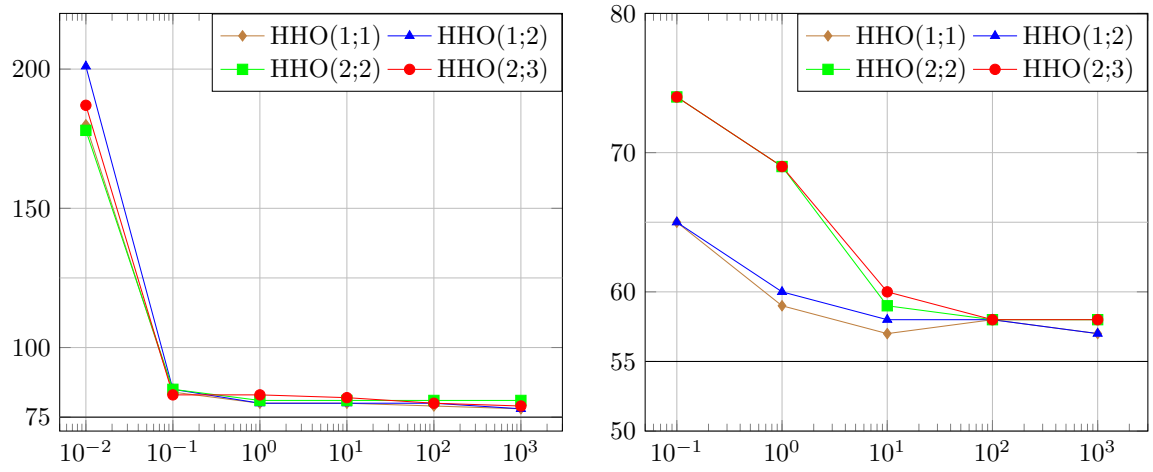

(a) Number of total Newton's iterations vs. β_0 for the Cook's membrane problem

(b) Number of total Newton's iterations vs. β_0 for the quasi-incompressible sphere under internal radial force

Figure 4.17: Influence of the stabilization parameter: Total number of Newton's iterations vs. β_0 for (a) the Cook's membrane and (b) the quasi-incompressible sphere under internal radial forces.

4.5.4 An industrial application: a pump under internal forces

This study based on an industrial problem focuses on the deformation of a pump and two of its pipes under the influence of a pressurized fluid, see Fig. 4.18a for the geometry. Since the study is restricted to the structural part of the problem, the force applied by the fluid on the walls of the pump and its pipes is replaced by an equivalent internal force. This surface force

corresponds to a pressure of 14 MPa in the reference configuration. Moreover, the bottom of the pump is clamped and the other surfaces are free. For this industrial application, strain-hardening plasticity is considered with the following material parameters: Young modulus $E = 200$ GPa, Poisson ratio $\nu = 0.3$, hardening parameter $H = 200$ MPa, initial and infinite yield stresses $\sigma_{y,0} = \sigma_{y,\infty} = 500$ MPa, and saturation parameter $\delta = 0$. The mesh is depicted in Fig. 4.18b and is composed of 23,837 tetrahedra and 41,218 triangular faces.

The computations are performed in parallel with `code_aster` for UPG and HHO(1;2) methods in order to compare the results. The discrete global problem to solve has around 190,000 dofs for UPG and 500,00 dofs for HHO(1;2). The Euclidean norm of the displacement is plotted in Fig. 4.19 on the deformed configuration for HHO(1;2). Note that the upper left part of the pump has the largest displacement. Moreover, the equivalent plastic strain p is plotted for UPG and HHO(1;2) methods in Fig. 4.20 at all the quadrature points on the deformed configuration. We remark that the plastic deformations are mainly present in the pipes and in particular at the junction between the pump and its pipes with nearly 97% of equivalent plastic strain p. The threshold of 10% of equivalent plastic strain having been largely reached, the finite deformation framework is preferable for this problem to the small deformation framework. Finally, the von Mises stress signed with the trace of the Cauchy stress tensor is showed in Fig. 4.21 and the trace of the Cauchy stress tensor in Fig. 4.22 at all the quadrature points on the deformed configuration. The results are in good agreement between UPG and HHO(1;2), and there is no sign of volumetric locking.

This simulation validates the results of HHO methods on industrial problems.

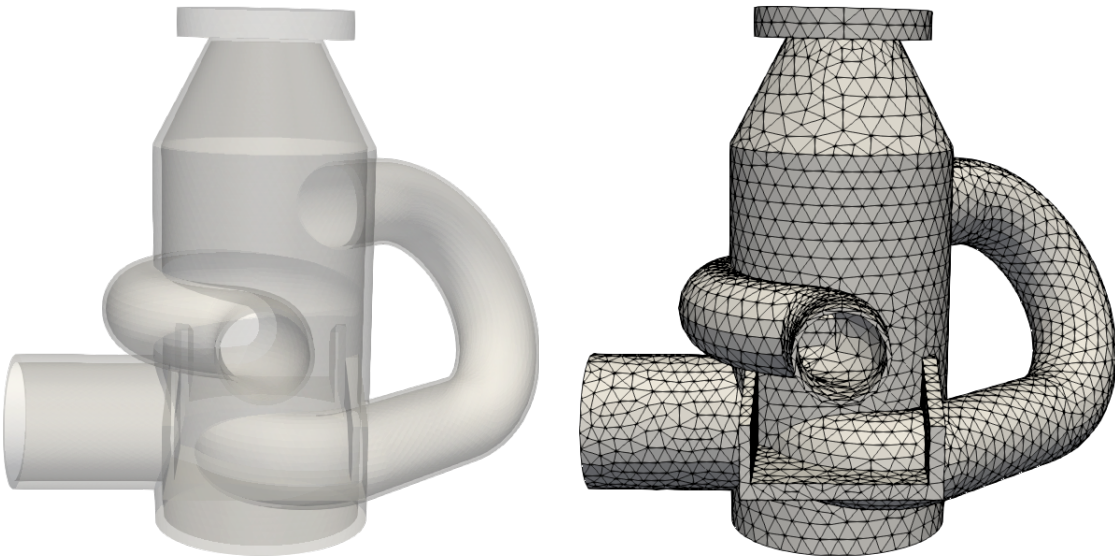

(a) Geometry of the pump (b) Mesh composed of 23,837 tetrahedra

Figure 4.18: Pump under internal forces: (a) Geometry of the pump (b) Mesh composed of 23,837 tetrahedra and 41,218 triangular faces.

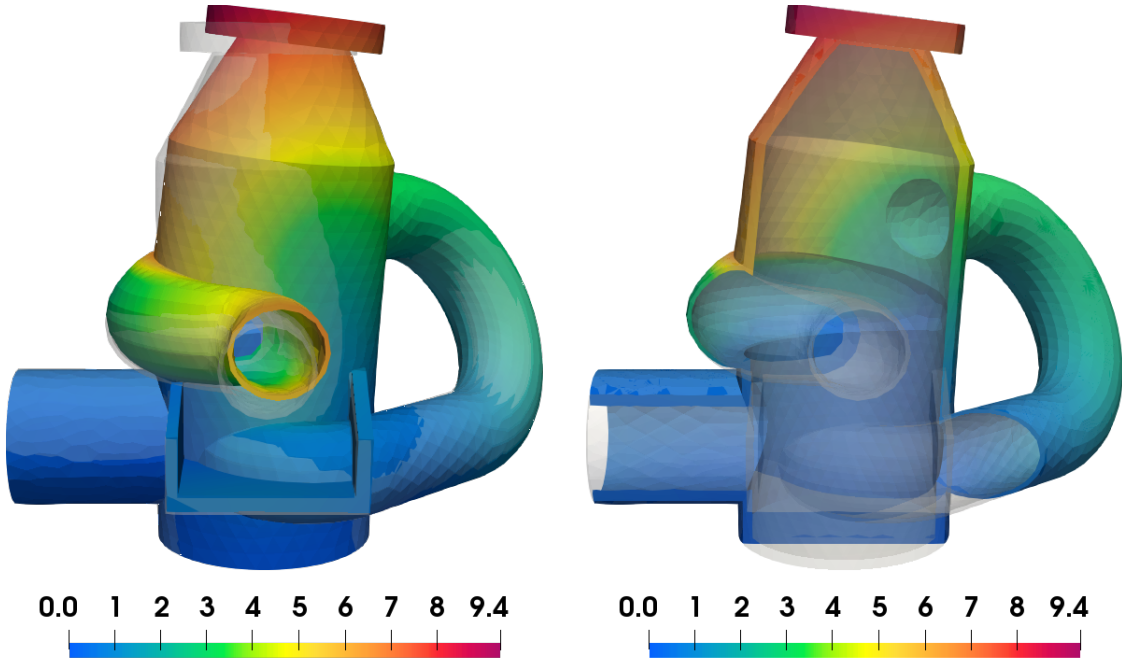

(a) Full pump (b) Cut in the x-plane

Figure 4.19: Pump under internal forces: Euclidean norm of the displacement (in mm) for HHO(1;2) on the deformed configuration (a) full pump with transparent reference configuration (b) cut in the x-plane.

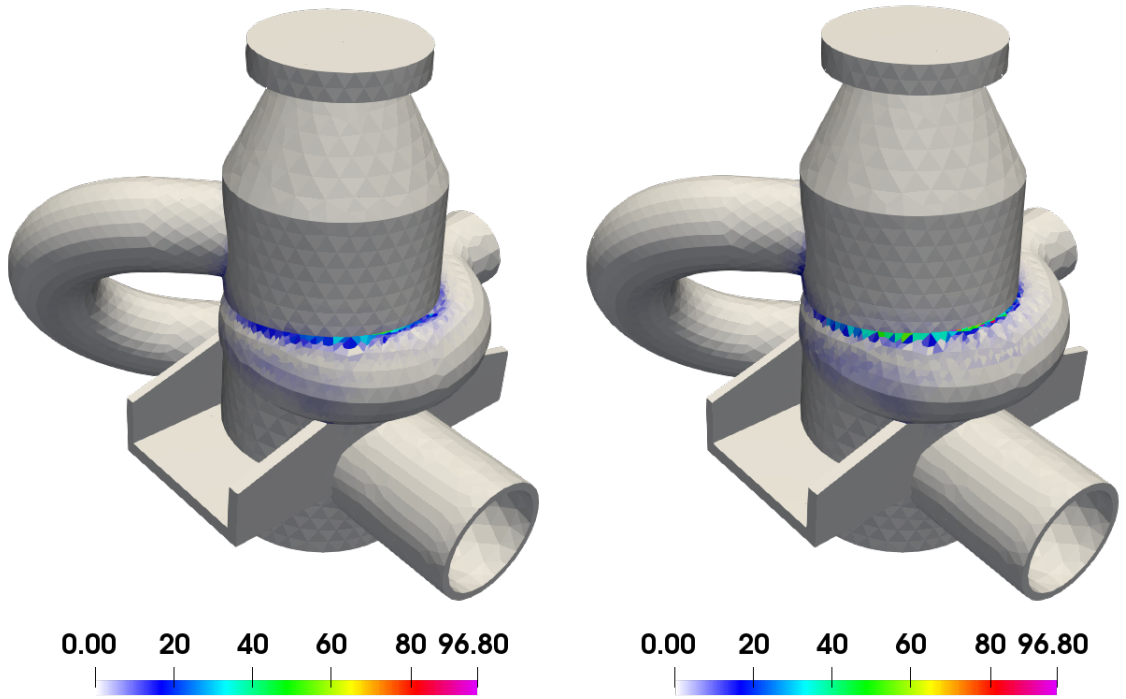

(a) UPG (b) HHO(1;2)

Figure 4.20: Pump under internal forces: equivalent plastic strain p (in %) at the quadrature points for UPG and HHO(1;2) methods on the deformed configuration.

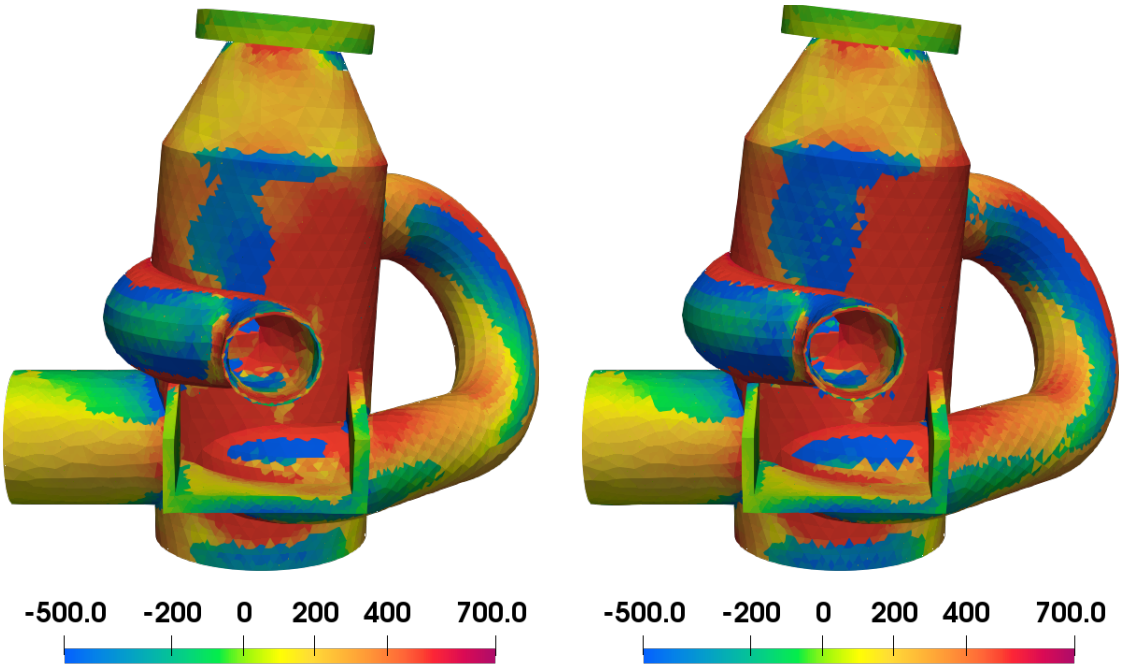

(a) UPG (b) HHO(1;2)

Figure 4.21: Pump under internal forces: von Mises stress signed with the trace of the Cauchy stress tensor (in MPa) at the quadrature points for UPG and HHO(1;2) methods on the deformed configuration.

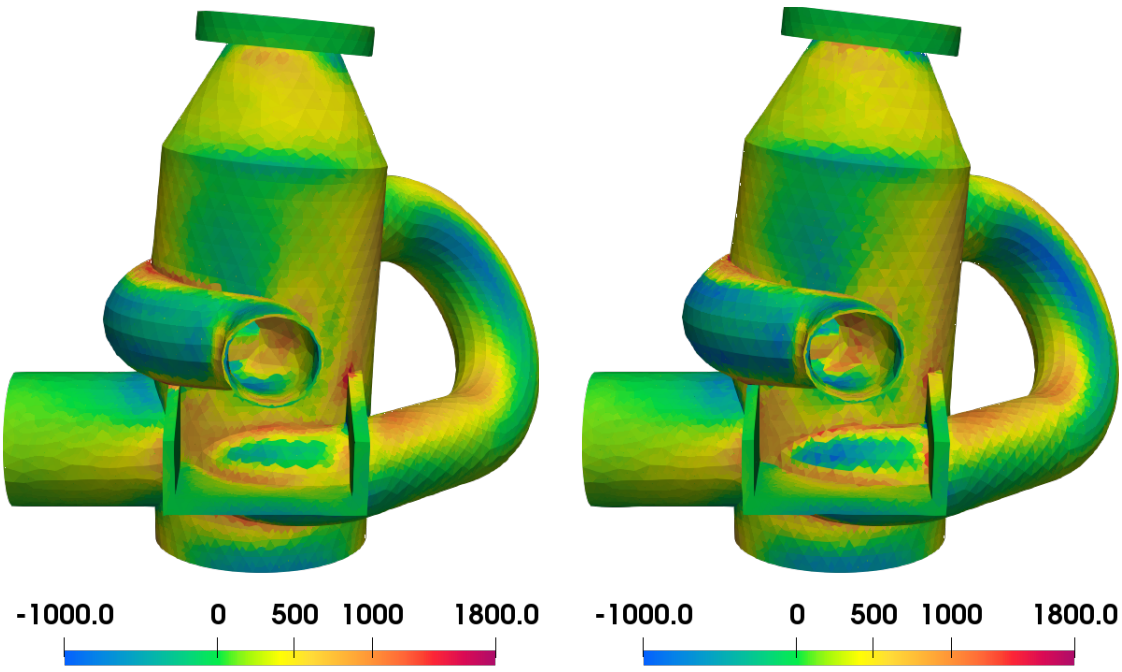

(a) UPG (b) HHO(1;2)

Figure 4.22: Pump under internal forces: trace of the Cauchy stress tensor $\boldsymbol{\sigma}$ (in MPa) at the quadrature points for UPG and HHO(1;2) methods on the deformed configuration.

4.6 Conclusion

We have devised and evaluated numerically a Hybrid High-Order (HHO) method to approximate finite elastoplastic deformations within a logarithmic strain framework. This framework allows one to re-use constitutive laws developed originally for small deformations in the context of finite deformations. The HHO method exhibits a robust behavior for strain-hardening plasticity as well as for perfect plasticity, and produces accurate solutions with a moderate number of degrees of freedom for various benchmarks from the literature. In particular, as mixed methods, the HHO method avoids volumetric locking due to plastic incompressiblity, but with less unknowns than mixed methods for the same accuracy. Moreover, the HHO method supports general meshes with non-matching interfaces.

This work can be pursued in several directions. One could use a non-local plasticity model, as for example a strain-gradient plasticity model, to take into account scale-dependent effects [166] and possibly prevent unphysical localization of the plastic deformations. Furthermore, the extension of the present HHO method to contact and friction problems is the subject of the following chapter.

CHAPTER 5

NITSCHE'S METHOD FOR CONTACT AND TRESCA FRICTION IN SMALL DEFORMATIONS

Abstract. We present the extension of a numerical method to weakly discretize contact and Tresca friction conditions in small strain elasticity, that was previously devised and studied for Dirichlet and scalar Signorini conditions [K. Cascavita et al. 'Hybrid High-Order discretizations combined with Nitsche's method for Dirichlet and Signorini boundary conditions'. Submitted]. This method supports polyhedral meshes with nonmatching interfaces and is based on a combination of the Hybrid high-order (HHO) method and Nitsche's method. Since HHO methods involve both cell unknowns and face unknowns, this leads to different formulations of Nitsche's consistency and penalty terms, either using the trace of the cell unknowns (cell version) or using directly the face unknowns (face version). This paper focuses on the face version, which has better robustness properties than the cell version in the incompressible limit. Also, we study different variants of Nitsche's formulation (symmetric, non-symmetric, skew-symmetric). We prove optimal error estimates for all these variants. Moreover these estimates are robust in the incompressible limit for bilateral contact. Numerical experiments in two and three dimensions for academic problems illustrate the theoretical results and reveal that, in practice, the method is robust for all the variants of Nitsche's formulation. Finally, an extension to associative plasticity is proposed and studied numerically.

This chapter results of a collaboration with Franz Chouly and an article entitled "*A Hybrid High-Order discretization combined with Nitsche's method for contact and Tresca friction in small strain elasticity*" [62] has been submitted.

5.1 Introduction

Hybrid high-order (HHO) methods have been introduced for linear elasticity in [89] and for linear diffusion problems in [91]. HHO methods are formulated in terms of face unknowns which are polynomials of arbitrary order $k \geq 0$ on each mesh face and in terms of cell unknowns which are polynomials of order $l \in \{k, k \pm 1\}$, with $l \geq 0$, in each mesh cell. The devising of HHO methods hinges on two operators, both defined locally in each mesh cell: a reconstruction operator and a stabilization operator. The cell unknowns can be eliminated locally by static condensation leading to a global transmission problem posed solely in terms of the face unknowns. HHO methods offer various assets: they support polyhedral meshes,

lead to local conservation principles, and optimal convergence rates. HHO methods have been bridged in [74] to Hybridizable Discontinuous Galerkin methods [76] and to nonconforming Virtual Element Methods [18]. HHO methods have been extended to many other PDEs. Examples in computational mechanics include nonlinear elasticity [40], hyperelasticity with finite deformations [2], and elastoplasticity with small [3] and finite [4] deformations.

The goal of the present work is to devise, analyze and evaluate numerically a HHO method to approximate contact problems with Tresca friction in small strain elasticity. Either unilateral or bilateral contact can be considered. The main ingredient is to employ a Nitsche-type formulation to enforce the nonlinear frictional contact conditions. The present HHO-Nitsche method can be deployed on polyhedral meshes. As is classical with Nitsche's technique, we can consider symmetric, incomplete and skew-symmetric variants. Our main results, Theorem 5.14 and Corollary 5.17, provide for all symmetry variants quasi-optimal energy error estimates with convergence rates of order $\mathcal{O}(h^r)$ for solutions with regularity H^{1+r}, $r \in (\frac{1}{2}, k+1]$, where h is the mesh size and $k \geq 1$ is the order of the polynomials for the cell and the face unknowns, except for the face unknowns located on the frictional contact boundary where polynomials of order $(k+1)$ are employed. Note that the optimal order of convergence is $\mathcal{O}(h^{k+1})$ obtained with $r = k+1$. These results are established under minimal thresholds for the penalty parameters weakly enforcing the contact and friction conditions, and do not require any assumption on the (a priori unknown) friction/contact set. Particular attention in the analysis is paid to the dependency of these parameters on the Lamé parameters, showing that the skew-symmetric variant enjoys more favorable properties regarding robustness in the incompressible limit, at least from a theoretical viewpoint. Our 2D and 3D numerical tests include comparisons with benchmarks from the literature and with solutions obtained with the industrial software `code_aster`. We also consider a prototype of an industrial application featuring a notched plug in a rigid pipe. Our numerical tests indicate a more favorable dependency of the penalty parameters on the material parameters since robustness in the quasi-incompressible regime is observed in all considered situations.

Let us put our work in perspective with the literature. For most discretizations, Tresca friction creates additional difficulties in order to establish optimal convergence in comparison to the frictionless case (see, e.g., [207, 141, 107] and the references therein for frictionless contact). As a consequence convergence results addressing Tresca friction are quite few. The rate $\mathcal{O}(h^r)$ for the energy error with a regularity $H^{1+r}(\Omega)$, $r \in (0, 1]$, has been obtained in the 2D case for a mixed low-order finite element method (FEM) under some technical assumptions on the contact/friction set [207, Theorem 4.9] (this is the first optimal bound to the best of our knowledge). In the 3D case the rate $O(h^{\min(\frac{1}{2}, r)})$ has also been reached without additional assumption [207, Theorem 4.10]. For the penalty method, the rate of $\mathcal{O}(h^{\frac{1}{2}+\frac{r}{2}+r^2})$ with a regularity $H^{\frac{3}{2}+r}(\Omega)$, $r \in (0, \frac{1}{2})$, and the quasi-optimal rate of $\mathcal{O}(h|\log h|^{\frac{1}{2}})$ with a regularity $H^2(\Omega)$ were established in [65] without additional assumptions on the contact/friction set. This result has been improved recently in [96] and optimal rates are recovered if the penalty parameter is large enough. An important advance to discretize contact problems was accomplished in [64] by combining Nitsche's method with FEM. The FEM-Nitsche method differs from standard penalty techniques which are generally not consistent. Moreover no additional unknown (Lagrange multiplier) is needed and therefore no discrete inf-sup condition must be fulfilled contrary to mixed methods. For contact problems with Tresca friction discretized with FEM-Nitsche, optimal energy-error convergence of order $O(h^r)$ has been proved in [61] with the regularity $H^{1+r}(\Omega)$, $r \in (\frac{1}{2}, k]$, where $k \geq 1$ is the polynomial degree of the Lagrange finite elements. To this purpose there is no need of any additional assumption on the contact/friction set. Note that the technical difficulties associated with the treatment of contact and friction condition when Nitsche's technique is not employed, are not limited to

FEM, but appear as well for other discretizations such as discontinuous Galerkin (dG) [205] or Virtual finite elements (VEM) [206].

The devising and analysis of HHO-Nitsche methods was started in [50] for the scalar Signorini problem. Therein a face version and a cell version were analyzed, depending on the choice of the discrete unknown used to formulate the penalty terms. The cell version used cell unknowns of order $(k+1)$ (these unknowns can be eliminated by static condensation) and a modified reconstruction operator inspired from the unfitted HHO method from [45], leading to energy error estimates of order $\mathcal{O}(h^r)$ with H^{1+r}-regularity, $r \in (\frac{1}{2}, k+1]$. Unfortunately, the modification of the reconstruction operator is not convenient in the context of elasticity as it hampers a key commuting property with the divergence operator which is crucial in the incompressible limit. This difficulty is circumvented in the present work by using a modified face version with face polynomials of order $(k+1)$ on the faces located on the contact/friction boundary. The numerical analysis also involves two novelties. Firstly, the error analysis, which adapts ideas from [67, 68] for FEM-Nitsche to HHO-Nitsche, is more involved than [50] since it covers all the symmetry variants and since it hinges on a sharper bound on the consistency error allowing for a sharper threshold on the penalty parameters, especially in the case of the skew-symmetric variant. Secondly, for the first time concerning FEM-Nitsche as well, we track explicitly the dependency of the penalty parameters on the Lamé parameters for the various symmetry variants. Furthermore the present study is completed with 2D and 3D numerical tests including a prototype for an industrial application. Finally, let us mention that polyhedral discretizations for contact and friction problems have received some attention recently, as motivated by some numerical evidence illustrating their flexibility and accuracy. These discretizations use for instance VEM [211, 206], the weak Galerkin (WG) method [125] or the hybridizable discontinous Galerkin (HDG) methods [216], combined with different techniques to handle contact and friction (such as a direct approximation of the variational equality, node-to-node contact, penalty, Lagrange multipliers). The present work constitutes, to our knowledge, the first polyhedral discretization method for frictional contact problems using Nitsche's technique.

This paper is organized as follows. The model problem is described in Section 5.2. The HHO-Nitsche method is introduced in Section 5.3, and the stability and error analysis is contained in Section 5.4. Numerical results are discussed in Section 5.5. Section 5.6 is concerned with an extension of the proposed method to contact with plasticity.

5.2 Model problem

Let Ω be a polygon/polyhedron in $\mathbb{R}^d$, $d \in \{2,3\}$, representing the reference configuration of an elastic body. The boundary $\partial\Omega$ is partitioned into three nonoverlapping parts (see Fig 5.1): the Dirichlet boundary Γ_{D}, the Neumann boundary Γ_{N}, and the contact/friction boundary Γ_{C}. We assume $\mathrm{meas}(\Gamma_{\mathrm{D}}) > 0$ to prevent rigid body motions and $\mathrm{meas}(\Gamma_{\mathrm{C}}) > 0$ to ensure that contact is present. The small strain assumption is made, as well as plane strain if $d = 2$. The linearized strain tensor associated with a displacement field $\underline{v} : \Omega \to \mathbb{R}^d$ is $\boldsymbol{\varepsilon}(\underline{v}) := \frac{1}{2}(\boldsymbol{\nabla}\underline{v} + \boldsymbol{\nabla}\underline{v}^T) \in \mathbb{R}^{d\times d}_{\mathrm{sym}}$. Assuming isotropic behavior, the Cauchy stress tensor resulting from the strain tensor $\boldsymbol{\varepsilon}(\underline{v})$ is denoted by $\boldsymbol{\sigma}(\underline{v})$ and is given by

$$\boldsymbol{\sigma}(\underline{v}) = 2\mu\boldsymbol{\varepsilon}(\underline{v}) + \lambda\,\mathrm{trace}(\boldsymbol{\varepsilon}(\underline{v}))\boldsymbol{I}_d \in \mathbb{R}^{d\times d}_{\mathrm{sym}}, \tag{5.1}$$

where μ and λ are the Lamé coefficients of the material satisfying $\mu > 0$ and $3\lambda + 2\mu > 0$, and $\boldsymbol{I}_d$ is the identity tensor of order d. In what follows, we set $\kappa := \max(1, \frac{\lambda}{2\mu})$. Let $\underline{n}$ be the unit outward normal vector to Ω. On the boundary we consider the following decompositions

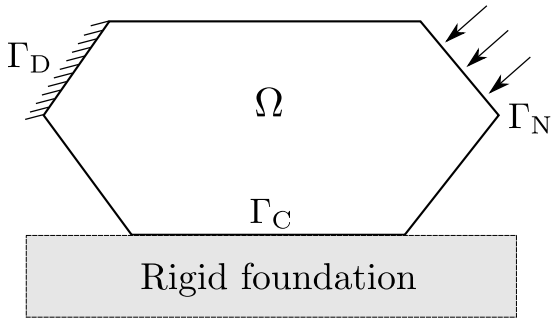

Figure 5.1: Geometry of the contact problem.

into normal and tangential components:

$$\underline{v} = v_n \underline{n} + \underline{v}_t \quad \text{and} \qquad \underline{\sigma}_n(\underline{v}) := \boldsymbol{\sigma}(\underline{v})\cdot\underline{n} = \sigma_n(\underline{v})\underline{n} + \underline{\sigma}_t(\underline{v})$$

where $v_n := \underline{v}\cdot\underline{n}$ and $\sigma_n(\underline{v}) := \underline{\sigma}_n(\underline{v})\cdot\underline{n}$ (so that $\underline{v}_t\cdot\underline{n} = 0$ and $\underline{\sigma}_t(\underline{v})\cdot\underline{n} = 0$).

The body is subjected to volume forces $\underline{f} \in L^2(\Omega;\mathbb{R}^d)$ in Ω and to surface loads $\underline{g}_N \in L^2(\Gamma_N;\mathbb{R}^d)$ on Γ_N, and it is clamped on Γ_D (for simplicity). The model problem consists in finding the displacement field $\underline{u} : \Omega \to \mathbb{R}^d$ such that

$$\begin{cases} \underline{\nabla}\cdot\boldsymbol{\sigma}(\underline{u}) + \underline{f} = \underline{0} & \text{in } \Omega, \\ \underline{u} = \underline{0} & \text{on } \Gamma_D, \\ \underline{\sigma}_n(\underline{u}) = \underline{g}_N & \text{on } \Gamma_N, \\ (5.3) \text{ and } (5.4) \text{ hold true} & \text{on } \Gamma_C, \end{cases} \tag{5.2}$$

where the unilateral contact conditions on Γ_C are as follows:

$$\text{(i) } u_n \le 0, \qquad \text{(ii) } \sigma_n(\underline{u}) \le 0, \qquad \text{(iii) } \sigma_n(\underline{u})\, u_n = 0, \tag{5.3}$$

whereas the Tresca friction conditions on Γ_C read:

$$\text{(iv) } |\underline{\sigma}_t(\underline{u})| \le s \quad \text{if } \underline{u}_t = \underline{0}, \qquad \text{(v) } \underline{\sigma}_t(\underline{u}) = -s\frac{\underline{u}_t}{|\underline{u}_t|} \quad \text{if } |\underline{u}_t| > 0, \tag{5.4}$$

where $s \ge 0$ is a given threshold and $|\cdot|$ stands for the Euclidean norm in $\mathbb{R}^d$ (or the absolute value depending on the context). More generally s can be a nonnegative-valued function on Γ_C.

Remark 5.1 *In the Tresca friction model (5.4), it is assumed that the amplitude of the normal friction threshold is known (i.e., $\mathscr{F}|\sigma_n(\underline{u})| = s$, see, e.g., [148, Section 10.3]). The introduction of the Tresca friction model is motivated more by its mathematical simplicity than by physical reasons, though it can be of use in special situations. For instance:*

- *when a thin belt/tape is pressed against an elastic body, with a known pressure (see, e.g., [148, Chapter 10]),*
- *for persistent contact between solids with high intensity of contact pressures, such as it may occur in earth sciences (see, e.g., [178] and references therein).*

Moreover the Tresca friction model can be useful for instance when Coulomb friction is approximated iteratively (see, e.g., [133] and [155, Section 9, Theorem 7]).

Remark 5.2 (Variants) *The case of frictionless contact is recovered by setting $s := 0$ in (5.4). The case of bilateral contact with Tresca friction can be considered by keeping (5.4) whereas (5.3) is substituted by the following equation:*

$$u_n = 0 \text{ on } \Gamma_C. \tag{5.5}$$

In the case of unilateral contact with Tresca friction, nonzero tangential stress can occur in regions with no-adhesion, which is rather unphysical. The setting of bilateral contact prevents such situations.

We introduce the Hilbert space $\underline{V}_{\mathrm{D}}$ and the convex cone $\underline{K}$ such that

$$\underline{V}_{\mathrm{D}} := \left\{ \underline{v} \in H^1(\Omega;\mathbb{R}^d) \mid \underline{v} = \underline{0} \text{ on } \Gamma_{\mathrm{D}} \right\}, \quad \underline{K} := \{ \underline{v} \in \underline{V}_{\mathrm{D}} \mid v_n \le 0 \text{ on } \Gamma_{\mathrm{C}} \},$$

i.e., the Dirichlet condition on Γ_{D} is explicitly enforced in the space $\underline{V}_{\mathrm{D}}$ and the non-interpenetration condition on Γ_{C} is explicitly enforced in the cone $\underline{K}$. We define the following bilinear form and the following linear and nonlinear forms:

$$a(\underline{v},\underline{w}) := (\boldsymbol{\sigma}(\underline{v}),\boldsymbol{\varepsilon}(\underline{w}))_{\boldsymbol{L}^2(\Omega)} = (2\mu\boldsymbol{\varepsilon}(\underline{v}),\boldsymbol{\varepsilon}(\underline{w}))_{\boldsymbol{L}^2(\Omega)} + (\lambda\nabla\cdot\underline{v},\nabla\cdot\underline{w})_{L^2(\Omega)}, \tag{5.6}$$

$$\ell(\underline{w}) := (\underline{f},\underline{w})_{\underline{L}^2(\Omega)} + (\underline{g}_{\mathrm{N}},\underline{w})_{\underline{L}^2(\Gamma_{\mathrm{N}})}, \qquad j(\underline{w}) := (s,|\underline{w}_t|)_{\underline{L}^2(\Gamma_{\mathrm{C}})}, \tag{5.7}$$

for any $\underline{v}$ and $\underline{w}$ in $\underline{V}_{\mathrm{D}}$. The weak formulation of (5.2) as a variational inequality of the second kind is

$$\begin{cases} \text{Find } \underline{u} \in \underline{K} \text{ such that} \\ a(\underline{u},\underline{w}-\underline{u}) + j(\underline{w}) - j(\underline{u}) \ge \ell(\underline{w}-\underline{u}), \quad \forall\, \underline{w} \in \underline{K}. \end{cases} \tag{5.8}$$

This problem admits a unique solution according, e.g., to [148, Theorem 10.2].

An important observation is that it is possible to reformulate the contact and friction conditions (5.3)-(5.4) as nonlinear equations. For any real number $x \in \mathbb{R}$, let $[x]_{\mathbb{R}^-} := \min(x,0)$ denote its projection onto the closed convex subset $\mathbb{R}^- := (-\infty,0]$. Moreover, let $[\cdot]_\alpha$ denote the orthogonal projection onto $\mathscr{B}(\underline{0},\alpha) \subset \mathbb{R}^d$, where $\mathscr{B}(\underline{0},\alpha)$ is the closed ball centered at the origin $\underline{0}$ and of radius $\alpha > 0$, i.e., for all $\underline{x} \in \mathbb{R}^d$, we have $[\underline{x}]_\alpha := \underline{x}$ if $|\underline{x}| \le \alpha$ and $[\underline{x}]_\alpha := \alpha\frac{\underline{x}}{|\underline{x}|}$ if $|\underline{x}| > \alpha$. The following result has been pointed out in [79] (see also [61] for formal proofs).

Proposition 5.3 (Reformulation as nonlinear conditions) *Let γ_n and γ_t be positive functions on Γ_C. The unilateral contact with Tresca friction conditions (5.3)-(5.4) can be reformulated as follows:*

$$\sigma_n(\underline{u}) = [\tau_n(\underline{u})]_{\mathbb{R}^-}, \qquad \tau_n(\underline{u}) := \sigma_n(\underline{u}) - \gamma_n u_n, \tag{5.9}$$

$$\underline{\sigma}_t(\underline{u}) = [\underline{\tau}_t(\underline{u})]_s, \qquad \underline{\tau}_t(\underline{u}) := \underline{\sigma}_t(\underline{u}) - \gamma_t\underline{u}_t. \tag{5.10}$$

Remark 5.4 *The conditions of Coulomb friction can be written similarly as:*

$$\begin{cases} |\underline{\sigma}_t(\underline{u})| \le \mathscr{F}|\sigma_n(\underline{u})|, & \text{if } \underline{u}_t = \underline{0}, \quad \text{(iv)} \\ \underline{\sigma}_t(\underline{u}) = -\mathscr{F}|\sigma_n(\underline{u})|\dfrac{\underline{u}_t}{|\underline{u}_t|} & \text{otherwise.} \quad \text{(v)} \end{cases} \tag{5.11}$$

where $\mathscr{F} \ge 0$ is the friction coefficient. Conditions (5.11) mean that, at a given contact point on Γ_C, sliding can not occur while the magnitude of the tangential stress $|\underline{\sigma}_t(\underline{u})|$ is strictly below the threshold $-\mathscr{F}\sigma_n(\underline{u})$. When the threshold $-\mathscr{F}\sigma_n(\underline{u})$ is reached, sliding may happen, in a direction opposite to $\underline{\sigma}_t(\underline{u})$ (see, e.g., [148, Chapter 10]). Remark that this static form of

Coulomb friction is an adaptation of the quasi-static (or dynamic) Coulomb's law, in which the tangential velocity $\dot{\underline{u}}_t$ plays the same role as the displacement $\underline{u}_t$ (see , e.g., [23, 109, 110]). A formulation such as (5.11) is obtained for instance when the quasi-static Coulomb's law is discretized with a time-marching scheme (see, e.g., [207]). The mathematical analysis of FEM-Nitsche with Coulomb friction is much more involved than for Tresca friction, due to the lack of strong monotonicity coming from the Coulomb term. Some first results of existence and well-posedness are however provided in [66].

5.3 HHO-Nitsche method

In this section we devise and analyze the HHO-Nitsche method to approximate the frictional contact problem (5.8).

5.3.1 Meshes and discrete unknowns

Let $(\mathcal{T}_h)_{h>0}$ be a mesh sequence, where for all $h > 0$, the mesh $\mathcal{T}_h$ is composed of nonempty disjoint cells such that $\overline{\Omega} = \bigcup_{T\in\mathcal{T}_h} \overline{T}$. The mesh cells are conventionally open subsets in $\mathbb{R}^d$, and they can have a polygonal/polyhedral shape with straight edges (if $d = 2$) or planar faces (if $d = 3$). This setting in particular allows for meshes with hanging nodes. The mesh sequence $(\mathcal{T}_h)_{h>0}$ is assumed to be shape-regular in the sense of [89]. In a nutshell, each mesh $\mathcal{T}_h$ admits a matching simplicial submesh $\mathfrak{S}_h$ having locally equivalent length scales to those of $\mathcal{T}_h$, and the mesh sequence $(\mathfrak{S}_h)_{h>0}$ is shape-regular in the usual sense of Ciarlet. The meshsize is denoted $h := \max_{T\in\mathcal{T}_h} h_T$, with h_T the diameter of the cell T and $\underline{n}_T$ denotes the unit outward normal to T. Discrete trace and inverse inequalities in the usual form are available on shape-regular polyhedral mesh sequences (see, e.g., [88]).

A closed subset F of $\overline{\Omega}$ is called a mesh face if it is a subset with nonempty relative interior of some affine hyperplane H_F and if (i) either there are two distinct mesh cells $T_1, T_2 \in \mathcal{T}_h$ so that $F = \partial T_1 \cap \partial T_2 \cap H_F$ (and F is called an interface) (ii) or there is one mesh cell $T_1 \in \mathcal{T}_h$ so that $F = \partial T_1 \cap \Gamma \cap H_F$ (and F is called a boundary face). The mesh faces are collected in the set $\mathcal{F}_h$ which is further partitioned into the subset of interfaces $\mathcal{F}_h^{\mathrm{i}}$ and the subset of boundary faces $\mathcal{F}_h^{\mathrm{b}}$. We assume that the meshes are compatible with the boundary partition $\partial\Omega = \overline{\Gamma_{\mathrm{D}}} \cup \overline{\Gamma_{\mathrm{N}}} \cup \overline{\Gamma_{\mathrm{C}}}$, which leads to the partition of the boundary faces as $\mathcal{F}_h^{\mathrm{b}} = \mathcal{F}_h^{\mathrm{b,D}} \cup \mathcal{F}_h^{\mathrm{b,N}} \cup \mathcal{F}_h^{\mathrm{b,C}}$ (with obvious notation).

Let $k \geq 1$ be the polynomial degree. For all $T \in \mathcal{T}_h$, let $\mathcal{F}_{\partial T}$ be the collection of the mesh faces that are subsets of ∂T, let $\mathcal{F}_{\partial T}^{\mathrm{i}} := \mathcal{F}_{\partial T} \cap \mathcal{F}_h^{\mathrm{i}}$, $\mathcal{F}_{\partial T}^{\mathrm{b,C}} := \mathcal{F}_{\partial T} \cap \mathcal{F}_h^{\mathrm{b,C}}$, and we use a similar notation for $\mathcal{F}_{\partial T}^{\mathrm{b,D}}$ and $\mathcal{F}_{\partial T}^{\mathrm{b,N}}$. We set $\mathcal{F}_{\partial T}^{\backslash} := \mathcal{F}_{\partial T}^{\mathrm{i}} \cup \mathcal{F}_{\partial T}^{\mathrm{b,D}} \cup \mathcal{F}_{\partial T}^{\mathrm{b,N}}$ for the collection of all the faces composing ∂T except those located on Γ_{C}. The local HHO unknowns belong to discrete space

$$\hat{\underline{U}}_T^k := \mathbb{P}_d^k(T;\mathbb{R}^d) \times \mathbb{P}_{d-1}^{k/k+1}(\mathcal{F}_{\partial T};\mathbb{R}^d),$$

where $\mathbb{P}_d^k(T;\mathbb{R}^d)$ is composed of the restrictions to T of d-variate polynomials of total degree at most k, and

$$\mathbb{P}_{d-1}^{k/k+1}(\mathcal{F}_{\partial T};\mathbb{R}^d) := \mathbb{P}_{d-1}^{k}(\mathcal{F}_{\partial T}^{\backslash};\mathbb{R}^d) \times \mathbb{P}_{d-1}^{k+1}(\mathcal{F}_{\partial T}^{\mathrm{b,C}};\mathbb{R}^d),$$

where $\mathbb{P}_{d-1}^{k}(\mathcal{F}_{\partial T}^{\backslash};\mathbb{R}^d)$ and $\mathbb{P}_{d-1}^{k+1}(\mathcal{F}_{\partial T}^{\mathrm{b,C}};\mathbb{R}^d)$ are composed of the restrictions to $\mathcal{F}_{\partial T}^{\backslash}$ and $\mathcal{F}_{\partial T}^{\mathrm{b,C}}$, respectively, of piecewise $(d-1)$-variate polynomials of total degree at most k and $(k+1)$, respectively. A generic element in $\hat{\underline{U}}_T^k$ is a pair $\hat{\underline{v}}_T := (\underline{v}_T, \underline{v}_{\partial T})$, where $\underline{v}_T \in \mathbb{P}_d^k(T;\mathbb{R}^d)$ is the cell unknown and $\underline{v}_{\partial T} \in \mathbb{P}_{d-1}^{k/k+1}(\mathcal{F}_{\partial T};\mathbb{R}^d)$ is the face unknown. The degrees of freedom are

illustrated in Fig. 5.2, where a dot indicates one degree of freedom (which is not necessarily computed as a point evaluation).

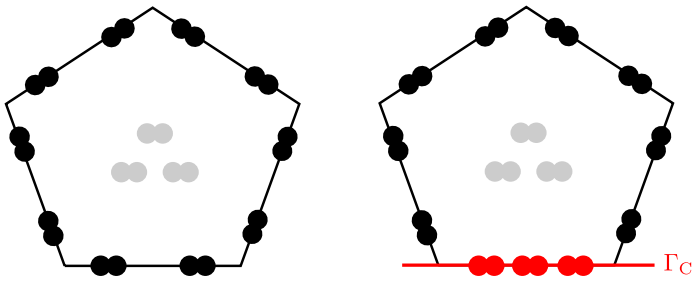

(a) Pentagonal cell with no contact face ($\mathcal{F}_{\partial T}^{\backslash} = \mathcal{F}_{\partial T}$)

(b) Pentagonal cell with a contact face in red ($\mathcal{F}_{\partial T}^{\backslash} \subsetneq \mathcal{F}_{\partial T}$)

Figure 5.2: Face (black or red) and cell (gray) degrees of freedom in $\underline{\hat{U}}_T^k$ for $k = 1$ and $d = 2$ (each dot represents a degree of freedom which is not necessarily a point evaluation).

Remark 5.5 (Face unknowns) *We use a polynomial order $(k+1)$ on the faces located on the contact boundary (it is also possible to use this order on all the boundary faces). This choice is motivated by the error analysis, where it will be shown that it allows one to recover error bounds with optimal convergence order. Moreover this choice increases only marginally the computational cost with respect to using the same order k for all the faces.*

5.3.2 Local HHO operators

The first key ingredient in the devising of the HHO method is a local symmetric strain reconstruction in each mesh cell $T \in \mathcal{T}_h$. Following [2, 40, 3], we define the local discrete symmetric gradient operator $\boldsymbol{E}_T^k : \underline{\hat{U}}_T^k \to \mathbb{P}_d^k(T;\mathbb{R}_{\mathrm{sym}}^{d\times d})$ such that, for all $\underline{\hat{v}}_T \in \underline{\hat{U}}_T^k$, $\boldsymbol{E}_T^k(\underline{\hat{v}}_T) \in \mathbb{P}_d^k(T;\mathbb{R}_{\mathrm{sym}}^{d\times d})$ solves the following local problem: For all $\boldsymbol{\tau} \in \mathbb{P}_d^k(T;\mathbb{R}_{\mathrm{sym}}^{d\times d})$,

$$(\boldsymbol{E}_T^k(\underline{\hat{v}}_T), \boldsymbol{\tau})_{\boldsymbol{L}^2(T)} := (\boldsymbol{\varepsilon}(\underline{v}_T), \boldsymbol{\tau})_{\boldsymbol{L}^2(T)} + (\underline{v}_{\partial T} - \underline{v}_{T|\partial T}, \boldsymbol{\tau}\cdot\underline{n}_T)_{\underline{L}^2(\partial T)}. \tag{5.12}$$

Moreover, the local discrete divergence operator $D_T^k : \underline{\hat{U}}_T^k \to \mathbb{P}_d^k(T;\mathbb{R})$ is simply defined by taking the trace of the discrete symmetric gradient: For all $\underline{\hat{v}}_T \in \underline{\hat{U}}_T^k$,

$$D_T^k(\underline{\hat{v}}_T) := \mathrm{trace}(\boldsymbol{E}_T^k(\underline{\hat{v}}_T)). \tag{5.13}$$

The second key ingredient is a local stabilization operator $\underline{S}_{\partial T}^k : \underline{\hat{U}}_T^k \to \mathbb{P}_{d-1}^{k/k+1}(\partial T;\mathbb{R}^d)$ used to penalize in a least-squares sense the difference between the face unknown $\underline{v}_{\partial T}$ and the trace of the cell unknown $\underline{v}_{T|\partial T}$. Let $\underline{\Pi}_{\partial T}^{k/k+1}$ and $\underline{\Pi}_T^k$ be the L^2-orthogonal projections onto $\mathbb{P}_{d-1}^{k/k+1}(\mathcal{F}_{\partial T};\mathbb{R}^d)$ and $\mathbb{P}_d^k(T;\mathbb{R}^d)$, respectively. Then we set, for all $\underline{\hat{v}}_T \in \underline{\hat{U}}_T^k$,

$$\underline{S}_{\partial T}^k(\underline{\hat{v}}_T) := \underline{\Pi}_{\partial T}^{k/k+1}\big(\underline{v}_{\partial T} - \underline{D}_T^{k+1}(\underline{\hat{v}}_T)_{|\partial T}\big) - \underline{\Pi}_T^k\big(\underline{v}_T - \underline{D}_T^{k+1}(\underline{\hat{v}}_T)\big)_{|\partial T}. \tag{5.14}$$

Here $\underline{D}_T^{k+1} : \underline{\hat{U}}_T^k \to \mathbb{P}_d^{k+1}(T;\mathbb{R}^d)$ is a local displacement reconstruction operator such that, for all $\underline{\hat{v}}_T \in \underline{\hat{U}}_T^k$, $\underline{D}_T^{k+1}(\underline{\hat{v}}_T) \in \mathbb{P}_d^{k+1}(T;\mathbb{R}^d)$ solves the following local problem: For all $\underline{w} \in \mathbb{P}_d^{k+1}(T;\mathbb{R}^d)$,

$$(\boldsymbol{\varepsilon}(\underline{D}_T^{k+1}(\underline{\hat{v}}_T)), \boldsymbol{\varepsilon}(\underline{w}))_{\boldsymbol{L}^2(T)} := (\boldsymbol{\varepsilon}(\underline{v}_T), \boldsymbol{\varepsilon}(\underline{w}))_{\boldsymbol{L}^2(T)} + (\underline{v}_{\partial T} - \underline{v}_{T|\partial T}, \boldsymbol{\varepsilon}(\underline{w})\cdot\underline{n}_T)_{\underline{L}^2(\partial T)}. \tag{5.15}$$

The reconstructed displacement is uniquely defined by prescribing additionally that $\int_T \underline{D}_T^{k+1}(\hat{\underline{v}}_T)dT := \int_T \underline{v}_T dT$ and $\int_T \boldsymbol{\nabla}^{ss}(\underline{D}_T^{k+1}(\hat{\underline{v}}_T))dT := \int_{\partial T} \frac{1}{2}(\underline{v}_{\partial T} \otimes \underline{n}_T - \underline{n}_T \otimes \underline{v}_{\partial T})d\partial T$ (see [89]). Comparing with (5.12), one readily sees that $\boldsymbol{\varepsilon}(\underline{D}_T^{k+1}(\hat{\underline{v}}_T))$ is the L^2-orthogonal projection of $\boldsymbol{E}_T^k(\hat{\underline{v}}_T)$ onto $\boldsymbol{\varepsilon}(\mathbb{P}_d^{k+1}(T;\mathbb{R}^d))$.

We use the above operators to mimic locally the exact local bilinear form a defined above by means of the following local bilinear form defined on $\hat{\underline{U}}_T^k \times \hat{\underline{U}}_T^k$ (compare with (5.6)):

$$\begin{aligned}\widehat{a}_T(\hat{\underline{v}}_T, \hat{\underline{w}}_T) :=& 2\mu(\boldsymbol{E}_T^k(\hat{\underline{v}}_T), \boldsymbol{E}_T^k(\hat{\underline{w}}_T))_{\boldsymbol{L}^2(T)} + \lambda(D_T^k(\hat{\underline{v}}_T), D_T^k(\hat{\underline{w}}_T))_{L^2(T)} \\ &+ 2\mu h_T^{-1}(\underline{S}_{\partial T}^k(\hat{\underline{v}}_T), \underline{S}_{\partial T}^k(\hat{\underline{w}}_T))_{\underline{L}^2(\partial T)}.\end{aligned} \tag{5.16}$$

The stabilization term is weighted (as in the linear case) by the Lamé coefficient μ.

5.3.3 Global discrete problem

For simplicity we employ the Nitsche technique only on the subset Γ_{C} where the nonlinear frictional contact conditions are enforced, whereas we resort to a strong enforcement of the homogeneous Dirichlet condition on the subset Γ_{D}. The global discrete space for the HHO-Nitsche method is

$$\hat{\underline{U}}_h^k := \mathbb{P}_d^k(\mathcal{T}_h;\mathbb{R}^d) \times \Big(\mathbb{P}_{d-1}^k(\mathcal{F}_h^{\mathrm{i}} \cup \mathcal{F}_h^{\mathrm{b,D}} \cup \mathcal{F}_h^{\mathrm{b,N}};\mathbb{R}^d) \times \mathbb{P}_{d-1}^{k+1}(\mathcal{F}_h^{\mathrm{b,C}};\mathbb{R}^d)\Big), \tag{5.17}$$

leading to the notation $\hat{\underline{v}}_h := \big((\underline{v}_T)_{T\in\mathcal{T}_h}, (\underline{v}_F)_{F\in\mathcal{F}_h}\big)$ for a generic element $\hat{\underline{v}}_h \in \hat{\underline{U}}_h^k$. For all $T \in \mathcal{T}_h$, we denote by $\hat{\underline{v}}_T := (\underline{v}_T, (\underline{v}_F)_{F\in\mathcal{F}_{\partial T}}) \in \hat{\underline{U}}_T^k$ the local components of $\hat{\underline{v}}_h$ attached to the mesh cell T and the faces composing ∂T, and for any mesh face $F \in \mathcal{F}_h$, we denote by $\underline{v}_F$ the component of $\hat{\underline{v}}_h$ attached to the face F. We enforce strongly the homogeneous Dirichlet condition on Γ_{D} by considering the subspace

$$\hat{\underline{U}}_{h,0}^k := \{\hat{\underline{v}}_h \in \hat{\underline{U}}_h^k \mid \underline{v}_F = \underline{0} \quad \forall F \in \mathcal{F}_h^{\mathrm{b,D}}\}.$$

The HHO-Nitsche method uses a symmetry parameter $\theta \in \{-1, 0, 1\}$ and two penalty parameters $\gamma_n > 0$ and $\gamma_t > 0$ to enforce weakly the contact and friction conditions on Γ_{C}, respectively. The penalty parameters γ_n and γ_t, which are proportional to 2μ, have to be chosen large enough as specified in Section 5.4. Choosing $\theta := 1$ leads to a symmetric formulation with a variational structure, choosing $\theta := 0$ is interesting to simplify the implementation by avoiding some terms in the formulation, and choosing $\theta := -1$ allows one to improve on the stability of the method by exploiting its skew-symmetry and making it more robust in the incompressible limit. It is convenient to define the subset $\mathcal{T}_h^{\mathrm{C}}$ as the collection of the mesh cells having at least one boundary face on Γ_{C} and to set $\partial T^{\mathrm{C}} := \partial T \cap \Gamma_{\mathrm{C}}$ for all $T \in \mathcal{T}_h^{\mathrm{C}}$. The subset $\mathcal{T}_h^{\mathrm{N}}$ is defined similarly, and we set $\partial T^{\mathrm{N}} := \partial T \cap \Gamma_{\mathrm{N}}$ for all $T \in \mathcal{T}_h^{\mathrm{N}}$. We consider the following discrete HHO-Nitsche problem:

$$\begin{cases} \text{Find } \hat{\underline{u}}_h \in \hat{\underline{U}}_{h,0}^k \text{ such that} \\ \widehat{b}_h(\hat{\underline{u}}_h; \hat{\underline{w}}_h) = \widehat{\ell}_h(\hat{\underline{w}}_h) \qquad \forall \hat{\underline{w}}_h \in \hat{\underline{U}}_{h,0}^k, \end{cases} \tag{5.18}$$

where the global discrete semilinear form $\widehat{a}_h$ and the global discrete linear form $\widehat{\ell}_h$ are defined

as follows:

$$\begin{aligned}\widehat{b}_h(\hat{\underline{v}}_h;\hat{\underline{w}}_h) &:= \sum_{T\in\mathcal{T}_h}\widehat{a}_T(\hat{\underline{v}}_T,\hat{\underline{w}}_T)\\ &- \sum_{T\in\mathcal{T}_h^{\mathrm{C}}}\theta\frac{h_T}{\gamma_n}(\sigma_n(\hat{\underline{v}}_T),\sigma_n(\hat{\underline{w}}_T))_{L^2(\partial T^{\mathrm{C}})} - \sum_{T\in\mathcal{T}_h^{\mathrm{C}}}\theta\frac{h_T}{\gamma_t}(\underline{\sigma}_t(\hat{\underline{v}}_T),\underline{\sigma}_t(\hat{\underline{w}}_T))_{\underline{L}^2(\partial T^{\mathrm{C}})}\\ &+ \sum_{T\in\mathcal{T}_h^{\mathrm{C}}}\frac{h_T}{\gamma_n}\Big([\tau_n(\hat{\underline{v}}_T)]_{\mathbb{R}^-},(\tau_n+(\theta-1)\sigma_n)(\hat{\underline{w}}_T)\Big)_{L^2(\partial T^{\mathrm{C}})}\\ &+ \sum_{T\in\mathcal{T}_h^{\mathrm{C}}}\frac{h_T}{\gamma_t}\left([\underline{\tau}_t(\hat{\underline{v}}_T)]_s,(\underline{\tau}_t+(\theta-1)\underline{\sigma}_t)(\hat{\underline{w}}_T)\right)_{\underline{L}^2(\partial T^{\mathrm{C}})},\end{aligned}$$

and

$$\widehat{\ell}_h(\hat{\underline{w}}_h) := \sum_{T\in\mathcal{T}_h}(\underline{f},\underline{w}_T)_{\underline{L}^2(T)} + \sum_{T\in\mathcal{T}_h^{\mathrm{N}}}(\underline{g}_{\mathrm{N}},\underline{w}_{\partial T})_{\underline{L}^2(\partial T^{\mathrm{N}})}.$$

Here, with a slight abuse of notation, we have written

$$\boldsymbol{\sigma}(\hat{\underline{w}}_T) := 2\mu\boldsymbol{E}_T^k(\hat{\underline{w}}_T) + \lambda D_T^k(\hat{\underline{w}}_T)\boldsymbol{I}_d \in \mathbb{P}_d^k(T;\mathbb{R}^{d\times d}_{\mathrm{sym}}), \tag{5.19}$$

together with the decomposition $\boldsymbol{\sigma}(\hat{\underline{w}}_T)\cdot\underline{n}_T := \sigma_n(\hat{\underline{w}}_T)\underline{n}_T + \underline{\sigma}_t(\hat{\underline{w}}_T)$, and we have introduced the linear operators (again with a slight abuse of notation)

$$\tau_n(\hat{\underline{w}}_T) := \sigma_n(\hat{\underline{w}}_T) - \frac{\gamma_n}{h_T}w_{\partial T,n}, \qquad \underline{\tau}_t(\hat{\underline{w}}_T) := \underline{\sigma}_t(\hat{\underline{w}}_T) - \frac{\gamma_t}{h_T}\underline{w}_{\partial T,t},$$

together with the decomposition $\underline{w}_{\partial T} := w_{\partial T,n}\underline{n}_T + \underline{w}_{\partial T,t}$ for the face polynomials. Note that in the definition of τ_n and $\underline{\tau}_t$, the penalty parameters are rescaled by h_T^{-1} in each mesh cell in $\mathcal{T}_h^{\mathrm{C}}$. Proposition 5.3 still holds true with this rescaling of the penalty parameters since the only requirement therein is that γ_n and γ_t be positive.

Remark 5.6 (Comparison with FEM-Nitsche) *In the FEM-Nitsche method devised in [61], one restricts the setting to simplicial meshes and considers the usual $\underline{H}^1$-confirming finite element space $\underline{V}_h$ composed of continuous functions that are piecewise polynomials of degree at most $k\geq 1$ in each mesh cell. The discrete problem is formulated in the subspace $\underline{V}_{h,0}$ explicitly enforcing the Dirichlet condition on Γ_D and involves the global discrete semilinear form*

$$\begin{aligned}b_h(\underline{v}_h;\underline{w}_h) := a(\underline{v}_h,\underline{w}_h) &- (\tfrac{\theta}{\tilde{\gamma}}\sigma_n(\underline{v}_h),\sigma_n(\underline{w}_h))_{L^2(\Gamma_C)} - (\tfrac{\theta}{\tilde{\gamma}}\underline{\sigma}_t(\underline{v}_h,\underline{\sigma}_t(\underline{w}_h))_{\underline{L}^2(\Gamma_C)}\\ &+ (\tfrac{1}{\tilde{\gamma}}[\tau_n(\underline{v}_h)]_{\mathbb{R}^-},(\tau_n+(\theta-1)\sigma_n)(\underline{w}_h))_{L^2(\Gamma_C)}\\ &+ (\tfrac{1}{\tilde{\gamma}}[\underline{\tau}_t(\underline{v}_h)]_s,(\underline{\tau}_t+(\theta-1)\underline{\sigma}_t)(\underline{w}_h))_{\underline{L}^2(\Gamma_C)},\end{aligned}$$

as well as the linear form $\ell_h(\underline{w}_h) := \ell(\underline{w}_h)$, where a and ℓ are the same as for the continuous problem, the notation τ_n, σ_n, $\underline{\tau}_t$, and $\underline{\sigma}_t$ is that employed for the exact solution, the symmetry parameter is taken again in $\{-1,0,1\}$, and the penalty parameter $\tilde{\gamma}$ is a piecewise constant function on Γ_C such that $\tilde{\gamma}_{|\partial T^C} = h_T^{-1}\gamma$ with $\gamma>0$ for all $T\in\mathcal{T}_h^C$. Note that there is only one penalty parameter in [61] since the analysis therein did not consider the scaling with respect to the Lamé parameters.

Remark 5.7 (Comparison with [50]) *There are various differences with the HHO-Nitsche method devised in [50] for the scalar Signorini problem. Herein we address the vector-valued case and include Tresca friction. Moreover we use the face polynomials in the definition of the operators τ_n and $\underline{\tau}_t$ which corresponds to the face version considered in [50]. However we employ here a higher polynomial degree on those faces located on Γ_C.*

5.4 Stability and error analysis

In this section we perform the stability and error analysis of the above HHO-Nitsche discretization of the frictional contact problem. We first collect some useful analysis tools. Then we establish a stability property and infer the well-posedness of the nonlinear discrete problem (5.18). The stability property hinges on a minimal value for the penalty parameters γ_n and γ_t, except if $\theta = -1$ where these parameters need only to be positive. Then we slightly tighten these minimal values to derive an error estimate bounding the energy error and the error on the nonlinear boundary condition on Γ_C and featuring optimal decay rates of order $(k+1)$ for smooth solutions. The following properties of projections onto a convex set will be useful:

$$([x]_{\mathbb{R}^-} - [y]_{\mathbb{R}^-})(x-y) \geq ([x]_{\mathbb{R}^-} - [y]_{\mathbb{R}^-})^2 \geq 0, \qquad \forall x, y \in \mathbb{R}, \tag{5.20}$$

$$([\underline{x}]_s - [\underline{y}]_s)\cdot(\underline{x}-\underline{y}) \geq \| [\underline{x}]_s - [\underline{y}]_s \|^2 \geq 0, \qquad \forall \underline{x}, \underline{y} \in \mathbb{R}^d. \tag{5.21}$$

We use the symbol C to denote a generic constant whose value can change at each occurrence as long as it is independent of the mesh size and the Lamé parameters. The value of C can depend on the mesh regularity and the polynomial degree $k \geq 0$. We abbreviate as $a \lesssim b$ the inequality $a \leq Cb$ with positive real numbers a, b and a constant $C > 0$ as above and whose value can change at each occurrence.

5.4.1 Analysis tools for HHO operators

We begin this section with an approximation property that involves the strain, and that will be useful in the sequel.

Lemma 5.8 *Let $k \geq 1$ be the polynomial degree. Let $\underline{\Pi}_T^k$ denote the L^2-orthogonal projection onto $\mathbb{P}_d^k(T;\mathbb{R}^d)$. Then, for any function $\underline{v} \in H^1(T;\mathbb{R}^d)$, we have*

$$\|\underline{v} - \underline{\Pi}_T^k(\underline{v})\|_{\underline{L}^2(T)} \leq C\, h_T \|\boldsymbol{\varepsilon}(\underline{v})\|_{\boldsymbol{L}^2(T)}. \tag{5.22}$$

Proof. Let $\underline{\Pi}_T^{\mathrm{RM}}$ be the projector such that for any function $\underline{v} \in H^1(T;\mathbb{R}^d)$:

$$\underline{\Pi}_T^{\mathrm{RM}}(\underline{v}) = \frac{1}{|T|_d}\int_T \underline{v}\, dT + \frac{1}{|T|_d}\Big(\int_T \boldsymbol{\nabla}^{ss}(\underline{v})\, dT\Big)(\underline{x} - \underline{x}_b),$$

where $\underline{x}_b$ denote the barycenter of T. We remark that $\underline{\Pi}_T^{\mathrm{RM}}(\underline{v}) \in \mathbb{P}_d^1(T;\mathbb{R}^d)$ and $(\underline{v} - \underline{\Pi}_T^{\mathrm{RM}}(\underline{v})) \in \mathcal{U}(T)$, where

$$\mathcal{U}(T) := \left\{ \underline{v} \in H^1(T;\mathbb{R}^d) \ : \ \int_T \underline{v}\, dT = \underline{0} \ \text{ and } \ \int_T \boldsymbol{\nabla}^{ss}\underline{v}\, dT = \mathbf{0} \right\}$$

Hence, we infer that,

$$\begin{aligned}
\|\underline{v} - \underline{\Pi}_T^k(\underline{v})\|_{\underline{L}^2(T)} &= \|(\underline{v} - \underline{\Pi}_T^{\mathrm{RM}}(\underline{v})) - \underline{\Pi}_T^k(\underline{v} - \underline{\Pi}_T^{\mathrm{RM}}(\underline{v}))\|_{\underline{L}^2(T)} \\
&\leq C\|\underline{v} - \underline{\Pi}_T^{\mathrm{RM}}(\underline{v})\|_{\underline{L}^2(T)} \\
&\leq C_{\mathrm{K}} h_T \, \|\boldsymbol{\varepsilon}(\underline{v})\|_{\boldsymbol{L}^2(T)}.
\end{aligned}$$

where we have used the fact that $\underline{\Pi}_T^{\mathrm{RM}}(\underline{v}) \in \mathbb{P}_d^k(T;\mathbb{R}^d)$ for $k \geq 1$, $\underline{\Pi}_T^k$ is a L^2-orthogonal projector, and a Korn's inequality since $(\underline{v} - \underline{\Pi}_T^{\mathrm{RM}}(\underline{v})) \in \mathcal{U}(T)$.

□

We equip the space $\hat{\underline{U}}_T^k$ with the following local discrete strain seminorm:

$$|\hat{\underline{v}}_T|_{1,T}^2 := \|\boldsymbol{\varepsilon}(\underline{v}_T)\|_{\boldsymbol{L}^2(T)}^2 + h_T^{-1}\|\underline{v}_{\partial T} - \underline{v}_{T|\partial T}\|_{\underline{L}^2(\partial T)}^2, \tag{5.23}$$

so that $|\hat{\underline{v}}_T|_{1,T} = 0$ implies that $\underline{v}_T$ is a rigid-body motion and that $\underline{v}_{\partial T}$ is the trace of $\underline{v}_T$ on ∂T. The following local stability and boundedness properties of the strain reconstructon and stabilization operators are established as in [89, Lemma 4].

Lemma 5.9 (Boundedness and stability) *Let $\boldsymbol{E}_T^k$ be defined by (5.12) and $\underline{S}_{\partial T}^k$ by (5.14). There are $0 < \alpha_\flat < \alpha_\sharp < +\infty$ such that, for all $T \in \mathcal{T}_h$, all $h > 0$, and all $\hat{\underline{v}}_T \in \hat{\underline{U}}_T^k$, we have*

$$\alpha_\flat|\hat{\underline{v}}_T|_{1,T} \le \left(\|\boldsymbol{E}_T^k(\hat{\underline{v}}_T)\|_{\boldsymbol{L}^2(T)}^2 + h_T^{-1}\|\underline{S}_{\partial T}^k(\hat{\underline{v}}_T)\|_{\underline{L}^2(\partial T)}^2\right)^{\frac{1}{2}} \le \alpha_\sharp|\hat{\underline{v}}_T|_{1,T}. \tag{5.24}$$

Proof. We prove only the stability property by adapting the arguments in [89, Lemma 4]. Let $T \in \mathcal{T}_h$ and $\hat{\underline{v}}_T \in \hat{\underline{U}}_T^k$, then we have:

$$\begin{aligned}
\|\boldsymbol{\varepsilon}(\underline{v}_T)\|_{\boldsymbol{L}^2(T)}^2 &= (\boldsymbol{\varepsilon}(\underline{v}_T), \boldsymbol{\varepsilon}(\underline{v}_T))_{\boldsymbol{L}^2(T)} \\
&= (\boldsymbol{\varepsilon}(\underline{v}_T), \boldsymbol{E}_T^k(\hat{\underline{v}}_T))_{\boldsymbol{L}^2(T)} - (\underline{v}_{\partial T} - \underline{v}_{T|\partial T}, \boldsymbol{\varepsilon}(\underline{v}_T)\underline{n}_T)_{\underline{L}^2(\partial T)} \\
&\le \|\boldsymbol{\varepsilon}(\underline{v}_T)\|_{\boldsymbol{L}^2(T)}\|\boldsymbol{E}_T^k(\hat{\underline{v}}_T)\|_{\boldsymbol{L}^2(T)} + \|\underline{v}_{\partial T} - \underline{v}_{T|\partial T}\|_{\underline{L}^2(\partial T)}\|\boldsymbol{\varepsilon}(\underline{v}_T)\underline{n}_T\|_{\underline{L}^2(\partial T)} \\
&\le \|\boldsymbol{\varepsilon}(\underline{v}_T)\|_{\boldsymbol{L}^2(T)}\|\boldsymbol{E}_T^k(\hat{\underline{v}}_T)\|_{\boldsymbol{L}^2(T)} + C_{dt}h_T^{-\frac{1}{2}}\|\underline{v}_{\partial T} - \underline{v}_{T|\partial T}\|_{\underline{L}^2(\partial T)}\|\boldsymbol{\varepsilon}(\underline{v}_T)\|_{\underline{L}^2(T)} \\
&\le \frac{1}{2}\|\boldsymbol{\varepsilon}(\underline{v}_T)\|_{\boldsymbol{L}^2(T)}^2 + \|\boldsymbol{E}_T^k(\hat{\underline{v}}_T)\|_{\boldsymbol{L}^2(T)}^2 + C_{dt}^2h_T^{-1}\|\underline{v}_{\partial T} - \underline{v}_{T|\partial T}\|_{\underline{L}^2(\partial T)}^2
\end{aligned}$$

where we have used the definition of the symmetric strain operator (5.12) with $\boldsymbol{\tau} = \boldsymbol{\varepsilon}(\underline{v}_T) \in \mathbb{P}_d^k(T;\mathbb{R}_{\mathrm{sym}}^{d\times d})$ in the second line, twice the Cauchy–Schwarz inequality in the third line, and the discrete trace inequality in the fourth line, and twice the Young's inequality in the last line. Then, it follows

$$\|\boldsymbol{\varepsilon}(\underline{v}_T)\|_{\boldsymbol{L}^2(T)}^2 \lesssim \|\boldsymbol{E}_T^k(\hat{\underline{v}}_T)\|_{\boldsymbol{L}^2(T)}^2 + h_T^{-1}\|\underline{v}_{\partial T} - \underline{v}_{T|\partial T}\|_{\underline{L}^2(\partial T)}^2. \tag{5.25}$$

Moreover, we set $\delta_T(\hat{\underline{v}}_T) = \underline{v}_T + \underline{D}_T^{k+1}(\hat{\underline{v}}_T) - \underline{\Pi}_T^k\underline{D}_T^{k+1}(\hat{\underline{v}}_T)$. Then,

$$\begin{aligned}
&h_T^{-\frac{1}{2}}\|\underline{v}_{\partial T} - \underline{v}_{T|\partial T}\|_{\underline{L}^2(\partial T)} \\
&\le h_T^{-\frac{1}{2}}\|\underline{v}_{\partial T} - \underline{\Pi}_{\partial T}^{k/k+1}(\delta_T(\hat{\underline{v}}_T)_{|\partial T})\|_{\underline{L}^2(\partial T)} + h_T^{-\frac{1}{2}}\|\underline{v}_{T|\partial T} - \underline{\Pi}_{\partial T}^{k/k+1}(\delta_T(\hat{\underline{v}}_T)_{|\partial T})\|_{\underline{L}^2(\partial T)} \\
&= h_T^{-\frac{1}{2}}\|\underline{S}_{\partial T}^k(\hat{\underline{v}}_T)\|_{\underline{L}^2(\partial T)} + h_T^{-\frac{1}{2}}\|\underline{\Pi}_{\partial T}^{k/k+1}(\underline{v}_{T|\partial T} - \delta_T(\hat{\underline{v}}_T)_{|\partial T})\|_{\underline{L}^2(\partial T)} \\
&= h_T^{-\frac{1}{2}}\|\underline{S}_{\partial T}^k(\hat{\underline{v}}_T)\|_{\underline{L}^2(\partial T)} + h_T^{-\frac{1}{2}}\|\underline{\Pi}_{\partial T}^{k/k+1}(\underline{D}_T^{k+1}(\hat{\underline{v}}_T)_{|\partial T} - \underline{\Pi}_T^k\underline{D}_T^{k+1}(\hat{\underline{v}}_T)_{|\partial T}\|_{\underline{L}^2(\partial T)} \\
&\lesssim h_T^{-\frac{1}{2}}\|\underline{S}_{\partial T}^k(\hat{\underline{v}}_T)\|_{\underline{L}^2(\partial T)} + C_{dt}h_T^{-1}\|\underline{D}_T^{k+1}(\hat{\underline{v}}_T)_{|\partial T} - \underline{\Pi}_T^k\underline{D}_T^{k+1}(\hat{\underline{v}}_T)_{|\partial T}\|_{\underline{L}^2(T)} \\
&\lesssim h_T^{-\frac{1}{2}}\|\underline{S}_{\partial T}^k(\hat{\underline{v}}_T)\|_{\underline{L}^2(\partial T)} + \|\boldsymbol{\varepsilon}(\underline{D}_T^{k+1}(\hat{\underline{v}}_T))\|_{\boldsymbol{L}^2(T)} \\
&\lesssim h_T^{-\frac{1}{2}}\|\underline{S}_{\partial T}^k(\hat{\underline{v}}_T)\|_{\underline{L}^2(\partial T)} + \|\boldsymbol{E}_T^k(\hat{\underline{v}}_T)\|_{\boldsymbol{L}^2(T)}
\end{aligned} \tag{5.26}$$

where we have inserted $\pm\underline{\Pi}_{\partial T}^{k/k+1}(\delta_T(\underline{v}_T)_{|\partial T})$ and used the triangular inequality in the first line, the fact that $\underline{v}_{\partial T} \in \mathbb{P}_{d-1}^{k/k+1}(\mathcal{F}_{\partial T};\mathbb{R}^d)$, the definition (5.14) of the stabilization operator $\underline{S}_{\partial T}^k$ and that $\underline{v}_{T|\partial T} \in \mathbb{P}_{d-1}^k(\mathcal{F}_{\partial T};\mathbb{R}^d) \subset \mathbb{P}_{d-1}^{k/k+1}(\mathcal{F}_{\partial T};\mathbb{R}^d)$ in the second line, using the stability

of the L^2-orthogonal projector $\underline{\Pi}_{\partial T}^{k/k+1}$ and a discrete trace inequality, using Lemma 5.8 with $\underline{v} = \underline{D}_T^{k+1}(\underline{\hat{v}}_T)$ since $k \geq 1$ in the fifth line and the fact that $\boldsymbol{\varepsilon}(\underline{D}_T^{k+1}(\underline{\hat{v}}_T))$ is the L^2-orthogonal projection of $\boldsymbol{E}_T^k(\underline{\hat{v}}_T)$ onto the subspace $\boldsymbol{\varepsilon}(\mathbb{P}_d^k(T;\mathbb{R}^d))$ and the stability of this projection. Then, the stability property follows directly from (5.25) and (5.26). The proof for the boundedness property use similar arguments and is omitted for brevity.

□

The key operator in the HHO error analysis is the local interpolation operator $\underline{\hat{I}}_T^k : H^1(T;\mathbb{R}^d) \to \underline{\hat{U}}_T^k$ such that

$$\underline{\hat{I}}_T^k(\underline{v}) := (\underline{\Pi}_T^k(\underline{v}), \underline{\Pi}_{\partial T}^{k/k+1}(\underline{v}_{|\partial T})) \in \underline{\hat{U}}_T^k, \tag{5.27}$$

for all $\underline{v} \in H^1(T;\mathbb{R}^d)$ and all $T \in \mathcal{T}_h$. The global version $\underline{\hat{I}}_h^k : \underline{V}_{\mathrm{D}} \to \underline{\hat{U}}_{h,0}^k$ is defined locally by setting the local HHO components of $\underline{\hat{I}}_h^k(\underline{v})$ to $(\underline{\hat{I}}_h^k(\underline{v}))_T := \underline{\hat{I}}_T^k(\underline{v}_{|T}) \in \underline{\hat{U}}_T^k$, for all $\underline{v} \in \underline{V}_{\mathrm{D}}$ and all $T \in \mathcal{T}_h$. This definition makes sense since the fields in $\underline{V}_{\mathrm{D}}$ do not jump across the mesh interfaces and vanish at the boundary faces located on Γ_{D}. The HHO interpolation operator allows one to obtain important local commuting properties satisfied by the reconstruction operators (see, e.g., [89, Proposition 3]), namely we have

$$\boldsymbol{E}_T^k(\underline{\hat{I}}_T^k(\underline{v})) = \boldsymbol{\Pi}_T^k(\boldsymbol{\varepsilon}(\underline{v})), \qquad D_T^k(\underline{\hat{I}}_T^k(\underline{v})) = \Pi_T^k(\nabla{\cdot}\underline{v}), \tag{5.28}$$

for all $\underline{v} \in H^1(T;\mathbb{R}^d)$, all $T \in \mathcal{T}_h$, and all $h > 0$, where $\boldsymbol{\Pi}_T^k$ is the L^2-orthogonal projection onto $\mathbb{P}_d^k(T;\mathbb{R}_{\mathrm{sym}}^{d\times d})$ and Π_T^k that onto $\mathbb{P}_d^k(T;\mathbb{R})$. For all $\underline{v} \in H^{1+\nu}(\Omega;\mathbb{R}^d)$, $\nu > \frac{1}{2}$, and all $\underline{\hat{w}}_h \in \underline{\hat{U}}_{h,0}^k$, let us set (the reason for the notation will become clear in the proof of Theorem 5.14 below)

$$\mathbb{T}'_{1,1}(\underline{v}, \underline{\hat{w}}_h) := \sum_{T\in\mathcal{T}_h} -\big((\underline{\nabla}\cdot\boldsymbol{\sigma}(\underline{v}), \underline{w}_T)_{\underline{L}^2(T)} + \widehat{a}_T(\underline{\hat{I}}_T^k(\underline{v}), \underline{\hat{w}}_T)\big) + \sum_{T\in\mathcal{T}_h^{\mathrm{N}}\cup\mathcal{T}_h^{\mathrm{C}}} (\underline{\sigma}_n(\underline{v}), \underline{w}_{\partial T})_{\underline{L}^2(\partial T^{\mathrm{N}}\cup\partial T^{\mathrm{C}})}, \tag{5.29}$$

where we recall that $\underline{\hat{w}}_T = (\underline{w}_T, \underline{w}_{\partial T})$ are the local components of the test function $\underline{\hat{w}}_h \in \underline{\hat{U}}_{h,0}^k$ attached to the mesh cell $T \in \mathcal{T}_h$. For a function $z \in H^{1+\nu}(T;\mathbb{R})$, $\nu > \frac{1}{2}$, we employ the notation

$$\|z\|_{\sharp,T}^2 := \|z\|_T^2 + h_T\|z\|_{\partial T}^2,$$

and the same notation for tensor-valued fields.

Lemma 5.10 (Consistency for linear elasticity) *Let $\mathbb{T}'_{1,1}(\underline{v}, \underline{\hat{w}}_h)$ be defined in (5.29) for all $\underline{v} \in H^{1+\nu}(\Omega;\mathbb{R}^d)$, $\nu > \frac{1}{2}$, and all $\underline{\hat{w}}_h \in \underline{\hat{U}}_{h,0}^k$. The following holds true:*

$$|\mathbb{T}'_{1,1}(\underline{v}, \underline{\hat{w}}_h)|^2 \lesssim \mathbb{A}_1(\underline{v}) \Big(\sum_{T\in\mathcal{T}_h} 2\mu|\underline{\hat{w}}_T|_{1,T}^2 \Big), \tag{5.30}$$

with the interpolation error

$$\mathbb{A}_1(\underline{v}) := \sum_{T\in\mathcal{T}_h} \frac{1}{2\mu} \Big((2\mu)^2\|\boldsymbol{\varepsilon}(\underline{v}) - \boldsymbol{\Pi}_T^k(\boldsymbol{\varepsilon}(\underline{v}))\|_{\sharp,T}^2 + (2\mu)^2\|\boldsymbol{\varepsilon}(\underline{v} - \underline{\Pi}_T^{k+1}(\underline{v}))\|_{\boldsymbol{L}^2(T)}^2 + \lambda^2\|\nabla{\cdot}\underline{v} - \Pi_T^k(\nabla{\cdot}\underline{v})\|_{\sharp,T}^2 \Big). \tag{5.31}$$

Proof. The proof essentially follows [89, Theorem 8] and is only sketched. Integrating by parts the term $(\underline{\nabla}\cdot\boldsymbol{\sigma}(\underline{v}), \underline{w}_T)_{\underline{L}^2(T)}$ for all $T \in \mathcal{T}_h$, using (5.1) together with the definitions (5.12)-(5.13) for $\boldsymbol{E}_T^k(\underline{\hat{w}}_T)$ and $D_T^k(\underline{\hat{w}}_T)$, respectively, re-arranging the terms, and setting $\boldsymbol{\eta}_T :=$

$\boldsymbol{\varepsilon}(\underline{v}) - \boldsymbol{E}_T^k(\hat{\underline{I}}_T^k(\underline{v})) = \boldsymbol{\varepsilon}(\underline{v}) - \boldsymbol{\Pi}_T^k(\boldsymbol{\varepsilon}(\underline{v}))$ and $\zeta_T := \nabla{\cdot}\underline{v} - D_T^k(\hat{\underline{I}}_T^k(\underline{v})) = \nabla{\cdot}\underline{v} - \Pi_T^k(\nabla{\cdot}\underline{v})$ (owing to the commuting properties (5.28)) leads to (details are skipped for brevity)

$$\begin{aligned}\mathbb{T}'_{1,1}(\underline{v},\hat{\underline{w}}_h) = \sum_{T\in\mathcal{T}_h}\Big(&2\mu(\boldsymbol{\eta}_T,\boldsymbol{\varepsilon}(\underline{w}_T))_{\boldsymbol{L}^2(T)} + 2\mu(\boldsymbol{\eta}_T{\cdot}\underline{n}_T,\underline{w}_{\partial T}-\underline{w}_T)_{\underline{L}^2(\partial T)}\\ &- 2\mu h_T^{-1}(\underline{S}_{\partial T}^k(\hat{\underline{I}}_T^k(\underline{v})),\underline{S}_{\partial T}^k(\hat{\underline{w}}_T))_{\underline{L}^2(\partial T)}\\ &+ \lambda(\zeta_T,\nabla{\cdot}\underline{w}_T)_{L^2(T)} + \lambda(\zeta_T\underline{n}_T,\underline{w}_{\partial T}-\underline{w}_T)_{\underline{L}^2(\partial T)}\Big).\end{aligned}$$

Invoking the Cauchy–Schwarz inequality and the upper bound from Lemma 5.9 to estimate $h_T^{-\frac12}\|\underline{S}_{\partial T}^k(\hat{\underline{w}}_T)\|_{\underline{L}^2(\partial T)}$, we infer that

$$\begin{aligned}|\mathbb{T}'_{1,1}(\underline{v},\hat{\underline{w}}_h)|^2 \lesssim &\Big(\sum_{T\in\mathcal{T}_h}\frac{1}{2\mu}\Big((2\mu)^2\|\boldsymbol{\eta}_T\|_{\sharp,T}^2 + (2\mu)^2h_T^{-1}\|\underline{S}_{\partial T}^k(\hat{\underline{I}}_T^k(\underline{v}))\|_{\underline{L}^2(\partial T)}^2 + \lambda^2\|\zeta_T\|_{\sharp,T}^2\Big)\Big)\\ &\times\Big(\sum_{T\in\mathcal{T}_h}2\mu|\hat{\underline{w}}_T|_{1,T}^2\Big).\end{aligned}$$

Finally combining the ideas used in [89, Eqs. (20)&(35)] with a local multiplicative trace inequality and a local Korn inequality, we infer that

$$h_T^{-1}\|\underline{S}_{\partial T}^k(\hat{\underline{I}}_T^k(\underline{v}))\|_{\underline{L}^2(\partial T)}^2 \lesssim \|\boldsymbol{\varepsilon}(\underline{v}-\underline{D}_T^{k+1}(\hat{\underline{I}}_T^k(\underline{v})))\|_{\boldsymbol{L}^2(T)}^2 \le \|\boldsymbol{\varepsilon}(\underline{v}-\underline{\Pi}_T^{k+1}(\underline{v}))\|_{\boldsymbol{L}^2(T)}^2,$$

which completes the proof of (5.30).

□

5.4.2 Stability and well-posedness

Let us first establish an important monotonicity property of the semilinear form $\widehat{b}_h$ under the assumption that the penalty parameters γ_n and γ_t are large enough. The lower bound on these parameters involves the constant C_{dt} from the following discrete trace inequality:

$$\|v_h\|_{L^2(\partial T^{\mathrm{C}})} \le C_{\mathrm{dt}}h_T^{-\frac12}\|v_h\|_{L^2(T)}, \tag{5.32}$$

for all $T\in\mathcal{T}_h^{\mathrm{C}}$, all $h>0$, and all $v_h\in\mathbb{P}^k(T;\mathbb{R}^q)$, $q\in\{1,d\}$. We equip the global HHO space $\hat{\underline{U}}_{h,0}^k$ with the norm

$$\|\hat{\underline{v}}_h\|_{\mu,\lambda}^2 := \sum_{T\in\mathcal{T}_h}\Big(2\mu|\hat{\underline{v}}_T|_{1,T}^2 + \lambda\|D_T^k(\hat{\underline{v}}_T)\|_{L^2(T)}^2\Big).$$

That $\|\cdot\|_{\mu,\lambda}$ defines a norm on $\hat{\underline{U}}_{h,0}^k$ follows from the usual arguments since face unknowns are null on all the faces in $\mathcal{F}_h^{\mathrm{b,D}}$ and this set is nonempty by assumption.

Lemma 5.11 (Monotonicity) *Assume that the penalty parameters are such that*

$$\min(\kappa^{-1}\gamma_n, 2\gamma_t) \ge 3(\theta+1)^2C_{\mathrm{dt}}^2\mu, \tag{5.33}$$

recalling that $\kappa := \max(1,\frac{\lambda}{2\mu})$. *Then the semilinear form* $\widehat{b}_h$ *is monotone and we have for all* $\hat{\underline{v}}_h,\hat{\underline{w}}_h\in\hat{\underline{U}}_{h,0}^k$,

$$\widehat{b}_h(\hat{\underline{v}}_h;\hat{\underline{v}}_h-\hat{\underline{w}}_h) - \widehat{b}_h(\hat{\underline{w}}_h;\hat{\underline{v}}_h-\hat{\underline{w}}_h) \ge \frac13\min(1,\alpha_\flat^2)\|\hat{\underline{v}}_h-\hat{\underline{w}}_h\|_{\mu,\lambda}^2. \tag{5.34}$$

Proof. Let $\underline{\hat{v}}_h, \underline{\hat{w}}_h \in \underline{\hat{U}}_{h,0}^k$ and set $\underline{\hat{z}}_h := \underline{\hat{v}}_h - \underline{\hat{w}}_h$. Recalling the definition of the HHO-Nitsche semilinear form $\widehat{b}_h$ and exploiting the positivity of the local HHO bilinear form $\widehat{a}_T$, we infer that

$$\sum_{T\in\mathcal{T}_h}\Big(2\mu\big(\|\boldsymbol{E}_T^k(\underline{\hat{z}}_T)\|_{\boldsymbol{L}^2(T)}^2 + h_T^{-1}\|\underline{S}_{\partial T}^k(\underline{\hat{z}}_T)\|_{\underline{L}^2(\partial T)}^2\big) + \lambda\|D_T^k(\underline{\hat{z}}_T)\|_{L^2(T)}^2\Big) \le \mathbb{T}_1 + \mathbb{T}_{2,n} + \mathbb{T}_{2,t} - \mathbb{T}_{3,n} - \mathbb{T}_{3,t}, \quad (5.35)$$

where

$$\mathbb{T}_1 := \widehat{b}_h(\underline{\hat{v}}_h;\underline{\hat{z}}_h) - \widehat{b}_h(\underline{\hat{w}}_h;\underline{\hat{z}}_h),$$
$$\mathbb{T}_{2,n} := \sum_{T\in\mathcal{T}_h^{\mathrm{C}}}\theta\frac{h_T}{\gamma_n}\|\sigma_n(\underline{\hat{z}}_T)\|_{L^2(\partial T^{\mathrm{C}})}^2, \qquad \mathbb{T}_{2,t} := \sum_{T\in\mathcal{T}_h^{\mathrm{C}}}\theta\frac{h_T}{\gamma_t}\|\underline{\sigma}_t(\underline{\hat{z}}_T)\|_{\underline{L}^2(\partial T^{\mathrm{C}})}^2,$$

and

$$\mathbb{T}_{3,n} := \sum_{T\in\mathcal{T}_h^{\mathrm{C}}}\frac{h_T}{\gamma_n}\Big([\tau_n(\underline{\hat{v}}_T)]_{\mathbb{R}^-} - [\tau_n(\underline{\hat{w}}_T)]_{\mathbb{R}^-}, \tau_n(\underline{\hat{z}}_T)\Big)_{L^2(\partial T^{\mathrm{C}})}$$
$$+ \sum_{T\in\mathcal{T}_h^{\mathrm{C}}}(\theta-1)\frac{h_T}{\gamma_n}\Big([\tau_n(\underline{\hat{v}}_T)]_{\mathbb{R}^-} - [\tau_n(\underline{\hat{w}}_T)]_{\mathbb{R}^-}, \sigma_n(\underline{\hat{z}}_T)\Big)_{L^2(\partial T^{\mathrm{C}})}$$
$$\mathbb{T}_{3,t} := \sum_{T\in\mathcal{T}_h^{\mathrm{C}}}\frac{h_T}{\gamma_t}\left([\underline{\tau}_t(\underline{\hat{v}}_T)]_s - [\underline{\tau}_t(\underline{\hat{w}}_T)]_s, \underline{\tau}_t(\underline{\hat{z}}_T)\right)_{\underline{L}^2(\partial T^{\mathrm{C}})}$$
$$+ \sum_{T\in\mathcal{T}_h^{\mathrm{C}}}(\theta-1)\frac{h_T}{\gamma_t}\left([\underline{\tau}_t(\underline{\hat{v}}_T)]_s - [\underline{\tau}_t(\underline{\hat{w}}_T)]_s, \underline{\sigma}_t(\underline{\hat{z}}_T)\right)_{\underline{L}^2(\partial T^{\mathrm{C}})}.$$

Let us consider $\mathbb{T}_{2,n} - \mathbb{T}_{3,n}$. Setting $\delta_T := [\tau_n(\underline{\hat{v}}_T)]_{\mathbb{R}^-} - [\tau_n(\underline{\hat{w}}_T)]_{\mathbb{R}^-}$, we infer that

$$\mathbb{T}_{2,n} - \mathbb{T}_{3,n} \le \sum_{T\in\mathcal{T}_h^{\mathrm{C}}}\Big(\theta\frac{h_T}{\gamma_n}\|\sigma_n(\underline{\hat{z}}_T)\|_{L^2(\partial T^{\mathrm{C}})}^2 - \|\delta_T\|_{L^2(\partial T^{\mathrm{C}})}^2 - (\theta-1)\frac{h_T}{\gamma_n}(\delta_T, \sigma_n(\underline{\hat{z}}_T))_{L^2(\partial T^{\mathrm{C}})}\Big)$$
$$\le \sum_{T\in\mathcal{T}_h^{\mathrm{C}}}\frac{1}{4}(\theta+1)^2\frac{h_T}{\gamma_n}\|\sigma_n(\underline{\hat{z}}_T)\|_{L^2(\partial T^{\mathrm{C}})}^2 \le \sum_{T\in\mathcal{T}_h^{\mathrm{C}}}\frac{1}{4}(\theta+1)^2\frac{C_{\mathrm{dt}}^2}{\gamma_n}\|\sigma_n(\underline{\hat{z}}_T)\|_{L^2(T)}^2,$$

where we used (5.20) in the first bound, Young's inequality and the fact that $\theta + \frac{1}{4}(\theta-1)^2 = \frac{1}{4}(\theta+1)^2$ in the second bound, and the discrete trace inequality (5.32) in the third bound. Recalling the definition (5.19) of the discrete HHO stress and using the triangle and Young's inequalities, we infer that

$$\mathbb{T}_{2,n} - \mathbb{T}_{3,n} \le \sum_{T\in\mathcal{T}_h^{\mathrm{C}}}\frac{1}{2}(\theta+1)^2\frac{C_{\mathrm{dt}}^2}{\gamma_n}\Big((2\mu)^2\|\boldsymbol{E}_T^k(\underline{\hat{z}}_T)\|_{\boldsymbol{L}^2(T)}^2 + \lambda^2\|D_T^k(\underline{\hat{z}}_T)\|_{L^2(T)}^2\Big)$$
$$\le \sum_{T\in\mathcal{T}_h^{\mathrm{C}}}(\theta+1)^2\frac{C_{\mathrm{dt}}^2}{\gamma_n}\mu\kappa \times \Big(2\mu\|\boldsymbol{E}_T^k(\underline{\hat{z}}_T)\|_{\boldsymbol{L}^2(T)}^2 + \lambda\|D_T^k(\underline{\hat{z}}_T)\|_{L^2(T)}^2\Big).$$

The reasoning to bound $\mathbb{T}_{2,t} - \mathbb{T}_{3,t}$ is similar except that $\underline{\sigma}_t(\underline{\hat{z}}_T)$ has only off-diagonal contributions and is therefore independent of λ. We infer that

$$\mathbb{T}_{2,t} - \mathbb{T}_{3,t} \le \sum_{T\in\mathcal{T}_h^{\mathrm{C}}}\frac{1}{2}(\theta+1)^2\frac{C_{\mathrm{dt}}^2}{\gamma_t}\mu \times 2\mu\|\boldsymbol{E}_T^k(\underline{\hat{z}}_T)\|_{\boldsymbol{L}^2(T)}^2.$$

Combining the above bounds and using the condition (5.33) leads to

$$\mathbb{T}_{2,n}+\mathbb{T}_{2,t}-\mathbb{T}_{3,n}-\mathbb{T}_{3,t}\leq\sum_{T\in\mathcal{T}_h}\frac{2}{3}\Big(2\mu\|\boldsymbol{E}_T^k(\hat{\underline{z}}_T)\|_{\boldsymbol{L}^2(T)}^2+\lambda\|D_T^k(\hat{\underline{z}}_T)\|_{L^2(T)}^2\Big).$$

Recalling (5.35) leads to

$$\mathbb{T}_1\geq\sum_{T\in\mathcal{T}_h}\frac{1}{3}\Big(2\mu\big(\|\boldsymbol{E}_T^k(\hat{\underline{z}}_T)\|_{\boldsymbol{L}^2(T)}^2+h_T^{-1}\|\underline{S}_{\partial T}^k(\hat{\underline{z}}_T)\|_{\underline{L}^2(\partial T)}^2\big)+\lambda\|D_T^k(\hat{\underline{z}}_T)\|_{L^2(T)}^2\Big).$$

Using the definition of $\mathbb{T}_1$, the lower bound from Lemma 5.9, and the definition of the norm $\|\cdot\|_{\mu,\lambda}$ concludes the proof.

□

Using the argument from [41, Corollary 15, p. 126] (see [64] for the application to FEM-Nitsche), we infer from Lemma 5.11 the following well-posedness result.

Corollary 5.12 (Well-posedness) *The discrete problem (5.18) is well-posed.*

Remark 5.13 (Lower bound (5.33)) *The monotonicity result is robust in the incompresible limit for the skew-symmetric variant $\theta=-1$ since the penalty parameters γ_n and γ_t need only to be positive real numbers (proportional to μ), independently of the value of the ratio κ which becomes large in the incompressible limit. Instead, for the two other variants $\theta\in\{0,1\}$, this property is lost for γ_n which scales as $\mu\kappa$. Instead the parameter γ_t still scales as μ, i.e., it remains independent of κ whatever the value of θ. Hence robustness is also achieved for bilateral contact for any value of θ.*

5.4.3 Error analysis

This section contains our main theoretical results on the convergence of the HHO-Nitsche method for the frictional contact problem.

Theorem 5.14 (Error estimate) *Let $\epsilon\in(0,1]$. Recall that $\kappa:=\max(1,\frac{\lambda}{2\mu})$. Assume that the penalty parameters are such that*

$$\min(\kappa^{-1}\gamma_n,2\gamma_t)\geq 3\big((\theta+1)^2+\epsilon(4+(\theta-1)^2)\big)C_{\mathrm{dt}}^2\mu. \tag{5.36}$$

Assume that the exact solution satisfies $\underline{u}\in H^{1+r}(\Omega;\mathbb{R}^d)$, $r\frac{1}{2}$. Let $\hat{\underline{u}}_h$ be the discrete solution of (5.18) with local components $\hat{\underline{u}}_T$ for all $T\in\mathcal{T}_h$. Then we have

$$\begin{aligned}&\sum_{T\in\mathcal{T}_h}\Big(2\mu\|\boldsymbol{\varepsilon}(\underline{u})-\boldsymbol{E}_T^k(\hat{\underline{u}}_T)\|_{\boldsymbol{L}^2(T)}^2+\lambda\|\nabla\cdot\underline{u}-D_T^k(\hat{\underline{u}}_T)\|_{L^2(T)}^2\Big)\\&+\frac{\epsilon}{2(1+\epsilon)}\sum_{T\in\mathcal{T}_h^C}\Big(\frac{h_T}{\gamma_n}\|[\tau_n(\underline{u})]_{\mathbb{R}^-}-[\tau_n(\hat{\underline{u}}_T)]_{\mathbb{R}^-}\|_{L^2(\partial T^C)}^2+\frac{h_T}{\gamma_t}\|\,[\underline{\tau}_t(\underline{u})]_s-[\underline{\tau}_t(\hat{\underline{u}}_T)]_s\,\|_{\underline{L}^2(\partial T^C)}^2\Big)\\&\lesssim\mathbb{A}_1(\underline{u})+\mathbb{A}_2(\underline{u}),\end{aligned} \tag{5.37}$$

$\mathbb{A}_1(\underline{u})$ defined in (5.31), and recalling the HHO interpolation operator defined in (5.27), $\mathbb{A}_2(\underline{u})$ is given by

$$\begin{aligned}\mathbb{A}_2(\underline{u}):=\sum_{T\in\mathcal{T}_h^C}\frac{2}{\epsilon}\Big(&\frac{h_T}{\gamma_n}\|\delta\sigma_{n,T}\|_{L^2(\partial T^C)}^2+\frac{\gamma_n}{h_T}\|\delta u_{n,T}\|_{L^2(\partial T^C)}^2\\&+\frac{h_T}{\gamma_t}\|\delta\underline{\sigma}_{t,T}\|_{\underline{L}^2(\partial T^C)}^2+\frac{\gamma_t}{h_T}\|\delta\underline{u}_{t,T}\|_{\underline{L}^2(\partial T^C)}^2\Big),\end{aligned} \tag{5.38}$$

with $\delta\sigma_{n,T} := \sigma_n(\underline{u}) - \sigma_n(\hat{\underline{I}}_T^k(\underline{u}))$, $\delta\underline{\sigma}_{t,T} := \underline{\sigma}_t(\underline{u}) - \underline{\sigma}_t(\hat{\underline{I}}_T^k(\underline{u}))$, *and* $\delta u_{n,T}$ *and* $\delta\underline{u}_{t,T}$ *are the normal and tangential components on* Γ_C *of* $\delta\underline{u}_T := \underline{u}_{|\partial T} - \underline{\Pi}_{\partial T}^{k+1}(\underline{u}_{|\partial T})$.

Proof. Let us set $\hat{\underline{z}}_h := \hat{\underline{u}}_h - \hat{\underline{I}}_h^k(\underline{u})$, where $\hat{\underline{I}}_h^k : \underline{V}_D \to \hat{\underline{U}}_{h,0}^k$ is the global HHO interpolation operator defined in Section 5.4.1. The same manipulations as in (5.35) lead to

$$\sum_{T\in\mathcal{T}_h}\Big(2\mu\big(\|\boldsymbol{E}_T^k(\hat{\underline{z}}_T)\|_{\boldsymbol{L}^2(T)}^2 + h_T^{-1}\|\underline{S}_{\partial T}^k(\hat{\underline{z}}_T)\|_{\underline{L}^2(\partial T)}^2\big) + \lambda\|D_T^k(\hat{\underline{z}}_T)\|_{L^2(T)}^2\Big) \le \mathbb{T}_1 + \mathbb{T}_{2,n} + \mathbb{T}_{2,t} - \mathbb{T}_{3,n} - \mathbb{T}_{3,t},$$

where the terms on the right-hand side are defined as above by setting $\hat{\underline{v}}_h := \hat{\underline{u}}_h$ and $\hat{\underline{w}}_h := \hat{\underline{I}}_h^k(\underline{u})$. We use the fact that $\hat{\underline{u}}_h$ is the discrete solution to infer that $\mathbb{T}_1 := b_h(\hat{\underline{u}}_h;\hat{\underline{z}}_h) - \widehat{b}_h(\hat{\underline{I}}_h^k(\underline{u}),\hat{\underline{z}}_h) = \widehat{\ell}_h(\hat{\underline{z}}_h) - \widehat{b}_h(\hat{\underline{I}}_h^k(\underline{u}),\hat{\underline{z}}_h)$. Recalling the definition of $\widehat{b}_h$ and $\widehat{\ell}_h$, we obtain $\mathbb{T}_1 := \mathbb{T}_{1,1} + \mathbb{T}_{1,2,n} + \mathbb{T}_{1,2,t} - \mathbb{T}_{1,3,n} - \mathbb{T}_{1,3,t}$ with

$$\mathbb{T}_{1,1} := \sum_{T\in\mathcal{T}_h}\big((\underline{f},\underline{z}_T)_{\underline{L}^2(T)} - \widehat{a}_T(\hat{\underline{I}}_T^k(\underline{u}),\hat{\underline{z}}_T)\big) + \sum_{T\in\mathcal{T}_h^N}(\underline{g}_N,\underline{z}_{\partial T})_{\underline{L}^2(\partial T^N)},$$

$$\mathbb{T}_{1,2,n} := \sum_{T\in\mathcal{T}_h^C}\theta\frac{h_T}{\gamma_n}(\sigma_n(\hat{\underline{I}}_T^k(\underline{u})),\sigma_n(\hat{\underline{z}}_T))_{L^2(\partial T^C)},$$

$$\mathbb{T}_{1,3,n} := \sum_{T\in\mathcal{T}_h^C}\frac{h_T}{\gamma_n}(\Big[\tau_n(\hat{\underline{I}}_T^k(\underline{u}))\Big]_{\mathbb{R}^-},(\tau_n + (\theta-1)\sigma_n)(\hat{\underline{z}}_T))_{L^2(\partial T^C)},$$

and similar expressions for $\mathbb{T}_{1,2,t}$ and $\mathbb{T}_{1,3,t}$. We add and subtract $\sigma_n(\underline{u})$ and $[\tau_n(\underline{u})]_{\mathbb{R}^-}$ in $\mathbb{T}_{1,2,n}$ and $\mathbb{T}_{1,3,n}$, respectively, and obtain

$$\mathbb{T}_1 := \mathbb{T}'_{1,1}(\underline{u},\hat{\underline{z}}_h) - \mathbb{T}'_{1,2,n} - \mathbb{T}'_{1,2,t} + \mathbb{T}'_{1,3,n} + \mathbb{T}'_{1,3,t}, \tag{5.39}$$

where $\mathbb{T}'_{1,1}(\underline{u},\hat{\underline{z}}_h)$ is defined in (5.29) and (recall that $\delta\sigma_{n,T} := \sigma_n(\underline{u}) - \sigma_n(\hat{\underline{I}}_T^k(\underline{u}))$)

$$\mathbb{T}'_{1,2,n} := \sum_{T\in\mathcal{T}_h^C}\theta\frac{h_T}{\gamma_n}(\delta\sigma_{n,T},\sigma_n(\hat{\underline{z}}_T))_{L^2(\partial T^C)},$$

$$\mathbb{T}'_{1,3,n} := \sum_{T\in\mathcal{T}_h^C}\frac{h_T}{\gamma_n}([\tau_n(\underline{u})]_{\mathbb{R}^-} - \Big[\tau_n(\hat{\underline{I}}_T^k(\underline{u}))\Big]_{\mathbb{R}^-},(\tau_n + (\theta-1)\sigma_n)(\hat{\underline{z}}_T))_{L^2(\partial T^C)},$$

and similar expressions for $\mathbb{T}'_{1,2,t}$ and $\mathbb{T}'_{1,3,t}$. To make appear the term $\mathbb{T}'_{1,1}(\underline{u},\hat{\underline{z}}_h)$ in (5.39), we used that $\underline{\nabla}\cdot\boldsymbol{\sigma}(\underline{u}) + \underline{f} = \underline{0}$ in Ω, $\underline{\sigma}_n(\underline{u}) = \underline{g}_N$ on Γ_N, whereas on Γ_C we used that $\sigma_n(\underline{u}) = [\tau_n(\underline{u})]_{\mathbb{R}^-}$ owing to Lemma 5.3, $\frac{h_T}{\gamma_n}(\theta\sigma_n(\hat{\underline{z}}_T) - (\tau_n + (\theta-1)\sigma_n)(\hat{\underline{z}}_T)) = z_{\partial T,n}$, a similar identity for the tangential component, and that $\underline{\sigma}_n(\underline{u})\cdot\underline{z}_{\partial T} = \sigma_n(\underline{u})z_{\partial T,n} + \underline{\sigma}_t(\underline{u})\cdot\underline{z}_{\partial T,t}$. Combining $\mathbb{T}_{2,n}$ with $\mathbb{T}'_{1,2,n}$, we infer that

$$\mathbb{T}'_{2,n} := \mathbb{T}_{2,n} - \mathbb{T}'_{1,2,n} = \sum_{T\in\mathcal{T}_h^C}\theta\frac{h_T}{\gamma_n}\big(\|\sigma_n(\hat{\underline{z}}_T)\|_{\partial T^C}^2 - (\delta\sigma_{n,T},\sigma_n(\hat{\underline{z}}_T))_{L^2(\partial T^C)}\big),$$

together with a similar expression for $\mathbb{T}'_{2,t} := \mathbb{T}_{2,t} - \mathbb{T}'_{1,2,t}$. Moreover, combining $\mathbb{T}_{3,n}$ with $\mathbb{T}'_{1,3,n}$, we infer that

$$\mathbb{T}'_{3,n} := -\mathbb{T}_{3,n} + \mathbb{T}'_{1,3,n} = \sum_{T\in\mathcal{T}_h^C}\frac{h_T}{\gamma_n}([\tau_n(\underline{u})]_{\mathbb{R}^-} - [\tau_n(\hat{\underline{u}}_T)]_{\mathbb{R}^-},(\tau_n + (\theta-1)\sigma_n)(\hat{\underline{z}}_T))_{L^2(\partial T^C)},$$

together with a similar expression for $\mathbb{T}'_{3,t} := -\mathbb{T}_{3,t} + \mathbb{T}'_{1,3,t}$. Putting everything together, we infer that

$$\sum_{T\in\mathcal{T}_h}\Big(2\mu\big(\|\boldsymbol{E}_T^k(\hat{\underline{z}}_T)\|^2_{\boldsymbol{L}^2(T)} + h_T^{-1}\|\underline{S}_{\partial T}^k(\hat{\underline{z}}_T)\|^2_{\underline{L}^2(\partial T)}\big) + \lambda\|D_T^k(\hat{\underline{z}}_T)\|^2_{L^2(T)}\Big)$$
$$\le \mathbb{T}'_{1,1}(\underline{u},\hat{\underline{z}}_h) + \mathbb{T}'_{2,n} + \mathbb{T}'_{2,t} + \mathbb{T}'_{3,n} + \mathbb{T}'_{3,t}. \tag{5.40}$$

Let us now bound the terms $(\mathbb{T}'_{2,n} + \mathbb{T}'_{3,n})$ and $(\mathbb{T}'_{2,t} + \mathbb{T}'_{3,t})$. We only detail the bound on $(\mathbb{T}'_{2,n} + \mathbb{T}'_{3,n})$ since the reasoning is similar for $(\mathbb{T}'_{2,t} + \mathbb{T}'_{3,t})$. Recalling the above expression for $\mathbb{T}'_{2,n}$ and using Young's inequality (with $\beta_1 > 0$) for the second term on the right-hand side, we infer that

$$\mathbb{T}'_{2,n} \le \sum_{T\in\mathcal{T}_h^{\mathrm{C}}}\frac{h_T}{\gamma_n}\big((\theta+\tfrac{\beta_1}{2})\|\sigma_n(\hat{\underline{z}}_T)\|^2_{\partial T^{\mathrm{C}}} + \tfrac{\theta^2}{2\beta_1}\|\delta\sigma_{n,T}\|^2_{L^2(\partial T^{\mathrm{C}})}\big).$$

Turning to $\mathbb{T}'_{3,n}$, since $\hat{\underline{z}}_T = \hat{\underline{u}}_T - \underline{\hat{I}}_T^k(\underline{u})$ and the operator τ_n is linear, we have

$$(\tau_n + (\theta-1)\sigma_n)(\hat{\underline{z}}_T) = -(\tau_n(\underline{u}) - \tau_n(\hat{\underline{u}}_T)) + (\tau_n(\underline{u}) - \tau_n(\underline{\hat{I}}_T^k(\underline{u}))) + (\theta-1)\sigma_n(\hat{\underline{z}}_T),$$

so that we can re-arrange the terms composing $\mathbb{T}'_{3,n}$ as follows:

$$\begin{aligned}\mathbb{T}'_{3,n} := \sum_{T\in\mathcal{T}_h^{\mathrm{C}}}\frac{h_T}{\gamma_n}\Big(&- ([\tau_n(\underline{u})]_{\mathbb{R}^-} - [\tau_n(\hat{\underline{u}}_T)]_{\mathbb{R}^-}, \tau_n(\underline{u}) - \tau_n(\hat{\underline{u}}_T))_{L^2(\partial T^{\mathrm{C}})}\\ &+ ([\tau_n(\underline{u})]_{\mathbb{R}^-} - [\tau_n(\hat{\underline{u}}_T)]_{\mathbb{R}^-}, \tau_n(\underline{u}) - \tau_n(\underline{\hat{I}}_T^k(\underline{u})))_{L^2(\partial T^{\mathrm{C}})}\\ &+ (\theta-1)([\tau_n(\underline{u})]_{\mathbb{R}^-} - [\tau_n(\hat{\underline{u}}_T)]_{\mathbb{R}^-}, \sigma_n(\hat{\underline{z}}_T))_{L^2(\partial T^{\mathrm{C}})}\Big).\end{aligned}$$

Using (5.20) for the first term on the right-hand side and letting $\omega_{n,T} := [\tau_n(\underline{u})]_{\mathbb{R}^-} - [\tau_n(\hat{\underline{u}}_T)]_{\mathbb{R}^-}$ and $\delta\tau_{n,T} := \tau_n(\underline{u}) - \tau_n(\underline{\hat{I}}_T^k(\underline{u}))$, we infer that

$$\mathbb{T}'_{3,n} \le \sum_{T\in\mathcal{T}_h^{\mathrm{C}}}\frac{h_T}{\gamma_n}\big(-\|\omega_{n,T}\|^2_{L^2(\partial T^{\mathrm{C}})} + (\omega_{n,T},\delta\tau_{n,T})_{L^2(\partial T^{\mathrm{C}})} + (\theta-1)(\omega_{n,T},\sigma_n(\hat{\underline{z}}_T))_{L^2(\partial T^{\mathrm{C}})}\big).$$

Using Young's inequality to bound the second and the third terms on the right-hand side (with $\beta_2 > 0$ and $\beta_3 > 0$), we infer that

$$\mathbb{T}'_{3,n} \le \sum_{T\in\mathcal{T}_h^{\mathrm{C}}}\frac{h_T}{\gamma_n}\big((-1+\tfrac{\beta_2}{2}+\tfrac{|\theta-1|}{2\beta_3})\|\omega_{n,T}\|^2_{L^2(\partial T^{\mathrm{C}})} + \tfrac{1}{2\beta_2}\|\delta\tau_{n,T}\|^2_{L^2(\partial T^{\mathrm{C}})} + \tfrac{|\theta-1|\beta_3}{2}\|\sigma_n(\hat{\underline{z}}_T)\|^2_{L^2(\partial T^{\mathrm{C}})}\big).$$

Putting the bounds on $\mathbb{T}'_{2,n}$ and $\mathbb{T}'_{3,n}$ together leads to

$$\begin{aligned}\mathbb{T}'_{2,n} + \mathbb{T}'_{3,n} \le \sum_{T\in\mathcal{T}_h^{\mathrm{C}}}\frac{h_T}{\gamma_n}\big(&-\rho_1\|\omega_{n,T}\|^2_{L^2(\partial T^{\mathrm{C}})} + \rho_2\|\sigma_n(\hat{\underline{z}}_T)\|^2_{L^2(\partial T^{\mathrm{C}})}\\ &+ \tfrac{\theta^2}{2\beta_1}\|\delta\sigma_{n,T}\|^2_{L^2(\partial T^{\mathrm{C}})} + \tfrac{1}{2\beta_2}\|\delta\tau_{n,T}\|^2_{L^2(\partial T^{\mathrm{C}})}\big),\end{aligned}$$

with

$$\rho_1 := 1 - \tfrac{\beta_2}{2} - \tfrac{|\theta-1|}{2\beta_3}, \qquad \rho_2 := \theta + \tfrac{\beta_1}{2} + \tfrac{|\theta-1|\beta_3}{2}.$$

Let $\epsilon \in (0,1]$ and let us choose $\beta_1 := 2\epsilon$, $\beta_2 := \frac{\epsilon}{1+\epsilon}$, and $\beta_3 := \frac{|\theta-1|(1+\epsilon)}{2}$. Then we have $\rho_1 = \frac{\epsilon}{2(1+\epsilon)}$ and $\rho_2 = \frac{(\theta+1)^2}{4} + \epsilon(1+\frac{(\theta-1)^2}{4})$, as well as $\frac{\theta^2}{2\beta_1} = \frac{\theta^2}{4\epsilon} \le \frac{1}{4\epsilon} \le \frac{1}{\epsilon}$ and $\frac{1}{2\beta_2} = \frac{1+\epsilon}{2\epsilon} \le \frac{1}{\epsilon}$.

Using the above bound on $\mathbb{T}'_{2,n}+\mathbb{T}'_{3,n}$ together with a similar bound on $\mathbb{T}'_{2,t}+\mathbb{T}'_{3,t}$ in (5.40), we infer that

$$\begin{aligned}
&\sum_{T\in\mathcal{T}_h}\Big(2\mu\big(\|\boldsymbol{E}_T^k(\hat{\underline{z}}_T)\|_{\boldsymbol{L}^2(T)}^2+h_T^{-1}\|\underline{S}_{\partial T}^k(\hat{\underline{z}}_T)\|_{\underline{L}^2(\partial T)}^2\big)+\lambda\|D_T^k(\hat{\underline{z}}_T)\|_{L^2(T)}^2\Big) \qquad (5.41)\\
&+\rho_1\sum_{T\in\mathcal{T}_h^{\mathrm{C}}}\Big(\frac{h_T}{\gamma_n}\|\omega_{n,T}\|_{L^2(\partial T^{\mathrm{C}})}^2+\frac{h_T}{\gamma_t}\|\underline{\omega}_{t,T}\|_{\underline{L}^2(\partial T^{\mathrm{C}})}^2\Big)\\
&\le\mathbb{T}'_{1,1}(\underline{u},\hat{\underline{z}}_h)+\sum_{T\in\mathcal{T}_h^{\mathrm{C}}}\rho_2\Big(\frac{h_T}{\gamma_n}\|\sigma_n(\hat{\underline{z}}_T)\|_{L^2(\partial T^{\mathrm{C}})}^2+\frac{h_T}{\gamma_t}\|\underline{\sigma}_t(\hat{\underline{z}}_T)\|_{\underline{L}^2(\partial T^{\mathrm{C}})}^2\Big)+\mathbb{A}'_2(\underline{u}),
\end{aligned}$$

with $\underline{\omega}_{t,T}:=[\underline{\tau}_t(\underline{u})]_s-[\underline{\tau}_t(\hat{\underline{u}}_T)]_s$ and

$$\begin{aligned}
\mathbb{A}'_2(\underline{u}):=&\sum_{T\in\mathcal{T}_h^{\mathrm{C}}}\frac{h_T}{\epsilon\gamma_n}\big(\|\delta\sigma_{n,T}\|_{L^2(\partial T^{\mathrm{C}})}^2+\|\delta\tau_{n,T}\|_{L^2(\partial T^{\mathrm{C}})}^2\big)\\
&+\sum_{T\in\mathcal{T}_h^{\mathrm{C}}}\frac{h_T}{\epsilon\gamma_t}\big(\|\delta\underline{\sigma}_{t,T}\|_{\underline{L}^2(\partial T^{\mathrm{C}})}^2+\|\delta\underline{\tau}_{t,T}\|_{\underline{L}^2(\partial T^{\mathrm{C}})}^2\big),
\end{aligned}$$

recalling that $\delta\sigma_{n,T}:=\sigma_n(\underline{u})-\sigma_n(\hat{\underline{I}}_T^k(\underline{u}))$, $\delta\underline{\sigma}_{t,T}:=\underline{\sigma}_t(\underline{u})-\underline{\sigma}_t(\hat{\underline{I}}_T^k(\underline{u}))$ are defined in the assertion, $\delta\tau_{n,T}:=\tau_n(\underline{u})-\tau_n(\hat{\underline{I}}_T^k(\underline{u}))$ is defined above, and $\delta\underline{\tau}_{t,T}:=\underline{\tau}_t(\underline{u})-\underline{\tau}_t(\hat{\underline{I}}_T^k(\underline{u}))$. Recalling the definitions of the operators τ_n and $\underline{\tau}_t$ and invoking the triangle and Young's inequalities, we infer that $\mathbb{A}'_2(\underline{u})\le\mathbb{A}_2(\underline{u})$, with $\mathbb{A}_2(\underline{u})$ defined in the assertion. Note importantly that the face component of $\hat{\underline{I}}_T^k(\underline{u})$ on ∂T^{C} is indeed $\underline{\Pi}_{\partial T}^{k+1}(\underline{u}_{|\partial T})$ since the polynomial order is $(k+1)$ on the faces located on Γ_{C}. Next, we absorb the traces of $\sigma_n(\hat{\underline{z}}_T)$ and $\underline{\sigma}_t(\hat{\underline{z}}_T)$ in (5.41) (in the term multiplied by ρ_2) by the positive terms from the left-hand side. To this purpose, we proceed as in the proof of Lemma 5.11, i.e., we invoke the discrete trace inequality (5.32) and the lower bound (5.36) on the penalty parameters. This yields

$$\begin{aligned}
&\sum_{T\in\mathcal{T}_h}\frac{1}{3}\Big(2\mu\big(\|\boldsymbol{E}_T^k(\hat{\underline{z}}_T)\|_{\boldsymbol{L}^2(T)}^2+h_T^{-1}\|\underline{S}_{\partial T}^k(\hat{\underline{z}}_T)\|_{\underline{L}^2(\partial T)}^2\big)+\lambda\|D_T^k(\hat{\underline{z}}_T)\|_{L^2(T)}^2\Big)\\
&+\frac{\epsilon}{2(1+\epsilon)}\sum_{T\in\mathcal{T}_h^{\mathrm{C}}}\Big(\frac{h_T}{\gamma_n}\|\omega_{n,T}\|_{L^2(\partial T^{\mathrm{C}})}^2+\frac{h_T}{\gamma_t}\|\underline{\omega}_{t,T}\|_{\underline{L}^2(\partial T^{\mathrm{C}})}^2\Big)\le\mathbb{T}'_{1,1}(\underline{u},\hat{\underline{z}}_h)+\mathbb{A}_2(\underline{u}).
\end{aligned}$$

Finally we invoke Lemma 5.10 and infer that $|\mathbb{T}'_{1,1}(\underline{u},\hat{\underline{z}}_h)|^2\lesssim\mathbb{A}_1(\underline{u})\sum_{T\in\mathcal{T}_h}2\mu|\hat{\underline{z}}_T|_{1,T}^2$. Owing to the lower bound from Lemma 5.9 and Young's inequality, we can hide the factor $\sum_{T\in\mathcal{T}_h}2\mu|\hat{\underline{z}}_T|_{1,T}^2$ on the left-hand side of the above inequality. We conclude the proof by means of a triangle inequality.

□

Remark 5.15 (Lower bound (5.36)) *The minimal value of the penalty parameters from the lower bound in (5.36) is slightly tighter than that from the lower bound (5.33) and tends to it as $\epsilon\downarrow 0$. Formally one recovers the arguments from the proof of Lemma 5.11 (which invole only the two functions $\hat{\underline{v}}_h,\hat{\underline{w}}_h$ instead of the three functions $\hat{\underline{u}}_h,\hat{\underline{I}}_h^k(\underline{u})$ and $\underline{u}$ as in the proof of Theorem 5.14) by setting $\epsilon:=0$ so that $\beta_1=\beta_2=0$, $\beta_3=\frac{|\theta-1|}{2}$, $\rho_1=0$ and $\rho_2=\frac{(\theta+1)^2}{4}$.*

Remark 5.16 (Choice of ϵ, robustness) *For $\theta\in\{0,1\}$, the value chosen for ϵ is not really important, and one can simply set $\epsilon:=1$. Then (5.36) shows that γ_n scales as $\mu\kappa$ and*

γ_t scales as μ. Moreover, after taking the square root in (5.37) and observing that $\mathbb{A}_1(\underline{u})$ is robust in the incompressible limit (when κ is large) since the term involving κ involves the approximation of $\nabla{\cdot}\underline{u}$, one notices that the the upper bound still scales as $\kappa^{\frac{1}{2}}$ owing to the terms depending on γ_n in $\mathbb{A}_2(\underline{u})$. Instead, for $\theta=-1$, an interesting choice is $\epsilon\approx\kappa^{-1}$ leading to $\gamma_n\sim\mu$ (as $\gamma_t\sim\mu$), whereby the error estimate (5.37) delivers an upper bound scaling as $\kappa^{\frac{3}{2}}$ (after taking the square root as above). In the case of bilateral contact, an interesting choice is $\epsilon\approx\kappa^{-\frac{1}{2}}$ since only the penalty parameter γ_t, whereby the error estimate (5.37) delivers an upper bound scaling as $\kappa^{\frac{1}{4}}$ (after taking the square root as above).

Convergence rates for smooth solutions can be inferred from Theorem 5.14 by using the approximation properties of the L^2-orthogonal projection on shape-regular polyhedral mesh sequences. Referring, e.g., to [88, 114] for proofs, we have

$$\begin{aligned}\|v-\Pi_T^{k+1}(v)\|_{L^2(T)}+h_T^{\frac{1}{2}}\|v-\Pi_T^{k+1}(v)\|_{L^2(\partial T)}+h_T\|\underline{\nabla}(v-\Pi_T^{k+1}(v))\|_{\underline{L}^2(T)}\\ +h_T^{\frac{3}{2}}\|\underline{\nabla}(v-\Pi_T^{k+1}(v))\|_{\underline{L}^2(\partial T)}\lesssim h_T^{1+r}|v|_{H^{1+r}(T)},\end{aligned}\tag{5.42}$$

for all $v\in H^{1+r}(T;\mathbb{R})$, $r\in(\frac{1}{2},k+1]$, all $T\in\mathcal{T}_h$, and all $h>0$. Similar bounds are available for the projection of fields. Using (5.42) to bound $\mathbb{A}_1(\underline{u})$ and $\mathbb{A}_2(\underline{u})$ in (5.37) readily leads to the following error estimate (note that one can assume $\gamma_t\le\gamma_n$ without loss of generality).

Corollary 5.17 (H^1-error estimate) *Keep the assumptions and notation from Theorem 5.14. Assume that the exact solution satisfies $\underline{u}\in H^{1+r}(\Omega;\mathbb{R}^d)$ and $\nabla{\cdot}\underline{u}\in H^r(\Omega;\mathbb{R})$, $r\in(\frac{1}{2},k+1]$. Then we have*

$$\begin{aligned}&\sum_{T\in\mathcal{T}_h}\Big(2\mu\|\boldsymbol{\varepsilon}(\underline{u})-\boldsymbol{E}_T^k(\hat{\underline{u}}_T)\|_{\boldsymbol{L}^2(T)}^2+\lambda\|\nabla{\cdot}\underline{u}-D_T^k(\hat{\underline{u}}_T)\|_{L^2(T)}^2\Big)\\ &\quad+\frac{\epsilon}{2(1+\epsilon)}\sum_{T\in\mathcal{T}_h^C}\Big(\frac{h_T}{\gamma_n}\|[\tau_n(\underline{u})]_{\mathbb{R}^-}-[\tau_n(\hat{\underline{u}}_T)]_{\mathbb{R}^-}\|_{L^2(\partial T^C)}^2+\frac{h_T}{\gamma_t}\|[\underline{\tau}_t(\underline{u})]_s-[\underline{\tau}_t(\hat{\underline{u}}_T)]_s\|_{\underline{L}^2(\partial T^C)}^2\Big)\\ &\lesssim\sum_{T\in\mathcal{T}_h}\Big(2\mu h_T^{2r}|\underline{u}|_{\underline{H}^{1+r}(T)}^2+\frac{1}{2\mu}\lambda^2h_T^{2r}|\nabla{\cdot}\underline{u}|_{H^r(T)}^2+\frac{1}{\epsilon}\Big(\frac{\mu^2\kappa^2}{\gamma_n}+\frac{\mu^2}{\gamma_t}+\gamma_n\Big)h_T^{2r}|\underline{u}|_{\underline{H}^{1+r}(T)}^2\Big).\end{aligned}\tag{5.43}$$

Remark 5.18 (Choice of k) *A usual smoothness assumption is $\underline{u}\in H^{\frac{5}{2}-\varepsilon}(\Omega;\mathbb{R}^d)$, $\varepsilon>0$, i.e., $r=\frac{3}{2}-\varepsilon$, as is generally the case when there is a transition between contact and no-contact. Then the maximal convergence rate is $\mathcal{O}(h^{\frac{3}{2}-\varepsilon})$ and is reached for $k=1$.*

Remark 5.19 (Face polynomials) *Using face polynomials of order $(k+1)$ on the faces located on Γ_C is crucial to obtain the above error estimate in the optimal case where $r=k+1$. This allows us to invoke the approximation properties of $\underline{\Pi}_{\partial T}^{k+1}$ on ∂T^C when bounding $\mathbb{A}_2(\underline{u})$.*

5.5 Numerical experiments

The goal of this section is to evaluate the proposed HHO-Nitsche method on two- and three-dimensional benchmarks: (i) a two-dimensional manufactured solution; (ii) a three-dimensional frictionless Hertz contact problem; (iii) a stick and slip transition, and (iv) a prototype for an industrial application. We employ the notation HHO(k) when using polynomials of order $k\ge1$. The implementation of HHO methods is discussed in [71] and an

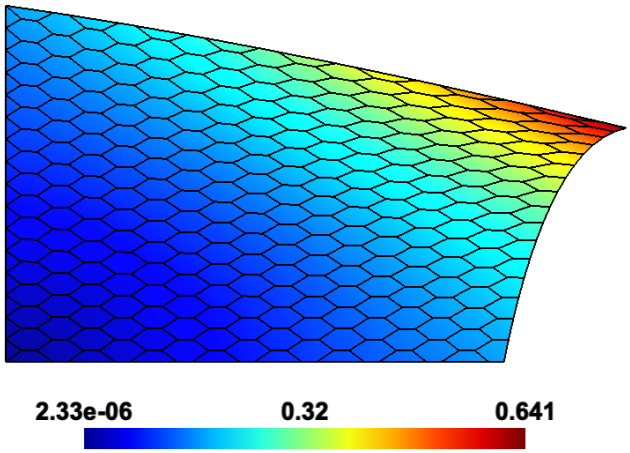

Figure 5.3: 2D manufactured solution: Euclidean displacement norm on the deformed configuration for HHO(1) and $\theta = 0$ for a hexagonal mesh ($h = 4.60\text{e-}2$) (the contact boundary Γ_C is the bottom side).

open-source software is available[1]. The discrete nonlinear problem (5.18) is solved by a generalized Newton method as in [79]. In the present implementation, the penalty parameters for the stabilization and the friction/Tresca condition are proportional to 2μ and are scaled by the reciprocal of the diameter of the local face rather than the diameter of the local cell. We compare our numerical results to the analytical solution whenever available or to numerical solutions obtained either from the literature or using the industrial open-source FEM software `code_aster` [111]. In this latter case we consider a mixed method called T2-LAC (see [1]) where the discrete unknowns are the piecewise quadratic displacement field and the piecewise constant contact pressure.

5.5.1 2D manufactured solution

We consider the unit square $\Omega := (0,1)^2$, we set $\Gamma_C := (0,1) \times \{0\}$ and $\Gamma_D := \{0,1\} \times (0,1) \cup (0,1) \times \{1\}$. The Lamé coefficients are $\mu := 2$ and $\lambda := 1000$ (which corresponds to a Poisson ratio of $\nu \simeq 0.499$). The manufactured solution is

$$u_x(x,y) := \left(1 + \frac{1}{1+\lambda}\right) x e^{x+y}, \qquad u_y(x,y) := \left(-1 + \frac{1}{1+\lambda}\right) y e^{x+y}. \tag{5.44}$$

The x-dependnent friction threshold is $s(x) := \mu \frac{\lambda+2}{6\lambda+6} x^2$. The displacement imposed on Γ_D is the trace of the manufactured solution, and the volume force is computed accordingly. The penalty parameters are taken as $\gamma_n = \gamma_t := 2\mu$. In this test case, we consider hexagonal meshes to illustrate the polyhedral capabilities of the proposed HHO-Nitsche method. The Euclidean displacement norm of the manufactured solution is plotted in Fig. 5.3 on the deformed configuration for a hexagonal mesh composed of 280 cells.

We first report in Tab. 5.1 the H^1-error (that is, the μ-dependnent part of the left-hand side in (5.43)) and convergence rates as a function of the average mesh size h for $k \in \{1,2\}$ on hexagonal mesh sequences and for the symmetric variant with $\theta = 1$. For all $k \in \{1,2\}$, the H^1-error converges with order $(k+1)$ as predicted in Corollary 5.17. The results are similar for the other variants with $\theta \in \{-1,0\}$ (not shown for brevity). These convergence rates are

[1] `https://github.com/wareHHOuse/diskpp`

Mesh size	$k=1$		$k=2$	
h	H^1-error	order	H^1-error	order
3.33e-1	5.423e-3	-	4.406e-4	-
1.75e-1	1.380e-3	2.13	5.871e-5	3.13
9.06e-2	3.472e-4	2.08	7.620e-6	3.07
4.60e-2	8.694e-5	2.05	9.719e-7	3.04

Table 5.1: 2D manufactured solution: H^1-error and convergence order vs. h for $\theta = 1$.

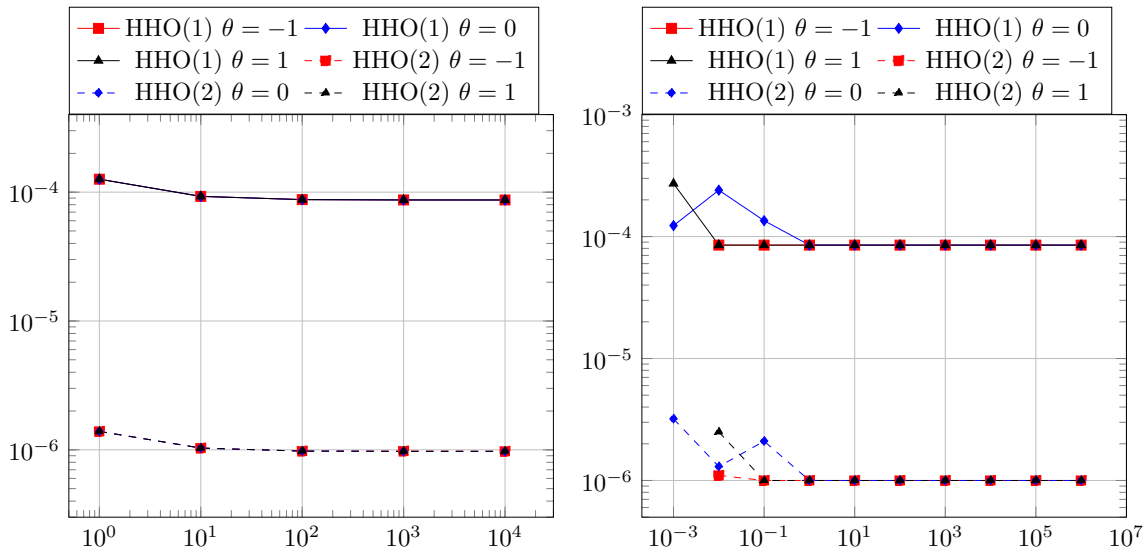

(a) H^1-error vs. λ ($\gamma_n = \gamma_t = 2\mu$) (b) H^1-error vs. $\frac{\gamma_n}{2\mu}$ ($\lambda = 1000$ and $\gamma_t = 2\mu$)

Figure 5.4: 2D manufactured solution: H^1-error vs. λ and $\frac{\gamma_n}{2\mu}$ for a hexagonal mesh ($h =$ 4.60e-2).

consistent with the predicted rates in Corollary 5.17 (we are not limited by the regularity of the solution in this test case).

In Fig. 5.4 we report on a fixed hexagonal mesh the H^1-error as a function of the material parameter λ (left panel) and of the penalty parameter $\frac{\gamma_n}{2\mu}$ with $\gamma_t = 2\mu$ fixed (right panel) for $k \in \{1, 2\}$ and for the three variants with $\theta \in \{-1, 0, 1\}$. We observe that the H^1-error is nearly independent of the values of λ and $\frac{\gamma_n}{2\mu}$. These results indicate that the HHO-Nitsche method appears to be locking-free in the incompressible limit despite that the theoretical analysis is somewhat more pessimistic. The same comment can be made regarding the necessity to enforce the lower bound in (5.36).

5.5.2 3D Hertz contact

The second benchmark is the well known three-dimensional Hertz contact problem of a half sphere in contact with a rigid foundation. The half sphere is centered at the point having coordinates $(0, 0, 100)$ and has a radius of 100. The contact boundary is the infinite plane $z := 0$ and a vertical displacement $u_z := -2$ is applied on the top surface. For symmetry reasons, one quarter of the half sphere is discretized. The material parameters are $\mu := 26.9$ and $\lambda := 40.3$. This benchmark is frictionless, i.e., $s := 0$, so as to compare our numerical results with a reference solution computed using the mixed quadratic formulation T2-LAC

implemented in the industrial software `code_aster`. For this test case, we do not expect HHO(2) to deliver a more accurate solution than HHO(1) since the geometry is discretized using tetrahedra with planar faces. We consider only the variant with $\theta = 0$ and we set $\gamma_n = \gamma_t := 2\mu$. The Euclidean displacement norm on the deformed configuration is plotted in Fig. 5.5a for HHO(1). In Fig. 5.5b, we compare for HHO(k), $k \in \{1, 2\}$, and the reference T2-LAC solution, the evolution of the normal component of the Cauchy stress tensor (see (5.19) for HHO) vs. the radial coordinate at the barycentrer of the contact faces. The results for HHO(k), which are computed on a mesh composed of 3,740 tetrahedra, are in good agreement with the reference solution which is computed on a finer mesh with 16,518 tetrahedra, although some differences are visible near $r = 15$ where the transition between contact and no-contact occurs.

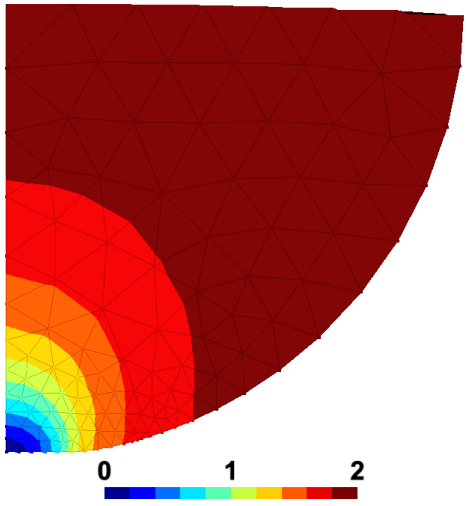

(a) Euclidean displacement norm on the deformed configuration for HHO(1)

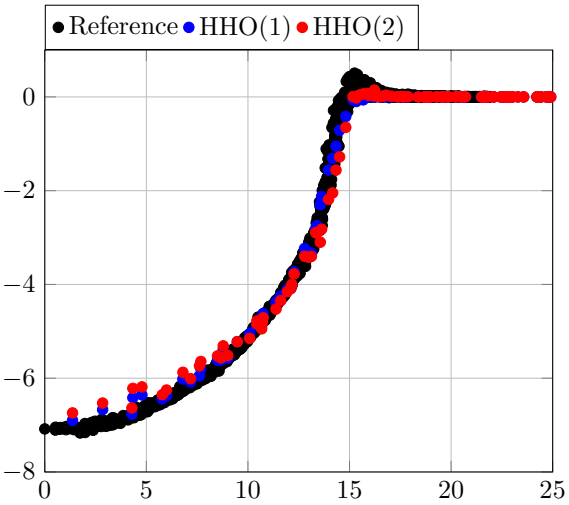

(b) $\sigma_{n,T}^k$ vs. radial-coordinate

Figure 5.5: 3D Hertz contact sphere: displacement field on the deformed configuration and contact pressure vs. radial coordinate.

5.5.3 Stick and slip transition (Bostan & Han test case)

This thrid benchmark has been studied previously in [37]. It consists of a rectangular domain $\Omega := (0, 8)\times(0, 4)$ which is clamped on the Dirichlet boundary $\Gamma_D := (0, 8)\times\{4\}$ and subjected to a horizontal surface load $\underline{g}_N := (400, 0)$ on the Neumann boundary $\Gamma_N := \{0\}\times(0, 4)$. The bilateral contact boundary is $\Gamma_C := (0, 8) \times \{0\}$, where a Tresca friction is considered with $s := 150$. Moreover the material parameters are $\mu := 384.6$ and $\lambda := 576.9$. The symmetry parameter is set to $\theta := 1$ and the penalty parameters to $\gamma_n = \gamma_t := 2\mu$. The reference solution, referred to as Bostan&Han, comes from [37, Example 6.2], where a mixed method with adaptive mesh refinement is used.

In Fig. 5.6 we compare the normalized quantity $\|\underline{\sigma}_t\|/s$ at the barycentrer of the contact faces for HHO(k), $k \in \{1, 2\}$, and the reference solution on two different meshes: a coarse mesh composed of 225 quadrangles and a fine mesh composed of 10,000 quadrangles. We observe that the results for the HHO(k) methods are close to the reference solution even on the coarse mesh. Moreover, on the fine mesh, both methods accurately capture the transition between slip ($\|\underline{\sigma}_t\|/s = 1$) and stick ($\|\underline{\sigma}_t\|/s < 1$) at $x \sim 2.7$. Moreover, the results are slightly more accurate for HHO(2) than for HHO(1) on the coarse mesh and quasi-identical on the

fine mesh. We note that increasing k does not improve significantly the results as expected, since the regularity of the solution is a limiting factor in this example.

To evaluate the influence of the penalty parameters γ_n and γ_t, we compare the total number of Newton's iterations needed to solve the nonlinear problem (5.18) versus the magnitude of the normalized penalty parameter $\gamma_0 := \frac{\gamma_n}{2\mu} = \frac{\gamma_t}{2\mu}$. The Newton's iterations are stopped under a relative residual convergence threshold of 10^{-7}, and convergence failure is reported after 200 iterations. We present the results in Fig. 5.7 for the coarse mesh composed of 225 quadrangles, for three symmetry variants, and for the polynomial degrees $k \in \{1, 2\}$. For HHO(1), we remark that the different symmetry variants need the same total number of Newton's iterations (5 here) if $\gamma_0 \geq 10^2$, whereas the skew-symmetric variant ($\theta = -1$) is the most robust since the number of Newton's iterations is almost independent of γ_0, contrary to the incomplete variant ($\theta = 0$) which suffers some degradation in the convergence for $\gamma_0 \leq 1$, and to the symmetric variant ($\theta = 1$) which does not converge anymore if $\gamma_0 < 10^{-2}$. For HHO(2), the skew-symmetric variant ($\theta = -1$) is again the most robust, as for HHO(1). However, both variants with $\theta = 0$ and $\theta = 1$ now exhibit a similar behavior and do not converge anymore if $\gamma_0 < 10^{-3}$ and $\gamma_0 < 10^{-2}$, respectively. Finally, we observe that for HHO(2), the number of iterations increases significantly for $\gamma_0 \geq 10^4$ whatever the value of the symmetry parameter (and do not converge anymore if $\gamma_0 > 10^5$). This effect is not observed for HHO(1). To sum up this numerical experiment, an optimal range of values for γ_0 seems to be $10^{-1} \leq \gamma_0 \leq 10^3$.

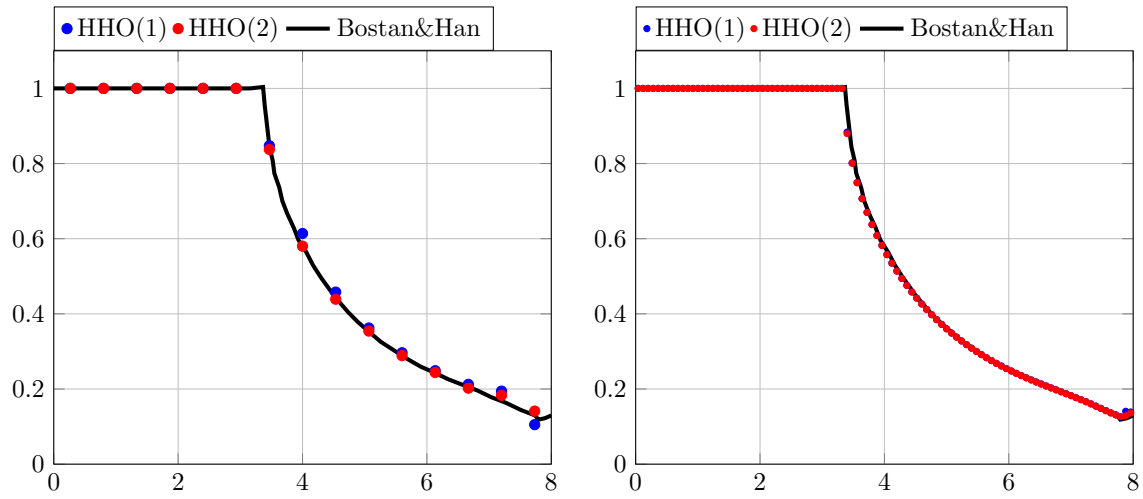

(a) mesh composed of 225 quadrangles

(b) mesh composed of 10000 quadrangles

Figure 5.6: Stick and slip transition (Bostan & Han test case): $\|\underline{\sigma}_t\|/s$ vs. x-coordinate at the barycentrer of the contact faces on a coarse and a fine mesh.

5.5.4 A prototype for an industrial application

This prototype simulates the installation of a notched plug in a rigid pipe. The mesh is composed of 21,200 hexahedra and 510 prisms in the reference configuration, see Fig. 5.10 (for symmetry reasons, only one quarter of the pipe is discretized). The notched plug has a length of 56mm and an outer radius of 8mm. The pipe is supposed to be rigid and has an inner radius of 8.77mm (there is an initial gap of 0.77mm between the plug and the pipe). The contact zone Γ_C with Tresca's friction ($s := 3{,}000$MPa) is between the rigid pipe and the ten notches of the plug. In the actual industrial setting, an indenter imposes a displacement

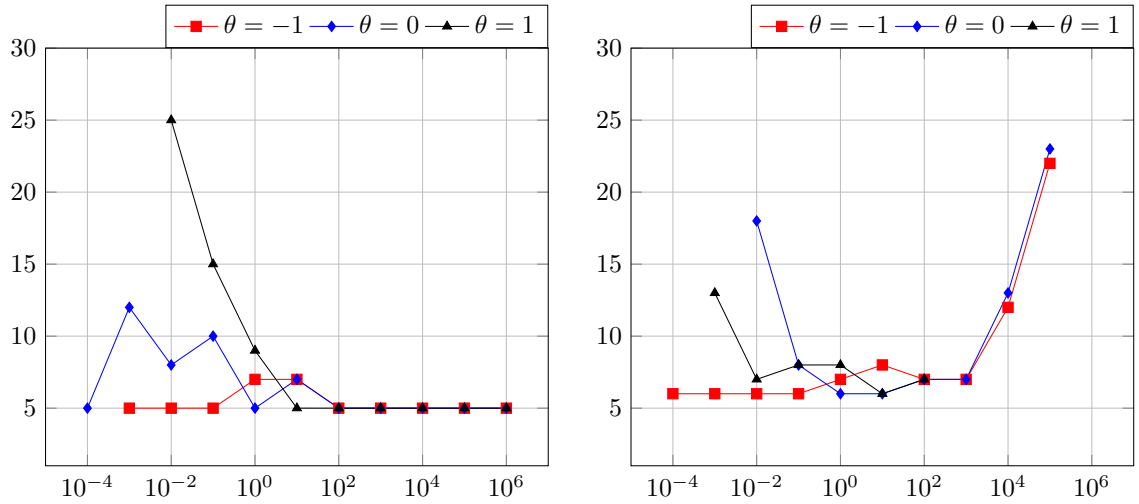

(a) HHO(1) (b) HHO(2)

Figure 5.7: Stick and slip transition (Bostan & Han test case): total number of Newton's iterations vs. the normalized penalty parameter γ_0 for a mesh composed of 225 quadrangles (no value is plotted if Newton's method has not converged after 200 iterations)

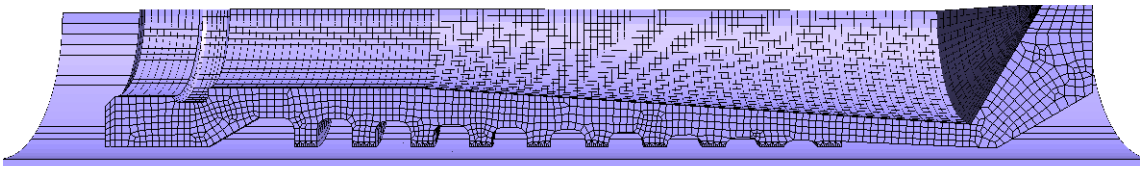

Figure 5.8: Notch plug : mesh composed of 21,200 hexahedra and 510 prisms in the reference configuration.

to the upper surface of the plug. To simplify, sufficiently large vertical and horizontal forces are applied to the upper surface of the plug to impose a contact between the pipe and the notches. The material parameters for the plug are $\mu := 80,769\text{MPa}$ and $\lambda := 121,154\text{MPa}$ (which correspond to a Young modulus $E := 210,000\text{MPa}$ and a Poisson ratio $\nu := 0.3$). The simulation is performed using HHO(1), the symmetry variant $\theta := 1$, and the penalty parameters $\gamma_n = \gamma_t := 2\mu$).

The von Mises stress is plotted in Fig. 5.9 on the deformed configuration. The maximal value is reached where the force is applied. Moreover, a zoom on the contact zone is plotted in Fig. 5.9b. We remark that there is contact between the notches and the pipe. Finally, the normal stress σ_n is visualized in Fig. 5.10 on the inferior surface of the plug. We remark that all the notches are in contact except the first three and the last one (where $\sigma_n = 0$), and that a transition between contact and non-contact is located at the fourth notch. Moreover, the maximal value of the contact pressure is reached at the extremity of the notches.

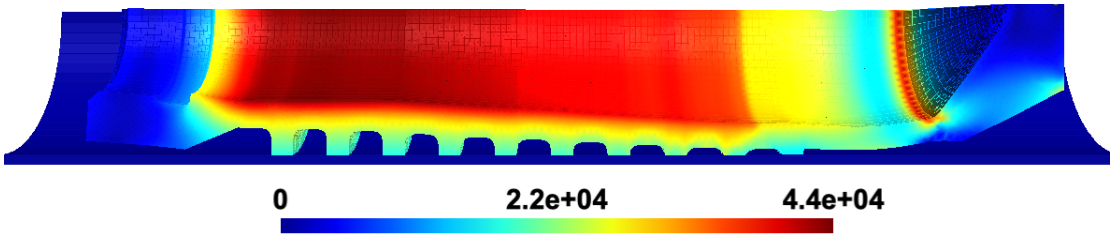

(a) Full structure

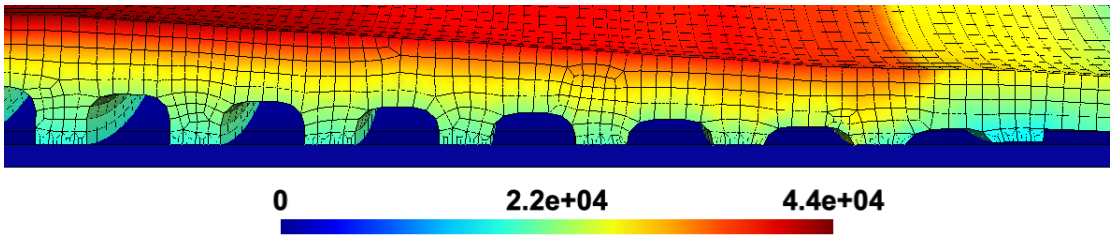

(b) Zoom on the contact zone

Figure 5.9: Notch plug: von Mises stress on the deformed configuration (in MPa).

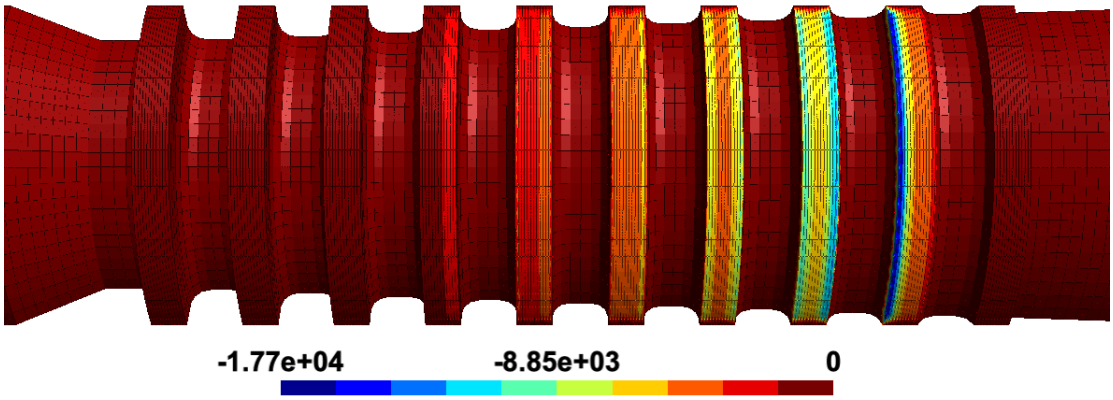

Figure 5.10: Notch plug: normal stress σ_n on the contact zone (in MPa).

5.6 Nitsche-HHO method for associative plasticity

The main goal of this section is to propose an extension to a plastic behavior of the face-based Nitsche-HHO method developed in Sect. 5.3 for a linear elastic behavior. The discrete symmetric strain reconstruction operator (5.12) and the stabilization operator (5.14) are keep unchanged. Moreover, the extension to a plastic behavior impose to reconstruct locally a discrete stress tensor and a discrete tangent modulus from the values computed at the quadrature points.

5.6.1 Frictional contact with plasticity

We adopt the plasticity model presented in Chap. 3. The plasticity model is assumed to be strain-hardening and rate independent, i.e., the time and the speed of deformations have no influence on the strains. For this reason, only the incremental plasticity problem is considered. Moreover, we place ourselves in the framework of generalized standard materials initially introduced in [127]. Hence, the local material state is described by the total strain tensor $\boldsymbol{\varepsilon} \in \mathbb{R}^{d\times d}_{\text{sym}}$, the plastic strain tensor $\boldsymbol{\varepsilon}^p \in \mathbb{R}^{d\times d}_{\text{sym}}$, and a finite collection of internal variables $\underline{\alpha} := (\alpha_1, \cdots, \alpha_m) \in \mathbb{R}^m$. For simplicity, we denote $\underline{\chi} := (\boldsymbol{\varepsilon}^p, \underline{\alpha}) \in \underline{\mathcal{X}}$ the generalized internal variables, where the space of the generalized internal variables is

$$\underline{\mathcal{X}} := \left\{ \underline{\chi} = (\boldsymbol{\varepsilon}^p, \underline{\alpha}) \in \mathbb{R}^{d\times d}_{\text{sym}} \times \mathbb{R}^m \mid \text{trace}(\boldsymbol{\varepsilon}^p) = 0 \right\}. \tag{5.45}$$

Since we consider a plasticity model, the Cauchy stress tensor $\boldsymbol{\sigma}$ does not depend linearly of the deformations when a plastic evolution occurs. Hence, the weak formulation (5.8) is no more valid. This problem is circumvented by adapting the idea developed in [168] for a Nitsche-FEM formulation with large deformations. We introduce the non-smooth operator $\mathcal{C}_\gamma : \underline{V}_0 \times \mathbb{R}^{d\times d}_{\text{sym}} \to \mathbb{R}^d$ such that

$$\mathcal{C}_\gamma(\underline{u}, \boldsymbol{\sigma}) = [\sigma_n - \gamma u_n]_{\mathbb{R}^-} \underline{n} + [\underline{\sigma}_t - \gamma \underline{u}_t]_s \,. \tag{5.46}$$

where $\gamma > 0$ is the Nitsche's penalty parameter (for simplicity we consider only one Nitsche's parameter $\gamma := \gamma_n := \gamma_t$). We are interested in finding the quasi-static evolution in the pseudo-time interval $[0, t_F]$, $t_F > 0$, of an elastoplastic material body that occupies the domain Ω in the reference configuration. The pseudo-time interval $[0, t_F]$ is discretized into M subintervals such that $t^0 = 0 < t^1 < \cdots < t^M = t_F$. Then the problem can be formulated as follows: For all $1 \le m \le M$, given $\underline{u}^{m-1} \in \underline{V}_0$ and $\underline{\chi}^{m-1} \in L^2(\Omega; \underline{\mathcal{X}})$ from the previous pseudo-time step or the initial condition, find $\underline{u}^m \in \underline{V}_0$ and $\underline{\chi}^m \in L^2(\Omega; \underline{\mathcal{X}})$ such that, for all $\underline{v} \in \underline{V}_0$,

$$\begin{aligned} &\int_\Omega \boldsymbol{\sigma}^m : \boldsymbol{\varepsilon}(\underline{v})\, d\Omega - \int_{\Gamma_C} \frac{\theta}{\gamma} \underline{\sigma}^m_n \cdot \left(\mathbb{C}^m_{ep} : \boldsymbol{\varepsilon}(\underline{v})\underline{n}\right) d\Gamma + \int_{\Gamma_C} \frac{1}{\gamma} \mathcal{C}_\gamma(\underline{u}^m, \boldsymbol{\sigma}^m) \cdot \left(\theta \mathbb{C}^m_{ep} : \boldsymbol{\varepsilon}(\underline{v})\underline{n} - \gamma \underline{v}\right) d\Gamma \\ &= \int_\Omega \underline{f}^m \cdot \underline{v}\, d\Omega + \int_{\Gamma_N} \underline{g}^m_N \cdot \underline{v}\, d\Gamma, \end{aligned} \tag{5.47a}$$

and

$$(\underline{\chi}^m, \boldsymbol{\sigma}^m, \mathbb{C}^m_{ep}) = \text{SMALL\_PLASTICITY}(\underline{\chi}^{m-1}, \boldsymbol{\varepsilon}(\underline{u}^{m-1}), \boldsymbol{\varepsilon}(\underline{u}^m) - \boldsymbol{\varepsilon}(\underline{u}^{m-1})). \tag{5.47b}$$

The procedure SMALL_PLASTICITY allows one to compute the new values of the generalized internal variables $\underline{\chi}$, the stress tensor $\boldsymbol{\sigma}$ and the consistent elastoplastic tangent modulus $\mathbb{C}_{ep}$ at each pseudo-time step. This procedure is detailed in Section 3.2.3 and requires to solve a constrained nonlinear problem.

5.6.2 Stress and tangent modulus reconstructions

A key feature of the present HHO method is that the discrete generalized internal variables are computed only at some quadrature points in each mesh cell. We introduce for all $T \in \mathcal{T}_h$, the quadrature points $\underline{\xi}_T = (\underline{\xi}_{T,j})_{1\le j\le m_Q}$, with $\underline{\xi}_{T,j} \in T$ for all $1 \le j \le m_Q$, and the quadrature weights $\omega_T = (\omega_{T,j})_{1\le j\le m_Q}$, with $\omega_{T,j} \in \mathbb{R}$ for all $1 \le j \le m_Q$. We denote by k_Q the order of the quadrature. Then, the discrete internal variables are sought in the space

$$\underline{\tilde{\mathcal{X}}}_{\mathcal{T}_h}^{m_Q} := \bigtimes_{T\in\mathcal{T}_h} \underline{\mathcal{X}}^{m_Q}, \tag{5.48}$$

that is, for all $T \in \mathcal{T}_h$, the internal variables attached to T form a vector $\underline{\tilde{\chi}}_T = (\tilde{\underline{\chi}}_T(\underline{\xi}_{T,j}))_{1\le j\le m_Q}$ with $\tilde{\underline{\chi}}_T(\underline{\xi}_{T,j}) \in \underline{\mathcal{X}}$ for all $1 \le j \le m_Q$. We will use the following notation for two tensor-valued functions $(\boldsymbol{p}, \boldsymbol{q})$ defined on T:

$$(\boldsymbol{p}, \boldsymbol{q})_{\boldsymbol{L}^2_Q(T)} := \sum_{j=1}^{m_Q} \omega_{T,j}\, \boldsymbol{p}(\underline{\xi}_{T,j}) : \boldsymbol{q}(\underline{\xi}_{T,j}). \tag{5.49}$$

We will also need to consider the case where we know the tensor $\tilde{\boldsymbol{p}}$ only at the quadrature nodes (we use a tilde to indicate this situation), i.e., we have $\tilde{\boldsymbol{p}} = (\tilde{\boldsymbol{p}}(\underline{\xi}_{T,j}))_{1\le j\le m_Q} \in (\mathbb{R}^{d\times d})^{m_Q}$. In this case, we slightly abuse the notation by denoting again by $(\tilde{\boldsymbol{p}}, \boldsymbol{q})_{\boldsymbol{L}^2_Q(T)}$ the quantity equal to the right-hand side of (5.49).

For the small plasticity problem, the discrete Cauchy stress $\tilde{\boldsymbol{\sigma}}$ tensor and its associated elastoplastic tangent modulus $\tilde{\mathbb{C}}_{ep}$ are computed and known only at the quadrature points (where the discrete generalized internal variables are computed). Then, for all mesh cell $T \in \mathcal{T}_h$, the reconstructed Cauchy stress tensor $\boldsymbol{\sigma}_T^k : (\mathbb{R}^{d\times d}_{\rm sym})^{m_Q} \to \mathbb{P}_d^k(T; \mathbb{R}^{d\times d}_{\rm sym})$ is obtained by solving the following local problem: For all $\boldsymbol{\tau} \in \mathbb{P}_d^k(T; \mathbb{R}^{d\times d}_{\rm sym})$,

$$(\boldsymbol{\sigma}_T^k(\tilde{\boldsymbol{\sigma}}_T), \boldsymbol{\tau})_{\boldsymbol{L}^2(T)} = (\tilde{\boldsymbol{\sigma}}_T, \boldsymbol{\tau})_{\boldsymbol{L}^2_Q(T)} \tag{5.50}$$

where $\tilde{\boldsymbol{\sigma}}_T = (\tilde{\boldsymbol{\sigma}}_T(\underline{\xi}_{T,j}))_{1\le j\le m_Q} \in (\mathbb{R}^{d\times d}_{\rm sym})^{m_Q}$. Concerning the elastoplastic tangent modulus, the reconstruction is obtained by remarking that the elastoplastic tangent modulus is always contracted to the reconstructed symmetric strain $\boldsymbol{E}_T^k$. This reconstruction is materialized by an operator

$$(\mathbb{C}_{ep} : \boldsymbol{E})_T^k : (\mathbb{S}^d_{\rm sym})^{m_Q} \times \underline{\hat{U}}_T^k \to \mathbb{P}_d^k(T; \mathbb{R}^{d\times d}_{\rm sym}),$$

where $\mathbb{S}^d_{\rm sym}$ is the space composed of fourth-order tensor having the minor and major symmetries. For all $\tilde{\mathbb{C}}_{ep,T} \in (\mathbb{S}^d_{\rm sym})^{m_Q}$ and $\underline{\hat{v}}_T \in \underline{\hat{U}}_T^k$, the reconstructed operator $(\mathbb{C}_{ep} : \boldsymbol{E})_T^k(\tilde{\mathbb{C}}_{ep,T}, \underline{\hat{v}}_T) \in \mathbb{P}_d^k(T; \mathbb{R}^{d\times d}_{\rm sym})$ is obtained by solving the following local problem: For all $\boldsymbol{\tau} \in \mathbb{P}_d^k(T; \mathbb{R}^{d\times d}_{\rm sym})$,

$$((\mathbb{C}_{ep} : \boldsymbol{E})_T^k(\tilde{\mathbb{C}}_{ep,T}, \underline{\hat{v}}_T), \boldsymbol{\tau})_{\boldsymbol{L}^2(T)} = (\tilde{\mathbb{C}}_{ep,T} : \boldsymbol{E}_T^k(\underline{\hat{v}}_T), \boldsymbol{\tau})_{\boldsymbol{L}^2_Q(T)}. \tag{5.51}$$

where $\tilde{\mathbb{C}}_{ep,T} = (\tilde{\mathbb{C}}_{ep,T}(\underline{\xi}_{T,j}))_{1\le j\le m_Q} \in (\mathbb{S}^d_{\rm sym})^{m_Q}$. Note that the associated mass matrix of this problem can be computed and factorized once for all, then inverted for each new right-hand side. Moreover, we prove the following invariance of the reconstructed stress and tangent modulus operators.

Lemma 5.20 (Invariance) *Assume that $k_Q \ge 2k$. Then, we have the following properties for all $T \in \mathcal{T}_h$,*

$$\boldsymbol{\sigma}_T^k(\tilde{\boldsymbol{p}}) = \boldsymbol{p}, \qquad \forall \boldsymbol{p} \in \mathbb{P}_d^k(T; \mathbb{R}^{d\times d}_{sym}) \tag{5.52}$$

where $\tilde{\boldsymbol{p}} = (\boldsymbol{p}(\underline{\xi}_{T,j}))_{1\le j\le m_Q} \in (\mathbb{R}^{d\times d}_{sym})^{m_Q}$, *and*

$$(\mathbb{C}_{ep} : \boldsymbol{E})^k_T(\mathbb{M}, \underline{\hat{v}}_T) = \mathbb{M} : \boldsymbol{E}^k_T(\underline{\hat{v}}_T), \qquad \forall (\mathbb{M}, \underline{\hat{v}}_T) \in \mathbb{P}^0_d(T; \mathbb{S}^d_{sym}) \times \underline{\hat{U}}^k_T. \tag{5.53}$$

Moreover, the reconstructed operators (5.50) *and* (5.51) *are consistant with those used for the linear elasticity problem in Sect. 5.3 where* $\boldsymbol{p} = 2\mu \boldsymbol{E}^k_T(\underline{\hat{v}}_T) + \lambda D^k_T(\underline{\hat{v}}_T)\boldsymbol{I}_d$ *and* $\mathbb{M} = \mathbb{C}$.

Remark 5.21 *Note that the reconstructed stress tensor* $\boldsymbol{\sigma}^k_T$ *is the operator which is used in Lemma 3.5 to prove a local principal of virtual work for plasticity with small deformations without contact (under the additional assumption* $k_Q \ge 2k$*).*

Remark 5.22 *An other possible reconstruction of the elastoplastic tangent modulus is such that for all* $\tilde{\mathbb{C}}_{ep,T} \in (\mathbb{S}^d_{sym})^{m_Q}$, *the reconstructed operator* $\mathbb{C}^k_{ep,T}(\tilde{\mathbb{C}}_{ep,T}) \in \mathbb{P}^k_d(T; \mathbb{S}^d_{sym})$ *is obtained by solving the following local problem: For all* $\mathbb{M} \in \mathbb{P}^k_d(T; \mathbb{S}^d_{sym})$,

$$(\mathbb{C}^k_{ep,T}(\tilde{\mathbb{C}}_{ep,T}), \mathbb{M})_{\mathbb{L}^2(T)} = (\tilde{\mathbb{C}}_{ep,T}, \mathbb{M})_{\mathbb{L}^2_Q(T)} \tag{5.54}$$

where $\tilde{\mathbb{C}}_{ep,T} = (\tilde{\mathbb{C}}_{ep,T}(\underline{\xi}_{T,j}))_{1\le j\le m_Q} \in (\mathbb{S}^d_{sym})^{m_Q}$. *Note that the first reconstruction* $(\mathbb{C}_{ep} : \boldsymbol{E})^k_T$ *use a smaller space than the second reconstruction* $\mathbb{C}^k_{ep,T}$. *Morover, the first reconstruction* $(\mathbb{C}_{ep} : \boldsymbol{E})^k_T$ *is used to compute the Newton's system in [3].*

5.6.3 Discrete problem

Let us denote $\mathcal{C}_{\gamma,T} : \underline{\hat{U}}^k_T \times (\mathbb{R}^{d\times d}_{\rm sym})^{m_Q} \to \mathbb{R}^d$ the discrete version of $\mathcal{C}_\gamma$.

$$\mathcal{C}_{\gamma,T}(\underline{\hat{v}}_T, \tilde{\boldsymbol{\sigma}}_T) = \left[\sigma^k_{n,T}(\tilde{\boldsymbol{\sigma}}_T) - \gamma v_{\partial T,n}\right]_{\mathbb{R}^-} \underline{n}_T + \left[\underline{\sigma}^k_{t,T}(\tilde{\boldsymbol{\sigma}}_T) - \gamma \underline{v}_{\partial T,t}\right]_s. \tag{5.55}$$

and $D\mathcal{C}_{\gamma,T}(\underline{\hat{v}}_T, \tilde{\boldsymbol{\sigma}}_T), \tilde{\mathbb{C}}_{ep,T})$ the directional derivative of $\mathcal{C}_{\gamma,\partial T}$ with respect to the displacement field (see [180] for details).

The global discrete problem consists in finding for any pseudo time-step $1 \le m \le M$, the discrete displacements $\underline{\hat{u}}^m_h \in \underline{\hat{U}}^k_{h,0}$ and the discrete internal variables $\tilde{\underline{\chi}}^m_{\mathcal{T}_h} \in \tilde{\underline{\mathcal{X}}}^{m_Q}_{\mathcal{T}_h}$ such that, for all $\delta\underline{\hat{v}}_h \in \underline{\hat{U}}^k_{h,0}$,

$$\begin{aligned}
&\sum_{T\in\mathcal{T}_h} (\boldsymbol{\sigma}^k_T(\tilde{\boldsymbol{\sigma}}^m_T), \boldsymbol{E}^k_T(\underline{\delta\hat{v}}_T))_{\boldsymbol{L}^2(T)} + \sum_{T\in\mathcal{T}_h} \beta(\eta_{\partial T}\underline{S}^k_{\partial T}(\underline{\hat{u}}^m_T), \underline{S}^k_{\partial T}(\underline{\delta\hat{v}}_T))_{\underline{L}^2(\partial T)} \\
&- \sum_{T\in\mathcal{T}^{\rm C}_h} \frac{\theta}{\gamma} \left(\boldsymbol{\sigma}^k_T(\tilde{\boldsymbol{\sigma}}^m_T)\underline{n}_T, (\mathbb{C}_{ep} : \boldsymbol{E})^k_T(\tilde{\mathbb{C}}^m_{ep,T}, \underline{\delta\hat{v}}_T)\underline{n}_T\right)_{\underline{L}^2(\partial T^{\rm C})} \\
&+ \sum_{T\in\mathcal{T}^{\rm C}_h} \frac{1}{\gamma} \left(\mathcal{C}_{\gamma,T}(\underline{\hat{u}}^m_T, \tilde{\boldsymbol{\sigma}}^m_T), \theta(\mathbb{C}_{ep} : \boldsymbol{E})^k_T(\tilde{\mathbb{C}}^m_{ep,T}, \underline{\delta\hat{v}}_T)\underline{n}_T - \gamma\delta\underline{v}_{\partial T}\right)_{\underline{L}^2(\partial T^{\rm C})} \\
&= \sum_{T\in\mathcal{T}_h} (\underline{f}^m, \delta\underline{v}_T)_{\underline{L}^2(T)} + \sum_{T\in\mathcal{T}^{\rm N}_h} (\underline{g}^m_{\rm N}, \delta\underline{v}_{\partial T})_{\underline{L}^2(\partial T^{\rm N})},
\end{aligned} \tag{5.56}$$

where for all $T \in \mathcal{T}_h$ and all $1 \le j \le m_Q$,

$$\begin{aligned}
&(\tilde{\underline{\chi}}^m_T(\underline{\xi}_{T,j}), \tilde{\boldsymbol{\sigma}}^m_T(\underline{\xi}_{T,j}), \tilde{\mathbb{C}}^m_{ep,T}(\underline{\xi}_{T,j})) = \\
&\quad \text{SMALL_PLASTICITY}(\tilde{\underline{\chi}}^{n-1}_T(\underline{\xi}_{T,j}), \boldsymbol{E}^k_T(\underline{\hat{u}}^{m-1}_T)(\underline{\xi}_{T,j}), \boldsymbol{E}^k_T(\underline{\hat{u}}^m_T)(\underline{\xi}_{T,j}) - \boldsymbol{E}^k_T(\underline{\hat{u}}^{m-1}_T)(\underline{\xi}_{T,j})),
\end{aligned} \tag{5.57}$$

with $\underline{\hat{u}}_h^{m-1} \in \underline{\hat{U}}_{h,0}^k$ and $\underline{\tilde{\chi}}_{\mathcal{T}_h}^{m-1} \in \underline{\tilde{\mathcal{X}}}_{\mathcal{T}_h}^{m_Q}$ given either from the previous pseudo time-step or the initial condition. Moreover, in the second line of (5.56), the stabilization employs a weight of the form $\beta = 2\mu\beta_0$ with $\beta_0 > 0$. In the original HHO method for linear elasticity [89], the choice $\beta_0 = 1$ is considered.

Remark 5.23 *If the material behavior remains elastic and $k_Q \geq 2k$, then the discrete plasticity problem (5.56)-(5.57) is equivalent to the discrete linear elasticity problem (5.18) since* $(\mathbb{C}_{ep} : \boldsymbol{E})_{T(F)}^k(\tilde{\mathbb{C}}_{ep,T(F)}^m, \underline{\delta\hat{v}}_{T(F)}) = \boldsymbol{\sigma}_T^k(\underline{\delta\hat{v}}_{T(F)})$.

5.6.4 Nonlinear solver

The nonlinear problem (5.56)-(5.57) arising at any pseudo-time step $1 \leq n \leq N$ is solved using a generalized Newton's method (see for example [10, 185]). Given $\underline{\hat{u}}_h^{m-1} \in \underline{\hat{U}}_{h,0}^k$ and $\underline{\tilde{\chi}}_{\mathcal{T}_h}^{m-1} \in \underline{\tilde{\mathcal{X}}}_{\mathcal{T}_h}^{m_Q}$ from the previous pseudo-time step or the initial condition, the Newton's method is initialized by setting $\underline{\hat{u}}_h^{m,0} = \underline{\hat{u}}_h^{m-1}$ and $\underline{\tilde{\chi}}_{\mathcal{T}_h}^{m,0} = \underline{\tilde{\chi}}_{\mathcal{T}_h}^{m-1}$. Then, at each Newton's step $i \geq 0$, one computes the incremental displacement $\delta\underline{\hat{u}}_h^{m,i} \in \underline{\hat{U}}_{h,0}^k$ and updates the discrete displacement as $\underline{\hat{u}}_h^{m,i+1} = \underline{\hat{u}}_h^{m,i} + \delta\underline{\hat{u}}_h^{m,i}$. The linear system of equations to be solved is

$$
\begin{aligned}
&\sum_{T\in\mathcal{T}_h} ((\mathbb{C}_{ep} : \boldsymbol{E})_T^k(\tilde{\mathbb{C}}_{ep,T}^{m,i}, \underline{\delta\hat{u}}_T^{m,i}), \boldsymbol{E}_T^k(\underline{\delta\hat{v}}_T))_{\boldsymbol{L}^2(T)} + \sum_{T\in\mathcal{T}_h} \beta(\gamma_{\partial T}\underline{S}_{\partial T}^k(\underline{\delta\hat{u}}_T^{m,i}), \underline{S}_{\partial T}^k(\underline{\delta\hat{v}}_T))_{\underline{L}^2(\partial T)} \\
&- \sum_{T\in\mathcal{T}_h^{\mathrm{C}}} \frac{\theta}{\gamma} \Big((\mathbb{C}_{ep} : \boldsymbol{E})_T^k(\tilde{\mathbb{C}}_{ep,T}^{m,i}, \underline{\delta\hat{u}}_T^{m,i})\underline{n}_T, (\mathbb{C}_{ep} : \boldsymbol{E})_T^k(\tilde{\mathbb{C}}_{ep,T}^{m,i}, \underline{\delta\hat{v}}_T)\underline{n}_T \Big)_{\underline{L}^2(\partial T^{\mathrm{C}})} \\
&+ \sum_{T\in\mathcal{T}_h^{\mathrm{C}}} \frac{1}{\gamma} \Big(D\mathcal{C}_{\gamma,T}(\underline{\delta\hat{u}}_T^{m,i}, \tilde{\boldsymbol{\sigma}}_T^{m,i}, \tilde{\mathbb{C}}_{ep,T}^{m,i}), \theta(\mathbb{C}_{ep} : \boldsymbol{E})_T^k(\tilde{\mathbb{C}}_{ep,T}^{m,i}, \underline{\delta\hat{v}}_T)\underline{n}_T - \gamma\underline{\delta v}_{\partial T} \Big)_{\underline{L}^2(\partial T^{\mathrm{C}})} \\
&= -R_{\theta,h}^{m,i}(\underline{\delta\hat{v}}_h),
\end{aligned}
\tag{5.58}
$$

for all $\underline{\delta\hat{v}}_h \in \underline{\hat{U}}_{h,0}^k$, where for all $T \in \mathcal{T}_h$ and all $1 \leq j \leq m_Q$,

$$
(\underline{\tilde{\chi}}_T^{m,i}(\underline{\xi}_{T,j}), \tilde{\boldsymbol{\sigma}}_T^{m,i}(\underline{\xi}_{T,j}), \tilde{\mathbb{C}}_{ep,T}^{m,i}(\underline{\xi}_{T,j})) = \mathrm{SMALL\_PLASTICITY}(\underline{\chi}_{T,j}^{m-1}, \boldsymbol{e}_{T,j}^{m-1}, \boldsymbol{e}_{T,j}^{m,i} - \boldsymbol{e}_{T,j}^{m-1}),
\tag{5.59}
$$

with $\underline{\chi}_{T,j}^{m-1} = \underline{\tilde{\chi}}_T^{m-1}(\underline{\xi}_{T,j})$, $\boldsymbol{e}_{T,j}^{m,i} = \boldsymbol{E}_T^k(\underline{\hat{u}}_T^{m,i})(\underline{\xi}_{T,j})$, $\boldsymbol{e}_{T,j}^{m-1} = \boldsymbol{E}_T^k(\underline{\hat{u}}_T^{m-1})(\underline{\xi}_{T,j})$, and the residual term

$$
\begin{aligned}
R_{\theta,h}^{m,i}(\underline{\delta\hat{v}}_h) = &\sum_{T\in\mathcal{T}_h} (\boldsymbol{\sigma}_T^k(\tilde{\boldsymbol{\sigma}}_T^{m,i}), \boldsymbol{E}_T^k(\underline{\delta\hat{v}}_T))_{\boldsymbol{L}^2(T)} + \sum_{T\in\mathcal{T}_h} \beta(\eta_{\partial T}\underline{S}_{\partial T}^k(\underline{\hat{u}}_T^{m,i}), \underline{S}_{\partial T}^k(\underline{\delta\hat{v}}_T))_{\underline{L}^2(\partial T)} \\
&- \sum_{T\in\mathcal{T}_h^{\mathrm{C}}} \frac{\theta}{\gamma} \Big(\boldsymbol{\sigma}_T^k(\tilde{\boldsymbol{\sigma}}_T^{m,i})\underline{n}_T, (\mathbb{C}_{ep} : \boldsymbol{E})_T^k(\tilde{\mathbb{C}}_{ep,T}^{m,i}, \underline{\delta\hat{v}}_T)\underline{n}_T \Big)_{\underline{L}^2(\partial T^{\mathrm{C}})} \\
&+ \sum_{T\in\mathcal{T}_h^{\mathrm{C}}} \frac{1}{\gamma} \Big(\mathcal{C}_{\gamma,T}(\underline{\hat{u}}_T^{m,i}, \tilde{\boldsymbol{\sigma}}_T^{m,i}), \theta(\mathbb{C}_{ep} : \boldsymbol{E})_T^k(\tilde{\mathbb{C}}_{ep,T}^{m,i}, \underline{\delta\hat{v}}_T)\underline{n}_T - \gamma\underline{\delta v}_{\partial T} \Big)_{\underline{L}^2(\partial T^{\mathrm{C}})} \\
&- \sum_{T\in\mathcal{T}_h} (\underline{f}^m, \underline{\delta v}_T)_{\underline{L}^2(T)} - \sum_{T\in\mathcal{T}_h^{\mathrm{N}}} (\underline{g}_{\mathrm{N}}^m, \underline{\delta v}_{\partial T})_{\underline{L}^2(\partial T^{\mathrm{N}})}.
\end{aligned}
\tag{5.60}
$$

The assembling of the stiffness matrix resulting from the left-hand side of (5.58) is local (and thus fully parallelizable). The discrete internal variables $\underline{\tilde{\chi}}_{\mathcal{T}_h}^m \in \underline{\tilde{\mathcal{X}}}_{\mathcal{T}_h}^{m_Q}$ are updated at the end of each pseudo-time step.

Remark 5.24 *The linearization is not full in (5.58) since few terms are omitted in the left-hand side. At the continuous level, we omit the terms where $\partial_{\boldsymbol{\varepsilon}}\mathbb{C}_{ep}$ appears. This term $\partial_{\boldsymbol{\varepsilon}}\mathbb{C}_{ep}$ is a sixth-order tensor which is in general never computed at the quadrature points by a generic behavior integrator. To have a complete linearization, $\partial_{\boldsymbol{\varepsilon}}\mathbb{C}_{ep}$ has to be computed by the procedure SMALL_PLASTICITY which requires a theoretical study for each behaviour law as well as a major development effort to adapt it in standard finite element software. Note that $\partial_{\boldsymbol{\varepsilon}}\mathbb{C}_{ep}$ is equal to zero if the behavior is elastic.*

Remark 5.25 *For the non-symmetric Nitsche variant $\theta = 0$, the tangent system can be simplified*

$$\sum_{T\in\mathcal{T}_h}((\mathbb{C}_{ep}:\boldsymbol{E})_T^k(\tilde{\mathbb{C}}_{ep,T}^{m,i},\delta\underline{\hat{u}}_T^{m,i}),\boldsymbol{E}_T^k(\delta\underline{\hat{v}}_T))_{\boldsymbol{L}^2(T)}+\sum_{T\in\mathcal{T}_h}\beta(\gamma_{\partial T}\underline{S}_{\partial T}^k(\delta\underline{\hat{u}}_T^{m,i}),\underline{S}_{\partial T}^k(\delta\underline{\hat{v}}_T))_{\underline{L}^2(\partial T)}$$
$$-\sum_{T\in\mathcal{T}_h^C}\Big(D\mathcal{C}_{\gamma,T}(\delta\underline{\hat{u}}_T^{m,i},\tilde{\boldsymbol{\sigma}}_T^{m,i},\tilde{\mathbb{C}}_{ep,T}^{m,i}),\delta\underline{v}_{\partial T}\Big)_{\underline{L}^2(\partial T^C)}=-R_{0,h}^{m,i}(\delta\underline{\hat{v}}_h),\tag{5.61}$$

with

$$\begin{aligned}R_{0,h}^{m,i}(\delta\underline{\hat{v}}_h)=&\sum_{T\in\mathcal{T}_h}(\boldsymbol{\sigma}_T^k(\tilde{\boldsymbol{\sigma}}_T^{m,i}),\boldsymbol{E}_T^k(\delta\underline{\hat{v}}_T))_{\boldsymbol{L}^2(T)}+\sum_{T\in\mathcal{T}_h}\beta(\eta_{\partial T}\underline{S}_{\partial T}^k(\delta\underline{\hat{u}}_T^{m,i}),\underline{S}_{\partial T}^k(\delta\underline{\hat{v}}_T))_{\underline{L}^2(\partial T)}\\&-\sum_{T\in\mathcal{T}_h^C}\Big(\mathcal{C}_{\gamma,T}(\underline{\hat{u}}_T^{m,i},\tilde{\boldsymbol{\sigma}}_T^{m,i}),\delta\underline{v}_{\partial T}\Big)_{\underline{L}^2(\partial T^C)}\\&-\sum_{T\in\mathcal{T}_h}(\underline{f}^m,\delta\underline{v}_T)_{\underline{L}^2(T)}-\sum_{T\in\mathcal{T}_h^N}(\underline{g}_N^m,\delta\underline{v}_{\partial T})_{\underline{L}^2(\partial T^N)}.\end{aligned}\tag{5.62}$$

In particular the linearization is full since the terms with $\partial_{\boldsymbol{\varepsilon}}\mathbb{C}_{ep}$ are absent and the implementation is simpler compare to the Nitsche's variant $\theta=-1$ and $\theta=1$.

5.6.5 Numerical experiments

The goal of this section is to evaluated the proposed Nitsche-HHO method on a two-dimensional frictionless Hertz's contact problem with linear isotropic hardening. We compare our results to those obtained using the industrial open-source FEM software `code_aster` [111]. We consider a linear, resp. quadratic, cG formulation, referred to as T1, resp. T2 where full integration is used, and a three-field mixed formulation in which the unknowns are the displacement, the pressure and the volumetric strain fields referred to as UPG [9]; in the UPG method, the displacement field is quadratic, whereas both the pressure and the volumetric strain fields are linear. Moreover, the contact conditions are imposed with a mixed method referred as LAC (see [1]) where the additional unknowns are the contact pressure which is piecewise constant. These three methods are referred as T1-LAC, T2-LAC, and UPG-LAC respectively. The T1-LAC and T2-LAC methods with full integration, are known to present volumetric locking due to plastic incompressibility, whereas the UPG-LAC method is known to be robust but costly. Numerical results obtained using the UPG-LAC method are used as a reference.

The combined linear isotropic and kinematic hardening plasticity model with a von Mises yield criterion described in Section 3.2.4 is used for the test case. A strain-hardening plasticity is considered with the following material parameters: Young modulus $E=70$, Poisson ratio $\nu=0.3$, hardening parameter $H=7$, kinematic hardening $K=0$, and initial yield stress $\sigma_{y,0}=2.5$. We employ the notation HHO(k) when using polynomial of order k. Moroverer, only the Nitsche's variant $\theta=0$ has been implemented in `disk++` for the moment since this is easier.

2D Hertz contact with plasticity

This benchmark is the well known two-dimensional Hertz's contact problem of a half disk in contact with a rigid foundation. The half disk is centred in $(0, 50)$ and has a radius of 50. The contact boundary is $\Gamma_D = \mathbb{R} \times \{0\}$ and a vertical displacement $u_y = -5$ is applied on the top end. The mesh is composed of 4899 triangles. The euclidean displacement norm on the deformed configuration is plotted in Fig. 5.11 for HHO(1). We plot the equivalent plastic strain p in Fig. 5.12 for the different methods at the quadrature points on the reference configuration. The results for HHO(1) and HHO(2) are in agreement with those obtained for T2-LAC and UPG-LAC, whereas, the result for T1-LAC is less smooth compare to the others. Moreover, the trace of the Cauchy stress tensor $\boldsymbol{\sigma}$ at the quadrature points on the reference configuration is plotted in Fig. 5.13. We observe the absence of oscillation for T2-LAC, UPG-LAC and HHO contrary to T1-LAC. This confirms numerically that HHO method prevents volumetric locking as mixed methods. Note that both for the equivalent plastic strain p and the trace of the Cauchy stress tensor, the results are slightly different between HHO and LAC methods. The main reason is that the contact terms are computed on the deformed contribution for the LAC method whereas they are computed on the reference configuration for the Nitsche-HHO method. Hence, a small difference is present since the reference and deformed configurations have to be distinguished for this benchmark.

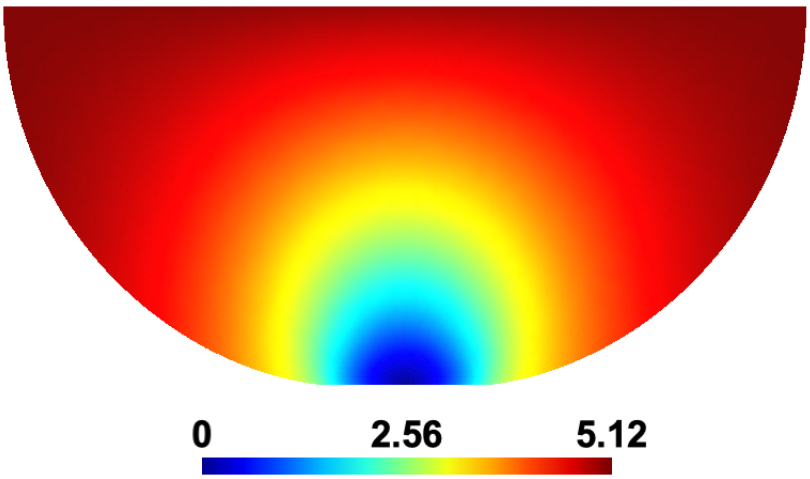

Figure 5.11: Euclidean displacement norm on the deformed configuration for HHO(1).

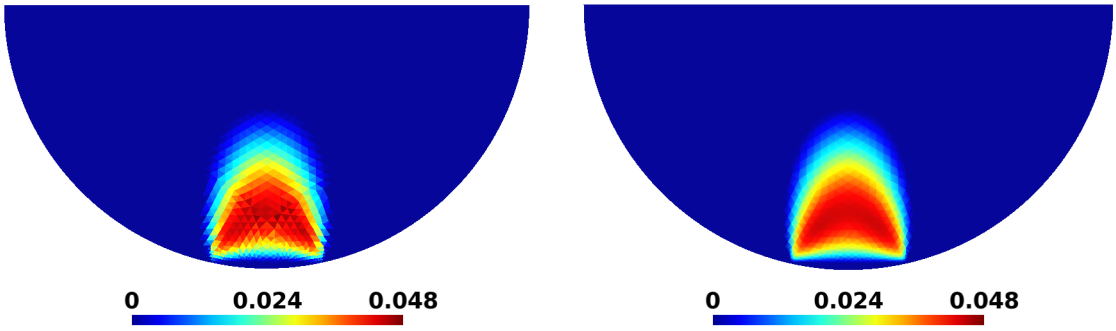

(a) T1-LAC

(b) T2-LAC

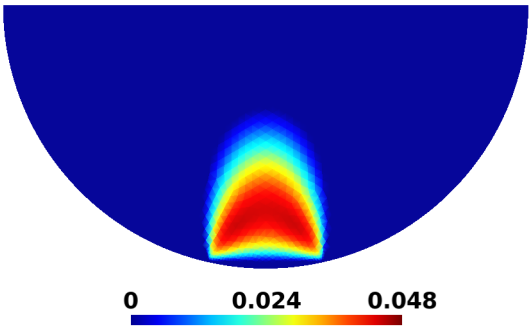

(c) UPG-LAC

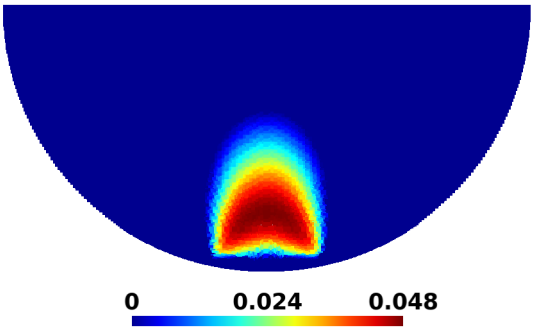

(d) HHO(1)

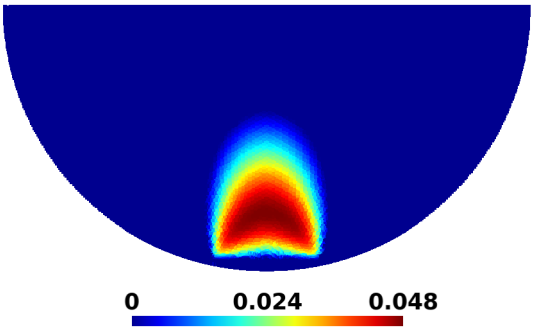

(e) HHO(2)

Figure 5.12: 2D Hertz contact with plasticity: equivalent plastic strain p at the quadrature points on the reference configuration for different methods.

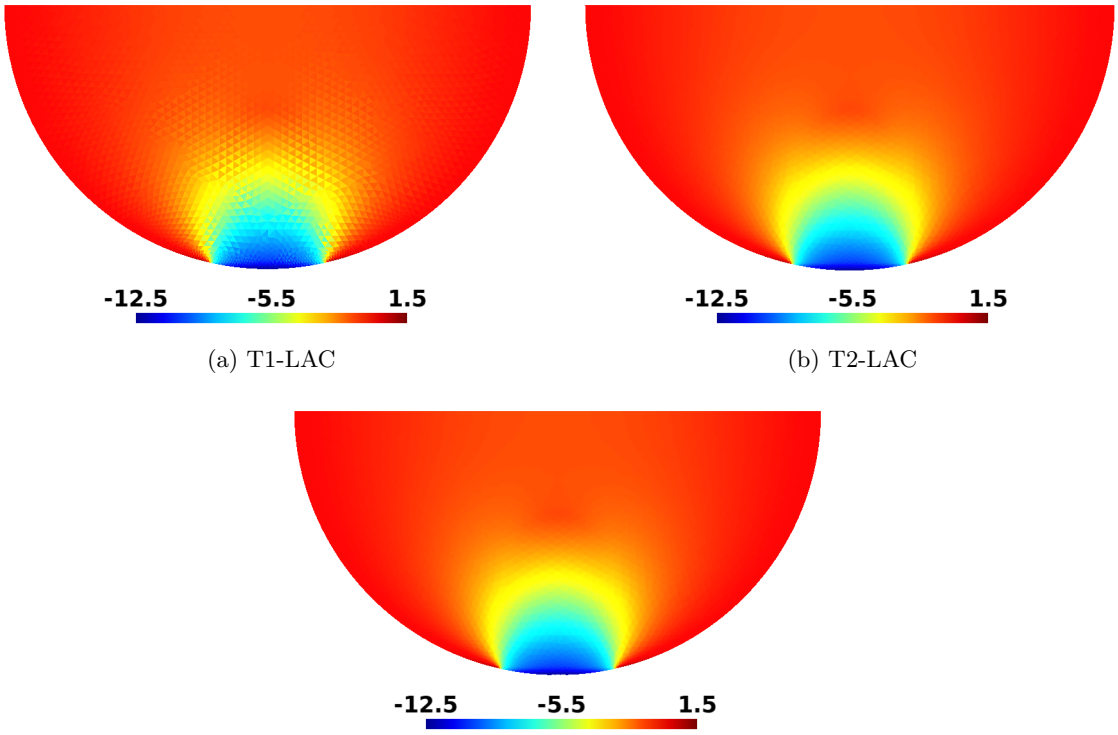

(a) T1-LAC (b) T2-LAC

(c) UPG-LAC

(d) HHO(1) (e) HHO(2)

Figure 5.13: 2D Hertz contact with plasticity: trace of the Cauchy stress tensor $\boldsymbol{\sigma}$ at the quadrature points on the reference configuration for different methods.

5.7 Conclusion

We have devised, analyzed, and evaluated numerically a HHO discretization combined with a Nitsche method to impose weakly contact and Tresca friction conditions in small strain elasticity. We have proved optimal error estimates for this nonlinear problem and have studied the robustness of the estimates in the incompressible limit. The numerical tests indicate that robustness is achieved in all configurations considered herein. Moreover, an extension to small plasticity problem has been proposed. This work can be pursued in several directions, such as extending the analysis to Coulomb friction and addressing further extensions (multi-body contact, large transformations, plasticity) for industrial applications.

CHAPTER 6

CONCLUSIONS AND PERSPECTIVES

In this thesis, we have devised Hybrid High-Order methods (HHO) to deal with finite hyperelastic and elastoplastic deformations and the unilateral contact problem with Tresca friction. Different primal HHO methods have been developed to solve these problems, i.e. without the need to introduce additional global unknowns to impose the incompressibility condition and prevent volumetric locking. For each problem, comparisons have been made with known solutions and with computed solutions using the industrial finite element software `code_aster`. In addition, the HHO methods presented in this thesis have been implemented both in the `disk++` and `code_aster` softwares (these developments are open-source and available online).

Firstly, the problem of finite hyperelastic deformations has been investigated where two primal HHO methods have been devised on simplicial meshes. One of these methods circumvents the need for stabilization on simplicial meshes. Thus, it is not necessary to determine (with difficulty) an appropriate value of the user-dependent stabilization parameter. Both methods prevent volumetric locking at the incompressible limit.

Secondly, a primal HHO method has been developed on general meshes to deal with the presence of small incompressible plastic deformations. This method has shown a robust behavior for different local plasticity models and produces solutions as accurate as mixed methods but with less unknowns.

Thirdly, the HHO method developed for small plastic deformations has been extended to finite elastoplastic deformations by using the logarithmic strain framework. This framework allows one to re-use behavior laws developed originally for small deformations by means of purely geometric transformations. As for small deformations, the HHO method prevents volumetric locking due to plastic incompressibility and delivers accurate results both in terms of displacement and stress. However, a non-physical localization of plastic deformations can appear for the lowest-order variant in a few situations.

Finally, the HHO methods has been combined with a Nitsche approach to impose weakly the unilateral contact and Tresca friction conditions on a part of the boundary for the linear elasticity problem with small deformations. More precisely, a primal face-based Nitsche-HHO method has been devised. Optimal convergence rates have been proven even in presence of Tresca friction and the method is robust at the incompressible limit. This results are confirmed numerically.

This work can be pursued in several directions. Concerning the problems in computational mechanics, we mention:

- Dynamic problems. In this thesis only static or quasi-static approaches have been

considered. However, the friction conditions for Tresca or Coulomb are initially written in terms of speed whereas we restricted ourselves in Chapter 5 to a static model. To go further, it is important to be able to simulate dynamic problems such as impact problems (see, e.g., Hauret & Le Tallec [135] and Hager & al. [126]). A possible approach is to follow the ideas used for elastodynamics with Hybridizable Discontinuous Galerkin methods by Nguyen, Peraire & Cockburn [172].

- Non-local plasticity models. Non-physical phenomena such as the localization of plastic deformations can occur when a local plasticity model is used (see Chapter 4 in our case). Then, a way to circumvent this problem can be to use a non-local plasticity model as for discontinuous Galerkin methods in small deformation by Djoko & al. [97, 98] and finite deformations by McBride & Reddy [166].

- Damage models. Above a given threshold in large plastic deformations, the material can begin to damage. Then, it is necessary to combine a damage model with a plasticity model which is generally non-local (see, e.g., Lorentz & al. [164, 215]).

- Deformable-deformable contact in finite elastoplastic deformations. Only a deformable elastic body coming into contact with a rigid surface has been considered in this thesis. The final goal is to be able to simulate the contact and friction between two (or more) deformable bodies in finite elastoplastic deformations. This was recently done for a Nitsche-FEM model by Seitz, Wall & Popp [186].

- Validation on industrial applications. Since the HHO methods presented in this manuscript have been implemented in `code_aster`, it is interesting to validate them on more challenging problems. This will also help to optimize the implementation.

From a mathematical and numerical point of view, the following directions are suggested:

- *a priori* error estimates. The analysis in Chapter 5 is limited to linear elasticity with Tresca friction. In many situations, the Coulomb friction is more physically relevant than the Tresca friction. However, the analysis is much more complicated and the theoretical results are very limited whatever the discretization method used. Moreover, error estimates can also be investigated for the plasticity problem in small deformations, possibly by taking inspiration from Alberty, Carstensen & Zarrabi [11] and Djoko & al. [97], where other discretization methods are analyzed for plasticity problems

- Adaptativity. The HHO methods could take benefit from adaptativity in different ways. The first one is to use an adaptive *hp*-refinement strategy to improve the accuracy of the computed solution as in Daniel & al. [81] for H^1-conforming methods. This could be facilitated for the HHO methods by the support of polyhedral meshes. The second one is an adaptation of the stabilization parameter in the case of finite elastoplastic deformations since the stiffness of the material can change significantly. For the moment, the value of the stabilization parameter is given *a priori* and does not change during the simulation. Since this parameter can have a sizeable influence on the robustness and the conditioning of HHO methods, it could be interesting to adapt automatically this parameter locally in each mesh cell and during the simulation, as can be done for the contact penalty parameter as well.

- Iterative solvers. To be able to perform massively parallel simulations, it is necessary to have efficient iterative solvers for HHO methods. Efficient preconditioners are also important. A possible approach is to follow the ideas developed for a diffusion problem with HDG methods by Cockburn & al. [75].

APPENDIX A

IMPLEMENTATION IN CODE_ASTER

Abstract. This appendix concerns the implementation of HHO methods for nonlinear solid mechanics in the industrial finite open-source element software code_aster [111]. The HHO methods have been officialy integrated in code_aster in version 15.0.8. The details about the implementation of HHO methods, i.e. computations of the different operators (gradient, divergence, stabilization...), choice of basis functions, static condensation..., are already given in [71] for the open-source library disk++ using generic programming tools. Hence, we limit ourselves here to explain the adaptations to the architecture of code_aster which were realized during this thesis.

Sommaire

code_aster is an industrial open-source software based on the finite element method which is developed since 1989 by EDF R&D. It allows one to simulate linear and nonlinear thermomechanical problems in static or dynamic settings. Moreover, strong assumptions have

been done when the architecture of code_aster has been devised . This can complicate the implementation of new numerical methods that differ from Lagrange finite element methods. We list here the main assumptions:

- limited number of different geometric elements present in the mesh, i.e., triangle and quadrangle in 2D, and tetrahedron, hexahedron, prism and pyramid in 3D (no support of polyhedral meshes);
- strong connection between the geometric element and the finite element, i.e., the approximation order of the method is determined by the geometric element. For example, a linear approximation for a 3-node triangle and a quadratic approximation for a 6-node triangle;
- finite element unknowns supported only by the physical nodes of the mesh (and not by the faces or the cells of the mesh as is the case for finite volume, discontinuous Galerkin, and HHO methods).

The main objective for the implementation of HHO methods in code_aster is to reuse as much as possible the architecture of the code and not to modify the critical points of code_aster which are:

- data structures;
- finite element catalogues;
- locality of elementary computations;
- assembly operator.

We limited ourselves to the implementation of HHO methods for nonlinear solid mechanics in code_aster for a limited number of geometric elements, i.e, triangle and quadrangle in 2D, and tetrahedron and hexahedron in 3D. Moreover, only the linear, $k = 1$, and quadratic, $k = 2$, HHO methods are implemented. Quite important, The different modifications are limited to two code_aster operators:

- CREA_MAILLAGE operator which allows one to create or transform a mesh.
- STAT_NON_LINE operator which is the quasi-static nonlinear solver for solid mechanics.

Remark A.1 *This appendix uses a terminology specific to code_aster that can hamper the understanding. However, the reader may find key elements to implement HHO methods in other existing finite element codes.*

A.1 Preliminaries

To implement HHO methods in a finite element code, two steps are particularly important and need a special attention. The first one is the static condensation (or Schur complement) which allows one to eliminate locally the cell unknowns in the local contributions (at the end, a smaller global problem composed only of the face unknowns is solved). The second important step is the assembly of the global problem composed only of the face unknowns from local contributions after static condensation. These two steps are showed in Fig. A.1.

We will show in the following sections how to perform these operations in code_aster with only minor modifications of the architecture of the code.

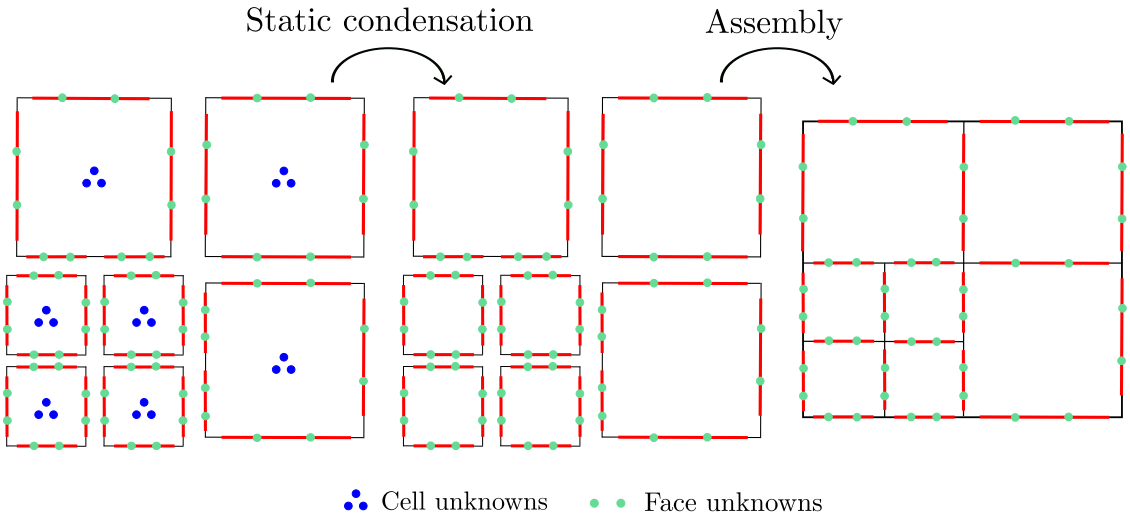

Figure A.1: The two important steps for the implementation of HHO methods: static condensation and assembly.

A.2 HHO unknowns and numbering

We recall that the local HHO unknowns $\hat{\underline{v}}_T = (\underline{v}_T, \underline{v}_{\partial T}) \in \hat{\underline{U}}_T^k$ that we have to compute are the coefficients of cell-based and face-based polynomials (these coefficients have a priori no physical meaning). After the static condensation, a global problem in term of the face unknowns has to be assembled. Since this assembly has to be done face by face and since the HHO unknowns can only be supported by a physical node of the mesh in `code_aster`, we need that each face of the mesh owns at least one node that is not shared with any other face of the mesh (typically a node located at the barycenter of the face). This is the case in 2D for the 6-node triangle (referred to as `TRIA6`) and the 8-node quadrangle (refereed to as `QUAD8`), and in 3D for the 27-node hexahedron (referred to as `HEXA27`). These geometric elements correspond to quadratic elements for the isoparametric elements. Unfortunately, there is no such standard tetrahedron, i.e. 4-node tetrahedron or 10-node tetrahedron. This is why, we have created the mesh converter `TETRA4_8` to have an eight-node tetrahedron (referred to as `TETRA8`) which has a node located at the barycenter of each face. This mesh converter is presented in Sect. A.4.

The face unknowns $\underline{v}_F$ for the face $F \in \mathcal{F}_h$ are supported by the node that is located at the barycenter of the face F. These physical nodes of the mesh which support the face unknowns are denoted `unknown nodes`. In addition, since the mesh faces are assumed to be planar, we use the vertex nodes to describe the geometry of the cells and the faces and to compute the different integrals. These physical nodes of the mesh which describe the geometry of the elements are denoted `geometric nodes`. Finally, in the case of the `HEXA27` element, the nodes located at the middle of the edges are not used. These physical nodes of the mesh are denoted `empty nodes`. These different categories of nodes are illustrated in Fig. A.2 for the geometric elements `TRIA6`, `QUAD8`, `TETRA8`, and `HEXA27`. Moreover, the cell unknowns $\underline{v}_T$ are saved in a field which is constant by cell.

These tips for the localization of HHO unknowns allow us to reuse the data structures and the assembly operator of `code_aster`. The resulting numbering is denoted `global numbering` because this is the numbering which is used to assemble the global problem. Moreover, we introduce also a local numbering which is used to sum the different local contributions from a given cell before the static condensation (this numbering is never used

to assemble the global problem). This is done by adding to a node of one of the faces the cell unknowns. These two numberings are illustrated in Fig. A.3 for the geometric element QUAD8.

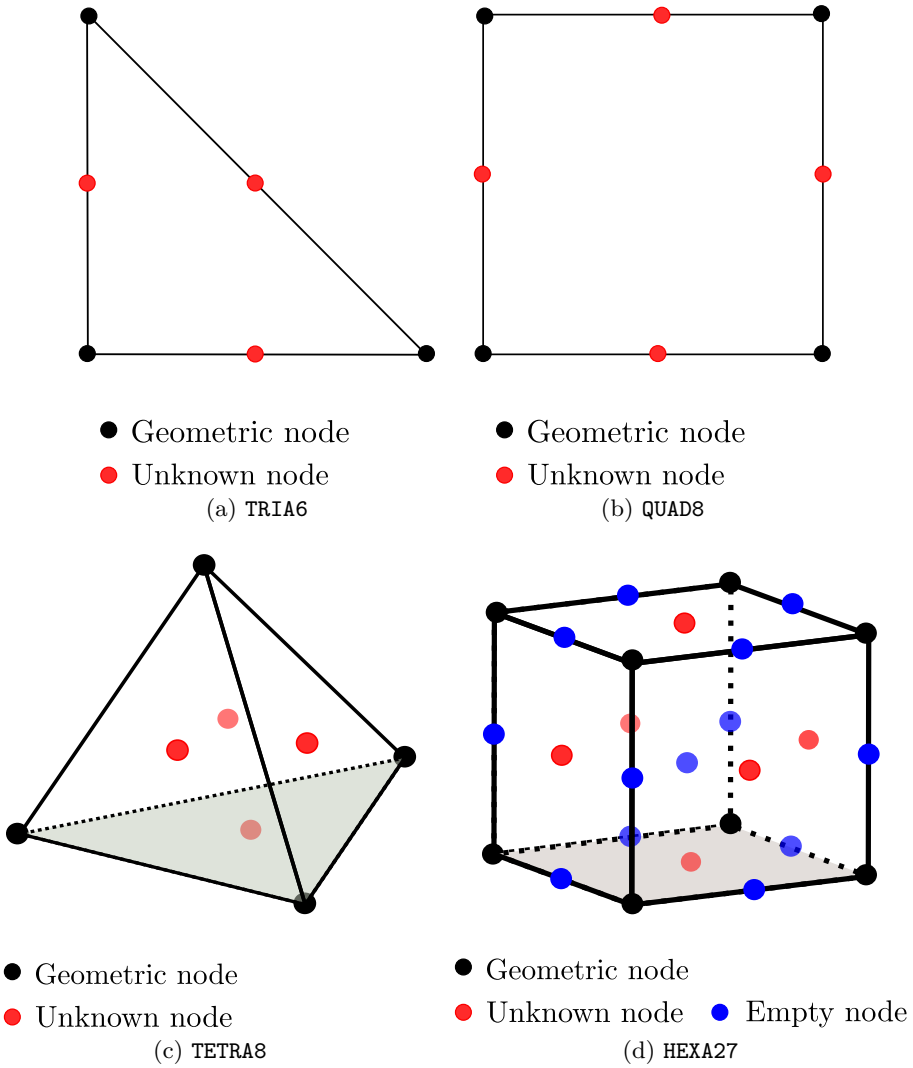

(a) TRIA6 (b) QUAD8 (c) TETRA8 (d) HEXA27

Figure A.2: Different categories of nodes considered in the implementation for the geometric elements TRIA6, QUAD8, TETRA8, and HEXA27.

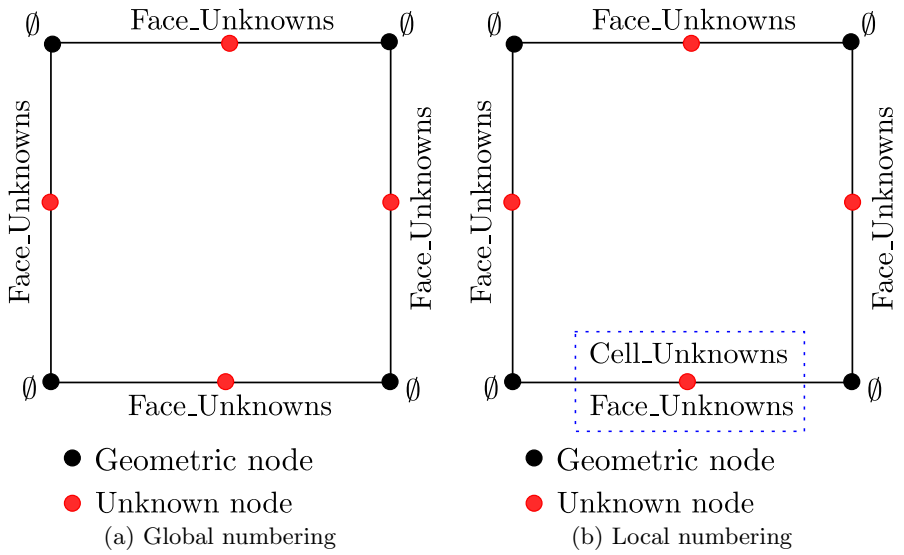

(a) Global numbering (b) Local numbering

Figure A.3: Global and local numbering for the geometric element `QUAD8`.

A.3 Summation and static condensation

One of the major difficulties encountered in the implementation of HHO methods in `code_aster` is the static condensation since the architecture of `code_aster` is not well adapted to this procedure. Indeed, in `code_aster`, the elementary contributions (rigidity, contact, Neumann loads...) are computed locally in an element (cell or face), then assembled directly in the global problem using the global numbering as illustrated in Fig. A.4 for primal and mixed conforming finite element methods. However, this is not possible for HHO methods since the static condensation procedure has to be performed before the assembly. Hence, for HHO methods, we have to add an intermediary step. To begin, all the elementary contributions coming from the same cell are summed locally in $\boldsymbol{A}_{\text{loc}}$ and $\underline{b}_{\text{loc}}$ using the local numbering such that

$$\boldsymbol{A}_{\text{loc}} = \sum_{i=1}^{n_{\text{contrib}}} \boldsymbol{A}_{\text{loc}}^{i} \qquad \text{and} \qquad \underline{b}_{\text{loc}} = \sum_{i=1}^{n_{\text{contrib}}} \underline{b}_{\text{loc}}^{i}. \tag{A.1}$$

This operation is denoted `Summation`. Moreover, assuming that the cell unknowns $\underline{v}_T$ are ordered before the faces unknowns $\underline{v}_{\partial T}$, the local problem to assemble reads as follows:

$$\begin{pmatrix} \boldsymbol{A}_{\text{loc}}^{T,T} & \boldsymbol{A}_{\text{loc}}^{T,\partial T} \\ \boldsymbol{A}_{\text{loc}}^{\partial T,T} & \boldsymbol{A}_{\text{loc}}^{\partial T,\partial T} \end{pmatrix} \begin{pmatrix} \underline{v}_T \\ \underline{v}_{\partial T} \end{pmatrix} := \begin{pmatrix} \underline{b}_{\text{loc}}^{T} \\ \underline{b}_{\text{loc}}^{\partial T} \end{pmatrix} \tag{A.2}$$

where $\boldsymbol{A}_{\text{loc}}$ and $\underline{b}_{\text{loc}}$ have been decomposed by block. The block $\boldsymbol{A}_{\text{loc}}^{T,T}$, composed only of contributions coming from the cell unknowns $\underline{v}_T$, is positive definite (this block is dense). Hence, we can eliminate the cell unknowns $\underline{v}_T$ to keep only the face unknowns $\underline{v}_{\partial T}$ leading to

$$\boldsymbol{A}_{\text{cond}}\, \underline{v}_{\partial T} := \underline{b}_{\text{cond}}. \tag{A.3}$$

where

$$\boldsymbol{A}_{\text{cond}} = \boldsymbol{A}_{\text{loc}}^{\partial T,\partial T} - \boldsymbol{A}_{\text{loc}}^{\partial T,T} (\boldsymbol{A}_{\text{loc}}^{T,T})^{-1} \boldsymbol{A}_{\text{loc}}^{T,\partial T}, \tag{A.4}$$

$$\underline{b}_{\text{cond}} = \underline{b}_{\text{loc}}^{\partial T} - \boldsymbol{A}_{\text{loc}}^{\partial T,T} (\boldsymbol{A}_{\text{loc}}^{T,T})^{-1} \boldsymbol{A}_{\text{loc}}^{T,\partial T} \underline{b}_{\text{loc}}^{T}. \tag{A.5}$$

$\boldsymbol{A}_{\text{cond}}$ and $\underline{b}_{\text{cond}}$ are formulated only in terms of the face unknowns $\underline{v}_{\partial T}$. This operation is denoted `Static condensation`. The main difficulty is that the inputs $\boldsymbol{A}_{\text{loc}}$ and $\underline{b}_{\text{loc}}$ of the static condensation use the local numbering whereas the outputs $\boldsymbol{A}_{\text{cond}}$ and $\underline{b}_{\text{cond}}$ use the global numbering. Finally, $\boldsymbol{A}_{\text{glob}}$ and $\underline{b}_{\text{glob}}$ are assembled in the global problem using the global numbering. The sequence of these different operations (elementary contributions, summations, and static condensation) for the HHO methods is summarized in Fig. A.5. Note that the contributions coming from Neumann loads are directly assembled in the global problem since they use only the face unknowns (and the global numbering). These tips allow us to follow the principles of `code_aster` and to reuse the architecture with only minor modifications.

Moreover, after solving the global problem, the values of the face unknowns $\underline{v}_{\partial T}$ are known. The static decondensation procedure allows us to compute the cell unknowns $\underline{v}_T$ from the face unknowns $\underline{v}_{\partial T}$ as follows:

$$\underline{v}_T = (\boldsymbol{A}_{\text{loc}}^{T,T})^{-1} \left(\underline{b}_{\text{loc}}^{T} - \boldsymbol{A}_{\text{loc}}^{T,\partial T} \underline{v}_{\partial T} \right). \tag{A.6}$$

To save computational time, the matrix $(\boldsymbol{A}_{\text{loc}}^{T,T})^{-1}\boldsymbol{A}_{\text{loc}}^{T,\partial T}$ and the vector $(\boldsymbol{A}_{\text{loc}}^{T,T})^{-1}\underline{b}_{\text{loc}}^{T}$ are saved locally to the cell in two fields (constant by cell) during the static condensation procedure and then reused in the static decondensation procedure.

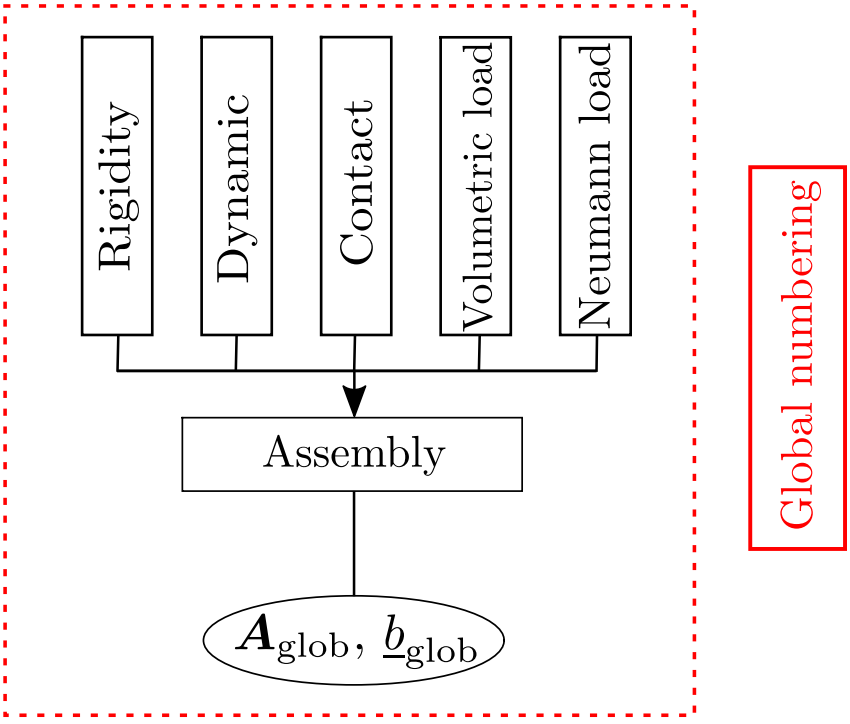

Figure A.4: Sequence of operations to assemble the global problem using the global numbering from the elementary contributions for primal and mixed conforming finite element methods.

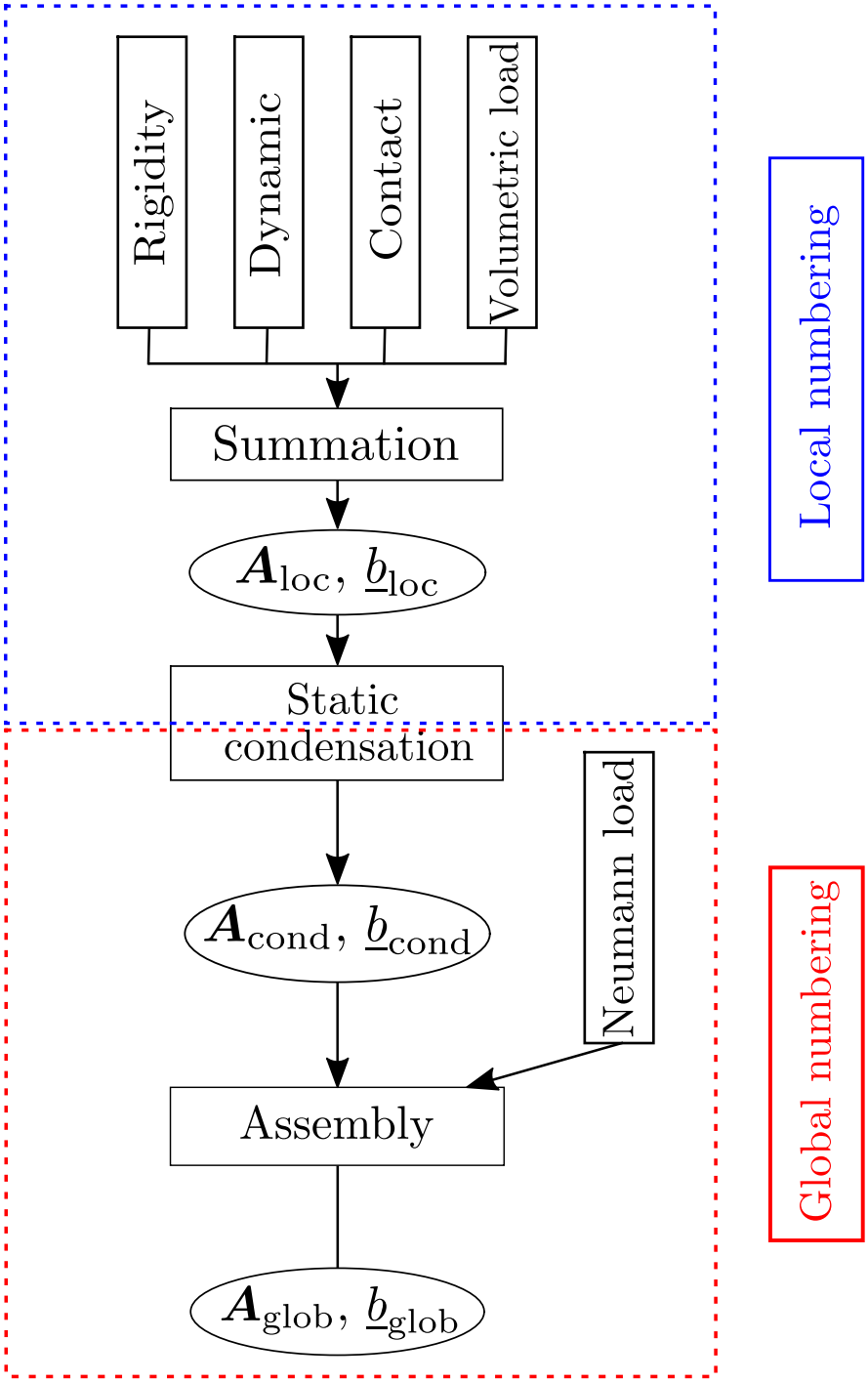

Figure A.5: Sequence of operations to assemble the global problem using both local and global numbering from the elementary contributions for HHO methods.

A.4 CREA_MAILLAGE

We have added a new option denoted TETRA4_8 in the CREA_MAILLAGE operator. The goal is to transform a 4-node tetrahedron (referred to as TETRA4) into an 8-node tetrahedron (referred to as TETRA8). The four new nodes of each tetrahedron are added to the barycenter of each face. Hence, each new node is shared only by a face and two cells (or one cell, if the face is a boundary face). This operation is illustrated in Fig. A.6. Moreover, the new geometric element TETRA8 has been added to code_aster.

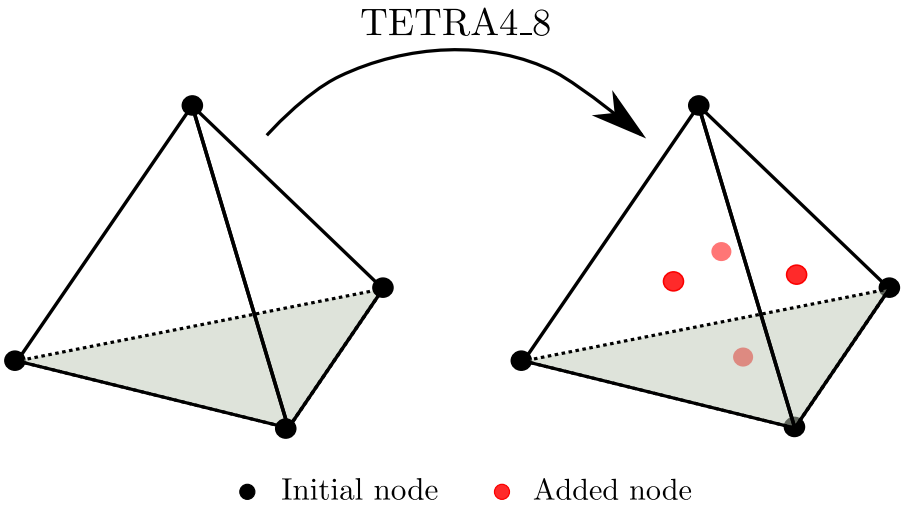

Figure A.6: New option TETRA4_8 in the CREA_MAILLAGE operator to transform a 4-node tetrahedron into an 8-node tetrahedron.

A.5 STAT_NON_LINE

The STAT_NON_LINE operator is the nonlinear solver for quasi-static thermomechanical problem in code_aster. The nonlinear problem is solved with a Newton's method. To integrate HHO methods in this solver, two intermediate operations are added. The first one is denoted HHO_COMB and includes the summation and the static condensation procedure. This operation is used between the computation of elementary contributions and the assembly. The second one is denoted HHO_DECOND and allows one to perform the static decondensation procedure after the solving. It is sufficient to add two boolean conditions in the STAT_NON_LINE operator to use these two operations if the HHO methods are used for the computation. The STAT_NON_LINE operator is summarized in Fig. A.7 with the appropriate modifications for HHO methods. Note that the modifications are very limited and circumscribed in the code.

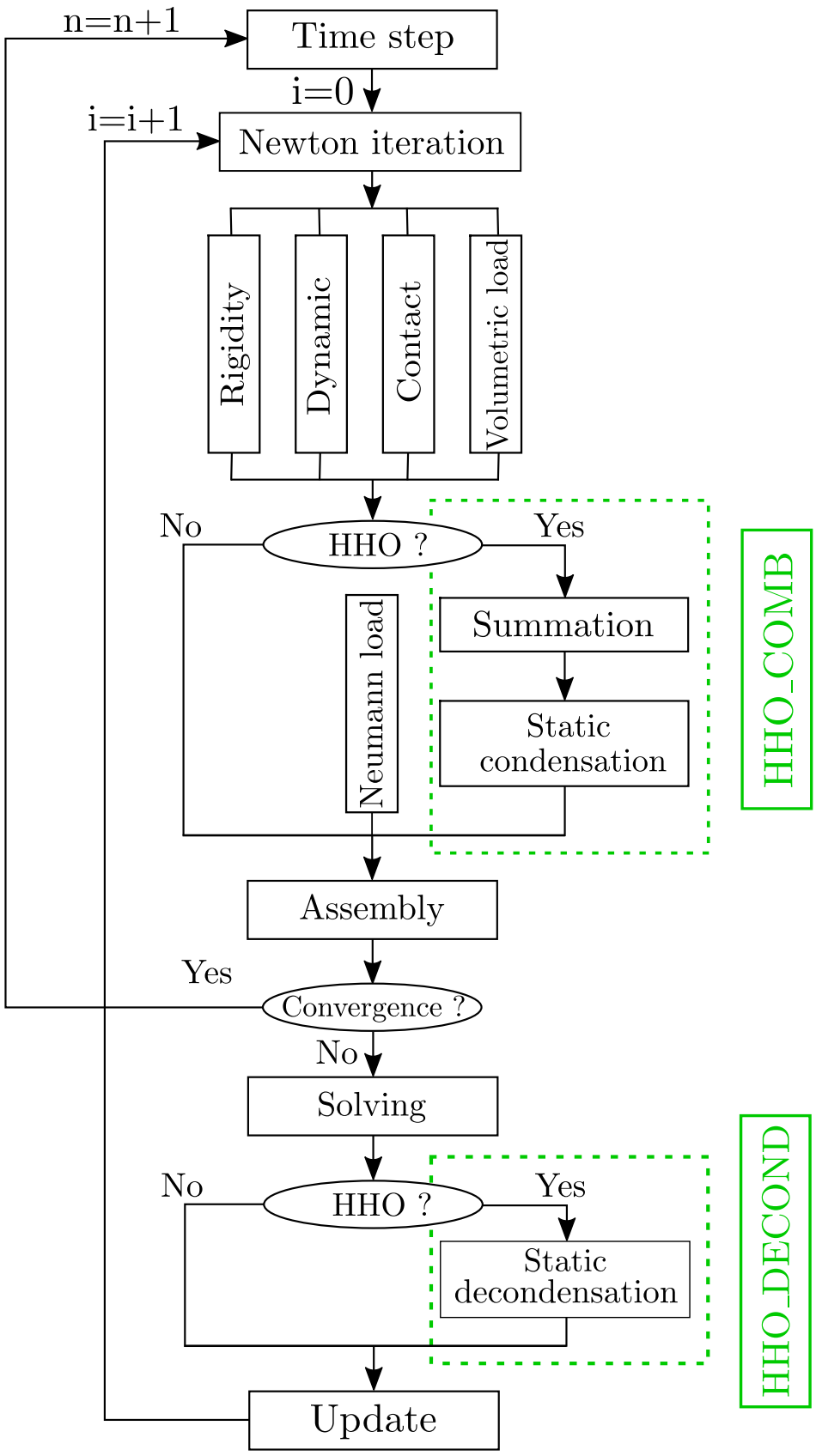

Figure A.7: Description of the quasi-static nonlinear solver STAT_NON_LINE where the modifications to implement HHO method are added (in green).

A.6 Dirichlet boundary conditions

The Dirichlet boundary conditions are imposed strongly in code_aster by modifying the matrix and the load. The user has to specify the imposed displacement field on the Dirichlet boundary. However, it is not straightforward for the user to give the values of face unknowns since these coefficients have a priori no physical meaning. We have added an automatic pre-processor which calculates the L^2-orthogonal projector $\underline{\Pi}_F^k(\underline{u}_{\mathrm{D}})$ and imposes the value $\underline{v}_F = \underline{\Pi}_F^k(\underline{u}_{\mathrm{D}})$ from the displacement field $\underline{u}_{\mathrm{D}}$ given at the nodes of the face (in the Lagrange meaning)

A.7 Post-processing

The HHO unknowns are the coefficients of polynomials. These coefficients have a priori no physical meaning. Hence, a post-processing has to be applied to visualize the results, typically yielding the values of the displacement at the nodes of the mesh, in a classic visualization software like paraview or gmsh. We have created a new field at the nodes of the mesh denoted HHO_DEPL. The value at a node is the average of the value of the cell unknowns $\underline{v}_T$ which contain this node. Note that this field is globally continuous.

A.8 Basic HHO objects for the implementation

The core of code_aster is written mainly in FORTRAN 90 (and a bit in FORTRAN 77) contrary to disk++ which is written in modern C++. Moreover, disk++ uses generic programming tools to implement HHO methods with different levels of abstraction. This is not possible in code_aster since it does not allow one to use Object-Oriented Programming (OOP). However, to reuse in code_aster the implementation ideas developed in disk++ , we use the possibilities offered by FORTRAN 2003. These possibilities allow one to create new types with public and private arguments, and member functions. This is close to the notion of class in C++ but without template. Hence, the implementation of HHO methods can be as generic as possible in code_aster.

We outline in what follows the eight basic objects that we have created to facilitate the implementation of HHO methods in code_aster. These objects have public and private arguments, and member functions to access and modify the private arguments or to compute the different quantities that we need.

- HHO_Field contains global information such as the numbering, the name of the global variables which are necessary for the assembly and other operators;
- HHO_Data contains information as the face degree, the cell degree, the gradient degree, and the stabilization coefficient;
- HHO_Face contains information about a face such as the topological dimension, the nodes coordinates, the type of the geometric element, the barycenter, the diameter, the measure, the outward normal...
- HHO_Cell contains the same information than for a face but for a cell. There is also a list of type HHO_Face to have information about the faces of the cell.
- HHO_Monomials contains information to generate quickly the monomials used to compute the basis functions;

- `HHO_Basis_Cell` and `HHO_Basis_Face` allow one to compute the basis functions for a cell and a face, respectively;
- `HHO_Quadrature` allows one to generate a quadrature on the physical element for a cell or a face.

We present in Listing A.1 a short example where we compute the scalar mass matrix associated with a cell.

```
SUBROUTINE hhoMassMatCell(hhoCell, hhoData, massMat)
   TYPE(HHO_CELL),  INTENT(IN)  :: hhoCell
   TYPE(HHO_DATA),  INTENT(IN)  :: hhoData
   REAL(KIND=8),    INTENT(OUT) :: massMat(MSIZE, MSIZE)
! ---------------------------------------------------------------
! Compute the scalar mass matrix of a Cell
! In hhoCell  : current HHO Cell
! In hhoData  : information about HHO parameters
! Out massMat : mass matrix
! ---------------------------------------------------------------
    TYPE(HHO_Basis_Cell) :: hhoBasisCell
    TYPE(HHO_Quadrature) :: hhoQuad
    REAL(KIND=8) :: basisScalEval(BSIZE), pg(3), wpg
    INTEGER :: dimMat, ipg, cell_degree
! ---------------------------------------------------------------
! --- Initialize basis functions
    call hhoBasisCell%initialize(hhoCell)
! --- Get cell degree
    cell_degree = hhoData%cell_degree()
! --- Dimension of the mass matrix
    dimMat = hhoBasisCell%BSSize(0, cell_degree)
! --- Initialize the mass matrix to zero
    massMat = 0.d0
! --- Get quadrature of order 2* cell_degree()
    call hhoQuad%GetQuadCell(hhoCell, 2*cell_degree)
! --- Loop on quadrature points
    do ipg = 1, hhoQuad%nbQuadPoints()
! ------ Get coordinates and weight of the quadrature point
       pg  = hhoQuad%points(1:3,ipg)
       wpg = hhoQuad%weights(ipg)
! ------ Evaluate scalar basis functions at the quadrature point
       call hhoBasisCell%BSEval(hhoCell, pg , 0, &
                                cell_degree, basisScalEval)
! ------ Evaluate massMat (use BLAS routine dsyr)
       call dsyr('U', dimMat, wpg, basisScalEval, 1, &
                 massMat, MSIZE)
    end do
! --- Copy the lower part
    call hhoCopySymPartMat('U', massMat(1:dimMat,1:dimMat))
END SUBROUTINE
```

Listing A.1: A short example on how to compute the scalar mass matrix associated with a cell.

We remark that the implementation is light and uses mainly the HHO objects since all the details are hidden in these objects. Note that to compute the scalar mass matrix associated with a face, it is only necessary to replace everywhere in the `hhoMassMatCell` routine the keyword "cell" by "face".

A.9 Comparison of performances with disk++

We compare the difference of performances between disk++ and code_aster for a mesh composed of 26,846 tetrahedra and 55,541 faces. We measure the time to compute the elementary contributions, the summation, the static condensation, and the assembly, i.e. the steps summarized in Fig. A.5. The results are shown in Tab. A.1 for the simulation of a problem in large elastoplastic deformations. We observe that the performances are similar between disk++ and code_aster for $k = 1$, whereas code_aster is 25% more efficient than disk++ for $k = 2$. We list here the main reasons of this difference of performance for $k = 2$ by level of importance:

- The implementation of HHO methods in disk++ is more generic than in code_aster (general meshes, arbitrary order...). Hence, a lot of optimization can be done in code_aster since we consider only four geometric elements and $k = 1$ and $k = 2$ (disk++ pays here its generic approach);
- The data structures and the architecture of code_aster are strongly optimized;
- The construction of the different operator is less segmented in code_aster than in disk++;
- There is no dynamic allocation for the computation of elementary contributions in code_aster contrary to disk++.

Method HHO	Time (in s)		Difference (in %)
	disk++	code_aster	
$k = 1$	16.2	17.2	+ 6 %
$k = 2$	60	48	- 25 %

Table A.1: Performance comparison between disk++ and code_aster.

BIBLIOGRAPHY

[1] M. Abbas, G. Drouet, and P. Hild. The local average contact (LAC) method. *Comput. Methods Appl. Mech. Engrg.*, 339:488–513, 2018.

[2] M. Abbas, A. Ern, and N. Pignet. Hybrid High-Order methods for finite deformations of hyperelastic materials. *Comput. Mech.*, 62(4):909–928, 2018.

[3] M. Abbas, A. Ern, and N. Pignet. A Hybrid High-Order method for incremental associative plasticity with small deformations. *Comput. Methods Appl. Mech. Engrg.*, 346:891–912, 2019.

[4] M. Abbas, A. Ern, and N. Pignet. A Hybrid High-Order method for finite elastoplastic deformations within a logarithmic strain framework. *Int. J. Numer. Methods Eng.*, 120(3):303–327, 2019.

[5] C. Adam, T. J. R. Hughes, S. Bouabdallah, M. Zarroug, and H. Maitournam. Selective and reduced numerical integrations for NURBS-based isogeometric analysis. *Comput. Methods Appl. Mech. Engrg.*, 284:732–761, 2015.

[6] C. Agelet de Saracibar, M. Chiumenti, Q. Valverde, and M. Cervera. On the orthogonal subgrid scale pressure stabilization of finite deformation J2 plasticity. *Comput. Methods Appl. Mech. Eng.*, 195(9):1224 – 1251, 2006.

[7] J. Aghili, D. A. Di Pietro, and B. Ruffini. An *hp*-Hybrid High-Order Method for Variable Diffusion on General Meshes. *Comput. Methods Appl. Math.*, 17(3):359–376, 2017.

[8] D. Al Akhrass. *Méthodes éléments finis mixtes robustes pour gérer l'incompréssibilité en grandes déformations dans un cadre industriel*. PhD thesis, Ecole Nationale Supérieure des Mines de Saint-Etienne, 2014.

[9] D. Al Akhrass, J. Bruchon, S. Drapier, and S. Fayolle. Integrating a logarithmic-strain based hyperelastic formulation into a three-field mixed finite element formulation to deal with incompressibility in finite-strain elastoplasticity. *Finite Elem. Anal. Des.*, 86:61–70, 2014.

[10] P. Alart. Méthode de Newton généralisée en mécanique du contact. *J. Math. Pures Appl. (9)*, 76(1):83–108, 1997.

[11] J. Alberty, C. Carstensen, and D. Zarrabi. Adaptive numerical analysis in primal elastoplasticity with hardening. *Comput. Methods Appl. Mech. Engrg.*, 171(3-4):175–204, 1999.

[12] D. N. Arnold, F. Brezzi, B. Cockburn, and L. D. Marini. Unified analysis of discontinuous Galerkin methods for elliptic problems. *SIAM J. Numer. Anal.*, 39(5):1749–1779, 2001/02.

[13] E. Artioli, L. Beirão da Veiga, C. Lovadina, and E. Sacco. Arbitrary order 2D virtual elements for polygonal meshes: part II, inelastic problem. *Comput. Mech.*, 60(4):643–657, 2017.

[14] F. Auricchio and L. Beirão da Veiga. On a new integration scheme for von Mises plasticity with linear hardening. *Int. J. Numer. Meth. Engrg.*, 56:1375–1396, 2003.

[15] F. Auricchio, L. Beirão da Veiga, C. Lovadina, A. Reali, R. L. Taylor, and P. Wriggers. Approximation of incompressible large deformation elastic problems: some unresolved issues. *Comput. Mech.*, 52(5):1153–1167, 2013.

[16] F. Auricchio, L. Beirão da Veiga, C. Lovadina, and A. Reali. A stability study of some mixed finite elements for large deformation elasticity problems. *Comput. Methods Appl. Mech. Engrg.*, 194(9-11):1075–1092, 2005.

[17] F. Auricchio, L. Beirão da Veiga, C. Lovadina, and A. Reali. The importance of the exact satisfaction of the incompressibility constraint in nonlinear elasticity: mixed FEMs versus NURBS-based approximations. *Comput. Methods Appl. Mech. Engrg.*, 199(5-8):314–323, 2010.

[18] B. Ayuso de Dios, K. Lipnikov, and G. Manzini. The nonconforming virtual element method. *ESAIM Math. Model. Numer. Anal.*, 50(3):879–904, 2016.

[19] L. Baillet and T. Sassi. Méthode d'éléments finis avec hybridisation frontière pour les problèmes de contact avec frottement. *C. R. Math. Acad. Sci. Paris*, 334(10):917–922, 2002.

[20] L. Baillet and T. Sassi. Mixed finite element methods for the Signorini problem with friction. *Numer. Methods Partial Differential Equations*, 22(6):1489–1508, 2006.

[21] J. M. Ball. Convexity conditions and existence theorems in nonlinear elasticity. *Arch. Rational Mech. Anal.*, 63(4):337–403, 1976/77.

[22] J. M. Ball. Discontinuous equilibrium solutions and cavitation in nonlinear elasticity. *Philos. Trans. Roy. Soc. London Ser. A*, 306(1496):557–611, 1982.

[23] P. Ballard. Steady sliding frictional contact problems in linear elasticity. *J. Elasticity*, 110(1):33–61, 2013.

[24] R. Bargellini, J. Besson, E. Lorentz, and S. Michel-Ponnelle. A non-local finite element based on volumetric strain gradient: Application to ductile fracture. *Computational Materials Science*, 45:762–767, 2009.

[25] P. T. Barton, D. Drikakis, and E. I. Romenski. An Eulerian finite-volume scheme for large elastoplastic deformations in solids. *Int. J. Numer. Meth. Engng*, 81:453–484, 2010.

[26] H. R. Bayat, J. Krämer, L. Wunderlich, S. Wulfinghoff, S. Reese, B. Wohlmuth, and C. Wieners. Numerical evaluation of discontinuous and nonconforming finite element methods in nonlinear solid mechanics. *Comput. Mech.*, 62(6):1413–1427, 2018.

[27] H. R. Bayat, S. Wulfinghoff, S. Kastian, and S. Reese. On the use of reduced integration in combination with discontinuous galerkin discretization: application to volumetric and shear locking problems. *Advanced Modeling and Simulation in Engineering Sciences*, 5(1):10, 2018.

[28] L. Beirão da Veiga, F. Brezzi, and L. D. Marini. Virtual elements for linear elasticity problems. *SIAM J. Numer. Anal.*, 51(2):794–812, 2013.

[29] L. Beirão da Veiga, F. Brezzi, L. D. Marini, and A. Russo. Virtual element implementation for general elliptic equations. In *Building bridges: connections and challenges in modern approaches to numerical partial differential equations*, volume 114 of *Lect. Notes Comput. Sci. Eng.*, pages 39–71. Springer, [Cham], 2016.

[30] L. Beirão da Veiga, C. Lovadina, and D. Mora. A virtual element method for elastic and inelastic problems on polytope meshes. *Comput. Methods Appl. Mech. Engrg.*, 295:327–346, 2015.

[31] F. Ben Belgacem and Y. Renard. Hybrid finite element methods for the Signorini problem. *Math. Comp.*, 72(243):1117–1145, 2003.

[32] D. Boffi, M. Botti, and D. A. Di Pietro. A nonconforming high-order method for the Biot problem on general meshes. *SIAM J. Sci. Comput.*, 38(3):A1508–A1537, 2016.

[33] F. Bonaldi, D. A. Di Pietro, G. Geymonat, and F. Krasucki. A Hybrid High-Order method for Kirchhoff-Love plate bending problems. *ESAIM Math. Model. Numer. Anal.*, 52(2):393–421, 2018.

[34] J. Bonelle, D. A. Di Pietro, and A. Ern. Low-order reconstruction operators on polyhedral meshes: application to compatible discrete operator schemes. *Comput. Aided Geom. Design*, 35/36:27–41, 2015.

[35] J. Bonelle and A. Ern. Analysis of compatible discrete operator schemes for elliptic problems on polyhedral meshes. *ESAIM Math. Model. Numer. Anal.*, 48(2):553–581, 2014.

[36] J. Bonet and R. D. Wood. *Nonlinear continuum mechanics for finite element analysis*. Cambridge university press, Cambridge, 1997.

[37] V. Bostan and W. Han. A posteriori error analysis for finite element solutions of a frictional contact problem. *Comput. Methods Appl. Mech. Engrg.*, 195:1252–1274, 2006.

[38] L. Botti and D. A. Di Pietro. Assessment of Hybrid High-Order methods on curved meshes and comparison with discontinuous Galerkin methods. *J. Comput. Phys.*, 370:58–84, 2018.

[39] L. Botti, D. A. Di Pietro, and J. Droniou. A Hybrid High-Order method for the incompressible Navier-Stokes equations based on Temam's device. *J. Comput. Phys.*, 376:786–816, 2019.

[40] M. Botti, D. A. Di Pietro, and P. Sochala. A Hybrid High-Order Method for Nonlinear Elasticity. *SIAM J. Numer. Anal.*, 55(6):2687–2717, 2017.

[41] H. Brezis. Équations et inéquations non linéaires dans les espaces vectoriels en dualité. *Ann. Inst. Fourier (Grenoble)*, 18(fasc. 1):115–175, 1968.

[42] F. Brezzi, K. Lipnikov, and M. Shashkov. Convergence of the mimetic finite difference method for diffusion problems on polyhedral meshes. *SIAM J. Numer. Anal.*, 43(5):1872–1896, 2005.

[43] F. Brezzi, K. Lipnikov, and V. Simoncini. A family of mimetic finite difference methods on polygonal and polyhedral meshes. *Math. Models Methods Appl. Sci.*, 15(10):1533–1551, 2005.

[44] U. Brink and E. Stein. On some mixed finite element methods for incompressible and nearly incompressible finite elasticity. *Comput. Mech.*, 19(1):105–119, 1996.

[45] E. Burman and A. Ern. An unfitted Hybrid High-Order method for elliptic interface problems. *SIAM J. Numer. Anal.*, 56(3):1525–1546, 2018.

[46] V. Calo, M. Cicuttin, Q. Deng, and A. Ern. Spectral approximation of elliptic operators by the Hybrid High-Order method. *Math. Comp.*, 88(318):1559–1586, 2019.

[47] P. Cardiff, A. Karač, and A. Ivanković. A large strain finite volume method for orthotropic bodies with general material orientations. *Comput. Methods Appl. Mech. Engrg.*, 268:318–335, 2014.

[48] C. Carstensen and F. Hellwig. Low-order discontinuous Petrov-Galerkin finite element methods for linear elasticity. *SIAM J. Numer. Anal.*, 54(6):3388–3410, 2016.

[49] K. L. Cascavita, J. Bleyer, X. Chateau, and A. Ern. Hybrid Discretization Methods with Adaptive Yield Surface Detection for Bingham Pipe Flows. *J. Sci. Comput.*, 77(3):1424–1443, 2018.

[50] K. L. Cascavita, F. Chouly, and A. Ern. Hybrid High-Order discretizations combined with nitsche's method for Dirichlet and Signorini boundary conditions. *IMA J. Numer. Anal.* To appear. hal-02016378.

[51] M. Cervera, M. Chiumenti, L. Benedetti, and R. Codina. Mixed stabilized finite element methods in nonlinear solid mechanics. Part III: compressible and incompressible plasticity. *Comput. Methods Appl. Mech. Engrg.*, 285:752–775, 2015.

[52] M. Cervera, M. Chiumenti, and R. Codina. Mixed stabilized finite element methods in nonlinear solid mechanics Part I: formulation. *Comput. Methods Appl. Mech. Engrg.*, 199(37-40):2559–2570, 2010.

[53] M. Cervera, M. Chiumenti, Q. Valverde, and C. Agelet de Saracibar. Mixed linear/-linear simplicial elements for incompressible elasticity and plasticity. *Comput. Methods Appl. Mech. Engrg.*, 192(49):5249–5263, 2003.

[54] F. Chave, D. A. Di Pietro, and L. Formaggia. A Hybrid High-Order method for Darcy flows in fractured porous media. *SIAM J. Sci. Comput.*, 40(2):1063–1094, 2018.

[55] F. Chave, D. A. Di Pietro, and L. Formaggia. A Hybrid High-Order method for passive transport in fractured porous media. *Int. J. Geomath.*, 10(12), 2019.

[56] F. Chave, D. A. Di Pietro, F. Marche, and F. Pigeonneau. A Hybrid High-Order method for the Cahn-Hilliard problem in mixed form. *SIAM J. Numer. Anal.*, 54(3):1873–1898, 2016.

[57] A. Chernov, M. Maischak, and E. Stephan. A priori error estimates for hp penalty BEM for contact problems in elasticity. *Comput. Methods Appl. Mech. Engrg.*, 196:3871–3880, 2007.

[58] H. Chi, L. Beirão da Veiga, and G. H. Paulino. Some basic formulations of the virtual element method (VEM) for finite deformations. *Comput. Methods Appl. Mech. Engrg.*, 318:148–192, 2017.

[59] M. Chiumenti, M. Cervera, and R. Codina. A mixed three-field FE formulation for stress accurate analysis including the incompressible limit. *Comput. Methods Appl. Mech. Engrg.*, 283:1095–1116, 2015.

[60] M. Chiumenti, Q. Valverde, C. Agelet de Saracibar, and M. Cervera. A stabilized formulation for incompressible plasticity using linear triangles and tetrahedra. *Int. J. Plasticity*, 20(8):1487–1504, 2004.

[61] F. Chouly. An adaptation of Nitsche's method to the Tresca friction problem. *J. Math. Anal. Appl.*, 411:329–339, 2014.

[62] F. Chouly, A. Ern, and N. Pignet. A Hybrid High-Order discretization combined with Nitsche's method for contact and Tresca friction in small strain elasticity. submitted.

[63] F. Chouly, M. Fabre, P. Hild, R. Mlika, J. Pousin, and Y. Renard. An overview of recent results on Nitsche's method for contact problems. In *Geometrically unfitted finite element methods and applications*, volume 121 of *Lect. Notes Comput. Sci. Eng.*, pages 93–141. Springer, Cham, 2017.

[64] F. Chouly and P. Hild. A Nitsche-based method for unilateral contact problems: numerical analysis. *SIAM J. Numer. Anal.*, 51(2):1295–1307, 2013.

[65] F. Chouly and P. Hild. On convergence of the penalty method for unilateral contact problems. *Appl. Numer. Math.*, 65:27–40, 2013.

[66] F. Chouly, P. Hild, V. Lleras, and Y. Renard. Nitsche-based finite element method for contact with Coulomb friction. In *Numerical Mathematics and Advanced Applications ENUMATH 2017*, volume 126 of *Lect. Notes Comput. Sci. Eng.*, pages 839–847. Springer, Cham, 2019.

[67] F. Chouly, P. Hild, and Y. Renard. Symmetric and non-symmetric variants of Nitsche's method for contact problems in elasticity: theory and numerical experiments. *Math. Comp.*, 84(293):1089–1112, 2015.

[68] F. Chouly, R. Mlika, and Y. Renard. An unbiased Nitsche's approximation of the frictional contact between two elastic structures. *Numer. Math.*, 139(3):593–631, 2018.

[69] P. G. Ciarlet. *The Finite Element Method for Elliptic Problems*. North-Holland, Amsterdam, 1978.

[70] P. G. Ciarlet. *Mathematical elasticity. Vol. I*, volume 20 of *Studies in Mathematics and its Applications*. North-Holland Publishing Co., Amsterdam, 1988. Three-dimensional elasticity.

[71] M. Cicuttin, D. A. Di Pietro, and A. Ern. Implementation of Discontinuous Skeletal methods on arbitrary-dimensional, polytopal meshes using generic programming. *J. Comput. Appl. Math.*, 344:852–874, 2018.

[72] M. Cicuttin, A. Ern, and S. Lemaire. A Hybrid High-Order method for highly oscillatory elliptic problems. *Comput. Methods Appl. Math.*, 2019. To appear.

[73] B. Cockburn. Discontinuous Galerkin methods. *ZAMM Z. Angew. Math. Mech.*, 83(11):731–754, 2003.

[74] B. Cockburn, D. A. Di Pietro, and A. Ern. Bridging the Hybrid High-Order and hybridizable discontinuous Galerkin methods. *ESAIM Math. Model. Numer. Anal.*, 50(3):635–650, 2016.

[75] B. Cockburn, O. Dubois, J. Gopalakrishnan, and S. Tan. Multigrid for an HDG method. *IMA J. Numer. Anal.*, 34(4):1386–1425, 2014.

[76] B. Cockburn, J. Gopalakrishnan, and R. Lazarov. Unified hybridization of discontinuous Galerkin, mixed, and continuous Galerkin methods for second order elliptic problems. *SIAM J. Numer. Anal.*, 47(2):1319–1365, 2009.

[77] B. Cockburn, J. Gopalakrishnan, N. C. Nguyen, J. Peraire, and F.-J. Sayas. Analysis of HDG methods for Stokes flow. *Math. Comp.*, 80(274):723–760, 2011.

[78] B. Cockburn, D. Schötzau, and J. Wang. Discontinuous Galerkin methods for incompressible elastic materials. *Comput. Methods Appl. Mech. Engrg.*, 195(25-28):3184–3204, 2006.

[79] A. Curnier and P. Alart. A generalized Newton method for contact problems with friction. *J. Méc. Théor. Appl.*, 7(suppl. 1):67–82, 1988.

[80] G. Dal Maso, A. DeSimone, and M. G. Mora. Quasistatic evolution problems for linearly elastic–perfectly plastic materials. *Arch. Ration. Mech. Anal.*, 180(2):237–291, 2006.

[81] P. Daniel, A. Ern, I. Smears, and M. Vohralík. An adaptive *hp*-refinement strategy with computable guaranteed bound on the error reduction factor. *Comput. Math. Appl.*, 76(5):967–983, 2018.

[82] E. A. de Souza Neto, F. M. Andrade Pires, and D. R. J. Owen. F-bar-based linear triangles and tetrahedra for finite strain analysis of nearly incompressible solids. Part I: formulation and benchmarking. *Int. J. Numer. Meth. Engng*, 62:353–383, 2005.

[83] E. A. de Souza Neto, D. Peric, and D. R. Owen. *Computational methods for plasticity: theory and applications*. John Wiley & Sons, 2011.

[84] D. A. Di Pietro and J. Droniou. A Hybrid High-Order method for Leray-Lions elliptic equations on general meshes. *Math. Comp.*, 86(307):2159–2191, 2017.

[85] D. A. Di Pietro and J. Droniou. $W^{s,p}$-approximation properties of elliptic projectors on polynomial spaces, with application to the error analysis of a Hybrid High-Order discretisation of Leray-Lions problems. *Math. Models Methods Appl. Sci.*, 27(5):879–908, 2017.

[86] D. A. Di Pietro, J. Droniou, and A. Ern. A discontinuous-skeletal method for advection-diffusion-reaction on general meshes. *SIAM J. Numer. Anal.*, 53(5):2135–2157, 2015.

[87] D. A. Di Pietro, J. Droniou, and G. Manzini. Discontinuous Skeletal Gradient Discretisation Methods on polytopal meshes. *J. Comput. Phys.*, 355:397–425, 2018.

[88] D. A. Di Pietro and A. Ern. *Mathematical aspects of discontinuous Galerkin methods*, volume 69. Springer Berlin Heidelberg, 2011.

[89] D. A. Di Pietro and A. Ern. A Hybrid High-Order locking-free method for linear elasticity on general meshes. *Comput. Methods Appl. Mech. Engrg.*, 283:1–21, 2015.

[90] D. A. Di Pietro and A. Ern. Hybrid High-Order methods for variable-diffusion problems on general meshes. *C. R. Math. Acad. Sci. Paris*, 353(1):31–34, 2015.

[91] D. A. Di Pietro, A. Ern, and S. Lemaire. An arbitrary-order and compact-stencil discretization of diffusion on general meshes based on local reconstruction operators. *Comput. Methods Appl. Math.*, 14(4):461–472, 2014.

[92] D. A. Di Pietro, A. Ern, and S. Lemaire. A review of Hybrid High-Order methods: formulations, computational aspects, comparison with other methods. In *Building bridges: connections and challenges in modern approaches to numerical partial differential equations*, volume 114 of *Lect. Notes Comput. Sci. Eng.*, pages 205–236. Springer, 2016.

[93] D. A. Di Pietro, A. Ern, A. Linke, and F. Schieweck. A discontinuous skeletal method for the viscosity-dependent Stokes problem. *Comput. Methods Appl. Mech. Engrg.*, 306:175–195, 2016.

[94] D. A. Di Pietro and S. Krell. A Hybrid High-Order method for the steady incompressible Navier–Stokes problem. *J. Sci. Comput.*, 74(3):1677–1705, 2018.

[95] D. A. Di Pietro and R. Tittarelli. An introduction to Hybrid High-Order methods. In *Numerical methods for PDEs*, volume 15 of *SEMA SIMAI Springer Ser.*, pages 75–128. Springer, Cham, 2018.

[96] I. Dione. Optimal convergence analysis of the unilateral contact problem with and without Tresca friction conditions by the penalty method. *J. Math. Anal. Appl.*, 472(1):266–284, 2019.

[97] J. K. Djoko, F. Ebobisse, A. T. McBride, and B. D. Reddy. A discontinuous Galerkin formulation for classical and gradient plasticity. I. Formulation and analysis. *Comput. Methods Appl. Mech. Engrg.*, 196(37-40):3881–3897, 2007.

[98] J. K. Djoko, F. Ebobisse, A. T. McBride, and B. D. Reddy. A discontinuous Galerkin formulation for classical and gradient plasticity. II. Algorithms and numerical analysis. *Comput. Methods Appl. Mech. Engrg.*, 197(1-4):1–21, 2007.

[99] M. Dobrowolski. A mixed finite element method for approximating incompressible materials. *SIAM J. Numer. Anal.*, 29(2):365–389, 1992.

[100] W. P. Doherty, E. L. Wilson, and R. L. Taylor. Stress analysis of axisymmetric solids utilizing higher-order quadrilateral finite elements. Technical report, University of California, 1969.

[101] J. Droniou and R. Eymard. A mixed finite volume scheme for anisotropic diffusion problems on any grid. *Numer. Math.*, 105(1):35–71, 2006.

[102] J. Droniou and R. Eymard. Study of the mixed finite volume method for Stokes and Navier-Stokes equations. *Numer. Methods Partial Differential Equations*, 25(1):137–171, 2009.

[103] J. Droniou, R. Eymard, T. Gallouët, and R. Herbin. A unified approach to mimetic finite difference, hybrid finite volume and mixed finite volume methods. *Math. Models Methods Appl. Sci.*, 20(2):265–295, 2010.

[104] J. Droniou, R. Eymard, T. Gallouët, and R. Herbin. Gradient schemes: a generic framework for the discretisation of linear, nonlinear and nonlocal elliptic and parabolic equations. *Math. Models Methods Appl. Sci.*, 23(13):2395–2432, 2013.

[105] J. Droniou, R. Eymard, and R. Herbin. Gradient schemes: generic tools for the numerical analysis of diffusion equations. *ESAIM Math. Model. Numer. Anal.*, 50(3):749–781, 2016.

[106] J. Droniou and B. P. Lamichhane. Gradient schemes for linear and non-linear elasticity equations. *Numer. Math.*, 129(2):251–277, 2015.

[107] G. Drouet and P. Hild. Optimal convergence for discrete variational inequalities modelling Signorini contact in 2D and 3D without additional assumptions on the unknown contact set. *SIAM J. Numer. Anal.*, 53(3):1488–1507, 2015.

[108] D. A. Dunavant. High degree efficient symmetrical Gaussian quadrature rules for the triangle. *Int. J. Numer. Methods Eng.*, 21(6):1129–1148, 1985.

[109] G. Duvaut and J.-L. Lions. *Les inéquations en mécanique et en physique*, volume 21 of *Travaux et Recherches Mathématiques*. Dunod, Paris, 1972.

[110] C. Eck, J. Jarušek, and M. Krbec. *Unilateral contact problems*, volume 270 of *Pure and Applied Mathematics (Boca Raton)*. Chapman & Hall/CRC, Boca Raton, FL, 2005.

[111] Electricité de France. Finite element *code_aster*, structures and thermomechanics analysis for studies and research. Open source on www.code-aster.org, 1989–2019.

[112] T. Elguedj, Y. Bazilevs, V. M. Calo, and T. J. R. Hughes. $\bar{B}$ and $\bar{F}$ projection methods for nearly incompressible linear and non-linear elasticity and plasticity using higher-order NURBS elements. *Comput. Methods Appl. Mech. Eng.*, 197(33):2732 – 2762, 2008.

[113] T. Elguedj and T. J. R. Hughes. Isogeometric analysis of nearly incompressible large strain plasticity. *Comput. Methods Appl. Mech. Engrg.*, 268:388–416, 2014.

[114] A. Ern and J.-L. Guermond. Finite element quasi-interpolation and best approximation. *ESAIM Math. Model. Numer. Anal.*, 51(4):1367–1385, 2017.

[115] A. T. Eyck, F. Celiker, and A. Lew. Adaptive stabilization of discontinuous Galerkin methods for nonlinear elasticity: analytical estimates. *Comput. Methods Appl. Mech. Engrg.*, 197(33-40):2989–3000, 2008.

[116] A. T. Eyck, F. Celiker, and A. Lew. Adaptive stabilization of discontinuous Galerkin methods for nonlinear elasticity: motivation, formulation, and numerical examples. *Comput. Methods Appl. Mech. Engrg.*, 197(45-48):3605–3622, 2008.

[117] A. T. Eyck and A. Lew. Discontinuous Galerkin methods for non-linear elasticity. *Int. J. Numer. Methods Eng.*, 67(9):1204–1243, 2006.

[118] A. T. Eyck and A. Lew. An adaptive stabilization strategy for enhanced strain methods in non-linear elasticity. *Int. J. Numer. Methods Eng.*, 81(11):1387–1416, 2010.

[119] R. Eymard, T. Gallouët, and R. Herbin. A new finite volume scheme for anisotropic diffusion problems on general grids: convergence analysis. *C. R. Math. Acad. Sci. Paris*, 344(6):403–406, 2007.

[120] R. Eymard, T. Gallouët, and R. Herbin. Discretization of heterogeneous and anisotropic diffusion problems on general nonconforming meshes SUSHI: a scheme using stabilization and hybrid interfaces. *IMA J. Numer. Anal.*, 30(4):1009–1043, 2010.

[121] R. Eymard and C. Guichard. Discontinuous Galerkin gradient discretisations for the approximation of second-order differential operators in divergence form. *Comput. Appl. Math.*, 37(4):4023–4054, 2018.

[122] G. Fu, B. Cockburn, and H. Stolarski. Analysis of an HDG method for linear elasticity. *Int. J. Numer. Methods Eng.*, 102(3-4):551–575, 2015.

[123] R. Glowinski. *Numerical methods for nonlinear variational problems.* Springer-Verlag, 2008.

[124] A. Grundmann and M. Moeller. Invariant integration formulas for the n-simplex by combinatorial methods. *SIAM J. Numer. Anal.*, 15(2):282–290, 1978.

[125] Q. Guan, M. Gunzburger, and W. Zhao. Weak-Galerkin finite element methods for a second-order elliptic variational inequality. *Comput. Methods Appl. Mech. Engrg.*, 337:677–688, 2018.

[126] C. Hager, P. Hauret, P. Le Tallec, and B. I. Wohlmuth. Solving dynamic contact problems with local refinement in space and time. *Comput. Methods Appl. Mech. Engrg.*, 201/204:25–41, 2012.

[127] B. Halphen and Q. Son Nguyen. Sur les matériaux standard généralisés. *J. Mecanique.*, 14:39–63, 1975.

[128] W. Han and B. D. Reddy. *Plasticity: Mathematical Theory and Numerical Analysis.* Springer, New York, 2013.

[129] W. Han and M. Sofonea. *Quasistatic contact problems in viscoelasticity and viscoplasticity*, volume 30 of *AMS/IP Studies in Advanced Mathematics.* American Mathematical Society, Providence, RI, 2002.

[130] P. Hansbo. Nitsche's method for interface problems in computational mechanics. *GAMM-Mitt.*, 28(2):183–206, 2005.

[131] P. Hansbo. A discontinuous finite element method for elasto-plasticity. *Int. J. Numer. Meth. Biomed. Engng.*, 26(6):780–789, 2010.

[132] P. Hansbo and M. G. Larson. Discontinuous Galerkin methods for incompressible and nearly incompressible elasticity by Nitsche's method. *Comput. Methods Appl. Mech. Engrg.*, 191(17-18):1895–1908, 2002.

[133] J. Haslinger and I. Hlaváček. Approximation of the Signorini problem with friction by a mixed finite element method. *J. Math. Anal. Appl.*, 86(1):99–122, 1982.

[134] J. Haslinger, I. Hlaváček, and J. Nečas. *Numerical methods for unilateral problems in solid mechanics*, volume IV of *Handbook of Numerical Analysis (eds. P.G. Ciarlet and J.L. Lions)*. North-Holland Publishing Co., Amsterdam, 1996.

[135] P. Hauret and P. Le Tallec. Energy-controlling time integration methods for nonlinear elastodynamics and low-velocity impact. *Comput. Methods Appl. Mech. Engrg.*, 195(37-40):4890–4916, 2006.

[136] P. Hauret and P. Le Tallec. A discontinuous stabilized mortar method for general 3D elastic problems. *Comput. Methods Appl. Mech. Engrg.*, 196(49-52):4881–4900, 2007.

[137] T. Helfer, B. Michel, J.-M. Proix, M. Salvo, J. Sercombe, and M. Casella. Introducing the open-source mfront code generator: Application to mechanical behaviours and material knowledge management within the PLEIADES fuel element modelling platform. *Comput. Math. Appl.*, 70(5):994–1023, 2015.

[138] P. Hild. Éléments finis non conformes pour un problème de contact unilatéral avec frottement. *C. R. Acad. Sci. Paris Sér. I Math.*, 324(6):707–710, 1997.

[139] P. Hild. Numerical implementation of two nonconforming finite element methods for unilateral contact. *Comput. Methods Appl. Mech. Engrg.*, 184(1):99–123, 2000.

[140] P. Hild and Y. Renard. A stabilized Lagrange multiplier method for the finite element approximation of contact problems in elastostatics. *Numer. Math.*, 115(1):101–129, 2010.

[141] P. Hild and Y. Renard. An improved a priori error analysis for finite element approximations of Signorini's problem. *SIAM J. Numer. Anal.*, 50(5):2400–2419, 2012.

[142] R. Hill. A general theory of uniqueness and stability in elastic-plastic solids. *J. Mech. Phys. Solids.*, 6(3):236 – 249, 1958.

[143] B. Hudobivnik, F. Aldakheel, and P. Wriggers. A low order 3D virtual element formulation for finite elasto-plastic deformations. *Comput. Mech.*, 2018.

[144] S. Hüeber and B. I. Wohlmuth. An optimal a priori error estimate for nonlinear multibody contact problems. *SIAM J. Numer. Anal.*, 43(1):156–173, 2005.

[145] T. J. R. Hughes. Generalization of selective integration procedures to anisotropic and nonlinear media. *Int. J. Numer. Meth. Engrg.*, 15(9):1413–1418, 1980.

[146] L. John, M. Neilan, and I. Smears. Stable discontinuous galerkin fem without penalty parameters. In B. Karasözen, M. Manguoğlu, M. Tezer-Sezgin, S. Göktepe, and Ö. Uğur, editors, *Numerical Mathematics and Advanced Applications ENUMATH 2015*, pages 165–173. Springer International Publishing, 2016.

[147] H. Kabaria, A. J. Lew, and B. Cockburn. A hybridizable discontinuous Galerkin formulation for non-linear elasticity. *Comput. Methods Appl. Mech. Engrg.*, 283:303–329, 2015.

[148] N. Kikuchi and J. T. Oden. *Contact problems in elasticity: a study of variational inequalities and finite element methods*, volume 8 of *SIAM Studies in Applied Mathematics*. Society for Industrial and Applied Mathematics (SIAM), Philadelphia, PA, 1988.

[149] N. Kikuchi and Y. J. Song. Penalty-finite-element approximation of a class of unilateral problems in linear elasticity. *Quart. Appl. Math.*, 39:1–22, 1981.

[150] O. Klaas, A. Maniatty, and M. S. Shephard. A stabilized mixed finite element method for finite elasticity.: Formulation for linear displacement and pressure interpolation. *Computer Methods in Applied Mechanics and Engineering*, 180(1):65 – 79, 1999.

[151] J. Krämer, C. Wieners, B. Wohlmuth, and L. Wunderlich. A hybrid weakly nonconforming discretization for linear elasticity. *Proc. Appl. Math. Mech.*, 16(1):849–850, 2016.

[152] P. Krysl. Mean-strain eight-node hexahedron with optimized energy-sampling stabilization for large-strain deformation. *Int. J. Numer. Methods Eng.*, 103(9):650–670, 2015.

[153] P. Krysl. Mean-strain 8-node hexahedron with optimized energy-sampling stabilization. *Finite Elem. Anal. Des.*, 108:41–53, 2016.

[154] Y. Kuznetsov, K. Lipnikov, and M. Shashkov. The mimetic finite difference method on polygonal meshes for diffusion-type problems. *Comput. Geosci.*, 8(4):301–324 (2005), 2004.

[155] P. Laborde and Y. Renard. Fixed point strategies for elastostatic frictional contact problems. *Math. Methods Appl. Sci.*, 31(4):415–441, 2008.

[156] T. A. Laursen. *Computational contact and impact mechanics*. Springer-Verlag, Berlin, 2002.

[157] P. Le Tallec, C. Rahier, and A. Kaiss. Three-dimensional incompressible viscoelasticity in large strains: formulation and numerical approximation. *Comput. Methods Appl. Mech. Engrg.*, 109(3-4):233–258, 1993.

[158] C. Lehrenfeld. *Hybrid Discontinuous Galerkin methods for solving incompressible flow problems*. PhD thesis, Rheinisch-Westfälischen Technischen Hochschule Aachen, Aachen, 2010.

[159] J. Lemaitre and J.-L. Chaboche. *Mechanics of Solid Materials*. University Press, Cambridge, 1994.

[160] A. Lew, P. Neff, D. Sulsky, and M. Ortiz. Optimal BV estimates for a discontinuous Galerkin method for linear elasticity. *AMRX Appl. Math. Res. Express*, 2004(3):73–106, 2004.

[161] Y. Lian and Z. Li. A numerical study on cavitation in nonlinear elasticity—defects and configurational forces. *Math. Models Methods Appl. Sci.*, 21(12):2551–2574, 2011.

[162] R. Liu, M. F. Wheeler, C. N. Dawson, and R. H. Dean. A fast convergent rate preserving discontinuous Galerkin framework for rate-independent plasticity problems. *Comput. Methods Appl. Mech. Engrg.*, 199(49-52):3213–3226, 2010.

[163] R. Liu, M. F. Wheeler, and I. Yotov. On the spatial formulation of discontinuous Galerkin methods for finite elastoplasticity. *Comput. Methods Appl. Mech. Engrg.*, 253:219–236, 2013.

[164] E. Lorentz and V. Godard. Gradient damage models: Toward full-scale computations. *Comput. Methods Appl. Mech. Engrg.*, 200:1927–1944, 2011.

[165] D. S. Malkus and T. J. Hughes. Mixed finite element methods - reduced and selective integration techniques: A unification of concepts. *Computer Methods in Applied Mechanics and Engineering*, 15(1):63 – 81, 1978.

[166] A. T. McBride and B. D. Reddy. A discontinuous Galerkin formulation of a model of gradient plasticity at finite strains. *Comput. Methods Appl. Mech. Engrg.*, 198(21-26):1805–1820, 2009.

[167] C. Miehe, N. Apel, and M. Lambrecht. Anisotropic additive plasticity in the logarithmic strain space: modular kinematic formulation and implementation based on incremental minimization principles for standard materials. *Comput. Methods Appl. Mech. Engrg.*, 191(47-48):5383–5425, 2002.

[168] R. Mlika, Y. Renard, and F. Chouly. An unbiased Nitsche's formulation of large deformation frictional contact and self-contact. *Comput. Methods Appl. Mech. Engrg.*, 325:265–288, 2017.

[169] L. Molari, G. Wells, K. Garikipati, and F. Ubertini. A discontinuous Galerkin method for strain gradient-dependent damage: study of interpolations and convergence. *Comput. Methods Appl. Mech. Engrg.*, 195:1480–1498, 2006.

[170] M. Moussaoui and K. Khodja. Régularité des solutions d'un problème mêlé Dirichlet-Signorini dans un domaine polygonal plan. *Comm. Partial Differential Equations*, 17(5-6):805–826, 1992.

[171] N. C. Nguyen and J. Peraire. Hybridizable discontinuous Galerkin methods for partial differential equations in continuum mechanics. *J. Comput. Phys.*, 231(18):5955–5988, 2012.

[172] N. C. Nguyen, J. Peraire, and B. Cockburn. High-order implicit hybridizable discontinuous Galerkin methods for acoustics and elastodynamics. *J. Comput. Phys.*, 230(10):3695–3718, 2011.

[173] J. Nitsche. Über ein Variationsprinzip zur Lösung von Dirichlet-Problemen bei Verwendung von Teilräumen, die keinen Randbedingungen unterworfen sind. *Abh. Math. Sem. Univ. Hamburg*, 36:9–15, 1971.

[174] L. Noels and R. Radovitzky. A general discontinuous Galerkin method for finite hyperelasticity. Formulation and numerical applications. *Int. J. Numer. Methods Eng.*, 68(1):64–97, 2006.

[175] J. T. Oden and N. Kikuchi. Finite element methods for constrained problems in elasticity. *Internat. J. Numer. Meth. Engrg.*, 18:701–705, 1982.

[176] J. T. Oden and S. J. Kim. Interior penalty methods for finite element approximations of the Signorini problem in elastostatics. *Comput. Math. Appl.*, 8(1):35–56, 1982.

[177] R. W. Ogden. *Non-linear elastic deformations*. Dover Publication, New-York, 1997.

[178] E. Pipping, O. Sander, and R. Kornhuber. Variational formulation of rate- and state-dependent friction problems. *ZAMM Z. Angew. Math. Mech.*, 95(4):377–395, 2015.

[179] J. P. Ponthot. *Mécanique des milieux continus en grandes transformations et traitement unifié par la méthode des éléments finis.* PhD thesis, Univerisité de Liège, 1995.

[180] K. Poulios and Y. Renard. An unconstrained integral approximation of large sliding frictional contact between deformable solids. *Comp. Struct.*, 153:75–90, 2015.

[181] S. Reese. On a consistent hourglass stabilization technique to treat large inelastic deformations and thermo-mechanical coupling in plane strain problems. *Int. J. Numer. Meth. Engrg.*, 57(8):1095–1127, 2003.

[182] S. Reese, H. R. Bayat, and S. Wulfinghoff. On an equivalence between a discontinuous Galerkin method and reduced integration with hourglass stabilization for finite elasticity. *Comput. Methods Appl. Mech. Engrg.*, 325:175–197, 2017.

[183] S. Reese, M. Küssner, and B. D. Reddy. A new stabilization technique for finite elements in non-linear elasticity. *Int. J. Numer. Meth. Engrg.*, 44(11):1617–1652, 1999.

[184] S. Reese and P. Wriggers. A stabilization technique to avoid hourglassing in finite elasticity. *Int. J. Numer. Meth. Engrg.*, 48(1):79–109, 2000.

[185] Y. Renard. Generalized Newton's methods for the approximation and resolution of frictional contact problems in elasticity. *Comput. Methods Appl. Mech. Engrg.*, 256:38–55, 2013.

[186] A. Seitz, W. A. Wall, and A. Popp. Nitsche's method for finite deformation thermo-mechanical contact problems. *Comput. Mech.*, 63(6):1091–1110, 2019.

[187] R. Sevilla, M. Giacomini, and A. Huerta. A locking-free face-centred finite volume (FCFV) method for linear elastostatics. *Computers and Structures*, 212:43–57, 2019.

[188] A. Signorini. Questioni di elasticità non linearizzata e semi-linearizzata. *Rend. di Matematica*, 18:95–139, 1959.

[189] J. C. Simo. A framework for finite strain elastoplasticity based on maximum plastic dissipation and the multiplicative decomposition. I. Continuum formulation. *Comput. Methods Appl. Mech. Engrg.*, 66(2):199–219, 1988.

[190] J. C. Simo. Algorithms for static and dynamic multiplicative plasticity that preserve the classical return mapping schemes of the infinitesimal theory. *Comput. Methods Appl. Mech. Engrg.*, 99:61–112, 1992.

[191] J. C. Simo and F. Armero. Geometrically nonlinear enhanced strain mixed methods and the method of incompatible modes. *Int. J. Numer. Methods Eng.*, 33(7):1413–1449, 1992.

[192] J. C. Simo, F. Armero, and R. L. Taylor. Improved versions of assumed enhanced strain trilinear elements for 3D finite deformation problems. *Comput. Methods Appl. Mech. Engrg.*, 110(3-4):359–386, 1993.

[193] J. C. Simo and T. J. R. Hughes. *Computational Inelasticity.* Springer, Berlin, 1998.

[194] J. C. Simo and M. S. Rifai. A class of mixed assumed strain methods and the method of incompatible modes. *Int. J. Numer. Methods Eng.*, 29(8):1595–1638, 1990.

[195] J. C. Simo and R. L. Taylor. Consistent tangent operators for rate-independent elasto-plasticity. *Comput. Methods Appl. Mech. Engrg.*, 48(1):101–118, 1985.

[196] J. C. Simo, R. L. Taylor, and K. S. Pister. Variational and projection methods for the volume constraint in finite deformation elasto-plasticity. *Comput. Methods Appl. Mech. Engrg.*, 51(1):177–208, 1985.

[197] S.-C. Soon. *Hybridizable Discontinuous Galerkin Method for Solid Mechanics*. PhD thesis, University of Minnesota, 2008.

[198] S.-C. Soon, B. Cockburn, and H. K. Stolarski. A hybridizable discontinuous Galerkin method for linear elasticity. *Int. J. Numer. Methods Eng.*, 80(8):1058–1092, 2009.

[199] R. Stenberg. On some techniques for approximating boundary conditions in the finite element method. *J. Comput. Appl. Math.*, 63(1-3):139–148, 1995.

[200] L. Szabó. On the eigenvalues of the fourth-order constitutive tensor and loss of strong ellipticity in elastoplasticity. *Int. J. Plasticity*, 13(10):809–835, 1998.

[201] L. Szabó. A semi-analytical integration method for J2 flow theory of plasticity with linear isotropic hardening. *Comput. Methods Appl. Mech. Engrg.*, 198:2151–2166, 2009.

[202] G. A. Taylor, C. Bailey, and M. Cross. A vertex-based finite volume method applied to non-linear material problems in computational solid mechanics. *Int. J. Numer. Meth. Engng*, 56:507–529, 2003.

[203] S. Terrana, N. C. Nguyen, J. Bonet, and J. Peraire. A hybridizable discontinuous Galerkin method for both thin and 3D nonlinear elastic structures. *Comput. Methods Appl. Mech. Engrg.*, 352:561–585, 2019.

[204] C. Wang, J. Wang, R. Wang, and R. Zhang. A locking-free weak Galerkin finite element method for elasticity problems in the primal formulation. *J. Comput. Appl. Math.*, 307:346–366, 2016.

[205] F. Wang, W. Han, and X. Cheng. Discontinuous Galerkin methods for solving the Signorini problem. *IMA J. Numer. Anal.*, 31(4):1754–1772, 2011.

[206] F. Wang and H. Wei. Virtual element method for simplified friction problem. *Appl. Math. Letters*, 85:125–131, 2018.

[207] B. Wohlmuth. Variationally consistent discretization schemes and numerical algorithms for contact problems. *Acta Numer.*, 20:569–734, 2011.

[208] P. Wriggers. *Computational Contact Mechanics*. Wiley, 2002.

[209] P. Wriggers and B. Hudobivnik. A low order virtual element formulation for finite elasto-plastic deformations. *Comput. Methods Appl. Mech. Engrg.*, 327:459–477, 2017.

[210] P. Wriggers, B. D. Reddy, W. Rust, and B. Hudobivnik. Efficient virtual element formulations for compressible and incompressible finite deformations. *Comput. Mech.*, 60(2):253–268, 2017.

[211] P. Wriggers, W. T. Rust, and B. D. Reddy. A virtual element method for contact. *Comput. Mech.*, 58(6):1039–1050, 2016.

[212] S. Wulfinghoff, H. R. Bayat, A. Alipour, and S. Reese. A low-order locking-free hybrid discontinuous Galerkin element formulation for large deformations. *Comput. Methods Appl. Mech. Engrg.*, 323:353–372, 2017.

[213] X. Xu and D. Henao. An efficient numerical method for cavitation in nonlinear elasticity. *Math. Models Methods Appl. Sci.*, 21(8):1733–1760, 2011.

[214] S. Yadav, A. K. Pani, and E. J. Park. Superconvergent discontinuous Galerkin methods for nonlinear elliptic equations. *Math. Comp.*, 82:1297–1335, 2013.

[215] Y. Zhang, E. Lorentz, and J. Besson. Ductile damage modelling with locking-free regularised GTN model. *Int. J. Numer. Methods Eng.*, 113:1871–1903, 2018.

[216] M. Zhao, H. Wu, and C. Xiong. Error analysis of HDG approximations for elliptic variational inequality: obstacle problem. *Numer. Algorithms*, 81(2):445–463, 2019.

[217] O. C. Zienkiewicz, R. L. Taylor, and J. M. Too. Reduced integration technique in general analysis of plates and shells. *Int. J. Numer. Methods Eng.*, 3(2):275–290, 1971.